THÈSE

présentée en vue d'obtenir le grade de Docteur de l'Université de Lille en *Sciences et technologies de l'information et de la communication*

École Doctorale: **072 Sciences pour l'Ingénieur**

Romain BEHAEGEL

Sub 6 GHz MIMO Channel sounder development based on Software Defined Radio boards and LTE signal

Développement d'un sondeur de canal MIMO Sub 6 GHz s'appuyant sur des cartes SDR et un signal LTE

Soutenance prévue le 20/05/2021 à Villeneuve d'Ascq,
devant le jury composé de :

Rapporteurs

- M. François Gallée	Maître de Conférences, HDR, IMT Atlantique, Brest
- M. Matthieu Crussière	Maître de Conférences, HDR, IETR, Rennes

Présidente

- Mme. Maryline Hélard	Professeure, IETR, Rennes

Examinateurs

- M. Iyad Dayoub	Professeur, UPHF, Valenciennes

Invités

- M. Juan Moreno García-Loygorri	Dr, Universidad Politécnica de Madrid, Madrid
- M. Karen Varedanyan	Engineer, National Instrument, Armenia

Directeurs de thèse

- Mme Marion BERBINEAU	Directrice de Recherche, Université Gustave Eiffel, COSYS, Villeneuve d'ascq
- M. Raffaele D'ERRICO	Researcher, CEA, LETI, MINATEC, Grenoble

Acknowledgments

I would like to start by thanking my Ph.D directors, Mme Marion BERBINEAU and M. Raffaele D'ERRICO, for their support during my Ph.D study. The realisation of this work could have not been possible without their guidance and patience.

I exploit this opportunity to thank my scholarship donors, CEA, CEA-Tech and the region "Hauts de France" and FEDER for their financial support that allowed me to conduct my Ph.D.

I would like to thank M. François GALLEE and M. Matthieu Cruissière for accepting to review and evaluate the thesis. Also, I thank Mme. Maryline HELARD and M. Iyad DAYOUB for accepting to be members of the jury.

Thank you to M. Karen VAREDANYAN, National engineer, for all his help on the channel sounder development during this PhD.

Thank you to M. Christophe ROSINSKI for all his help during measurement campaigns.

Thank you to Olivier, Pascal, Audrey, Boris and all the other people from CEA-Tech Haut-de-France for their support throughout these 3 years.

Special thanks to my friends and colleagues at Gustave Eiffel University: Michel, Anthony, Mohamed, Kawtar, Ali, Malik and all the others with whom I have worked. Thanks for the time and all the advice you gave me.

I thank all of my family who have been there for me and always believed in my success

Ultimately, I would like to thank Sana, who accepts me and carries me through good and bad days.

Abstract

With the development of the digital society and the Internet of Things, the development of communication systems is more and more important with a need to further increase transmission rates per user, capacity, security and flexibility. This trend is general in all areas of society and in particular in the field of transport. In particular, the era of the digitization of services and autonomous and connected mobility requires the development of V2X (vehicles for all) communication systems offering increasingly higher transmission speeds, capacity and a level of security. Fifth generation (5G) cellular networks promise significant improvements in throughput, capacity, latency and reliability.

Given the possibilities offered by this technology and due to the obsolescence of the current ground-train communication system used in Europe, the GSM-R (Global System for Mobile Communication - Railway) will be replaced by the FRMCS (Future Railway Communication System), which provides for the parallel use of several radio access techniques including 5G. It is therefore possible to envisage ever more robust telecommunications applications such as automatic train monitoring, control and regulation of rail traffic. In addition, the performance promised by this 5G technology will allow the emergence of new services: remote driving of trains without a driver on board, deployment of automated trains, coupling / decoupling of line trains, etc. Thus, 5G paves the way for the rail networks of the future that are more connected, more automated and, therefore, more available, safer and more respectful of the environment.

The development of these new services requires in particular to guarantee the robustness, reliability and operational safety of the wireless links on which they are based. To do this, it is necessary to be able to assess the different communication systems before their deployment in railway environments representative of those encountered along the railways (cuttings, urban areas, rural areas, stations, viaducts, tunnels, etc.) by emulating these environments in channel emulators using representative models obtained by measurements or simulations (ray tracing/launching).

In this context, this thesis objective is to implement a 4x4 MIMO (Multiple-input, Multiple-output) channel sounder in the sub 6 GHz range in order to characterize different railway environments for which models do not exist yet. The equipment developed is based on the use of software radio cards and specific software that have been modified. It is a LTE (Long Term Evolution) type telecommunications system composed by a base station that will be installed alongside the infrastructures, and a mobile station on the train. The radio channel characteristics are obtained by calculating the channel estimate via the pilots of an LTE-OFDM symbol. It can be used on the move. The assembly is compact enough to be transported and allow measurements of the channel in any type of environment.

In this PhD thesis, we describe the different channel models in the literature and we analyze the existing models in the rail sector in order to identify the environments where it is necessary to carry out measurements. We focus on simple Tapped Delay Line–TDL models. Secondly, we

provide a state of the art of the different types of channel sounder and radio channel sounding techniques. This work allowed us to choose the sounder technology developed, namely a system based on the use of reconfigurable SDR (Software Defined Radio) platforms and an LTE type signal. We then detail the architecture, principle and implementation of the channel sounder and its validation by simple measurements. This part constitutes the main contribution of the thesis. Finally, the last chapter is devoted to field measurements. We conclude and give the very many perspectives of the work

Keywords : Channel sounder, MIMO, Channel Estimation, SDR, Railway, 5G.

Résumé

Avec le développement de la société numérique et de l'Internet des objets, le développement des systèmes de communication est de plus en plus important avec un besoin d'accroître toujours plus les débits de transmission par utilisateur, la capacité, la sécurité et la flexibilité. Cette tendance est générale dans tous les domaines de la société et en particulier dans le domaine des transports. En particulier l'ère de la digitalisation des services et la mobilité autonome et connectée nécessite le développement de systèmes de communication V2X (Vehicules à tout) offrant des débits de transmission, une capacité et un niveau de sécurité de plus en plus élevés. Les réseaux cellulaires de cinquième génération (5G) promettent des améliorations importantes en termes de débit, de capacité, de latence et de fiabilité.

Ainsi, grâce aux possibilités offertes par cette technologie et en raison de l'obsolescence du système actuel de communication sol-train utilisé en Europe, le GSM-R (Global System for Mobile Communication – Railway) sera remplacé par le FRMCS (Future Railway Communication System) qui prévoit l'utilisation en parallèle de plusieurs techniques d'accès radio dont la 5G. Ainsi il est possible d'envisager des applications des télécommunications toujours plus robustes telles que la surveillance automatique des trains, le contrôle, la régulation du trafic ferroviaire. En outre, les performances promises par cette technologie 5G permettront l'émergence de nouveaux services : conduite à distance de trains sans conducteur à bord, déploiement de trains automatisés, couplage/découplage de trains en ligne, etc. Ainsi, la 5G ouvre la voie aux réseaux ferroviaires du futur plus connectés, plus automatisés et, ainsi, plus disponibles, plus sûrs et plus respectueux de l'environnement. Le développement de ces nouveaux services nécessite notamment de garantir la robustesse, la fiabilité et la sûreté de fonctionnement des liens sans fils sur lesquels ils reposent. Pour ce faire, il convient de pouvoir évaluer les différents systèmes de communication en amont de leur déploiement dans des environnements ferroviaires représentatifs de ceux rencontrés le long des voies ferrées (tranchées, zones urbaines, zones rurales, gares, viaducs, tunnels, etc.) grâce à l'émulation de ces environnements dans des émulateurs de canaux en utilisant des modèles de canaux. Les modèles de canaux représentatifs sont obtenus par des mesures ou des simulations (Tracer/lancer de rayons).

Ainsi ce travail de thèse se focalise sur la mise en œuvre d'un sondeur de canal MIMO (Multiple-input, Multiple-output) 4x4 dans la gamme sub 6 GHz afin de caractériser différents environnements ferroviaires dont les modèles n'existent pas encore. L'équipement développé s'appuie sur l'utilisation de cartes radio logicielles et de logiciels spécifiques qui ont été modifiés. C'est un système de télécommunications de type LTE (Long Term Evolution) constitué par une station de base qui sera installée le long de l'infrastructure, et une station mobile dans le train. La mesure des caractéristiques du canal radioélectrique s'effectue grâce au calcul de l'estimation du canal via les pilotes d'un symbole LTE-OFDM. Il peut être utilisé en mobilité. L'ensemble est assez compact pour être transporté et permettre des mesures du canal dans tout type d'environnement.

Dans ce mémoire nous décrivons les différents modèles de canaux de la littérature et nous analysons les modèles existants dans le domaine ferroviaire afin d'identifier les environnements où il faudra réaliser des mesures. Nous nous focalisons sur des modèles simples de type ligne à retard (Tapped Delay Line –TDL). Dans un deuxième temps nous proposons un état de l'art des différents types de sondeur de canaux et techniques de sondage du canal radioélectrique. Ce travail nous a permis de choisir la technologie du sondeur développé, à savoir un système reposant sur l'utilisation de cartes SDR reconfigurables (Software Defined Radio) et d'un signal de type LTE. Nous détaillons ensuite l'architecture, le principe et la mise en œuvre du sondeur de canal et sa validation par des mesures simples. Cette partie constitue le cœur de la thèse. Enfin le dernier chapitre est consacré à des mesures terrains. Nous concluons et donnons les perspectives très nombreuses du travail

Mots-clés : Sondeur de canal, MIMO, SDR, Estimation de canal, ferroviaire, 5G.

Contents

List of Figures

List of Tables

Mathematical Notations and Acronyms

List of Mathematical Notations and Operators

$(.)^*$	Conjugate operation
$(.)^T$	Transpose operation
$(.)^H$	Hermitian conjugate transpose
$E(.)$	Expectation operator
$\|.\|$	Absolute value operator

List of Notations

f_c	Operating frequency
f_d	Maximal Doppler spread
$x(t)$	Transmitted complex signal
$y(t)$	Received complex signal
$v(t)$	Additive noise
$h(t)$	Complex impulse response
$X(f)$	Fourier transform of x(t)
$Y(f)$	Fourier transform of y(t)
$H(f)$	Fourier transform of h(t)
$V(f)$	Fourier transform v(t)
σ^2	Variance of the signal
n	nth antenna at the MS
m	mth antenna at the BS
k	subcarrier position
c	cth cluster
l	Channel index of the CIR
L	Total CIR length
P_c	Power of the cth cluster
δ	Dirac delta function
P_p	Power to the pth path
τ	Delay
H_{record}	Recorded vector by the channel sounder
Hn	Estimation applied to the receiving antenna n
$H_{meas}(m,n)$	CFR measured by the channel sounder
$H_{calib}(m,n)$	CFR of the calibration by the channel sounder
$H_{est}(m,n)$	CFR estimation after calibration by the channel sounder

σ_{SF}	Lognormal shadow fading, applied as a bulk parameter to the cth cluster for a given drop
P	Number of paths per cluster.
p	pth path
$\theta_{c,p,AoD}$	AoD for the pth subpath of the cth cluster
$\theta_{c,p,AoA}$	AoA for the pth subpath of the cth cluster
$G_{BS}(\theta_{c,p,AoD})$	BS antenna gain of each array element
$G_{MS}(\theta_{c,p,AoA})$	MS antenna gain of each array element
j	Square root of -1
i	OFDM symbol
N_w	Wave number $\frac{2\pi}{\lambda}$ where λ is the carrier wavelength in meters
d_m	Distance in meters from BS antenna element m from the reference (m = 1) antenna. For the reference antenna $m = 1$, d_1=0
d_n	Distance in meters from MS antenna element n from the reference (n = 1) antenna. For the reference antenna$n = 1$, d_1 =0
$\Theta_{c,p}$	Phase of the pth subpath of the cth cluster
$\|v\|$	Magnitude of the MS velocity vector
θ_v	Angle of the MS velocity vector
Kf	is the K factor
$\chi_{BS}^{v}\theta_{c,p,AoD}$	BS antenna complex response for the V-pol component
$\chi_{BS}^{h}\theta_{n,m,AoD}$	BS antenna complex response for the H-pol component
$\chi_{MS}^{v}\theta_{n,m,AoA}$	MS antenna complex response for the V-pol component
$\chi_{MS}^{h}\theta_{n,m,AoA}$	MS antenna complex response for the H-pol component
$\|\chi^{\cdot}(.)\|^2$	Antenna gain
r_{n1}	Random variable representing the power ratio of waves of the pth path leaving the BS in the vertical direction and arriving at the MS in the horizontal direction (v-h) to those leaving in the vertical direction and arriving in the vertical direction (v-v)
r_{n2}	Random variable representing the power ratio of waves of the pth path leaving the BS in the horizontal direction and arriving at the MS in the vertical direction (h-v) to those leaving in the vertical direction and arriving in the vertical direction (v-v)
$\Theta_{c,p}^{x,y}$	Phase offset of the pth subpath of the cth cluster between the x component (either the horizontal h or vertical v) of the BS element and the y component (either the horizontal h or vertical v) of the MS element
r_{n1} and r_{n2}	i.i.d variable
$F_{N,n,V}$ –	Antenna element n field patterns for vertical and horizontal
$F_{N,n,H}$	polarization respectively
$F_{M,m,V}$ –	Antenna element m field patterns for vertical and horizontal
$F_{M,m,H}$	polarization respectively
$K_{c,p}$	Complex gain of the path p in the cluster c
λ_c	Wave length of the carrier frequency
$\Phi_{c,p}$	Initial phase of the path p in the cluster c
$\phi_{c,p}$	AoD of the path p in the cluster c

$\varphi_{c,p}$	AoA of the path p in the cluster c
$v_{c,p}$	Doppler frequency component of the path p in the cluster c
$\overline{r}_m$	Location vector of Tx array element m,
x_m, y_m and z_m	Component of $\overline{r}_m$ to x,y and z axis respectively,
$\overline{r}_n.\overline{\psi}_{c,p}$	Scalar product of Rx antenna element n and arrival angle of the path p
$\overline{r}_m.\overline{\psi}_{c,p}$	Scalar product of Tx antenna element m and arrival angle of the path p
v_{rx} and v_{tx}	Velocity vectors of the receiver and transmitter respectively
$\Omega_{BS,p}$	Propagation directions of the *pth* path at the BS
$\Omega_{MS,p}$	Propagation directions of the *pth* path at the MS
$S[n,n]$	SSS sequences
$FSPL(d)$	Free space path loss
$PL(d)$	Path loss
$PDP(\tau)$	Power delay profile

List of Acronyms

AA	Arrival Area
AoA	Angle of Arrival
AoD	Angle of Departure
AWGN	Additive White Gaussian Noise
BER	Bit Error Rate
BS	Base Station
CA	Close Area
CEA	Closer Area
CDL	Cluster Delay Line
CDM	Code Division multiplexing
CDMA	Code Division Multiple Access
CIR	Channel Impulse Response
CFR	Channel Frequency Response
CP	Cyclic Prefix
CPICH	Common Pilot Channel
CRS	Cell-specific Reference Signal
DA	Distant area
DFT	Discrete Fourier Transform
DOA	Direction of arrival
DOD	Direction of Departure
FDD	Frequency Division Duplex
FDM	Frequency Division Multiplexing
FFT	Fast Fourier Transform
FIFO	First In First Out
FT	Fourier Transform
GI	Guard Interval
GBSCM	Geometry-based stochastic channel models
GPSDO	GPS-disciplined oscillator
GSM	Global System for Mobile communications
HSL	High Speed Line
HSR	High Speed Railway

IFFT	Inverse Fast Fourier Transform
ICI	Inter-Carrier Interference.
IID	Independent and Identical Distribution
ISI	Inter-Symbol Interference
LL model	Link-Level model
LMMSE	Linear Minimum Mean Square Error
LO	Local Oscillators
LOS	Line Of Sight
LS	Least Square
LTE	Long Term Evolution
MLE	Maximum likelihood estimate
MRS	Moving Relay Stations
MS	Mobile Station
MSE	Mean Square Error
NGSCM	Non-Geometric Stochastic Channel Model
NLOS	Non Line Of Sight
OCXO	Oven Controlled Crystal Oscillator
OFDM	Orthogonal Frequency Division Modulation
PDP	Power Delay Profil
PL	Path-Loss
PN	Pseudo Noise
PR	Pseudo-random sequence
PRBS	Pseudo random binary sequence
PSS	Primary Synchronization Signal
QPSK	Quadrature Phase Shift Keying
RA	Remote Area
RE	Resource Element
RS	Ressource Signal
RMa	Rural Macro
RMS	Root Mean Square
SCM	Spatial Channel Model
SCME	Spatial Channel Model Extended
SDR	Software Defined Radio
SIMO	Single Input Multiple Output
SNR	Signal to Noise Ratio
SL model	System-Level model
STCC	Sliding Time Cross Correlator
SAGE	Space-Alternating Generalized Expectation Maximization
SV	Saleh-Valenzuela
SVD	Singular Value Decomposition
TA	Toward Area
TDL	Time Delay Line
TDD	Time Division Duplex
TDM	Time Division Multiplexing
TOA	Time of Arrival
TSPM	Time Spatial Propagation Model
UCA	Uniform Circular Array
UE	User Equipment
ULA	Uniform Linear Array

URA	Uniform rectangular Array
US	Uncorrelated Scatterers
USRP	Universal Software Radio Peripheral
UWB	Ultra Wide Band
WCDMA	Wide band CDMA
WSS	Wide-Sense Stationary
WSSUS	Wide Sense Stationary Uncorrelated Scattering.

General Introduction

Context and Motivations

With the development of digital technology and the Internet of Things, there is a growing need for very high transmission rates per user, network capacity, security and flexibility of communications systems. This trend is general in all domains of the society and particularly in the field of transport. The digitization of services and autonomous and connected mobility requires the development of V2X (vehicles for all) communication systems offering increasingly high transmission speeds, capacity and a level of safety and security for some applications. Fifth generation (5G) cellular networks promise significant improvements in throughput, capacity, latency and reliability. Thus, thanks to the possibilities of this technology and due to the obsolescence of the current train-to-ground communication system used in Europe, GSM-R (Global System for Mobile Communication - Railway) will be replaced by FRMCS (Future Railway Communication System), which considers parallel use of several radio bearers, based on different radio access techniques, namely Wi-Fi, LTE (Long Term Evolution), Satcom and 5G. This technology will allow the emergence of new critical services: remote driving of trains without a driver on board, deployment of automated trains, coupling / decoupling of trains while moving, *etc.* Thus, 5G technology paves the way for the rail networks of the future that are more connected, more automated and, therefore, more available, safer and more respectful of the environment.

The development of these new critical services requires to guarantee the robustness, reliability and operational safety of the wireless links on which they are based. For this purpose, it is necessary to be able to assess the various communication systems upstream of their deployment in railway environments representative of those encountered along railways (cuttings, urban areas, rural areas, stations, marshalling yards, tunnels, viaducts, *etc.*). In this context, there is an urgent need to avoid long and costly trials on the tracks by emulating both the radio access technologies and the railway radio channels representative of railway environments in channel emulators. This approach is called *"zero on site testing"* or *"digital testing"*. It exists since several years in the automotive domain [1] and a specific action is dedicated to this topic in the Shift2Rail program (`https://shift2rail.org/`). *"zero on site testing"* of communication systems should also allow to perform tests taking into account various type of perturbations such as network load, network perturbations, electromagnetic perturbations, which cannot be accessed directly during trials along railway lines. As a consequence, a virtual test laboratory requires the emulation of realistic and representative radio environments that rely on properly modelled radio channels obtained when possible with measurements or simulations (Ray tracing/ Ray launching on general).

Railway radio channel environments are very specific depending on the type of trains (High speed trains, regional trains, freight, *etc.*). In addition, one can consider train-to-ground (T2G), Train-to-train (T2T) and intra-train communications. The dynamic aspects (speed of the train)

should be also taken into account in the modelling. All these differences induce to consider different type of channel models.

Radio channel models can be empirical/statistic or deterministic, semi deterministic or site specific. A widely adopted model is based on systems theory where the parameters of the model can be deterministic or statistical. The model is in general a mathematical representation of the Channel Impulse Response (CIR) or the Channel Frequency Response (CFR). With the development and complexity increase of cellular systems, channel characterisation and modelling is a very intensive field of research in the scientific community and also in the telecommunication industry. Several channel models have been developed within European projects and are now considered as "standardized" channel models and considered as reference models in the standardisation groups, such as 3GPP or 5GPPP to evaluate fairly different bricks of the communication technology in development. We can mention for example ITU, SCM, WINNER, METIS models. The model complexity is ever evolving with the increasing complexity of geographical environments and the technologies, such as MIMO (Multiple Input Multiple Output), Massive MIMO, Beam forming, intelligent antennas, *etc.* More and more statistical parameters are taken into account such as angles of arrival and departure, antenna radiating diagram, *etc.* in order to model radio channels as close as possible to real radio channels.

To develop the *zero on site testing* for communication systems in the Railway domain, there is a need to develop the appropriate testing platforms in which the appropriate representative channel models can be implemented. For a given environment, all channel parameters have to be extracted from the statistical variations of the CIRs or CFRs measured with a channel sounder in Single Input – Single Output (SISO) or MIMO configurations. To do so, different types of channel sounders have been developed in recent years based on different types of excitation signal, antenna distribution, center frequency and bandwidth used for measurements. A particular interest was brought to the systems based on Software Defined Radio (SDR) platforms and Orthogonal Frequency Division Multiplexing (OFDM) excitation signal. This kind of platform offers a programmable and flexible hardware and software channel sounder and generally more portability for on-site measurements.

In this context, after a first of state of the art to identify existing Railway channel models that can be considered for *zero on site testing* of communication systems and identification of environments were additional measurements are needed, the motivation of this thesis were twofold. First, the aim was to develop and validate a new 4x4 MIMO channel sounder based on SDR platforms and modified standardized LTE Time Division Duplex (TDD) signal in the sub 6 GHz band able to support high speed. Second to perform measurements in railway environments not yet covered by existing models. The SDR-based channel sounder was verified and used in different indoor and outdoor scenarios at different speed. Unfortunately, due to the COVID-19 and lock down in Europe, it was not possible to envisage measurements in railway environment during the PhD duration.

Thesis Organization

This thesis manuscript is divided into five Chapters. After a reminder of the channel propagation characteristics and definitions, a literature survey on existing wide band radio channel models for wireless systems will be proposed in Chapter 1. It is important to notice that we will focus the survey on radio channel models that are considered for system performance evaluation at physical layer and standardized channel model in the world.

Thereafter, in Chapter 2, we will present a state of the art on existing radio channel models in the railway domain. We will highlight first the railway environments characteristics. Then,

the literature survey will show that mainly the case of High Speed Line is treated with specific environments namely open air rural, cutting, viaduct, station and tunnel. We will detail then the main Tap Delay Line (TDL) and Cluster Delay Line (CDL) channel models for each of these HSL environment as they constitutes models easy to implement in simple channel emulators. In this Chapter, we will highlight also the absence of channel models for the tunnel case.

In Chapter 3, we will propose a state of the art of the channel sounding techniques in time and frequency in order to position our work. We will present MIMO channel sounders in sub-6 GHz band and millimetre waves bands. Then we will detail the SDR-based channel sounders category and particularly the ones that consider LTE signal. Based on this analysis, we have decided to built a 4x4 MIMO SDR-based channel sounder based on the use of a standardized LTE transmission.

Chapter 4 is devoted to the description and validation of the developed SDR-based MIMO channel sounder in the sub 6 GHz band. After a detailed presentation of the hardware and software bricks, we will provide the description of the excitation signal based on a modified LTE standard signal. In a second part, we will explain the sounding method used to be able to perform real time measurements and acquisition at high speed. We will present how the CFRs are recorded and stored, then exploited in post-processing. The last part of this chapter will show the different validation steps of the channel sounder.

Chapter 5 will present the results of two measurement campaigns: indoor measurements in a corridor of the laboratory for LOS and NLOS 2x2 MIMO scenarios at 2.7 GHz and outdoor measurements at 3.5 GHz for LOS and NLOS scenarios at 6 and 20 km/h. We will present and comment the CFRs, CIRs and Path Loss measured. The main channel parameters are extracted when possible based on the Power Delay Profile (PDP).

Finally, we will conclude the thesis manuscript and we will propose some perspectives of this work.

Thesis Contributions

International Journal papers

- M. Berbineau and R. Behaegel and J. M. Garcia-Loygorri and R. Torrego and R. D'errico and A. Sabra and Y. Yan and J. Soler, "Channel models for performance evaluation of wireless systems in Railway environments," in IEEE Access Journal, 2021, Vol. 9, pages 45903-45918, . doi: 10.1109/ACCESS.2021.3066112

National Conference Papers

- R. Behaegel, Y Cocheril, R D'Errico, M Berbineau, "Sondeur de canal MIMO 4x4 pour des applications ferroviaires," in Journée Nationale Micro-ondes, 14-17 May 2019.

Miscellaneous Publications

European Project Deliverable

- Second main contributor to "Deliverable D 1.3, Characterization of the railway environment: channel models & general characteristics," J. Moreno, R. Behaegel, M. Berbineau, 31/12/2020, Public, Eu Project Emulradio4rail, GA 826152 (`http://www.emulradio4rail.eu/`)

Reports

- R. Behaegel, M. Berbineau, R. D'Errico, "Rapport d'activité," CEA, January 2020.

- R. Behaegel, M. Berbineau, R. D'Errico, "Rapport d'avancement de thèse," IFSTTAR, July 2020.
- R. Behaegel, M. Berbineau, R. D'Errico, "Rapport d'activité," CEA, January 2019.
- R. Behaegel, M. Berbineau, R. D'Errico, "Rapport d'avancement de thèse," IFSTTAR, June 2019.
- R. Behaegel, M. Berbineau, R. D'Errico, "Rapport d'activité," CEA, February 2018.

Posters and Presentations

- R. Behaegel, M. Berbineau, R. D'Errico, "Journée des thèse PRTT Haut-de-France," CEA, September 2020.
- R. Behaegel, M. Berbineau, R. D'Errico, "Journée des doctorants COSYS," IFSTTAR, October 2019.
- R. Behaegel, M. Berbineau, Y. Cocheril, "séminaire LEOST," IFSTTAR, September 2019.
- R. Behaegel, M. Berbineau, R. D'Errico, "Journée des thèse PRTT Haut-de-France," CEA, July 2019.
- R. Behaegel, M. Berbineau, Y. Cocheril, "Journée des doctorants COSYS," IFSTTAR, October 2018.
- R. Behaegel, M. Berbineau, R. D'Errico, "Journée des thèse PRTT Haut-de-France," CEA, July 2018.
- R. Behaegel, M. Berbineau, Y. Cocheril, "séminaire LEOST," CEA, April 2018.
- R. Behaegel, M. Berbineau, R. D'Errico, "Journée des thèse PRTT Haut-de-France," CEA, August 2017.

Chapter 1

Generalities on Radio channel models

1.1 Introduction

Wireless communications are a key technology to increase railway transport efficiency and safety. Consequently, the deployment of wireless communication devices is ever increasing in the railway domain not only for passenger applications but mainly for train exploitation. Particularly the need for safe and reliable radio links is becoming huge with the development of applications such as radio-based control command, remote control of engines, virtual coupling and decoupling of trains (platooning). These needs are accentuated with the development of Autonomous Train applications.

In order to be able to demonstrate the safety level and the reliability of safety-related of radio links, the evolution of key performance indicators at physical layer or at application layer (bit error rate, frame error rate, packet error rate, end-to-end delays, latency, etc.) should be known in different types of environments encountered by trains and metros. This requires to be able to perform radio system performance assessment in realistic environment conditions. In order to avoid large and expensive tests along the railway lines, the performance evaluation of the different radio links should be based on simulations and emulations employing realistic channel models related to railway context. Railway environments are generally very different than the environments considered in general in the wireless communication domains (cellular system development) or in other transport modes (automotive, maritime and aeronautical). Railway environments are composed of tunnels, cuttings, viaducts, open area, railway stations, the inside of the trains, various obstacles such as pylons and some combined scenarios.

This chapter presents a literature survey on existing radio channel models in the railway domain for wireless system performance evaluation. Consequently, on this work it is important to notice that we focus on radio channel models that are considered for system performance evaluation at physical layer, namely radio channel models able to express the complex impulse response or the transfer function of the channel and to be implemented in simulation or emulation chains. The aim of this analysis is to highlight the channel parameters we will need to extract during the channel sounding measurements in order to model the measured channel.

The rest of the chapter is organized as follows. Section1.2 will remind generalities regarding mobile radio propagation. Then, we will present the main used wide band radio channel models in the wireless telecommunications world. The models are detailed and presented trying to follow a chronological order of apparition at standardization bodies.

1.2 Mobile radio channel generalities and modelling

1.2.1 Introduction

In this part of the chapter we will first present the mobile radio channel characteristics. Secondly, the mathematical representation of SISO (Single Input Single Output) and MIMO (Multiple Input Multiple Output) systems are detailed with the impulse response and the transfer function of the channel. Then, the Bello functions are described to introduce the delay Doppler spread and the frequency Doppler spread functions.

1.2.2 Main mobile radio channel characteristics

In a SISO transmission, the various obstacles in the environment between the transmitter and the receiver (terrain geometry, buildings, vegetation...) generate various perturbations of the signal[2],[3]. These perturbations are related to physical phenomena: reflection, diffraction and diffusion. The wave direction, the amplitude, phase and polarization are affected by these phenomena [4] that generate multipaths between the transmitter and the receiver. In addition, when the vehicle is moving, frequency shift called Doppler shifts, are introduced on each path arriving to the receiver and create a Doppler spectrum that affects the signal. The multipaths phenomenon determines the main properties of the radio wave propagation channel [4]:

- time variability due to dynamic modifications of the radio propagation environment;
- spacial variability that describes a different behavior of the propagation channel when the transmitter and the receiver are moving. This provokes the large and small scale variations of the signal also called slow and fast fading.
- Frequency selectivity directly linked to multipaths phenomenon is illustrated on the impulse response or the transfer function respectively in time or in frequency.

1.2.2.1 Longitudinal attenuation (path loss)

In general, during a mobile radio transmission, the channel attenuates the power of the transmitted signal. Two types of attenuation exist:

- Large-scale attenuation that depends mainly on the distance between transmitter and receiver. It corresponds to the average attenuation of the signal received over distances of a hundred wavelengths and appears classically in the link budget of a transmission [5]. The attenuation at medium scale which corresponds to the variations of the received power over distances of the order of ten times the wavelength. It is caused mainly by the effects of masking the signal due to the various environmental obstacles present on the wave trajectory.
- The small-scale attenuation that corresponds to the fluctuations of the signal received over distances of the order of the wavelength. These variations are due to the physical phenomenon of multiple paths [6].

1.2.2.2 Multipaths

Following the optical analogy, the different obstacles between the transmitter and the receiver cause multiple copies of the signal (rays) traveling with different paths with different propagation delays τ .

These rays add constructively or destructively at the receiver, thereby giving rise to rapid fluctuations of the signal amplitude. This allows the reception of a signal even if there is no direct visibility between the transmitter and the receiver. Multipath provokes small scale variations that can reach several tens of dB.

Signal variations due to phenomena such as reflections, diffraction, scattering and diffusion as illustrated on 1.1. The transmission path between the transmitter and the receiver can vary from a simple direct path (Line Of Sight-LOS) to several indirect paths (Non Line Of Sight - NLOS) due to several obstacles (buildings, mountains, trees, etc.).

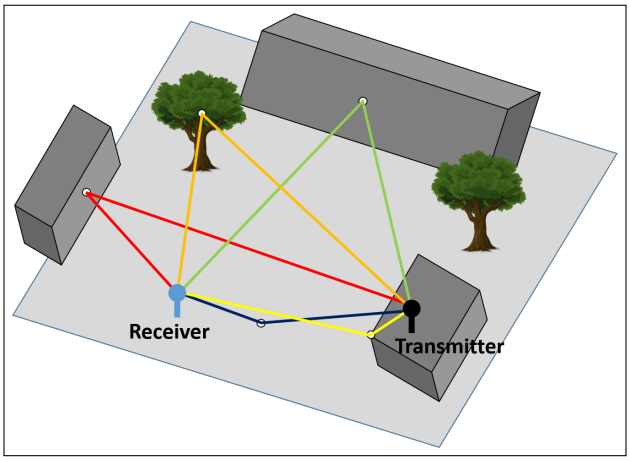

Figure 1.1: Illustration of propagation phenomena of multi-paths

As already mentioned, the wave direction, the amplitude, phase and polarization are affected by these phenomena that generate multipath between the transmitter and the receiver. The multipath phenomenon determines the main properties of the radio propagation channel. This is illustrated on 1.2. In addition, vehicle motion generates frequency shift called Doppler shifts, introduced on each path received. This creates a Doppler spectrum that affects the signal.

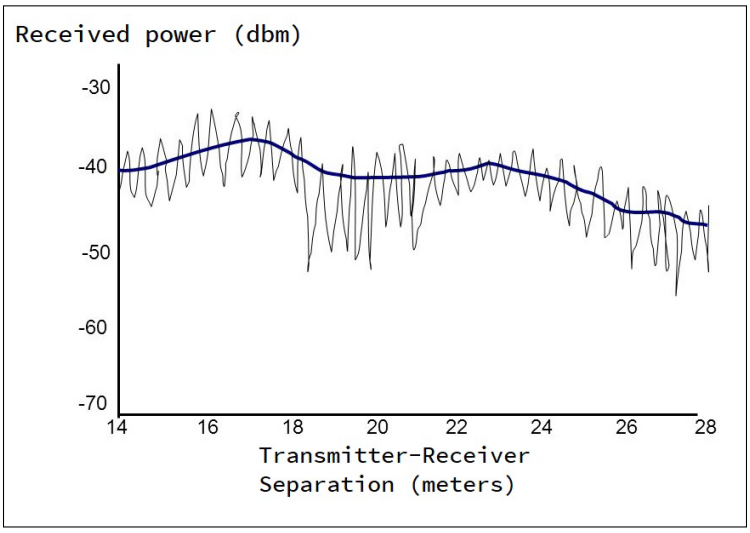

Figure 1.2: Illustration of slow and fast fading

1.2.2.3 Delay spread

The combinations of the different signal replicas that follow different propagation paths can be constructive or destructive depending if the signals are in phase or not. The delay spread Dr characterizes the variations of the delays of the different paths around the mean delay. The delay spread is given by the following relation:

$$D_r = \sqrt{\frac{\sum_p (\tau_p - \tau_m)^2 P_p}{\sum_p P_p}} \quad with \quad \tau_m = \frac{\sum_p \tau_p P_p}{\sum_p P_p} \tag{1.1}$$

where τ and P_p are respectively the associated delay and power to the pth path of the impulse response. The parameters characterizing the path delays in the channel are in general: First-Arrival Delay, Mean Excess Delay, Maximal Excess Delay, RMS (Root Mean Square) Delay Spread.

The First-Arrival Delay (τ_A) is a time delay corresponding to the arrival of the first transmitted signal at the receiver. It is usually measured at the receiver. This delay is set by the minimum possible propagation path delay from the transmitter to the receiver. It serves as a reference, and all delay measurements are made relative to it. Any measured delay longer than this reference delay is called an excess delay.

The Maximum Excess Delay (τ_m), also called Maximum Delay Spread, denoted as τ_m, is the relative time difference between the first signal component arriving at the receiver to the last component whose power level is above some threshold. The RMS Delay (τ_{rms}) is referred to the variance of the excess delay.

These parameters are illustrated in Figure 1.3 that represents the so called Power Delay Profile $P_h(\tau)$ at a given position. It refers to the average power associated with a given multipath delay when a short pulse is sent into the channel.

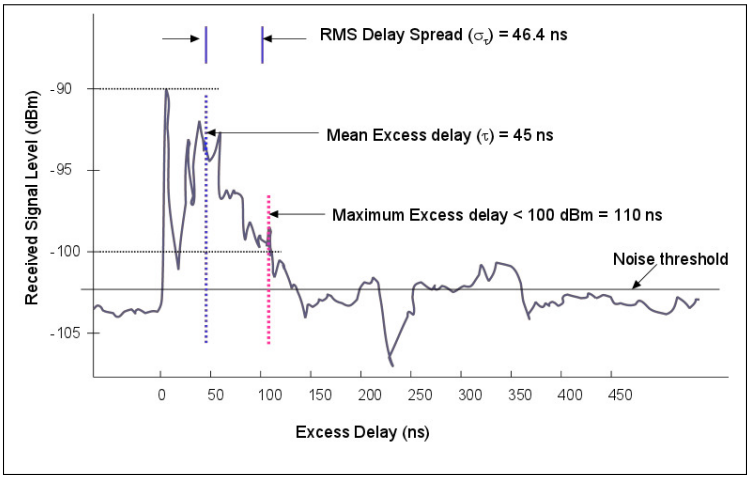

Figure 1.3: Illustration of Power delay profile measured

In the frequency domain, the channel coherence bandwidth D_r is defined as $Bc = \frac{1}{D_r}$ as a dual variable of D_r. B_c corresponds to the frequency band on which the transfer function will not vary. On this frequency band, the spectral components of the signal are affected similarly. Both parameters are used to characterize frequency selectivity of a channel. When the signal bandwidth B_s is much lower than the coherence bandwidth $B_s << B_c$, the channel is considered as non selective in frequency. On the contrary, the channel is frequency selective. This results in inter symbol interferences (ISI). Channel selectivity impacts the system performance.

1.2.2.4 Doppler effect

Doppler effect refers to the apparent shift of the radio signal frequency due to the mobility of the mobile station or variations in the environment. The Doppler shift is proportional to the mobile speed and the carrier frequency. The Doppler effect is characterized by a frequency

spread that corresponds to the difference between the largest and the smallest frequency shift due to multipath.

In the time domain, the Doppler effect corresponds to a time variation of the impulse response of the channel. T_c is the coherence time of the channel. T_c is dual to the Doppler shift. T_c indicates the duration for which the channel impulse response is stationary. When the symbol time Ts is much lower than the coherence time $T_s << T_c$, the channel is constant during the transmission. The channel is not selective in time. When Ts is much greater than $T_c(T_s >> T_c)$, the channel varies during a symbol duration, the channel is frequency selective.

The maximal Doppler shift denoted f_d in case of 1 path p with an angle of arrival θ on the mobile receiver compared to the direction of the mobile can be expressed as:

$$f_d = f_c - f_{in} = \frac{v}{c} f_c \cos\theta_p \tag{1.2}$$

were f_c is the operating frequency and c is the light speed, v is the mobile speed in m/s and f_{in} is the instantaneous frequency in Hz. Each individual path arriving with an angle θ_i experiences a Doppler shift f_{di}. Then depending of the angle of arrival distribution, a Doppler spectrum is observed. The most used Doppler spectrum representation are:

If the angle of arrival has a uniform distribution between $[-\pi, +\pi]$ the Doppler spectrum can be expressed by equation 1.3 [7] and represented by Figure 1.4. It is called "Classic" or "Jakes" Doppler spectrum.

$$S(f) = \begin{cases} \frac{\sigma^2}{\pi f_d} \cdot \frac{1}{\sqrt{1-\frac{f}{f_d}^2}}, & where - f_d \leq f \geq +f_d \\ 0, & otherwise \end{cases} \tag{1.3}$$

where σ^2 is the variance of the signal and f_d the maximal Doppler spread.

Depending on the distribution of the angles of arrival due to the environment but also due to the characteristics of receiving antenna, various Doppler spectrum shape exist. The most well known are the Flat, the Gaussian and the Rice Doppler spectrum.

The *Flat*, *Gaussian* and *Rice* Doppler spectra can be expressed by the following equations (1.4, 1.5, 1.6) [7] and are illustrated in Figure 1.4.

$$S(f) = \frac{1}{2f_d}, f_d \neq 0 \tag{1.4}$$

$$S(f) = \begin{cases} \frac{1}{\sqrt{2\pi\sigma^2}} exp(\frac{f^2}{2\sigma^2}), & |f| \leq f_d \\ 0, & |f| > f_d \end{cases} \tag{1.5}$$

$$S(f) = \begin{cases} \frac{0.41}{2\pi f_d} \cdot \frac{1}{\sqrt{1+10^9-(\frac{f}{f_d})^2}}, & |f| \leq f_d \\ 0, & |f| > f_d \end{cases} \tag{1.6}$$

where $\sigma = \sigma_g \times f_d$ with σ_g the standard deviation of the Gaussian classical function.

1.2.2.5 Radio electric noise

Noise is the main perturbing element in a digital communication. It is defined as any signal containing no useful information to find the original message. This noise has a power and allows

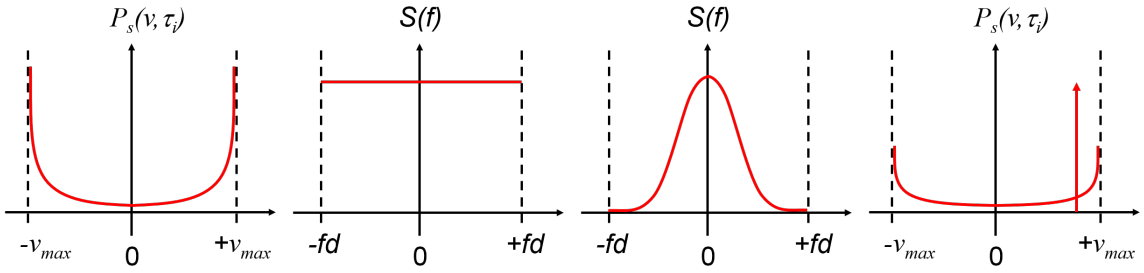

Figure 1.4: Representation of the *Classic* [8], *Flat* [7], *Gaussian* [7] and *Rice* [7] Doppler spectrum, from left to right respectively

to introduce a reference parameter: the signal to noise ratio (SNR) defined as the ratio of the power of the useful signal to the power of the noise: $SNR = \frac{P0}{\sigma^2}$. One of the benefits of digital communications is to offer lower noise sensitivity than analog communications.

The sources of noise are many, here is a non-exhaustive list: the internal noise of the components (thermal noise due to the activity of the electrons in the semiconductors), the cosmic radiation, human activity as the emission of other signals (non intentional perturbations) and also intentional noises (such as electromagnetic attacks with jammers). The noise is a stochastic value that neither transmitter nor receiver can control. It is necessary to assign a statistical model to noise. The most conventionally used is a complex Gaussian additive white noise with zero mean and variance equals to σ^2. In the case of railway environments, [9] has highlighted the presence of specific impulsive noise due to bad sliding contact between the catenary and the pantograph.

1.2.2.6 Diversity notion

Diversity is used in wireless transmission systems to combat small-scale fading caused by multipath and to improve overall system performance. It reflects the fact that the same bit of information experiences several independent representations of the channel during its transmission. The reception of independent replicas of the same signal makes it possible to increase the reliability of the link. The diversity gain at transmitter side is given by:

$$G_d = -\lim_{SNR\to\infty} \frac{log(P_e)}{logSNR} \tag{1.7}$$

where Pe corresponds to a binary probability of error and SNR is the signal to noise ratio.

Several diversity techniques exist, namely space, time, frequency, polarization. Space diversity consists of using multiple antennas separated at least by the distance of coherence from the channel (minimal distance for independent fading). In general minimal distance to be considered is $\lambda/2$ where λ is the wavelength. Spatial diversity exists on transmission and reception. Time diversity applies for the selective channels in time. The information is repeated in time at larger intervals than the coherence time of the channel (minimal duration between two independent fades).Time diversity is generally used with interleaving and error correction coding. Frequency diversity is used for frequency selective channels. The information is repeated over a frequency band wider than the channel coherency band (minimum frequency spacing between two frequencies with independent fading). Frequency diversity is the foundation of spread spectrum or multi-carrier techniques. Polarization diversity considers replicas of the same signal polarized differently.

The most common solution is the use of two orthogonal polarization, such as vertical and horizontal or circular right and left or more or less 45 degrees for example. Polarization diversity can be considered with collocated antennas. MIMO systems generally exploit spatial diversity by considering multiple antennas also combined with the other type of diversity. The propagation characteristics of the two waves must be different.

1.2.2.7 Correlation

Correlation between antennas is an important parameter for the performance of MIMO systems. It reflects the degree of average resemblance between the signals. Indeed, it conditions the spatial diversity that can be recovered by the multiple antennas, as well as the number of independent flows that can be transmitted over the same time and frequency resources. This correlation between channels depends on the angular dispersion (the difference between the extreme angles), the spacing of the antennas and their polarization. The correlation between two channels h_1 and h_2 is expressed as follows:

$$Cor(h_1, h_2) = E[h_1.h_2^*] \tag{1.8}$$

where E denotes the expectation and the exponent * indicates the complex conjugation. If we model $h1$ and $h2$ as Gaussian random variables of zero mean and unit variance, a unit correlation means that these two channels are identical, whereas a zero correlation means that they are completely independent. Between these two extremes, two channels may be more or less correlated. In practice, the correlation can be measured by the time average of the product $h1 \times h2$.

In a general propagation environment, the various signal replicas generated by the multi-paths are more or less correlated in time, in frequency or in space and are not affected by the same attenuation if they are low correlated. The introduction of MIMO techniques allows taking into account the different diversities. MIMO techniques exploit an additional dimension in the propagation channel: spatial diversity that can be characterized by the correlation degree at transmission and at reception side. This correlation degree depends on space between antennas, angle of arrival, angle of departure of the paths, angular spread that are related to the geometric distribution of obstacles in the propagation channel [10]. Variations of the signal polarization influence also the correlation degree in the channel.

1.2.3 Mathematical representation of the channel

1.2.3.1 Representation of the SISO channel

For a time-variant channel, the SISO channel can be defined by its impulse response, in the time domain or with the transfer function in the frequency domain [10]. The complex based band impulse response $h(t)$ is generally described with the input signal at the transmitter and with the output signal at the receiver as equation 1.9 [10].

$$y(t) = h(t) * x(t) + v(t) \tag{1.9}$$

where $x(t)$ and $y(t)$ are the transmitted and received complex signal respectively. And $v(t)$ is the additive noise at the receiver. The operator * is the convolution operator.

The system equation can be written as 1.10 in the frequency domain, where $Y(f)$ and $X(f)$ are the Fourier transform of $y(t)$ and $x(t)$ respectively.

$$Y(f) = H(f)X(f) + V(f) \tag{1.10}$$

where $Y(f)$, $H(f)$, $X(f)$ and $V(f)$ are respectively the Fourier transform of y(t), h(t), x(t) and v(t). $H(f)$ represent the transfer function of the channel.

With the effect of the environment on the signal, the impulse response h depends of the absolute time t and delay τ due to multi-paths components as presented before. The input signal x and output y of the channel are related to a convolution product as follow:

$$y(t) = \int_{-\infty}^{+\infty} h(t,\tau).x(t-\tau)d\tau \tag{1.11}$$

The transfer function is the frequency response of the channel in the frequency domain when it is excited by a sinusoïd with a frequency f at a moment t. The transfer function can be calculated by a Fourier transform (FT) from the impulse response as follows :

$$H(t,f) = \int_{-\infty}^{+\infty} h(t,\tau)exp(-j2\pi f\tau)d\tau \tag{1.12}$$

The relationship between the spectrum transmit signal X(f) and the received signal y(t) is given by :

$$y(t) = \int_{-\infty}^{+\infty} H(t,f).X(f)exp(j2\pi ft)df \tag{1.13}$$

1.2.3.2 Bello functions

The four system functions are known as Bello functions [11]. $h(t,\tau)$ is the Impulse response, $H(t,f)$ the Transfer function or frequency response, $S(\tau,f_d)$ the Delay Doppler spread function and $D(f,f_d)$ the Doppler spread function illustrated in Figure 1.5 :

- $h(t,\tau)$: Impulse response,
- $H(f,t)$:Transfer function,
- $S(\tau,f_d)$: Delay Doppler spread function,
- $D(f,f_d)$: Doppler spread function.

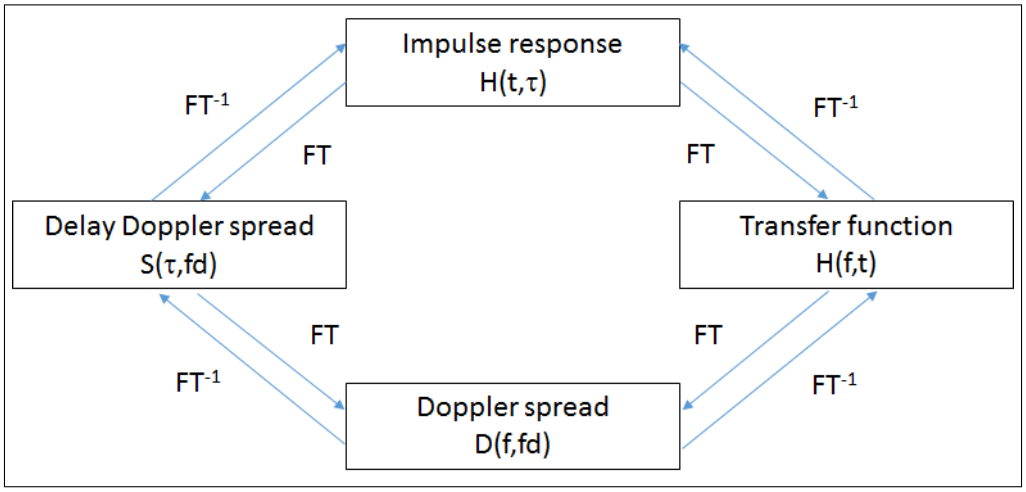

Figure 1.5: Relation between Bello functions

This representation shows that two other channel functions named delay Doppler function and frequency Doppler function exist. They are derived from a FT to the time variant impulse response and time variant frequency response respectively (transfer function) and given in [10].

Delay Doppler spread function $S(\tau, f_d)$

It gives information on the frequency Doppler spread for a delay τ. This function represents the impact of the Doppler effect on the temporal variation of the channel. The delay spread Doppler function can be calculated by a Fourier transform from the impulse response following equation 1.14:

$$h(t,\tau) = \int_{-\infty}^{+\infty} S(\tau, f_d) exp(j2\pi f_d t) df d \tag{1.14}$$

The $S(\tau, fd)$ function represents the temporal and frequency dispersion of the propagation channel. It gives also a representation of the mean power by delay τ and maximal Doppler spread f_d. It can be calculated by the following equation:

$$S(\tau, f_d) = \int_{-\infty}^{+\infty} h(t,\tau) exp(-j f_d t) dt \tag{1.15}$$

The receive signal can be written to replace 1.10 in 1.11 following the equation 1.16:

$$y(t) = \int_{-\infty}^{+\infty} \int_{-\infty}^{+\infty} S(\tau, f_d).x(t-\tau).exp(j2\pi f_d t).df_d.d(\tau) \tag{1.16}$$

Doppler spread function $D(f, f_d)$

$D(f, f_d)$ corresponds to the spectral response of the channel at a frequency offset f_d hertz with respect to the injected frequency f. the transfer function $H(f,t)$ and the delay Doppler spread function $S(\tau, f_d)$ are connected to $D(f, f_d)$ by the Fourier transform according to 1.17 and 1.18

$$D(f, f_d) = \int_{-\infty}^{+\infty} H(f,t) exp(-j2\pi f_d t) dt \tag{1.17}$$

$$S(\tau, f_d) = \int_{-\infty}^{+\infty} D(f, f_d) exp(j2\pi f_d t) df \tag{1.18}$$

Channel correlation function

The properties of the propagation channel vary versus time. Only a stochastic approach allows to access to the characteristic quantities of the channel. This approach should allow in theory to identify the laws of variations of the four functions of Bello in a multidimensional space (time, delay, frequency, Doppler spread).

The correlation Bello functions are defined by:

- $R_h(t_1, t_2; \tau_1, \tau_2) = E[h(t_1, \tau_1).h^*((t_2, \tau_2)]$
- $R_H(f_1, f_2; t_1, t_2) = E[H(f_1, t_1).H^*((f_2, t_2)]$
- $R_D(f_1, f_2; f_{d1}, f_{d2}) = E[D(f_1, f_{d1}).D^*((f_2, f_{d2})]$
- $R_S(\tau_1, \tau_2; f_{d1}, f_{d2}) = E[S(\tau_1, f_{d1}).S^*(\tau_2, f_{d2})]$

As with Bello functions, the correlation Bello functions are link each others by Fourier transform function. The difference is that with correlation, the Fourier transform is a double Fourier transform function. The relations between correlation Bello functions are presented in Figure 1.6.

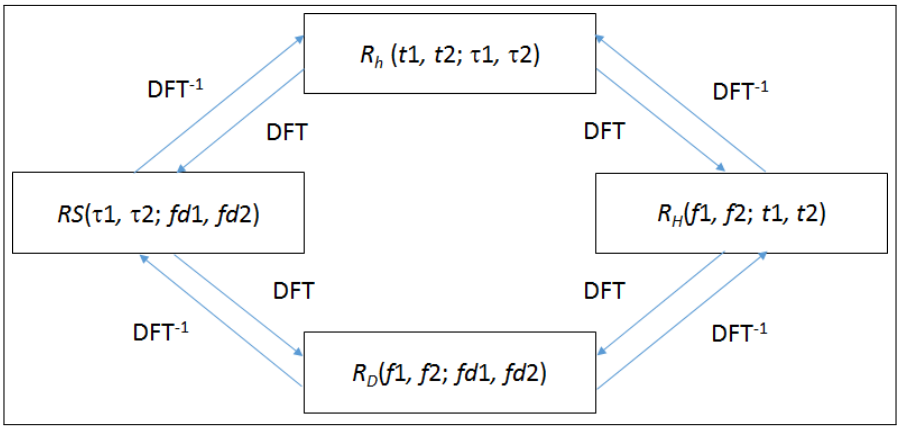

Figure 1.6: Relation between correlation Bello functions

The correlation function of Bello function can be simplified with different hypothesis relative to the stationary of the channel. The channel stationary can be in the time domain, frequency domain or a wide sens stationary with uncorrelated scatterers. A Wide sens stationary uncorrelated scatterers assume the channel stationary both in temporal and frequency domains.

1.2.3.3 Representation of the MIMO channel

A MIMO system is defined by the number of antennas at transmitter m side and the number of antennas at receiver side n. The classical representation of a MIMO channel relies on a channel description based on m x n independent SISO channels modeled with the **H** matrix. The equivalent diagonal matrix system allows expressing the channel as the superposition of several eigen-decorrelation channels. As recall in [12], it was demonstrated that the MIMO radio propagation channel is constituted of the superposition of several independent sub channels each carrying a fraction of the transmitted signal [13], [14]. The MIMO channel appears as a linear application of the emitted signal **X** towards the received signal **Y**. The singular value decomposition [15] of the **H** matrix allows the diagonalization of the linear system of equations. This singular value decomposition allows the diagonalization of the MIMO matrix system.

The MIMO propagation channel can be modeled in two different ways. The first approach is to represent the MIMO propagation channel by a matrix of impulse responses containing all the impulse responses between each SISO link in the system.

For a $m \times n$ MIMO system, where m and n are respectively the number of antennas at the transmitter and the receiver. The time variant MIMO matrix is defined by the equation 1.19:

$$H(t,\tau) = \begin{bmatrix} h_{11}(t,\tau) & h_{12}(t,\tau) & \dots & h_{1n}(t,\tau) \\ h_{21}(t,\tau) & h_{22}(t,\tau) & \dots & h_{2n}(t,\tau) \\ \vdots & \vdots & \ddots & \vdots \\ h_{m1}(t,\tau) & h_{m2}(t,\tau) & \dots & h_{mn}(t,\tau) \end{bmatrix} \tag{1.19}$$

where $h_{mn}(t,\tau)$ is the SISO impulse response between the mth transmitter antenna and the nth receiver antenna.

The MIMO impulse response matrix, equation 1.19 can be used as a formalism of a MIMO input-output system between the transmitted signal vector $x(t)$ of size m and the vector of output signals $y(t)$ of size n as follows:

$$y(t) = \int_T H(t,\tau)x(t-\tau)d\tau + v(t) \tag{1.20}$$

where $v(t)$ is the noise and interferences.

The second way to model the MIMO propagation channel is to represent the propagation channel by its doubly directional impulse response [16], [17] between the transmitter and the receiver. The doubly directional impulse response defined by Steinbauer and Molisch corresponds to the impulse response defined as follow.

[18] shows that the Fourier analysis makes it possible to demonstrate the duality between space and wave in the same way as it exists between the time and frequency spaces [11]. The wave vector corresponds to the direction of propagation of a path.

As a result, the impulse response of a MIMO channel between a pair of transceiver-receiver antennas can be written as:

$$h(t,\tau,\Omega_{BS},\Omega_{MS}) = \sum_{p=0}^{P-1} \alpha_p(t) exp(-j\Phi_p(t))\delta(\tau-\tau_p(t)) \\ \delta(\Omega_{BS}-\Omega_{BS,p}(t))\delta(\Omega_{MS}-\Omega_{MS,p}(t)) \tag{1.21}$$

where $\Omega_{BS,p}$ and $\Omega_{MS,p}$ are the propagation directions of the pth path at the BS and MS respectively. Ω is a direction characterized by an azimuth angle φ and elevation angle θ as presented Figure 1.7.

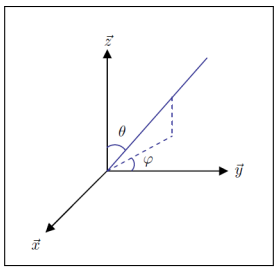

Figure 1.7: Representation of azimuth and elevation angles

The polarization diversity is taken into account by decomposing the impulse response according to the vertical and horizontal components. The impulse response of the radio propagation channel is then a matrix containing the different states of polarization (VV, VH, HH and HV) illustrate by equation 1.22

$$h(t,\tau,\Omega_{BS},\Omega_{MS}) = \begin{bmatrix} h_{VV}(t,\tau,\Omega_{BS},\Omega_{MS}) & h_{VH}(t,\tau,\Omega_{BS},\Omega_{MS}) \\ h_{HV}(t,\tau,\Omega_{BS},\Omega_{MS}) & h_{HH}(t,\tau,\Omega_{BS},\Omega_{MS}) \end{bmatrix} \tag{1.22}$$

The propagation channel is completely described if there are the knowledge of the complex amplitude of each polarization states, propagation delay, direction of arrival at the base station (BS) and direction of arrival at the mobile station (MS).

1.2.3.4 Wide Sense Stationary Channel (WSSUS) [19]

The autocorrelation function depends on four variables, and is thus a rather complicated form for the characterization of the channel. Further assumptions about the physics of the channel

can lead to a simplification of the correlation function. The most frequently used assumptions are the so-called Wide-Sense Stationary (WSS) assumption and the Uncorrelated Scatterers (US) assumption. A model using both assumptions simultaneously is called a WSSUS model. This assumption is very frequent even though it is far from reality. This assumption considers that over short periods of time or over small spatial distances, the mobile radio channels is assumed to be stationary. Physically speaking, WSS means that the statistical properties of the channel do not change with time. Moreover, US means the channel response associated with a given multipath component of delay τ is uncorrelated with the response associated with a multipath component at a different delay $\tau' \neq \tau$, since the two components are caused by different scatterers.

1.2.4 Conclusion

This section has described the fundamentals of the radio propagation channel and the mathematical representation for the SISO and MIMO systems. We started with a general description of the mobile radio channel with the definition of different physical phenomena in the environment. Then the large scale parameters and small scale parameters are introduced. Finally, a description of the mathematical impulse response, transfer function, delay Doppler spread and frequency Doppler spread for the SISO and MIMO systems are given.

1.3 Mobile Radio Channel models for cellular applications

1.3.1 Introduction

As already mentioned, channel models are generally based on mathematical representation of the impulse response of the channel. This topic is widely treated in the literature and the channel models are changing in relation with the increasing complexity of the communication systems. More and more parameters are taken into account in order to model radio channels as close as possible to real channels. The modeling is generally based on statistical models of the different parameters that influence the channel behaviour. From a very general point of view, we can distinguish analytical, geometric and non geometric statistical channel models.

In this part, we will present only some of them, starting with the analytical MIMO channel models, namely the Kronecker channel model and the Weischelberger channel model. Then we will describe the non geometric stochastic channel model with the description of the Tapped Delay Line (TDL) channel model and the ITU channel model, which is based on TDL to characterize pedestrian and vehicular environment. After, we will introduced the Saleh-Valenzuela channel model and its extension. Finally, the geometrical based stochastic channel model family will be presented. It is composed by a description of the one and two rings models, the distributed scattering model and some channel models proposed by international working groups as the SCM, SCME, WINNER, IMT-A and METIS channels models. The aim of this section is the understanding of the different channel models existing in the literature in order to allow us to identify which parameters we will need to extract from the measurements planned with the channel sounder developed during the PhD works. This section will also highlight the complexity of the standardized channel models.

1.3.2 Analytical channel models

1.3.2.1 Introduction

Analytical channel models are used to describe directly the MIMO matrix without the spatial description and geometry description of the environment. This models are based on the correlation properties of the channel. We will describe the Kronecker and the Weichselberger channel models.

In the case of stationary channels, the Kronecker model [20] assumes perfect independence of the correlation between transmission and reception sides. The coupling between the transmitting and receiving arrays can be taken into account using the Weichselberger model [21].

The two models are based on the following decomposition of the channel matrix $\mathbf{H}$, filled with complex coefficients, which can be written as follows:

$$\mathrm{vec}\left\{\mathbf{H}\right\} = \mathbf{R}_{\mathrm{H}}^{1/2}\,\mathbf{g} \tag{1.23}$$

$\mathbf{R}_{\mathrm{H}}$ is the correlation/co-variance matrix of the channel, $\mathbf{g}$ is an i.i.d. random fading vector with unit variance and the operator $\mathrm{vec}\left\{\cdot\right\}$ stacks a matrix into a vector, column wise.

1.3.2.2 Kronecker channel model

The Kronecker model assumes a correlation at the transmitter independent from the correlation at the receiver. So the total correlation of the channel $\mathbf{R}_{\mathrm{H}}$ can be expressed as the Kronecker product ($\otimes$) of the correlation matrices at the transmitter $\mathbf{R}_{\mathrm{Tx}}$ and at the receiver $\mathbf{R}_{\mathrm{Rx}}$:

$$\mathbf{R}_{\mathrm{H}} = \mathbf{R}_{\mathrm{Tx}} \otimes \mathbf{R}_{\mathrm{Rx}} \tag{1.24}$$

Thus, using (1.24) in (1.23), we obtain the following relation for the Kronecker model:

$$\mathbf{H} = \mathbf{R}_{\mathrm{Rx}}^{1/2}\,\mathbf{G}\,\left(\mathbf{R}_{\mathrm{Tx}}^{1/2}\right)^{T} \tag{1.25}$$

Notice that the covariance matrices can be used instead of the correlation matrices in (1.25). This formulation is very simple and easily usable once we have obtained the correlation/covariance matrices.

1.3.2.3 Weichselberger channel model

Contrary to the Kronecker model, **the Weichselberger model** takes into account the correlation in the channel between the transmitter and the receiver.

Its formulation is based on the well known Singular Value Decomposition (SVD) of the correlation matrices $\mathbf{R}_{\mathrm{Tx}}$ and $\mathbf{R}_{\mathrm{Rx}}$, as:

$$\mathbf{R}_{\mathrm{Tx}} = \mathbf{U}_{\mathrm{Tx}}\,\mathbf{\Lambda}_{\mathrm{Tx}}\,\mathbf{U}_{\mathrm{Tx}}^{H} \tag{1.26}$$

$$\mathbf{R}_{\mathrm{Rx}} = \mathbf{U}_{\mathrm{Rx}}\,\mathbf{\Lambda}_{\mathrm{Rx}}\,\mathbf{U}_{\mathrm{Rx}}^{H} \tag{1.27}$$

where:

- $\mathbf{U}_{\mathrm{Tx}}$ and $\mathbf{U}_{\mathrm{Rx}}$ are unitary matrices; their columns contain the eigen vectors of $\mathbf{R}_{\mathrm{Tx}}$ and $\mathbf{R}_{\mathrm{Rx}}$ respectively,
- $\mathbf{\Lambda}_{\mathrm{Tx}}$ and $\mathbf{\Lambda}_{\mathrm{Rx}}$ are diagonal matrices filled with the eigen values of $\mathbf{R}_{\mathrm{Tx}}$ and $\mathbf{R}_{\mathrm{Rx}}$ respectively.

Using (1.26) and (1.27) in (1.25), the following relation can be obtained:

$$\mathbf{H} = \mathbf{U}_{\mathrm{Tx}}\,\left(\mathbf{\Omega} \odot \mathbf{G}\right)\,\mathbf{U}_{\mathrm{Rx}}^{T} \tag{1.28}$$

where $\odot$ is the Schur-Hadamard product, and $\mathbf{\Omega}$ traduces the coupling between the transmitter and the receiver. Its coefficients $w_{mn} > 0$ are equal to:

$$w_{mn} = \sqrt{E_{\mathrm{H}}\left\{\left|\mathbf{U}_{\mathrm{Rx},m}^{H}\,\mathbf{H}\,\mathbf{U}_{\mathrm{Tx},n}^{*}\right|^{2}\right\}} \tag{1.29}$$

In (1.29), $E_{\mathrm{H}}\{\cdot\}$ denotes expectation with respect to $\mathbf{H}$.

These models have been used for performance evaluation of MIMO systems in [22].

1.3.3 Non-Geometric stochastic channel model

1.3.3.1 Introduction

A non-geometric stochastic channel model (NGSCM) describes the paths between the transmitter and the receiver using statistical description of specific parameters. The real geometry of the physical scenario is not taken into account. Two kinds of NGSCM exist, namely the Tapped Delay Line model that represents the channel with different paths in time/delay ans angular domain, and the Saleh-Valenzuela model, which represents the channel with several clusters of paths in time/delay and angular domain. We will introduce both models and the ITU model, which uses TDL model to describe some cellular environments.

1.3.3.2 Tapped Delay Line channel model

The Tapped Delay line channel model is a non-geometric channel model that is a simple way to represent the channel impulse response in time domain. Indeed, the impulse response will be represented only by a discrete number of taps with their own time varying coefficients, amplitude and delay, as represented by 1.30. The tap is represented by a weighted Dirac delta function.

$$h(t,\tau) = \sum_{p=1}^{P} \alpha_p(t)\delta(\tau - \tau_p) \tag{1.30}$$

The impulse response h varies in time and is represented by the sum of all delayed taps. P represent the number of paths, $\alpha_p(t)$ is an amplitude coefficient, δ is a Dirac delta function and τ_p is the arrival time of the path. This kind of model assumes that the channel impulse response is a finite representation of the channel by the maximal number of paths P.

The resolution δt between two paths is limited by the bandwidth of the system W with $\delta t = \frac{1}{W}$. For example, with a bandwidth equals to 20 MHz, the maximal time resolution is inversely proportional to 20 MHz, which is 50 ns.

1.3.3.3 ITU models

The ITU models were developed by the IMT-2000 group to evaluate the IMT technologies like UMTS, LTE (3G) [23]. The purpose of these channel models is to help system designers and network planners with a standard channel model to facilitate the system design and performance evaluation. The ITU model is used to model the time dispersion of the time variant wireless propagation channel as a Tapped Delay Line model.

A set of four channel models is defined: Indoor office, Outdoor to indoor pedestrian, vehicular, Mixed-cell pedestrian/vehicular. The models are constructed to simulate the multi-path fading of the channel with a 5 MHz of bandwidth at 2 GHz. The equation of the CIR is similar to the TDL channel model cited previously (1.30). The multi-path fading is modeled as a TDL with six taps with non uniform delay distribution. Each tap associates an amplitude characterized by a distribution (Ricean with a K-factor>0, or Rayleigh with K-factor=0) and the maximal Doppler frequency.

The recommendation specifies two different delay spreads for each test environment: low delay spread represented by 'A', and medium delay spread represented by 'B'. Each profile has a probability to emerge along time following the description in Table 1.1.

Test environment	Channel A		Channel B	
	r.m.s (ns)	P (%)	r.m.s (ns)	P(%)
Indoor office	35	50	100	45
Outdoor to indoor and pedestrian	45	40	750	55
Vehicular - high antenna	370	40	4000	55

Table 1.1: Probability of occurrence for low delay spread and medium delay spread for each ITU scenarios [23]

The key parameters to describe each propagation scenario have to include: time delay spread, path loos and exceed path loss, shadow fading, multi-path fading characteristics (Doppler spectrum), operating radio frequency.

The path loss model for vehicular environment is given by (1.31). The slow variation is considered as a log-normal distribution. This equation is given for urban and suburban areas with a nearly uniform height for buildings.

$$L = 40(1 - 4 \times 10^{-3}\delta h_b)log_{10}R - 18log_{10}\delta h_b + 21log_{10}f + 80 \tag{1.31}$$

where R is the distance between base station and mobile station in kilometer,f is the carrier frequency equal to 2 GHz and δh_b is the base station antenna height in meters. The slow fading over the distance implies that the adjacent fading values are correlated. The normalized auto-correlation function is approximated by an exponential function as indicated by equation (1.32).

$$R(\Delta x) = exp(-\frac{|\Delta x|}{d_{corr}}ln2) \tag{1.32}$$

where Δx is the distance between fading and d_{corr} is the decorrelation length.

The scenario Vehicular B is defined for a speed up to 120 km/h with a six taps TDL channel model. It is characterized by the number of taps, time delay relative to the first tap, average power relative to the strongest tap and Doppler spectrum as presented in the Figure 1.2.

Tap	Channel A		Channel B		Doppler spectrum
	Relative delay (ns)	Average power (dB)	Relative delay (ns)	Average power (dB)	
1	0	0.0	0	-2.5	Classic
2	310	-1.0	300	0	Classic
3	710	-9.0	8 900	-12.8	Classic
4	1090	-10.0	12 900	-10.0	Classic
5	1730	-15.0	17 100	-25.2	Classic
6	2510	-20.0	20 000	-16.0	Classic

Table 1.2: ITU channel model for vehicular-A (30 km/h) and vehicular-B (120 km/h) scenarios [24]

1.3.3.4 Saleh-Valenzuela channel model

The Saleh-Valenzuela (SV) was originally developed for SISO wideband channel [25] and was further extended to MIMO system by including angle of arrival (AoA) [26]. The SV channel model is similar to the TDL model in term of using path representation with delay and magnitude identification. It considers a "cluster" representation. A cluster is a group of paths that comes from the same scatterer with path characteristics varying in the same range of values (for example,similar delays).

The CIR of the channel follows the equation (1.33).

$$h(t,\tau) = \sum_{c=1}^{C-1}\sum_{p=1}^{P-1}\beta_{pc}exp(j\phi_{pc})\delta(t - T_c - \tau_{pc}) \tag{1.33}$$

where c is the cluster number, p the path number, β_{pc} is the real positive gain, ϕ_{pc} is the phase, T_c is the arrival time of the c_{th} cluster. The magnitude of the paths into a cluster is assumed to decrease following an exponential function. The same principle is assumed between cluster.

With measurement campaign [27], it was found that the clusters are spread in time and also spread in angle of arrival. The SV channel model was extended to MIMO by adding angle of arrival statistics in 1.33. The corresponding equation is then given by (1.34):

$$h(t) = \sum_{c} \sum_{p} \beta_{pc} exp(j\phi_{pc}) \delta(t - T_c - \tau_{pc}) \delta(\theta - \Theta_c - \theta_{pc}) \tag{1.34}$$

where c is the cth cluster, p is the pth paths in the cluster$c$ and θ follows zero mean Laplacian distribution and Θ_c is uniformly distributed between 0 and 2π.

1.3.4 Geometry-based stochastic channel models

1.3.4.1 Introduction

Geometry-based stochastic channel model (GBSCM) describes the statistics of the channel using a geometrical representation of the physical environment and more particularly, a statistical geometrical description of the scatters positions. The GBSCM chooses scholastically the localization of scatterers following a certain distribution probability [28]. There are three common techniques named : One Ring, Two Rings and Distributed scattering. The GBSCM is used by different organizations (3GPP, ITU, European 7th framework project) to model the channel in different scenarios. The spatial channel model (SCM), its extension (SCME), WINNER, ITU-Advanced and METIS will be presented.

1.3.4.2 One Ring model

The One ring model for MIMO system [29] defines scatterers located around the mobile station following a given distribution. The base station is assumed to be elevated to prevent obstruction from local scatterers. Each path is assumed to be reflected only once by the scatterers located on ring and all paths have the same power on the receive antenna array. A representation of one ring model is given Figure 1.8 .

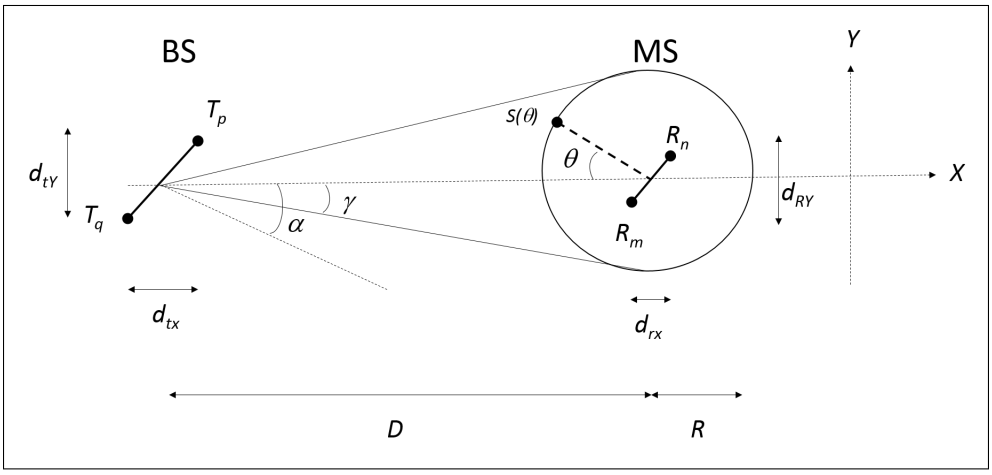

Figure 1.8: Representation of one ring model for MIMO system [29]

where T_p is the pth transmitter antenna, R_n is the nth receiver antenna, D is the distance between the transmitter and receiver array, R is the radius of the scatterers ring, α is the AoA at the receiver, λ is the angle spread at the transmitter from the scatterers ring, $S(\theta)$ the effective scatterers on the ring and θ the angle between scatterer and receiver array.

If the distance D and radius R are much larger than the receive antennas spacing then the angle spread $\lambda \approx arcsin(\frac{R}{D})$. $S(\theta)$ is assumed to be uniformly distributed on the ring and the phase shift of each scatterer is uniformly distributed over $[-\pi, \pi)$.

If p represent the effective scatterer S(θ_k) with $k \in (1, K)$ distributed on the ring, the complex channel coefficient between the mth transmitter antenna and the nth receiver antenna is represented by the equation (1.35) from [29].

$$H_{m,n} = \frac{1}{\sqrt{K}} \sum_{p=1}^{K} exp\left[-j\frac{2\pi}{\lambda}(D_{Tp\to S(\theta_k)} + D_{S(\theta_k)\to R_n)} + j\Phi(\theta_k)\right] \tag{1.35}$$

where $D_{X\to Y}$ represents the distance between element X and Y and λ is the wavelength of the transmit signal.

1.3.4.3 Two Rings model

The two rings model for MIMO system [30] follows the same principle as the one ring model presented before. The difference comes from an additional ring localized around the transmitter antennas array. This model still have one ring localized around the mobile station as shown in Figure 1.9. Both BS and MS are surrounded by scatterers. Each path is assumed to be reflected twice. The complex channel coefficient equation (1.35) becomes the following equation (1.36) presented in [30]:

$$H_{p,n} = \frac{1}{\sqrt{K1K2}} \sum_{k=1}^{K1} \sum_{l=1}^{K2} exp\left[-j\frac{2\pi}{\lambda}(D_{Tp\to S1(\theta_k)} + D_{S1(\alpha_k)\to D_{S2(\beta_l)}} + D_{S2(\beta_l\to R_n)} + j\Phi_1(\alpha_k) + j\Phi_2(\beta_l)\right] \tag{1.36}$$

where K1 and K2 are respectively the number of effective scatterers at BS and MS, k is the kth scatterer on the ring $S1(\alpha_k)$, l the lth scatterer on the ring $S2(\beta_l)$, α and β are respectively the angle between scatterer and antenna array for transmitter and receiver.

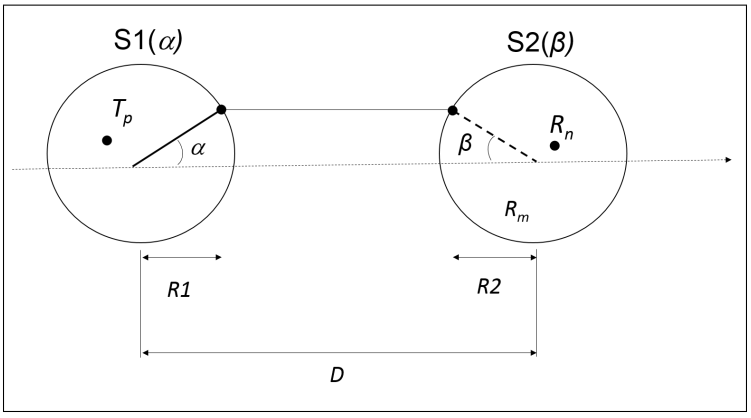

Figure 1.9: Representation of two rings model for MIMO system [10]

1.3.4.4 Distributed scattering model

The distributed scattering model is presented in [31] for MIMO system and it is represented on Figure 1.10. As the two rings model, both BS and MS are surrounded by significant near field scatterers with the difference that the scatterers are distributed linearly in front of the antenna array with a sufficient distance to assume plane wave. The number of scatterers on both sides have to be large enough to allow random fading ($S > 10$). The linear scatterers at the receiver side can be approximated to a virtual array of S virtual antennas with an average spacing

equal to $\frac{2D_r}{S}$ where D_r is the distance between horizontal plan and the most distant scatterer as presented Figure 1.10. The MIMO channel transfer function is given by the equation (1.37) from [31].

$$H = \frac{1}{\sqrt{S}} R^{1/2}_{\theta_r,dr} G_r R^{1/2}_{\theta_s,\frac{2D_r}{S}} G_t R^{1/2}_{\theta_t,dt} \tag{1.37}$$

where $\frac{1}{\sqrt{S}}$ is a normalization factor, $\mathbf{G}_t$ and $\mathbf{G}_r$ are i.i.d Rayleigh fading matrix of size (SxM) and (NxS) respectively, N is the number of receiving antennas, M is the number of transmitting antennas, S is the number of virtual antennas, θ_r is the angle spread at receiver, θ_t is the angle spread at transmitter and d_r and d_t are the distance between antennas at receiver and transmitter respectively.

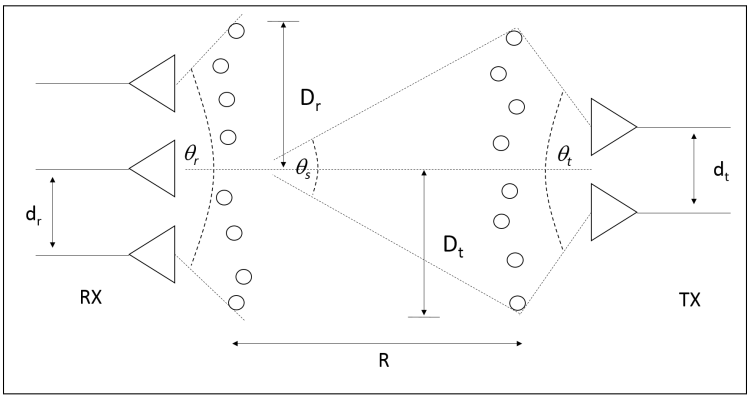

Figure 1.10: Representation of distributed model for MIMO system [10]

1.3.4.5 Spatial channel model (SCM)

The SCM [32] was developed by 3GPP/3GPP2 (Third Groupe Partnership Project) to evaluate channel properties with multi-antennas systems and algorithms in outdoor environments with a bandwidth of 5 MHz for Code division multiple access (CDMA) channel at 2 GHz. The SCM distinguishes three different environments:

- Suburban macrocell,
- Urban macrocell,
- Urban microcell.

The modeling and simulation methodologies are identical for all environments but the statistical distribution of parameters such as azimuth spread, delay spread, shadow fading and path loss are different [33]. The SCM specifies paths between the Base Station (BS) and the Mobile Station (MS) based on a stochastic model of correlated random variables. This model implies to know the space, time, and propagation characteristics for a channel realization. The models are antenna independent and specifies paths characteristics to realize the fading and correlation behavior between antennas elements. The SCM model is based on a sum-of-sinusoïds technique [34] where the paths are assumed to be composed of a 20 sinusoïds. The SCM defines a drop concept where a MS is placed in a sequence of different network locations as presented with Figure 1.11. The locations are random or predefined by the user and each drop represents a snapshot of the fading channel. A drop is a time laps where the statistics of the large scale parameters in a single drop are assumed to be fix for the duration of the drop [32]. SCM is composed of two parts: a link level simulation model and a system level simulation.

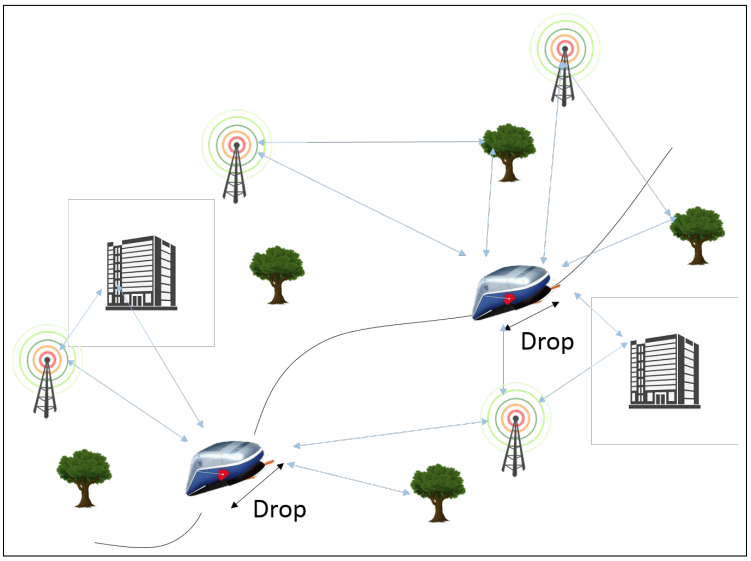

Figure 1.11: Representation of drop concept in a channel simulation [32]

The link-level model (LL model)

The LL model is a reference model with a single link. It considers a single BS transmitting to a single MS. It provides, for manufacturers, a good representation of the interface for their communication systems to compare their implementations of the same signal processing algorithms. Link-level simulations is not enough for performance testing of different algorithms because it is relative to only one snapshot of the dynamic channel. The wide band characteristics of the channel are modeled as a TDL model. Each path is independently faded and angular spectrum of the azimuth Direction of Departure (DOD) and Direction of arrival (DOA) are identified by an uniform distribution for MS and a Laplacian distribution for BS. The average direction and angular spread at BS and MS has to be fixed to represent the stationary channel conditions.

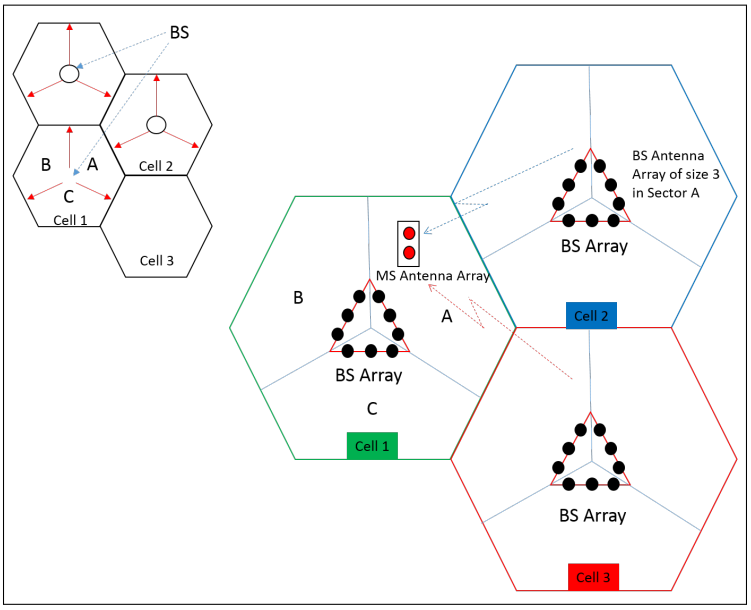

Figure 1.12: Representation of clustered scatterers, multipath and sub-path [32]

The system-level model (SL model)

The SL model is a multi link physical model built to complete the performance evaluation. Each link is composed by a MIMO antenna array (MS and BS) that represents a cell or a sector within a cell. A system level model is presented Figure 1.12 where the MS receives interferences from adjacent cells or sectors. The excess delays of sub-paths are closely clustered around the delay of their parent multi-paths as represented in Figure 1.13. This figure shows a distribution of sub-paths and multi-paths (parent paths) for different clusters. A simple representation of the DoD is shown for one cluster (without all sub-paths) and a simple representation of power delay profile is given for three cluster.

The system-level simulation is performed as a successive number of drops, where the duration of a drop is assumed to be short enough to have the AS, mean AoA, DS and shadowing as being constant over the drop. The SCM model defines, for each scenario, six clusters with 20 sub-paths in each. For a M elements linear BS array and a N elements linear MS array, the channel coefficients for one of the c cluster components are given by a (NxM) matrix of complex amplitudes.

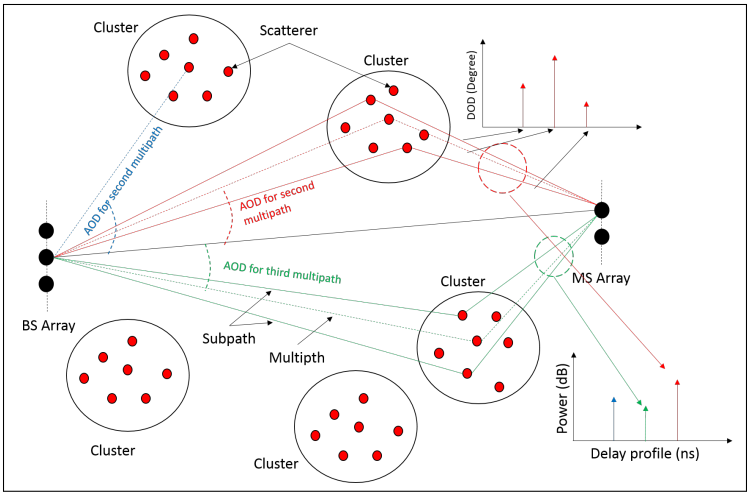

Figure 1.13: System level simulation representation [32]

The channel matrix for the cth cluster component (c = 1,. . . ,C) as $\mathbf{H}_c(t)$. The (p, c)th component of $\mathbf{H}_c(t)$ is given by equations (1.38) for NLOS and (1.39) for LOS scenario from [32] :

$$h_{n,m,c}(t) = \sqrt{\frac{P_p \sigma_{SF}}{P}} \sum_{p}^{P} \begin{bmatrix} \sqrt{G_{BS}(\theta_{c,p,AoD})} exp(j[N_w d_m sin(\theta_{c,p,AoD} + \Phi_{p,c}]) \times \\ \sqrt{G_{MS}(\theta_{c,p,AoA})} exp(jN_w d_n sin(\theta_{c,p,AoA})) \times \\ exp(jN_w ||v|| cos(\theta_{c,p,AOA} - \theta_v)t) \end{bmatrix} \tag{1.38}$$

$$h^{LOS}_{n,m,c}(t) = \sqrt{\frac{1}{Kf+1}} h_{n,m,c}(t) \tag{1.39}$$

where parameters are described in Table 1.3.

Each 20 sub-paths of each cluster introduces the angular dispersion of the channel model. The 20 sub-paths in a cluster are assumed to arrive at the same time but with different angles. The distribution of AoD, for macrocell and microcell, and AoA of the MS are described in the Table 1.4.

Parameters	Description
n	is the nth antenna at the MS
m	is the mth antenna at the BS
c	is the cth cluster
P_c	is the power of the cth cluster
σ_{SF}	is the lognormal shadow fading, applied as a bulk parameter to the cth cluster for a given drop.
P	is the number of paths per cluster.
$\theta_{c,p,AoD}$	is the the AoD for the pth subpath of the cth cluster
$\theta_{c,p,AoA}$	is the the AoA for the pth subpath of the cth cluster
$G_{BS}(\theta_{c,p,AoD})$	is the BS antenna gain of each array element
$G_{MS}(\theta_{c,p,AoA})$	is the MS antenna gain of each array element
j	is the square root of -1
N_w	is the wave number $\frac{2\pi}{\lambda}$ where λ is the carrier wavelength in meters
d_m	is the distance in meters from BS antenna element m from the reference (m = 1) antenna. For the reference antenna m = 1, d_1=0
d_n	is the distance in meters from MS antenna element n from the reference (n = 1) antenna. For the reference antenna n = 1, d_1 =0
$\Theta_{c,p}$	is the phase of the pth subpath of the cth cluster
$\|v\|$	is the magnitude of the MS velocity vector
θ_v	is the angle of the MS velocity vector
Kf	is the K factor

Table 1.3: Parameters of channel impulse response from SCM model

Sub-Path (p)	Offset for 2 deg AS at BS (Macrocell)	Offset for 5 deg AS at BS (Microcell)	Offset for a 35 deg AS at MS
1,2	± 0.0894	± 0.2236	± 1.5649
3,4	± 0.2826	± 0.7064	± 4.9447
5,6	± 0.4984	± 1.2461	± 8.7224
7,8	± 0.7431	± 1.8578	± 13.0045
9,10	± 1.0257	± 2.5642	± 17.9492
11,12	± 1.3594	± 3.3986	± 23.7899
13,14	± 1.7688	± 4.4220	± 30.9538
15,16	± 2.2961	± 5.7403	± 40.1824
17,18	± 3.0389	± 7.5974	± 53.1816
19,20	± 4.3101	± 10.7753	± 75.4274

Table 1.4: Sub-path AoD and AoA offset of SCM

The SCM channel model has an optional system simulation, which take in account the polarized arrays and is able to give the polarization model illustrated by equation (1.40) where the parameters are described in Tables 1.5:

$$h_{n,m,c}(t) = \sqrt{\frac{P_c \sigma_{SF}}{P}} \sum_{p}^{P} \left[\begin{array}{c} \begin{bmatrix} \chi^{v}_{BS}(\theta_{c,p,AoD}) \\ \chi^{h}_{BS}(\theta_{c,p,AoD}) \end{bmatrix}^{T} \begin{bmatrix} exp(j\Phi^{vv}_{c,p} & \sqrt{r_{n1}} exp(j\Phi^{vh}_{c,p} \\ \sqrt{r_{n2}} exp(j\Phi^{hv}_{c,p} & exp(j\Phi^{hh}_{c,p} \end{bmatrix} \begin{bmatrix} \chi^{v}_{MS}(\theta_{c,p,AoA}) \\ \chi^{h}_{MS}(\theta_{c,p,AoA}) \end{bmatrix} \times \\ exp(jN_w d_m sin(\theta_{c,p,AoD})) \times exp(jN_w d_n sin(\theta_{c,p,AoA})) \times \\ exp(jN_w ||v|| cos(\theta_{c,p,AOA} - \theta_v)t) \end{array} \right] \tag{1.40}$$

Parameters	Description
$\chi^{v}_{BS}\theta_{c,p,AoD}$	is the BS antenna complex response for the V-pol component
$\chi^{h}_{BS}\theta_{n,m,AoD}$	is the BS antenna complex response for the H-pol component
$\chi^{v}_{MS}\theta_{n,m,AoA}$	is the MS antenna complex response for the V-pol component
$\chi^{h}_{MS}\theta_{n,m,AoA}$	is the MS antenna complex response for the H-pol component
$\|\chi^{\cdot}(.)\|^2$	is the antenna gain
r_{n1}	is the random variable representing the power ratio of waves of the pth path leaving the BS in the vertical direction and arriving at the MS in the horizontal direction (v-h) to those leaving in the vertical direction and arriving in the vertical direction (v-v)
r_{n2}	is the random variable representing the power ratio of waves of the pth path leaving the BS in the horizontal direction and arriving at the MS in the vertical direction (h-v) to those leaving in the vertical direction and arriving in the vertical direction (v-v)
$\Theta^{x,y}_{c,p}$	is phase offset of the pth subpath of the cth cluster between the x component (either the horizontal h or vertical v) of the BS element and the y component (either the horizontal h or vertical v) of the MS element
The variables r_{n1} and r_{n2} are	i.i.d variable

Table 1.5: Parameters of polarization model

1.3.5 Extended Spatial Channel Model (SCME)

SCME described in [35] is an extension of SCM. It takes back the same idea of the original SCM with an extension of some parameters. This model was developed by the WINNER project for the development and testing of the 3GPP Long Term Evolution (LTE) standard.

The bandwidth of the SCM channel model is extended from 5 MHz to 20 MHz, then extended to 100 MHz for both 2 GHz and 5 GHz center frequency. SCM has a limited range of scenarios and in some scenarios, does not incorporate the Rician K-factor to support Line of Sight (LOS) paths.

SCME uses intra-cluster delay spread propagation to perform bandwidth expansion.The bandwidth is extended by introducing a different delay and power in clusters. In SCM, each cluster has 20 sub-paths with identical delay. In SCME each cluster is subdivided into three or four sub-cluster for the macro-cell and micro-cell scenarios respectively. The number of delays is increased from 6 in SCM to 18 or 24 in SCME.

The 20 sub-paths are divided in different groups of 10, 6 and 4 sub-paths for Suburban Macro-cell and Urban Macro-cell and in groups of 6, 6, 4 and 4 sub-paths for Urban Micro-cell. The

number of sub-paths per sub-cluster with their own delay and relative power is presented in Table 1.6. The expression of the channel impulse response is identical as the SCM.

Mid-path	Sub-paths	Relative Power	Excess Delay	Sub-path Index	AS mid-path/AS sub-path
1	10	0.5	0 ns	1,2,3,4,5,6,7,8,19,20	0.9865
2	6	0.3	12.5 ns	9,10,11,12,17,18	1.0056
3	4	0.2	25 ns	13,14,15,16	1.0247

Table 1.6: Sub-cluster decomposition of SCME channel model [36]

Each sub-path into a sub-cluster has the same azimuth spread as in SCM. SCME is a continuous evolution model since it allows drifting of AoA, AoD and delays for every clusters at each simulation step within a drop. [35] defines Cluster Delay-Line parameters for each six clusters with a definition of relative path power, delay, delay spread and angular parameters (AoA, AoD, angle spread) as shown in Table 1.7.

Scenario		Suburban Macro		Urban Macro				Urban Micro	
Power delay parameters : Relative path power (dB)/delay(us)	1	0	0	0		0		0	0
	2	-2.6682	0.1408	-2.2204		0.3600		-1.2661	0.2840
	3	-6.2147	0.0626	-1.7184		0.2527		-2.7201	0.2047
	4	-10.4132	0.4015	-5.1896		1.0387		-4.2973	0.6623
	5	-16.4735	1.3820	-9.0516		2.7300		-6.0140	0.8066
	6	-22.1898	2.8280	-12.5013		4.5977		-8.4306	0.9227
Resulting total DS (us)		0.231		0.841				0.294	
Path AS at BS, MS (deg)		2, 35		2, 35				5, 35	
Angular parameters: AoA (deg)/ AoD (deg)	1	156.1507	-101.3376	65.7489	81.9720	76.4750	-127.2788	0.6966	6.6100
	2	-137.2020	-100.8629	45.6454	80.5354	-11.8704	-129.9678	-13.2268	14.1360
	3	39.3383	-110.9587	143.1863	79.6210	-14.5707	-136.8071	146.0669	50.8297
	4	115.1626	-112.9888	32.5131	98.6319	17.7089	-96.2155	-30.5485	38.3972
	5	91.1897	-115.5088	-91.0551	102.1308	167.6567	-159.5999	-11.4412	6.6690
	6	4.6769	-118.0681	-19.1657	107.0643	139.0774	173.1860	-1.0587	40.2849
Resulting total AS at BS,MS (deg)		4.70, 64;78		7.87, 62.35		15.76, 62.19		18.21, 67.80	

Table 1.7: Cluster delay line parameters for each cluster of SCME scenarios [35]

1.3.6 WINNER channel model

Despite the extension of the SCM model with greater bandwidth and increased center frequency, it was still considered inadequate for advanced simulations of LTE and future systems. A new model was introduced: the WINNER model. The WINNER II/+ channel model described in the Deliverable 1.1.2 [37] and Delivrable 5.1.3 [38], are defined for both link-level and system-level simulations in the frequency range from 2 GHz to 6 GHz with a bandwidth up to 100 MHz as in SCME. The WINNER channel model can be described in two parts. The generic WINNER channel model and the CDL channel model.

The phase I of the WINNER project established five scenarios from measurement campaigns at 2 GHz and 5 GHz:

- Indoor
- Urban Micro-cell
- Urban Macro-cell
- Suburban Macro-cell
- Rural Macro-cell

Phase II of the WINNER project, the number of scenarios increases up to 12 thanks to measurement campaigns at 2 GHz and 6 GHz:

- A1: Indoor office

- A2: Indoor-to-outdoor
- B1: Urban micro-cell
- B2: Bad Urban micro-cell
- B3: Indoor hotspot
- B4: Outdoor to indoor
- B5: Stationary Feeder
- C1: Suburban macro-cell
- C2: Urban macro-cell
- C3: Bad urban macro-cell
- C4: Urban macro outdoor to indoor
- D1: Rural macro-cell
- D2: Moving networks

1.3.6.1 The generic WINNER channel model

It is a double-directional geometry-based stochastic channel model illustrated in Figure 1.14. The channel parameters are determined stochastically based on statistical distributions extracted from channel measurement campaigns. A channel realization is obtained from the different distributions as delay spread, delay values, angle spread, shadow fading, and cross-polarization ratio.

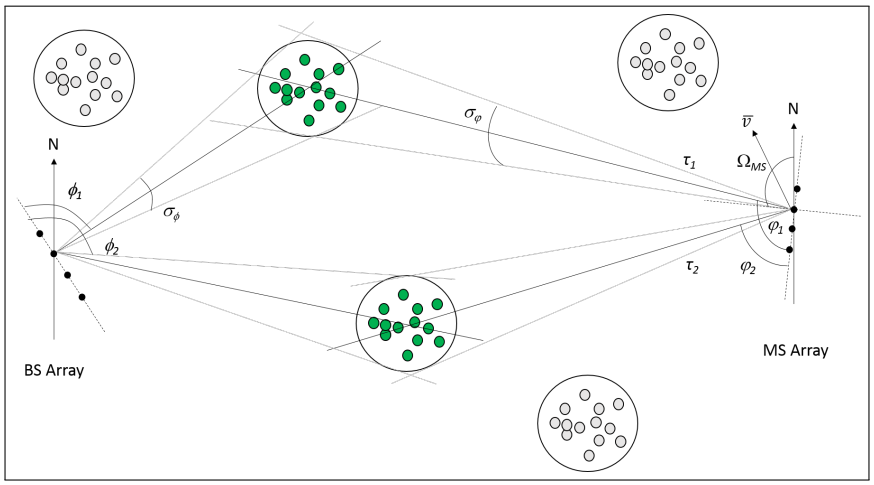

Figure 1.14: Single link representation of WINNER channel model approach [39]

The channel is modeled by a number of clusters between 8 and 20 depending on the scenario. Each cluster is composed by 20 paths.

Drop-based simulation is the principal approach used by both SCM and SCME. WINNER II adds time evolution where the drops are correlated and a smooth transition between consecutive drops is engineered. This smooth transition between channel segments is realized by spacing the segments in time by the quasi stationary duration and dividing the transition region into a number of sub-intervals.

This cluster time varying approach is shown in Figure 1.15.

The transfer matrix of the MIMO channel is given by the sum of all cluster representations. If C is the number of cluster, t is the absolute time and τ the delay, then the MIMO transfer matrix is (1.41) [37]:

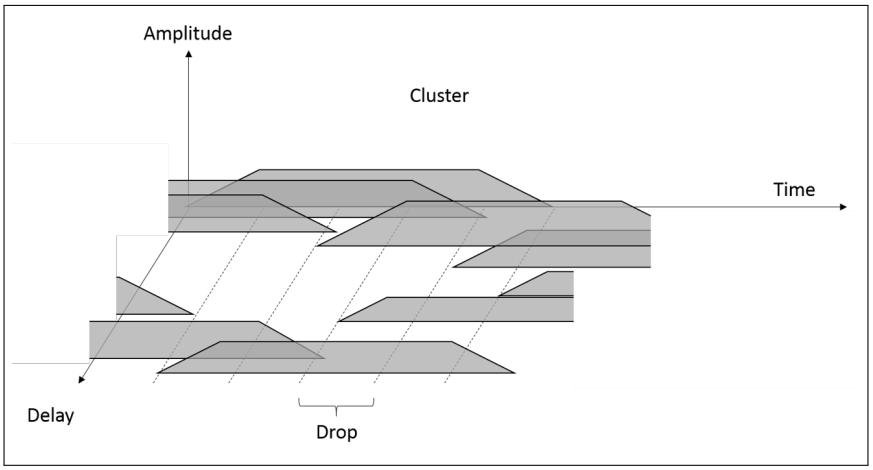

Figure 1.15: Representation of smoothing cluster time varying [37]

$$H(t,\tau) = \sum_{c=1}^{C} H_c(t,\tau) \tag{1.41}$$

It is composed of antenna array response matrices $\mathbf{F}_M$ for the transmitter, $\mathbf{F}_N$ for the receiver and the propagation channel response matrix h_C for cluster c as the following equation (1.42) :

$$H_c(t,\tau) = \int\int F_N(\varphi) h_c(t,\tau,\phi,\varphi) F_M^T(\phi) d\phi d\varphi \tag{1.42}$$

For a cluster c, the channel propagation between antenna m from BS and antenna n from MS is given by the following equation (1.43) :

$$\begin{gathered}\mathcal{H}_{n,m,c}(t) = \sqrt{P_n}\sum_{p=1}^{P} \\ \begin{bmatrix} F_{M,m,V}(\varphi_{c,p}) \\ F_{M,m,H}(\varphi_{c,p}) \end{bmatrix}^T \begin{bmatrix} exp(j\Phi_{c,p}^{vv}) & \sqrt{K_{c,p}} exp(j\Phi_{c,p}^{vh}) \\ \sqrt{K_{c,p}} exp(j\Phi_{c,p}^{hv}) & exp(j\Phi_{c,p}^{hh}) \end{bmatrix} \begin{bmatrix} F_{N,n,V}(\phi_{c,p}) \\ F_{N,n,H}(\phi_{c,p}) \end{bmatrix} \times \\ exp(jd_m 2\pi\lambda_0^{-1} sin(\phi_{c,p})) \times exp(jd_n 2\pi\lambda_0^{-1} sin(\varphi_{c,p})) \times exp(j2\pi v_{c,p} t)\end{gathered} \tag{1.43}$$

where the definitions of the n, m, c, p, $F_{N,n,V}$, $F_{N,n,H}$, $F_{M,m,V}$, $F_{M,m,H}$,$\Phi_{c,p}$, $\phi_{c,p}$, $\varphi_{c,p}$ and λ, are summarized in the Table 1.8.

In the LOS case the channel coefficients of the cluster c between antenna m and n become:

$$\begin{gathered}\mathcal{H}_{n,m,c}(t)^{LOS} = \sqrt{\tfrac{1}{Kf+1}}\mathcal{H}_{n,m,c}(t) + \delta(c-1)\sqrt{\tfrac{Kf}{Kf+1}} \times \\ \begin{bmatrix} F_{M,m,V}(\varphi_{LOS}) \\ F_{M,m,H}(\varphi_{LOS}) \end{bmatrix}^T \begin{bmatrix} exp(j\Phi_{LOS}^{vv}) & 0 \\ 0 & exp(j\Phi_{LOS}^{hh}) \end{bmatrix} \begin{bmatrix} F_{N,n,V}(\phi_{LOS}) \\ F_{N,n,H}(\phi_{LOS}) \end{bmatrix} \times \\ exp(jd_m 2\pi\lambda_0^{-1} sin(\phi_{LOS})) \times exp(jd_n 2\pi\lambda_0^{-1} sin(\varphi_{LOS})) \times exp(j2\pi v_{LOS} t)\end{gathered} \tag{1.44}$$

The Large scale parameters modeled by the generic WINNER II channel model are:

- Delay spread and distribution
- Angle of Departure spread and distribution
- Angle of Arrival Spread and distribution
- Shadow Fading standard deviation

Parameters	Description
n	is the nth antenna at the MS
m	is the mth antenna at the BS
c	is the cth cluster
p	is the pth path in the cluster c
$F_{N,n,V} - F_{N,n,H}$	are the antenna element n field patterns for vertical and horizontal polarization respectively
$F_{M,m,V} - F_{M,m,H}$	are the antenna element m field patterns for vertical and horizontal polarization respectively
$K_{c,p}$	is the complex gain of the path p in the cluster c
λ_0	is the wave length of the carrier frequency
$\Phi_{c,p}$	is the initial phase of the path p in the cluster c
$\phi_{c,p}$	is the AoD of the path p in the cluster c
$\varphi_{c,p}$	is the AoA of the path p in the cluster c
$v_{c,p}$	is the Doppler frequency component of the path p in the cluster c

Table 1.8: Parameters of WINNER channel equation

- Ricean K-factor

And the supported parameters are:

- Scaling parameter for Delay distribution
- Cross-polarization power ratios
- Number of clusters
- Cluster Angle Spread of Departure
- Cluster Angle Spread of Arrival
- Per Cluster Shadowing
- Auto-correlations of the LS parameters
- Cross-correlations of the LS parameters
- Number of rays per cluster

The WINNER channel modeling process can be divided into three parts. The first one, is the definition of general parameters as the scenario, propagation conditions, path loss calculation and correlated large scale parameters generation. The second part, is the generation of small scale parameters as delays, cluster power, AoA, AoD and cross-correlation. The third part, is the channel coefficient generation. This procedure is illustrated by the Figure 1.16

1.3.6.2 CDL models

These models are similar to the TDL models. The difference comes from the definition of a cluster, which is a group of paths with the same delay value but different AoD and AoA. The fading process is applied to each sub-paths of the cluster and then modeled by the sum of sinusoïds method. The angular spread within clusters can be different at the BS and the MS. The offset angles represent the Laplacian PAS of each cluster. For the two strongest clusters, the 20 sub-paths are divided into three sub-clusters with different delays. The delays, and the composition of sub-clusters are assumed to be fixed by the WINNER model following the distribution in Table 1.9.

An example of WINNER II channel model is provided in Table 1.10 for the D2a scenario, which is the moving network scenario. This scenario will be explain in section 3. An example of extraction of WINNER II channel model based on Ray tracing is given in [40] at 5.8 GHz.

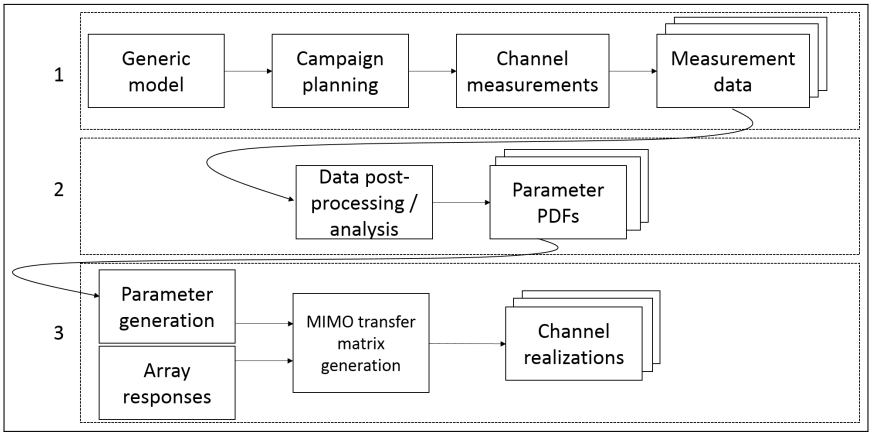

Figure 1.16: Channel coefficient generation procedure for WINNER channel model [37]

Sub-cluster	Mapping of path	Power	Delay offset
1	1,2,3,4,5,6,7,8,19,20	10/20	0 ns
2	9,10,11,12,17,18	6/20	5 ns
3	13,14,15,16	4/20	10 ns

Table 1.9: Distribution of path within sub-clusters [37]

Cluster	Delay (ns)			Power (dB)			AoD (°)	AoA (°)	Ray power (dB)				
1	0			0			0	0	-0.12	-28.8	Cluster ASD = 2°	Cluster ASA = 3°	XPR = 12 dB
2	45	50	55	-17.8	-20.1	-21.8	12.7	-80		-27.8			
3	60			-17.2			-13.6	86		-30.2			
4	85			-16.5			13.4	84.4		-29.5			
5	100	105	110	-18.1	-20.4	-22.1	-13.9	87.5		-28.1			
6	115			-15.7			-13	-82.2		-28.7			
7	130			-17.7			-13.9	87.5		-30.8			
8	210			-17.3			-13.7	86.2		-30.3			

Table 1.10: LOS Clustered delay line model for D2a scenario [37]

1.3.6.3 The WINNER+ channel model

It is an extension of WINNER II channel model. It extends the frequency range from 450 MHz to 2 GHz. This model adds the angle elevation information to increase the accuracy of the CIR representation. The elevation parameters are included in the equation (1.43) as follows:

$$\mathcal{H}_{n,m,c}(t) = \sqrt{P_c}\sum_{k=1}^{K}\begin{bmatrix}F_{N,n,V}(\phi_{c,p})\\F_{N,n,H}(\phi_{c,p})\end{bmatrix}^T\begin{bmatrix}exp(j\Phi_{c,p}^{vv} & \sqrt{K_{c,p}}exp(j\Phi_{c,p}^{vh})\\K_{c,p}exp(j\Phi_{c,p}^{hv}) & exp(j\Phi_{c,p}^{hh}\end{bmatrix}\begin{bmatrix}F_{M,m,V}(\phi_{c,p})\\F_{M,m,H}(\phi_{c,p})\end{bmatrix} \times exp(j2\pi\lambda_0^{-1}(\overline{r}_m.\overline{\Phi}_{c,p})) \times exp(j2\pi\lambda_0^{-1}\overline{r}_n.\overline{\psi}_{c,p})) \times exp(j2\pi v_{c,p}t) \quad (1.45)$$

where scalar product is given by:

$$\overline{r}_m.\overline{\Phi}_{c,p} = x_m\cos(\gamma_{c,p})\cos(\phi_{c,p}) + y_m\cos(\gamma_{c,p})\sin(\phi_{c,p}) + z_m\sin(\gamma_{c,p}) \quad (1.46)$$

The added parameters in equation (1.45) from equation (1.43) are:

$K_{c,p}$ is the power attenuation
$\overline{r}_m$ is location vector of Tx array element s,
$\overline{\Phi}_{c,p}$ is departure angle unit vector of path n, m,
x_m, y_m and z_m are component of $\overline{r}_s$ to x,y and z axis respectively,
$\phi_{c,p}$ and $\gamma_{n,m}$ are arrival azimuth angle and arrival elevation angle of the path n, m,
$\overline{r}_n.\overline{\psi}_{c,p}$ is the scalar product of Rx antenna element n and arrival angle of the path p
$\overline{r}_m.\overline{\psi}_{c,p}$ is the scalar product of Tx antenna element m and arrival angle of the path p

The motion of the MS will be defined with elevation angle by the equation (1.47):

$$v_{c,p} = \frac{\overline{v}.\overline{\psi_{c,p}}}{\lambda_0} = \frac{|v|\cos\theta_v\cos\gamma_{c,p}\cos\phi_{c,p} + |v|\sin\theta_v\cos\gamma_{c,p}\sin\phi_{c,p}}{\lambda_0} \quad (1.47)$$

1.3.7 IMT-Advanced channel models

The IMT-A channel models are based on WINNER II channel model and include the generic and CDL models. For the evaluation of IMT-A systems (4G) the ITU-R has defined five channel models in [23] with a frequency band from 450 MHz to 6 GHz with a bandwidth up to 100 MHz. The scenarios are:

- Indoor Hot-spot (InH)
- Urban Macro-cell (UMa)
- Urban Micro-celle (UMi)
- Rural Macro-cell (RMa)
- Suburban Macro-cell (SMa)

For the evaluation of IMT-A systems, IMT-A channel model can be illustrated by a the primary module and an extension module, Figure 1.17.

The primary module contains the same CIR calculation methodology than WINNER II channel model. The equations of CIR are the same as WINNER II channel model equation (1.43). All scale parameters are covered for the 4 scenarios (excepted Suburban macro) in the primary module. The Extension module can improve capacities of channel reality representation with extra parameters of environment for macro-cell scenarios like street width, city structure, *etc*

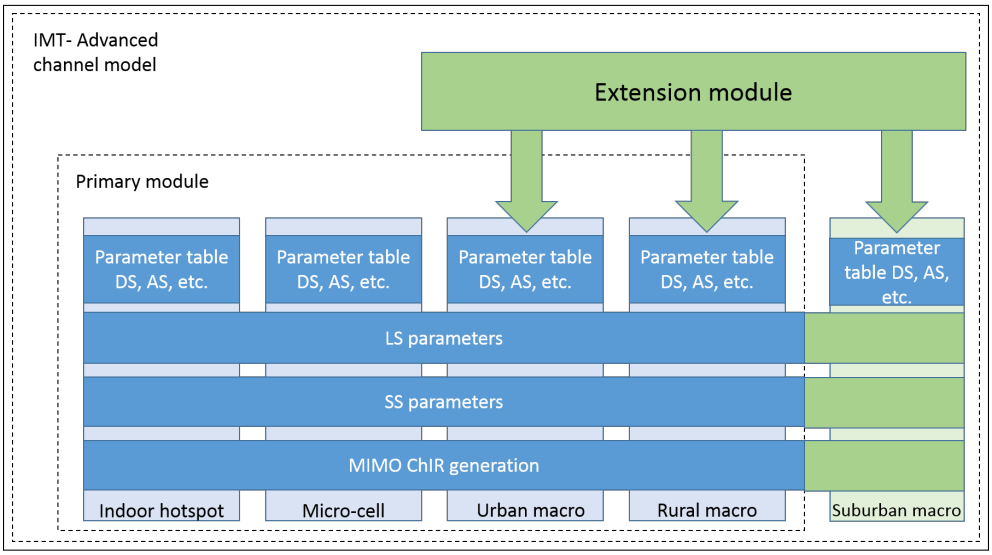

Figure 1.17: Architecture of IMT-A channel model [24]

1.3.7.1 The generic model

It is a double directional GBSM model that specifies the geometric distribution of scatterers, the mathematical model and the algorithms used to model the channel scenario. This model is able to separate the propagation parameters to antennas. The generic model has two levels of randomness. The large scale parameters and the small scale parameters are drawn randomly following the distribution function defined for each scenario. The only parameters that is not fixed is the initial phase of the scatterers.

The channel coefficient generation procedure is composed by three parts described in Figure 1.18. The first is a user defined parameters as the selection of the scenario, the network layout and the antennas field. The second part is the propagation parameter generation, which defines the large scale and small scale parameters. The third part is the CIR generation.

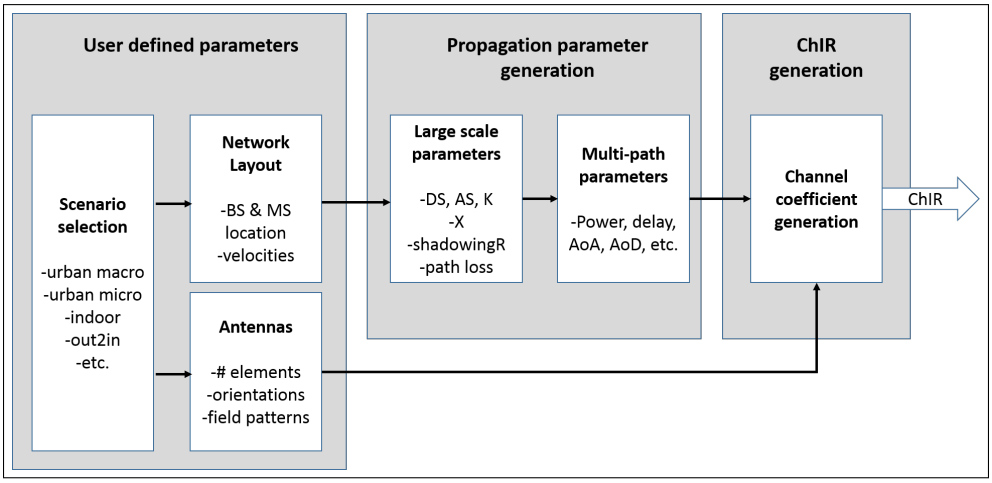

Figure 1.18: Channel coefficient generation procedure for IMT-A channel model [24]

1.3.7.2 IMT-CDL channel model

It is a less complex model than the generic model, using reduced variability where all parameters are fixed except for the phases of paths. However, three other options can be applied with CDL

model: the main direction of the paths can be variable, a set of reference antenna geometries and antenna patterns can be proposed and relation to correlation-matrix based models can be introduced.

1.3.7.3 Time Spatial Propagation Model (TSPM)

It is generated by the extension module. The TSP model defined three profiles called: long term time spatial profile model, short term time spatial model, instantaneous time spatial profile model. Each profile is a representation in three dimension combining AoA, power spectrum and delay. This will vary with the distance. Instantaneous time spatial profile is a TSP model representation from a single snapshot of the channel at a given distance. Short term time spatial profile is a representation of an average over a tens of wavelength and Long term time spatial model is a representation of an average over hundreds wavelengths. These representations are illustrated Figure 1.19.

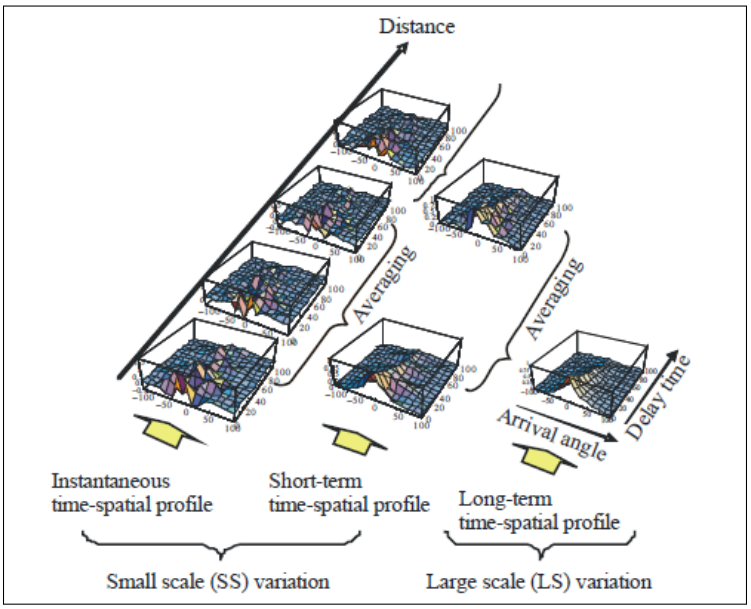

Figure 1.19: Time Spatial propagation model (TSPM) [24]

An example of IMT-A CDL channel model is provided in Table 1.11 for the RMa scenario, which is a train speed scenario (350 km/h) for continuous wide area. This scenario will be explained in Chapter 2.

Cluster	Delay (ns)			Power (dB)			AoD (°)	AoA (°)	Ray power (dB)			
1	0	5	10	0	-17.8	-19.5	0	0	-0.12	-25.6	Cluster ASD = 2°	Cluster ASA = 3°	XPR = 12 dB
2	35	40	45	-16.9	-19.1	-20.9	24	99	-26.9				
3	45			-16.8			23	95	-29.8				
4	65			-18.3			24	99	-31.3				
5	65			-21.2			-25	-106	-34.2				
6	110			-17.1			-23	96	-30.1				
7	125			-19.7			-25	-103	-32.7				
8	125			-23.8			27	113	-36.8				
9	170			-22.9			27	110	-35.9				
10	170			-20.9			25	106	-33.9				
11	200			-21.9			-26	-108	-34.9				

Table 1.11: CDL channel model for RMa LOS scenario from IMT-A channel model [24]

1.3.8 METIS channel models

The Mobile and wireless communications Enablers for the Twenty-twenty Information Society (METIS) [41] channel models come from the 7th European framework program. They are develop for 5G networks performance evaluation. The METIS channel model is defined as a GSCM model and a map-based model. Map-based model uses a simplified description of radio environment using a simplified ray tracing method. This simplified description considers geographical maps or 3D indoor models. METIS project proposed different scenarios for both GSCM and map-based models where some scenarios are present in both models. If a geometrical environment is already defined, the propagation paths are calculated based on the deterministic geometry with added elements. If no geometrical environment are defined, the propagation paths are fully generated stochastically. An hybrid model is also presented. Various antenna models can be applied for both models. The frequency bands are defined between 6 to 100 GHz in the mm-Waves range.

1.3.8.1 Geometry-based stochastic model

proposed in the METIS project follows the WINNER II/+ CIR calculation procedure with the 3GPP 3D channel model CIR equations. This model allows a channel representation, without any predefined geometric environment, for the following scenarios. These models are specified for a frequency from 450 MHz to 6 GHz, therefore extended frequency bands are defined from 50 GHz to 70 GHz only for indoor environments and outdoor square.

- Urban micro-cell outdoor to outdoor and outdoor to indoor,
- Urban macro-cell outdoor to outdoor and outdoor to indoor,
- Rural macro-cell,
- Indoor office,
- Highway,
- Open air festival.

The generation of channel coefficients for each cluster c and each link between transmitter antenna m and receiver antenna n for a NLOS and LOS scenario is given by equations (1.48) and (1.49) respectively. The parameters are described in Table 1.12.

$$\begin{aligned} H_{n,m,c}^{NLOS}(t) = \tfrac{P_c}{P} \textstyle\sum_{p=1}^{P} & \begin{bmatrix} F_{\theta,GCS,rx,n}(\theta_{c,p}^a, \phi_{c,p}^a) \\ F_{\phi,GCS,rx,n}(\theta_{c,p}^a, \phi_{c,p}^a) \end{bmatrix}^T \begin{bmatrix} exp(j\Phi_{c,p}^{\theta\theta}) & \frac{exp(j\Phi_{c,p}^{\theta\phi})}{\sqrt{K_{c,p}}} \\ \frac{exp(j\Phi_{c,p}^{\phi\theta})}{\sqrt{K_{c,p}}} & exp(j\Phi_{c,p}^{\phi\phi}) \end{bmatrix} \\ & \begin{bmatrix} F_{\theta,GCS,tx,m}(\theta_{c,p}^d, \phi_{c,p}^d) \\ F_{\phi,GCS,tx,m}(\theta_{c,p}^d, \phi_{c,p}^d) \end{bmatrix} exp(j\tfrac{2\pi}{\lambda_0}(e_r(\theta_{c,p}^a, \phi_{c,p}^a)^T d_{rx,n})) \\ & exp(j\tfrac{2\pi}{\lambda_0}(e_r(\theta_{c,p}^d, \phi_{c,p}^d)^T d_{tx,m}))exp(j\tfrac{2\pi}{\lambda_0}(e_r(\theta_{c,p}^a, \phi_{c,p}^a)^T v_{rx} t)) \\ & exp(j\tfrac{2\pi}{\lambda_0}(e_r(\theta_{c,p}^d, \phi_{c,p}^d)^T v_{tx} t)) \end{aligned} \tag{1.48}$$

$$\begin{aligned} H_{n,m,c}^{LOS}(t) = \tfrac{1}{Kf+1} H_{n,m,c}^{NLOS}(t) + \delta(c-1)\tfrac{Kf}{Kf+1} & \begin{bmatrix} F_{\theta,GCS,rx,n}(\theta_{LOS}^a, \phi_{LOS}^a) \\ F_{\phi,GCS,rx,n}(\theta_{LOS}^a, \phi_{LOS}^a) \end{bmatrix}^T \\ & \begin{bmatrix} exp(j\Phi_{LOS}^{\theta\theta}) & 0 \\ 0 & exp(j\Phi_{LOS}^{\phi\phi}) \end{bmatrix} \begin{bmatrix} F_{\theta,GCS,tx,m}(\theta_{LOS}^d, \phi_{LOS}^d) \\ F_{\phi,GCS,tx,m}(\theta_{LOS}^d, \phi_{LOS}^d) \end{bmatrix} \\ & exp(j\tfrac{2\pi}{\lambda_0}(e_r(\theta_{LOS}^a, \phi_{LOS}^a)^T d_{rx,n}))exp(j\tfrac{2\pi}{\lambda_0}(e_r(\theta_{LOS}^d, \phi_{LOS}^d)^T d_{tx,m})) \\ & exp(j\tfrac{2\pi}{\lambda_0}(e_r(\theta_{LOS}^a, \phi_{LOS}^a)^T v_{rx} t))exp(j\tfrac{2\pi}{\lambda_0}(e_r(\theta_{LOS}^d, \phi_{LOS}^d)^T v_{tx} t)) \end{aligned} \tag{1.49}$$

Parameters	Description
m	is the mth transmitter antenna
n	is the n receiver antenna
c	is the cth cluster
p	is the pth path
P_c	is the power of cluster c
$F_{\theta,GCS,rx,n}$ and $F_{\Phi,GCS,rx,n}$	are the radiation field patterns in the direction of the spherical basis vector e_Θ and e_Φ respectively for antenna n
$F_{\theta,GCS,tx,m}$ and $F_{\Phi,GCS,tx,m}$	are the radiation field patterns in the direction of the spherical basis vector e_Θ and e_Φ respectively for antenna m
$d_{rx,n}$ and $d_{tx,m}$	are the positions vector of the receive n and transmitter m given in global coordinate system
λ_c	is the wavelenght of the carrier frequency
v_{rx} and v_{tx}	are the velocity vectors of the receiver and transmitter respectively
Kf	is the Rician K-factor
δ	is the Dirac delta function
$\Phi_{c,p}$	is the initial random phase of the path p in the cluster c, which is uniformly distributed within $[0, 2\pi)$
$\phi^a_{c,p}$ and $\phi^d_{c,p}$	are azimuth angles of arrival and departure respectively
$\theta^a_{c,p}$ and $\theta^d_{c,p}$	are the elevation angles of arrival and departure respectively

Table 1.12: Parameters of equation 1.50 from METIS map-based channel model

As the METIS GSCM channel model follows the WINNER procedure, the two weakest clusters are divided in three sub-clusters with included extra delay and power distribution following Table 1.13.

Sub-cluster	Mapping of path	Power	Delay offset
1	1,2,3,4,5,6,7,8,19,20	10/20	0 ns
2	9,10,11,12,17,18	6/20	5 ns
3	13,14,15,16	4/20	10 ns

Table 1.13: Sub-cluster information from [41]

1.3.8.2 Map-Based Model

is a simplified ray tracing where the geometry environment is known. The METIS project defines seven scenarios as follows:

- Urban micro-cell,
- Urban macro-cell,
- Indoor office,
- Indoor shopping mall,
- Highway,
- Open air festival,
- Stadium.

The channel impulse response is generated by a 16 steps procedure presented in 1.50 where parameters are defined in Table 1.12. Detailed scenarios are included in this procedure to create the radio environment, localization of the transmitter and the receiver, definition of the propagation paths and channel coefficient matrices. Then the radio channel transfer function is calculated. Finally, the CIR is calculated between the transmitter antenna m and the receiver antenna n with true motion of the transceiver. The model defines two kinds of motion, the true motion and virtual motion. The true motion is defined by a trajectory and a speed. The virtual

motion assumes that the velocity of the receiver causes small-scale effect (Doppler) but is fixed in the large scale geometry.

$$H_{n,m}(t,\tau) = \sum_{p=1}^{P} g_n^{RX}(-k_{p,n,m}^{RX}(t))^T exp(\frac{j2\pi d_{p,i,n,m}(t)}{\lambda_0} F_{p,i,n,m}^{T_{ki}}(t)) g_s^{TX}(k_{p,n,m}^{TX}(t))\delta(\tau - \tau_{p,n,m}(t)) \quad (1.50)$$

where parameters are defined in Table 1.14.

The scattering gain is modeled based on the scattering cross section for a perfectly conducting sphere. The CIR between the transmitter antenna m and receiver antenna n for a true motion is given by equation (1.51) where parameters are defined in Table 1.14:

$$H_{n,m}(t,\tau) = \sum_{p=1}^{P} g_n^{RX}(-k_{p,n,m}^{RX}(t))^T exp(\frac{j2\pi d_{p,i,n,m}(t)}{\lambda_0} (\prod_{i=1}^{I_p} h_{p,i,n,m}(t) F_{p,i,n,m}^{T_{ki}}(t)) g_s^{TX}(k_{p,n,m}^{TX}(t))\delta(\tau - \tau_{p,n,m}(t)) \quad (1.51)$$

Parameters	Description
p	is the pth path
i	is the ith interaction in the path p
I_p	is the number of interactions segment of the path p
m	is the mth transmitting antenna
n	$n$receiving antenna
g_u^{RX} g_s^{TX}	complex polarimetric antenna pattern vector for RX and TX respectively
$F_{p,i,n,m}^{T_{ki}}$	is the divergent factor for the corresponding segment i
k_p^{RX} and k_p^{TX}	is the wave vector pointing from RX and TX of the path p
w_p^D	a is the Doppler frequency of path p
$d_{p,n,m}$	is the total length of the path p equal to $\sum_i^{I_p} d_{p,i,n,m}$
$k_{p,n,m}^{RX}$	is the wave vector pointing from the last interaction point to RX
$k_{p,n,m}^{TX}$	is the wave vector pointing from TX to the first interaction point
$\tau_{p,n,m}$	is the propagation delay of the path p equal to $\frac{d_{p,n,m}}{c}$ where c is the speed of light
τ_p	is the delay of the path p

Table 1.14: Parameters of equations 1.50, 1.51, 1.52 and 1.53 from METIS models

The CIR between the transmitter antenna m and receiver antenna n for a virtual motion is given by equation (1.52), where parameters are defined in Table 1.14:

$$H_{n,m}(t,\tau) = \sum_{p=1}^{P} g_n^{RX}(-k_{p,n,m}^{RX})^T \times exp(\frac{j2\pi d_{p,n,m}(t)}{\lambda_0}) \times (\prod_{i=1}^{I_p} h_{p,i,n,m}(t) F_{p,i,n,m}^{T_{ki}}) g_s^{TX}(k_{p,n,m}^{TX}) \times exp(jtw_p^D \delta(\tau - \tau_{p,n,m})) \quad (1.52)$$

METIS channel model gives a simplification of CIR equation for virtual motion in case of the array antennas at transceiver and receiver are small enough to assume plane wave. This CIR simplification equation is given by (1.53), where parameters are defined in Table 1.14.

$$H_{n,m}(t,\tau) = \sum_{p=1}^{P} g_n^{RX}(-k_p^{RX})^T exp(\frac{j2\pi d_p(t)}{\lambda_0} (\prod_{i=1}^{I_p} h_{p,i}(t) F^{T_{ki}}) g_s^{TX}(k_p^{TX}) exp(jtw_p^D \delta(\tau - \tau_k) \quad (1.53)$$

1.3.8.3 Hybrid model

This model is a combination of a stochastic model and a map-based model. The map-based model is used to define the Path loss and shadowing of the scenario with extra random shadowing object. The stochastic model is used to defined all other parameters. The hybrid model can be used only with the knowledge of the fixed BS and MS location on the map. Only scenarios from stochastic model are available for hybrid model. There are described in a chronological optic to see the evolution of channel models and CIR representation from the third generation technology to the fifth generation technology.

1.4 Conclusion

This chapter summarized the literature survey on channel models performed during the PhD works. In the first part of the chapter, we described the generalities on mobile radio wave propagation with a brief description of the main mobile radio channel effects and the mathematical representation of the channel for a SISO and MIMO configuration respectively.

Then, we presented the channel models generally considered to evaluate system performance for cellular applications. The channel models can be classify into non-geometrical stochastic channel model represented as a TDL or Saleh-Valenzuela model. The IMT-2000 group using a TDL channel model describes pedestrian and vehicular channel. Geometry-based stochastic channel model is an other way to describe CIR. We detail one ring, two rings and distributed scattering MIMO models. Then we have explained SCM, SCME, WINNER, ITU-A and METIS model. The SCM is the first GSCM channel model considered in some standardization groups. It was followed by the the SCME, WINNER I, WINNERII/+ and METIS channel models. All these model are based on the SCM expressions and improve the definition and the number of parameters. From the WINNER channel model to the METIS channel model, a simplification of the proposed complex model is given as Generic model, CLD model and TDL model. These channel models came from standardization group: IMT and 3GPP. Channel models continue to evolve since 2 000 as shown on Figure 1.20. A comparison between the well known channel models is provided in the Table 1.15 which come from [41].

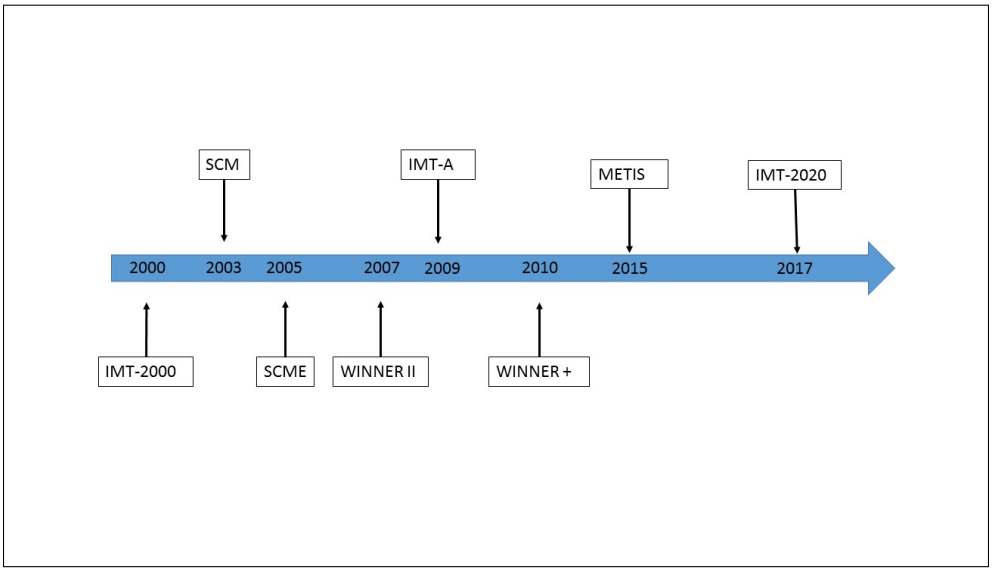

Figure 1.20: Evolution of general channel models versus time

Parameters	SCM	ITU	SCME	WINNER I	WINNER II	IMT-A	METIS
Max Bandwidth	5 MHz	5-25 MHz	100 MHz	100 MHz	100 MHz	100 MHz	100-600 MHz
Frequency range	2 GHz	2 GHz	2-5 GHz	2-6 GHz	2-6 GHz	2-6 GHz	up to 100 GHz
Shadow fading	4-10 dB	3-10 dB	4-10 dB	1-8 dB	3-8 dB	3-8 dB	0.3-20.60 dB
RMS dely spread	160-660 ns	0-2000 ns *	231-841 ns	2-235 ns	16-630 ns	20 - 365 ns	x
Nb scenarios	3	5	3	7	12	5	4
Nb of taps	6	1-6	18-24	8-24	12-24	14-24	20
Nb of cluster	6	x	6	8-24	8-20	10-20	8-24
Nb of mid-path per cluster	1	x	3-4	1	1-3	1-3	1-3
Nb of sub-path per cluster	20	x	20	10	20	20	20
MS angle spread	68	x	62-68 *	10-53 *	16-55 *	30-74 *	X
* relative delay							

Table 1.15: Comparison between classical channel models

We can mention here that the complexity of these channel models is increasing as well as the number of channel parameters to consider. The number of parameters to be considered during future measurements will depend also on the potentialities of the channel sounder developed during the PhD. In the next chapter, we will analyze the literature regarding channel models in the railway domain in order to extract some existing channel models and select gaps for which it will be interesting to perform trials with the developed channel sounder.

Chapter 2

Radio channel models in typical railway environments

2.1 Introduction

With the development of wireless communications in the railway domain, the development of channel models for railways is a very active field. The authors generally considered Train to Ground (T2G), Train to Train (T2T) and intra-train communications for high speed train environments and also tunnels in the case of metro.

The literature analysis we performed shows that the majority of the papers are dealing with radio propagation models and they mainly present narrow band parameters, such as path loss, fading statistics, angle distribution statistics and sometimes the delays and RMS delays distributions. Nevertheless, we also identified some papers that present Tapped Delay Line (TDL) and Cluster Delay Lines (CDL) models in different railway environments and mainly in HSL environments. A Winner model extracted from Ray tracing simulations in tunnels have been proposed. Recently a new TDL model in tunnels based on Ray tracing tool have been published.

In this chapter, we will describe first the main characteristics of the different railway environments. In general, railway stakeholders distinguish: main lines, regional lines, urban lines, freight and high speed lines. After this context, we will detail the different TDL and CDL models identified in each type of environments. We will differentiate open environment, viaduct, cutting, hilly terrain and tunnels.

The rest of the chapter is organized as follows. Section 2.2 describes the railway environments. Section 2.3 details the models that refer to high speed lines (HSL) with the distinction between the encountered environments. Section 2.3.7 focuses on the tunnel case.

2.2 General description of railway environments

Railway environments are quite different depending on the train category. For high speed lines (HSL) the profile of the line is generally quite linear (large curvature radius). Along HSL, classical environments are cuttings, viaducts, and large tunnels. Different obstacles as pylons carrying catenary, buildings, vegetation, *etc.* can be encountered as illustrated on Figure 2.1. Intercity lines or regional lines are mainly built in rural environment that can be open area where it is possible to cross open field, forest, mountains, suburban areas, medium size tunnels and also areas with a lot of pylons and catenaries like when approaching big cities.

Figure 2.1: Example of railway environments

Metro are generally deployed in underground environments. The type, size and shape of the tunnels will vary depending if the metro line is old or new. Different tunnel structures can be found as illustrated on Figure 2.2, rectangular, arched, horse-shoe shaped and semicircular tunnel. The tunnel can be one track or double tracks. There are a lot of various tunnels shape and structure. We consider here free radio propagation inside the tunnel using antennas. The free radio-wave propagation characteristics depend on the size of the tunnel compared to the wavelength of the signal to propagate inside the tunnel.

Figure 2.2: Different tunnel structures

In the following sections we will focus first on the HSL case and then on the tunnel case.

Table 2.1 presents a classification of the different papers related to high speed lines and Table 2.2 proposes an equivalent classification for the tunnel scenarios. We refer to incomplete model when all the important parameters are not reported in the paper. In that case, it will be impossible to implement such a model in a channel emulator for example. We will detail in the following sections the main results extracted from the papers.

2.3 Train to Ground channel model for high speed line scenarios

For some years now, journal papers presenting results of channel measurements along high-speed lines are quite numerous with the development of new HSL particularly in China. These environments are built to allow trains to run generally up to 350 km/h. Such a speed involves a lot of constraints for the measurements such as: large Doppler spread and fast variations of the

Scenario	Description of statistical propagation parameters (PL, K-factor...)	TDL models	CDL models	Incomplete models
Rural	[42], [43], [44],[45], [46] [47]	[48], [13]	[37], [24]	[43] [49] [50]
Viaduct	[51], [52], [53], [54]	[55], [56], [57]		[58]
Cutting	[59], [60], [52], [54]	[48], [61], [57]		[58]
Hilly terrain		[48], [62], [63]		
Station	[64]	[48]		[58]

Table 2.1: Classification of channel model for HSL

Scenario	Description of statistical propagation parameters (PL, K-factor, AoA, AoD...)	Incomplete Saleh-Valenzuela model	Kronecker Weichselberger model	CDL model	TDL model
Tunnel	[65], [66], [67], [68], [69], [70], [71], [72], [73], [74], [75], [76], [77], [78], [79], [80], [81], [82], [83], [83], [84]	[85]	[86]	[40]	[87]

Table 2.2: Classification of channel model for tunnels

channels parameters. A high speed train can, on a same line, pass over several scenarios. In [88], the HSL geographical environment is divided in sub environments, namely open space, viaduct, cutting, station and large tunnel as illustrated in Figure 2.3. We will follow this classification for the channel models.

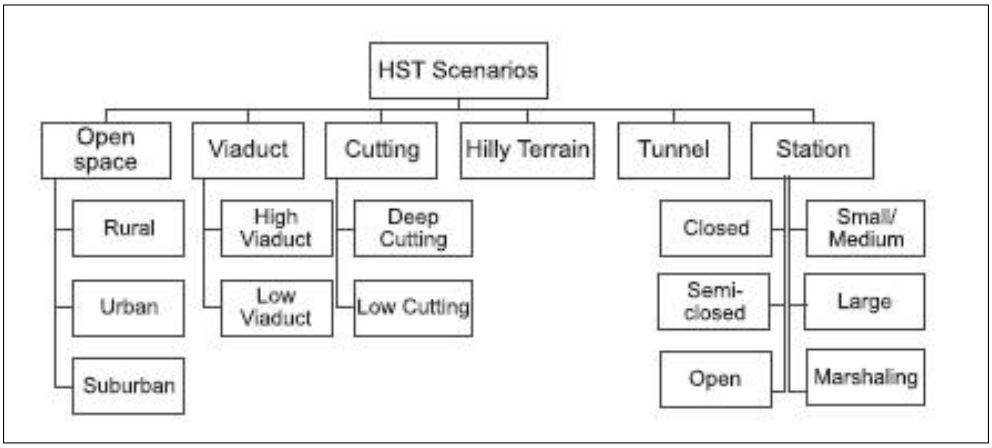

Figure 2.3: Classification of High Speed Train environments [88]

As mentioned before, most of the results in the literature present the statistical properties of narrow band channel characteristics such as Path Loss and K-factor and distributions of angle of arrival or departure of the paths. In [42, 43, 48, 44, 45, 46, 47] authors present results for various rural railway scenarios. A description of the radio propagation characteristics is given in [52, 51, 53, 54] for viaduct scenario. The same is presented in different cutting scenarios in [59, 60, 52, 54]. An analysis of path loss and K-factor is performed in [64] for a station scenario.

In this chapter we decided to focus on wide band channel models that can be used for system evaluation thanks to implementation in channel emulator for example or with simulations at link or system level, *i.e.* models that provide a description of the complex impulse response of

the channel. Several TDL channel models are considered in [13, 37, 24] for rural scenario. [55, 56, 57] treat the case of viaduct scenario. [48, 61, 57] deal with cutting scenario. [48, 62, 63] present results for hilly terrain scenario and [48] for station scenario. We will present all these channel models starting with the TDL models then we will describe the CDL models.

2.3.1 Open space scenario

This scenario is the most common HSL environment. If we consider T2G communications, the base stations are generally distributed along the tracks. Consequently, the LoS component is generally dominant between the transmitter and the receiver. As the distance between the transmitter and the receiver increases, the impact of the scatters becomes important and causes many multi-paths.

In [13], the authors present a measurement campaign in China between Beijing South Railway Station and Wuqing Station over 30 km. The speed of train is equal to 300 km/h. They use a NI-USRP 2952 (National Instrument-Universal Software Radio Peripheral) board as receiver to get channel information from LTE standard signal. A 10 MHz OCXO clock (Oven Controlled Crystal Oscillator) is used to increase the synchronization and frequency accuracy.

The measurements are performed with SISO antenna configuration at 1.85 GHz with 20 MHz bandwidth and 30.72 MS/s sampling rate. Due to the bandwidth, the maximal delay resolution is equal to 0.06 µs. The maximal time delay which can be calculate is 11 µs because of the 90 kHz between two successive cell-specific reference signal (CRS). The receive antenna is located inside the train. The authors are able to define a two taps model for this open area scenario represented in the Table 2.3. The characteristics of the antennas are not given.

Parameters	Value	
Center Frequency	1.85 GHz	
Bandwidth	20 MHz	
Speed	300 km/h	
Antenna configuration	SISO	
Path	Delay (µs)	Relative power (dB)
LOS path	0.2	-35.10
Second path	1.2	-49.60

Table 2.3: Two taps model for open area scenario at 300 km/h [13]

At the moment of the writing of the report, only two CDL channel model have been found for open scenario: the WINNER II channel model D2a [37] and the IMT-A MRa channel model [24].

The Deliverables D1.1.2 V1.0 [39] and V1.2 [37] of WINNER II project related to channel models present a typical open rural area scenario for HSL. The frequency range is from 2 GHz to 6 GHz with a bandwidth up to 100 MHz. The antennas (Huber+Suhner rooftop antenna SWA 0859 – 360/4/0/DFRX30 - 5.25 GHz) are located on the roof of the train. The measurements were performed with Propsound multi dimensional radio channel sounder from Elektrobit. This scenario is available for a speed of 350 km/h using Moving Relay Stations (MRS) on the train at 2.5 m high and with the BS at 50 m away from the track at 30 m high every 1 000-2 000 m. This scenario is presented on the Figure 2.4. For this WINNER II model, the total number of paths in a cluster is set at 20. While the total number of clusters is given by N = 8. Since the scenario is set in a rural area, the NLOS case is not considered.

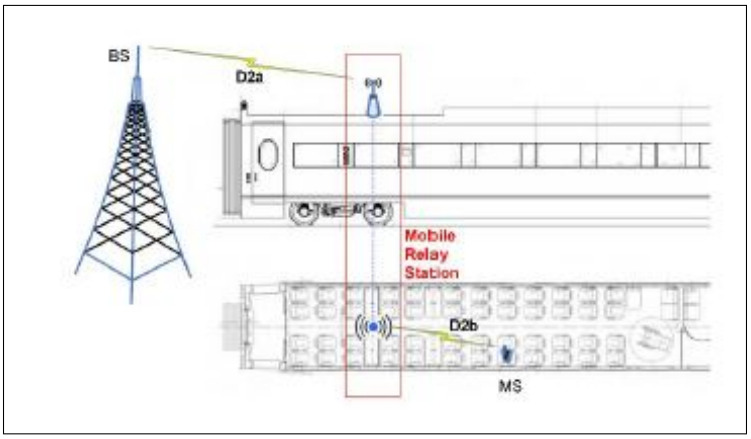

Figure 2.4: D2a scenario [37]

The model is expressed as CDL channel model. The parameters of LOS condition are given in Table 2.4. In the LOS model Ricean K-factor is 7 dB. The deliverables also give all the propagation parameters for the D2a scenario.

Parameters	Value									
Center frequency	2-6 GHz									
Bandwidth	Up to 100 MHz									
Speed	350 km/h									
Antenna configuration	SISO-MIMO									
Cluster number	Delay (ns)			Relative Power (dB)			AoD (°)	AoA (°)	Ray power (dB)	
1	0			0.0			0.0	0.0	-0.12*	-28.8**
2	45	50	55	-17.8	-20.1	-21.8	12.7	-80		-27.8
3	60			-17.2			-13.6	86		-30.2
4	85			-16.15			13.4	84.4		-29.5
5	100	105	110	-18.1	-20.4	-22.1	-13.9	87.5		-28.1
6	115			-15.7			-13	-82.2		-28.7
7	130			-17.7			-13.9	87.5		-30.8
8	210			-17.3			13.7	86.2		-30.3
* power of dominant ray / ** Power of each other ray Cluster ASD = 2°/ Cluster ASA = 3°/ Cross polarisation XPR = 12 dB										

Table 2.4: CDL parameters channel model for D2a scenario [39] and [37]

The guidelines for evaluation of radio interface technologies for IMT-Advanced is also presented in [24]. A model composed by a rural macro (RMa) cell scenario is referred as the typical open rural railway scenario. The frequency range, only for this RMa scenario, is from 450 MHz to 6 GHz with a bandwidth up to 100 MHz. A High Speed Line scenario is defined as B3 scenario for a train speed up to 350 km/h. This scenario covers a wide area, which can be up to 10 km. The BS antenna height is generally in the range from 20 to 70 m. Two CDL channel models are given for the RMa channel model, the LOS and NLOS ones. This paper also defines all the path loss parameters for the RMa scenario.

2.3.2 Viaduct scenarios

In Viaduct scenarios the LoS component is dominant and the scatters have a minor impact on the receiver. In [55] a measurement campaign is performed in a viaduct scenario in China on Beijing-Tianjin HSL. The transmitter antenna is 3 m above the rail, on the top of the train and the receiver is located on the road at 83 m far from the viaduct as presented in Figure 2.5.

The antennas configuration is SISO with a wide band vertical-polarized Sencity Rail Antenna HUBER+SUHNER [89] transmit antenna and a dipole for the receiver antenna. The train speed is equal to 240 km/h and the receiver is an Elektrobit Propsound TM Channel Sounder working at 2.35 GHz with 10 MHz bandwidth. A direct sequence spread spectrum signal is used to extract the CIR with a length of 127 bits.

Two Rubidium clocks are used to synchronize the transmitter and receiver. Authors divide the environment into five sub-regions depending on the average number of taps obtained in each sub region. They set up five corresponding TDL channel models for the viaduct scenario. The five areas are Remote Area (RA) with two paths, Toward Area (TA) with four paths, Close Area (CA) with eight paths, Closer Area (CEA) with three paths and Arrival Area (AA) into one tap. The number of path depends of resolvable multi-path components over the distance between the transmitter to the receiver. Each sub-region is defined by different number of path and relative time delay as illustrated Figure 2.5. The Doppler information is also presented for the CEA region.

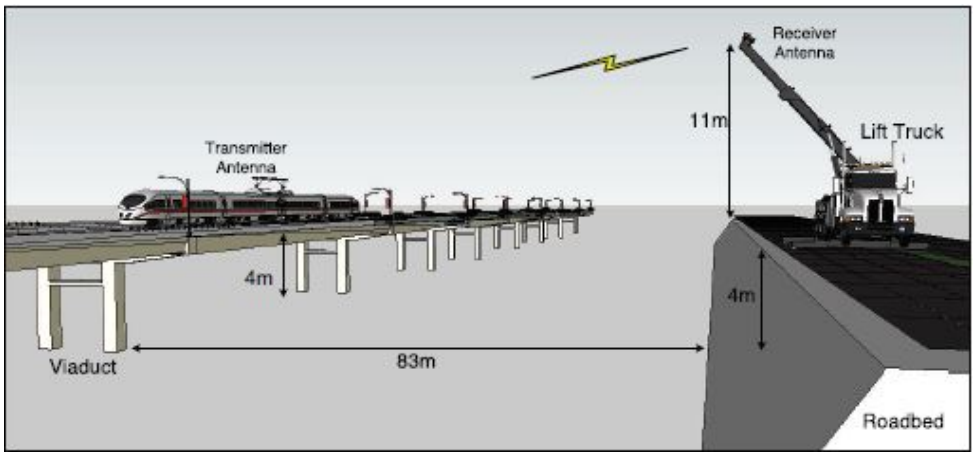

Figure 2.5: A - Relative positions over the distance. The blue dashed line denotes D_{min}, the blue point represents IP of D_{min} and the rail. D_{AA}, D_{CEA}, D_{CA} and D_{TA} are the distances from IP to the corresponding area bound, respectively. B - Schematic illustration of D_{CEA} . [55]

In [57], a measurement campaign is performed for a special scenario composed of 4 parts: a viaduct scenario situated between two cutting scenarios followed by a tunnel, as shown in Figure 2.6. Here we focus only on the viaduct results. The measurements are performed for a SISO antenna configuration where the transmitter is 20 m away from the tunnel entrance at 35 m high. The transmit antenna is a directional L-Com HG72714P-090 panel with vertical polarization with 17°vertical and 90°horizontal beam width. The receive antenna is a L-Com HG72107U vertically polarized. The omnidirectional receiving antenna moves along the track. The channel sounder uses a narrow pulse technology with a pulse period of 1 µs. Pulse width is equal to 30 ns, 45 ns and 60 ns. Two frequencies are investigated: 950 MHz and 2150 MHz. The sampling interval is 50 ns. Authors are able to provide a TDL channel model for two regions, near cutting 1 and near cutting2 as shown in Table 2.6.

This channel model is validated by a Ray-tracing method which considers the same geometrical parameters as the measurement campaign performed at 310 km/h. The authors investigate the correlation coefficients between delay and Doppler. For viaduct scenario the correlation coefficient equals 0.0308 and 0.0143 respectively for 950 MHz and 2150 MHz.

Parameters	Value				
Center Frequency	2.35 GHz				
Bandwidth	10 MHz				
Speed	240 km/h				
Antenna configuration	SISO				
Scenario	Tap number	Relative time delay (μs)	Average path gain (dB)	K factor	Doppler shift
RA ($D_{CEA}+2300<D_s/2$)	1	0	0	K_{LOS_2}	f_{max}
	2	1.3	-13.7	K_{NLOS_1}	f_V
TA ($D_{CEA}+1300<D_s/2\leq D_{CEA}+2300$)	1	0	0	K_{LOS_2}	f_{max}
	2	0.6	-11.2	K_{NLOS_1}	f_V
	3	1.3	-14.9	K_{LOS_2}	f_V
	4	2.0	-15.9	K_{LOS_2}	f_V
CA ($D_{CEA}<D_s/2\leq D_{CEA}+1300$)	1	0	0	K_{LOS_2}	f_{max}
	2	0.5	-12.9	K_{NLOS_1}	f_V
	3	1.2	-15.7	K_{NLOS_2}	f_V
	4	1.6	-18.9	K_{NLOS_2}	f_V
	5	2.0	-20.8	K_{NLOS_2}	f_V
	6	3.1	-19.8	K_{NLOS_2}	f_V
	7	3.5	-21.3	K_{NLOS_2}	f_V
	8	5.6	-21.0	K_{NLOS_2}	f_V
CEA ($D_{AA}<D_s/2\leq D_{CEA}$)	1	0	0	K_{LOS_1}	f_d
	2	0.4	-15.2	K_{NLOS_1}	f_V
	3	1.2	-19.7	K_{NLOS_1}	f_V
$AAD_s/2\leq D_{AA}$	1	0	0	K_{LOS_1}	f_d

Notes
(1) $D_s/2$ is the initial distance of the train from IP in meters, both 1300 m and 2300 m are empirical values based on experimental results;
(2) $K_{LOS_1}=-0.0337d+23.05$, $K_{LOS_2}\sim N(8.25,1.05^2), K_{NLOS_1}\sim N(5.9,1.5^2), K_{NLOS_2}\sim N(1.7,0.2^2)$;
(3) $f_V\in 0.5f_{max}, 0.7f_{max}, 0.9f_{max}$ with probabilities of 9%, 43% and 48%; $f_d(t)=f_{max}cos(\theta(t))$ with θ : arrival angle of receiver;
(4) In the Adjacent Area (AA), according to the arriving or departing process, two K_{LOS_1} piece-wise linear models with a positive or negative slope can be obtained;

Table 2.5: TDL channel model for viaduct scenario with f_{max} equal to 524 Hz [55]

Parameters	Value			
Center frequency	950 MHz		2.15 GHz	
Bandwidth	20 MHz		20 MHz	
Speed	310 km/h		310 km/h	
Antenna configuration	SISO		SISO	
Scenario	Delay (µs)	Relative power (dB)	Delay (µs)	Relative power (dB)
Near cutting 1	0	0	0	0
	108.3	-37.27	106.5	-22.95
			428.4	-39.6
Near cutting 2	0	0	0	0
	89.5	-9.5	107.3	-21.46

Table 2.6: TDL model for viaduct scenario [57]

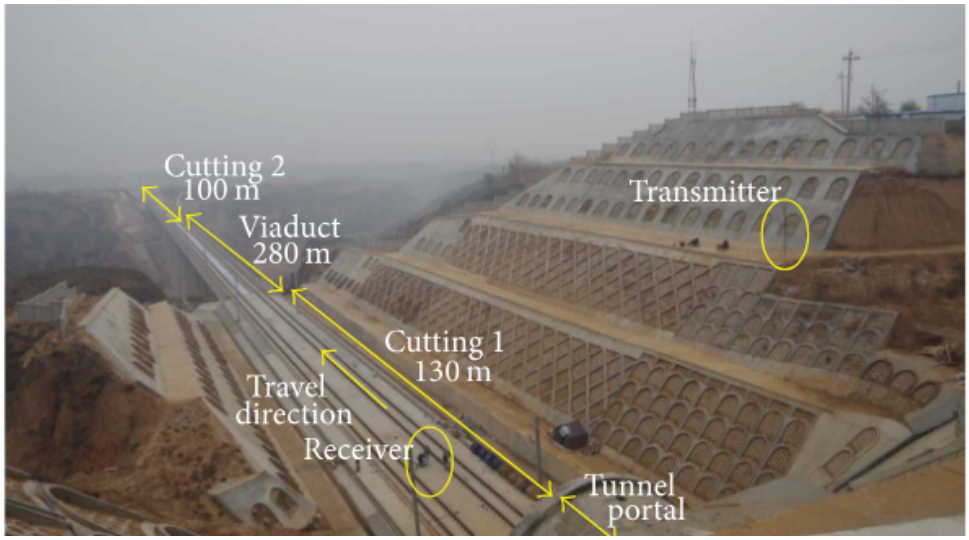

Figure 2.6: Description of viaduct scenario from [57]

In [56], measurement campaign is performed for viaduct scenario on Harbin-Dalian HSL. The measurements are performed for a 2x2 MIMO antenna configuration where the transmitter is 15 m away from the viaduct at 40 m height. The transmit antenna is omnidirectional with 45 degrees of vertical polarization with 65° and 7° vertical beam width.

The receive antennas are positioned on the roof of the train. The sounding signal is a M-sequence with a length of 1023 using Binary Phase Shift Keying (BPSK) modulation. The measurement campaign is performed at 2.6 GHz with a 20 MHz bandwidth. The train speed is equal to 370 km/h.

Two AgilentN9020 spectrum analyzers are used with a sampling rate of 19.53 ns. Contrary to the viaduct TDL models presented before, this model do not define sub-regions and provide a four taps delay model as described in Table 2.7. The mean RMS delay equals 203 ns higher than the one obtained with WINNER II channel model for LOS rural environment.

Parameters	Value	
Center frequency	2.6 GHz	
Bandwidth	20 MHz	
Speed	370 km/h	
Antenna configuration	MIMO 2X2	
Taps	Delay (µs)	Relative power (dB)
1	0	0
2	78	-4.304
3	195	-6.523
4	332	-9.468

Table 2.7: 4 Taps channel model for viaduct scenario [56]

2.3.3 Cutting scenarios

In cutting scenario, a measurement campaign was performed on Beijing-Tianjin HSL [48] as illustrated in Figure 2.7. The authors use R&S TSMQ Radio Network Analyzer to extract the resolvable multipath component with a maximal resolvable time delay of 20 µs.

A SISO antenna configuration is used to sound the channel signal using both WCDMA signal at 2.4 GHz with 5 MHz bandwidth at 240 km/h. The transmitter antenna is at 30 m away from the track on the top of the one slope wall. The receive antenna is on the roof of the train. The antenna characteristics are not given. The authors provide a four taps TDL channel model of this cutting scenario illustrated by the Table 2.9 with a Classical/Rice Doppler spectrum distribution for the first tap and a classical Doppler spectrum distribution for the others.

Parameters	Value			
Center frequency	950 MHz		2.15 GHz	
Bandwidth	20 MHz		20 MHz	
Speed	310 km/h		310 km/h	
Antenna configuration	SISO		SISO	
Scenario	Delay (µs)	Relative power (dB)	Delay (μs)	Relative power (dB)
Cutting 1	0	0	0	0
	82.9	-36.86	95.7	-32.16
	138.1	-51.26	180.4	-55.39
	192.6	-52.93	254.7	-57.35
	241.4	-55.66	305.1	-55.71

Table 2.8: TDL model for cutting scenario [57]

An other model for cutting is proposed in [57]. The measurements have been described previously. The environment refer to Figure 2.6. The corresponding TDL model is given in Table 2.8.

Figure 2.7: Illustration of U-shape cutting scenario corresponding to the TDL model given in table 2.9

2.3.4 Hilly terrain scenarios

This environment is densely scattered with objects distributed irregularly and non uniformly. With high altitude transmit antennas and low-altitude obstacles, the LoS component is observable and it can be detected along the entire railway line. However, multi path components scattered/reflected from the surrounding obstacles will cause serious constructive or destructive effects on the received signal and therefore influence the channel's fading characteristics [90].

In [63], a TDL model is proposed for hilly scenario with a train speed equal to 295 km/h at 2.4 GHz with 40 MHz bandwidth on Guangzhou-Shenzhen HSL using Tsinghua University (THU) channel sounder [91]. The transmitted signal is a linear frequency modulated sequence

Parameters	Value	
Center frequency	2.4 GHz	
Bandwidth	5 MHz	
Speed	240 km/h	
Antenna configuration	SISO	
Taps	Delay (ns)	Relative power (dB)
1	0	0
2	300	-7.3
3	900	-22.9
4	2100	-24

Table 2.9: TDL channel model for cutting railway scenario [48]

(LFM) of length 12.8 µs. The transmitter antenna is a directional antenna and is located at 10 m far from the railway track and 30 m high. The receiver antenna is omnidirectional and is placed on the roof of the train. Subspace Alternating Generalized Expectation (SAGE) algorithm is used to extract the multi path component. Authors divide into four sub-regions, the hilly terrain scenario depending of the number of predominant paths in each area: Remote Area (RA) with three paths, Distant area (DA) with five paths, Close Area (CA) with thirteen and Adjacent Area (AA) with three paths. Four TDL channel models are set up as presented in Table 2.10.

In [62], a measurement campaign, in hilly terrain at 2.6 GHz with 20 MHz of bandwidth along the Harbin-Dalian HSL at 370 km/h is studied. A 1023 bit length pseudo noise (PN) sequence modulated by a BPSK generated by Agilent E4438C VSG is used. The antenna configuration is SISO one where the transmitter antenna is fixed on the operator BS. This antenna is a cross-polarization directional antenna with 65°horizontal and 6.8°vertical beam width. The receiver antenna is omnidirectional placed on the roof of the train.

The authors defined two sub-regions with different number of predominant paths: near region and far region and they defined for each a TDL model as illustrated on Table 2.11.

In [48], a measurement campaign is performed in hilly terrain scenario on Beijing-Tianjin HSL. The scenario is composed by a plain environment on one side and a mountain at a distance of 800 m on the other side. The environments studied are plain, hilly terrain, U-shape cutting and station scenario. Here we focus only on the hilly terrain scenario.

The authors use R&S TSMQ Radio Network Analyzer to extract the resolvable multipath component with a maximum resolvable time delay of 20 µs. A SISO antenna configuration is used to sound the channel signal using both WCDMA signal at 2.4 GHz with 5 MHz bandwidth at 240 km/h. The transmitter antenna is at 30 m away from the track on the top of the one slope wall. The receive antenna is on the roof of the train.

The authors provide a three taps TDL channel model of this hilly terrain scenario illustrated by the Table 2.12 with a Classical/Rice Doppler spectrum distribution for the first tap and a classical Doppler spectrum distribution for the others.

2.3.5 Station scenario

In the same paper as before [48], authors defined a three taps TDL channel model for the station scenario presented in Table 2.13. The Doppler distribution is the same as before.

2.3.6 Summary

In this section we presented the main results found in the literature regarding radio channel models in HSL scenarios that can be considered to evaluate system performances (able to be

Parameters	Value			
Center Frequency	2.4 GHz			
Bandwidth	40 MHz			
Speed	295 km/h			
Antenna configuration	SISO			
Scenario	Tap number	Relative time delay (ns)	Average path gain (dB)	Doppler shift
AA	1	0	0	- f_{max}
	2	280	-8.7	f_V
	3	640	-17.5	f_V
	4	1350	-27.2	f_V
CA	1	0	0	- f_{max}
	2	200	-11.4	f_V
	3	450	-27.6	f_V
	4	520	-12.7	f_V
	5	860	-29.0	f_V
	6	1160	-28.0	f_V
	7	1230	-27.6	f_V
	8	1330	-23.8	f_V
	9	1390	-23.1	f_V
	10	1480	-25.9	f_V
	11	1590	-18.7	f_V
	12	1770	-29.1	f_V
	13	2100	-29.7	f_V
DA	1	0	0	- f_{max}
	2	230	-9.2	f_{max}
	3	1.2	-15.7	f_{max}
	4	1.6	-18.9	f_{max}
	5	2.0	-20.8	f_{max}
RA	1	0	0	- f_{max}
	2	0.4	-15.2	f_{max}
	3	1.2	-19.7	f_{max}
Notes (1) f_V is a random variable and $f_V \sim$ U [- f_{max},+ f_{max}]. (2) The Doppler shift values are corresponding to the case when the train departs from the intersection point.				

Table 2.10: TDL channel models for hilly terrain sub-regions [63]

Parameters	Value		
Center frequency	2.6 GHz		
Bandwidth	20 MHz		
Speed	370 km/h		
Antenna configuration	SISO		
Scenario	Delay (ns)	Relative power (dB)	Doppler shift*
Near region	0	0	f_{max}
	97.65	-6.77	0.5.f_{max}
	216.79	X	0.5.f_{max}
Far region	0	0	f_{max}
	78.12	-3.23	0.5.f_{max}
	175.77	-7.79	0.5.f_{max}
	234.36	-11.60	0.5.f_{max}
	312.48	-16.55	0.5.f_{max}

Table 2.11: TDL channel model for near and far region of hilly terrain with f_{max} equal to 875 Hz [62]

Parameters	Value	
Center frequency	2.4 GHz	
Bandwidth	5 MHz	
Speed	240 km/h	
Antenna configuration	SISO	
Taps	Delay (μs)	Relative power (dB)
1	0	0
2	0.3	-7.6
3	0.6	-22

Table 2.12: TDL model for hilly terrain [48]

Parameters	Value	
Center frequency	2.4 GHz	
Bandwidth	5 MHz	
Speed	240 km/h	
Antenna configuration	SISO	
Taps	Delay (μs)	Relative power (dB)
1	0	0
2	0.3	-5.2
3	0.6	-8.2

Table 2.13: TDL model for station scenario [48]

implemented in a radio channel emulator). The analysis conducted shows that there are a lot of papers dealing with a representation of some statistical channel parameters as path loss, K-factor, angle of arrival, etc. but there are not a lot of complete channel models that give a representation of the complex impulse response of the channel.

A quite general and straightforward methodology to implement channel model is the TDL model. We provide a review of some TDL channel model for rural, viaduct, cutting, hilly terrain and station scenarios. It is shown that, for a same scenario, different channel models can be defined depending of the number of representative paths for example. An other channel model that can be found in the literature is the CDL channel model which is more complex than TDL channel model.

There are not a lot of CDL channel model in the literature due to the complexity of model. We are able, for now, to describe only two CDL channel model. The first one is presented in the WINNER II model created by the 3GPP. The second one is presented in the IMT-A model created by ITU. Both of them describe a CDL model for rural scenario. No more CDL channel model has been found for other HSL scenario in the literature.

2.3.7 The specific case of tunnels

2.3.7.1 Free propagation in tunnel

From a general point of view, the traditional free space radio wave propagation laws are no more valid in tunnels. When the tunnel length can be considered as infinite without curve, if the tunnel is not metallic and if the dimensions of the transverse section of the tunnel are large compared to the wavelength of the operating signal, the tunnel can be considered as an oversize dielectric wave guide [92]. In this case, there are different approaches and methodologies to describe radio wave propagation in tunnels. The objective of the different existing methodologies is to express the

complex electromagnetic field in the confined area thanks to the resolution of Maxwell equations with specific boundary conditions imposed by the characteristics of the tunnel walls.

The most used methods are: rigorous description by solving Maxwell equations [93] with mathematical methods (integral methods or parabolic vector equations [94], [95]), asymptotic approach to solve the equations by using the optical approximation using ray tracing [96], [97], [98], [74] and [84] or ray launching [99]. The modal theory is also often considered and permits physical interpretation of some phenomenon [93]. [100] and [92] have developed the electromagnetic field equations in the case of rectangular linear tunnel.

The case of circular tunnel was treated in [101] and [102]. More details can be found in [99] and [103]. This theory allows to express the electromagnetic field for rectangular and circular infinite linear tunnels. Between 1 to 10 GHz, the tunnel walls (in concrete for example) behave as low loss dielectric material with the dielectric constant ϵ varying between 5 and 10 and with dielectric conductivity. The permittivity σ varies between 0.01 and 0.06 S/m. In this case, the propagation of an electromagnetic wave inside an infinite of tunnel with a rectangular cross section and with dielectric walls is the consequence of the existence of an infinity propagation modes called hybrid modes EH_{mn}. All these modes are lossy modes because the reflections on the walls imply that a part of the signal is refracted inside the wall and an other part is reflected on the wall. The consequence is a power decrease with propagation inside tunnel.

As mentioned in the introduction of this part, most of the results in the literature present the statistical properties of narrow band channel characteristics such as Path Loss and K-factor and distributions of angle of arrival or departure of the paths [65]-[84].

As for the high speed line part, we decided to focus on channel models that can be used for system evaluation, *ie* models that provide a description of the complex impulse response of the channel. In [85], a Saleh-Valenzuela channel model is identified with two main clusters. However, these papers do not give enough information about them in order to use it as a reference channel model. In [86], the authors focused on the Kronecker and Weichselberger channel models. Finally, [40] provides a CDL channel model based on the WINNER procedure using a ray tracing method. As mentioned previously, in the scientific literature we did not find TDL-based model for tunnels. This could be due to many different reasons, one of them could be the high temporal resolution that is needed in order to solve the multipath components that may exist on a tunnel. Considering existing ray-tracing tools, the development of several TDL models based on realistic tunnel description, using simulations, is an open topic. As a consequence of this observation, a new model has been proposed recently by [87].

Recent papers present results obtained thanks to narrow band measurements or ray tracing simulations. Table 2.2 given in section 2.2 presents a classification of the different papers that we will detail in the following paragraphs. We recall that in this study, we focus on papers that present channel models that can be considered to evaluate performances (expression of the complex impulse response of the channel).

Most of the measurement campaigns in tunnel are performed at 900 MHz, 2.4 GHz and 5.8 GHz which correspond today to the frequency bands considered for railway communications systems [67, 81, 83, 85, 104, 105, 106, 79, 75] highlight only on large scale fading parameters. In [79] a MIMO configuration is used to defined also the PL, PDP, K-factor and delay spread channel characteristics at 2.1376 GHz.

2.3.7.2 Some general remarks for MIMO case in tunnels

It is important to note the particularity of the case of MIMO systems in tunnels. [107] highlighted the decorrelation observed due to interference between the various hybrid modes. In [108],

the hypothesis of the authors is that modal diversity can be compared to spatial diversity for MIMO techniques. Depending on the transverse or longitudinal receiver position in the tunnel, different modes EH_{mn} can be excited. This hypothesis was confirmed in [103]. In [86], the authors have illustrated very clearly the influence of the hybrid modes excitation on a MIMO system performance. Using ray tracing simulations in a straight tunnel with rectangular cross section, they highlighted that when the antennas are perpendicular to the tunnel longitudinal axis, the MIMO channel capacity is maximal. In contrary, when the antennas are parallel to the longitudinal axis, the MIMO channel capacity is minimal. These results have been also confirmed in underground mines by [109, 110, 111] and in railway tunnels by [106].

Keyholes phenomenon was highlighted by [112]. This phenomenon occurs when the distance between the transmitters and the receivers is large compared to the radius of the circle in which the scatters at transmission and receptions sides are situated [113]. This phenomenon exists when the signals propagate in a corridor or a tunnel or when the transmitter ans receiver are very far to each other in outdoor. These channels are degenerated and can be represented by a channel matrix of rank 1 despite a total decorrelation.

The existence of a keyhole highlight the fact that a certain position in the channel, all the paths are correlated. In this case, the channel matrix is degenerated with only one degree of freedom (only one non zero eigenvalue). This is very negative for MIMO performances. In [114], the authors analyze the probability of presence of keyholes [115], [116] in various tunnel types (old and new ones). They showed the big influence of tunnel dimensions and changes in the cross section dimension as well as the fact that the tunnel is new or not. Paradoxically, in some tunnels, the presence of keyholes does not impact too much the capacity[114].

In [117] the authors analyze the influence of the variations of dimension of the tunnel transverse section on the probability of presence of keyhole. References to keyhole effects appear also in [118], [108], [119]. Generally, the higher is the correlation between the signals, the lower is the channel capacity. Nevertheless, when the correlation between antennas is low, the channel matrix $\mathbf{H}$ presents a low rank (equal to 1) and a keyhole phenomenon can occur. The example generally chose, is a scenario with a small hole in a wall that separates the environment between transmitter and receiver. The mathematical description of the phenomenon is given in [116].

2.3.7.3 TDL channel model for tunnel scenario

As illustrated in Table 2.2, only three papers give all the parameters of the models for T2G transmissions. We identified a Saleh-Valenzuela representation in [85] where authors defined two clusters but do not provide information on the various parameters to use it. Thus, we will not take it into account. The Kronecker and Weichselberger models based on correlation can also be considered for performance evaluations as presented in [86] but it is difficult to consider them for channel emulation. Finally, a WINNER CDL channel model is defined for metro tunnels scenarios in [40] based on ray tracing. In [87], HSL and metro tunnels are simulated with a ray tracing tool and also the presence of trains inside the tunnels.

2.3.7.4 WINNER CDL channel for tunnel environment

Only one channel model based on WINNER channel model has been set up in [40] at 5.8 GHz. The model was obtained using a Ray-Tracing tool to simulate free propagation in a given realistic dynamic scenario with two tracks and two trains. The four receiving antennas patch are fixed on the roof of the moving train. The scenario is represented Figure 2.8. The simulated train was running at 50 km/h. The authors present a 4x4 MIMO model based on 5 clusters. Each path of each cluster is defined in terms of delay, power, AoA and AoD.

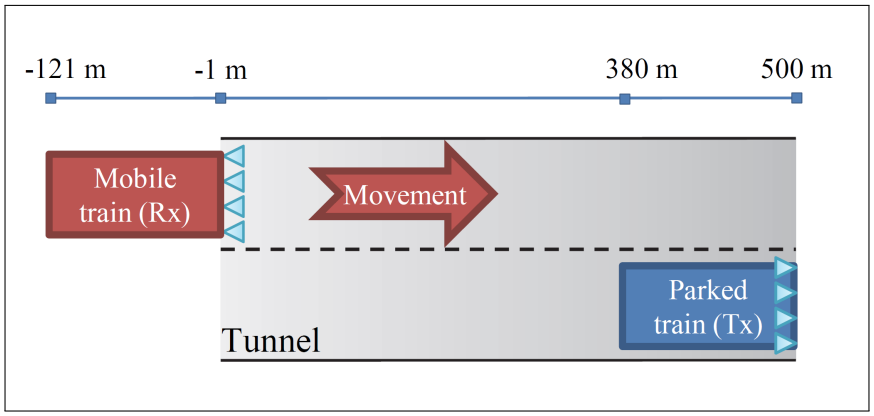

Figure 2.8: Representation of the scenario simulated [40]

2.3.8 Train to Train TDL channel model for tunnel scenario

Recent papers deal with the case of T2T measurement in metro of Madrid [120]. The authors provide TDL models for the Inter-Consist link which mean T2T link between 2 successive cars and Intra-consist link, which is a link inside the same wagon. The authors present two different results for three tunnel lines from metro of Madrid (line 6 line 10 and line 11).

For inter-consist scenario over the line 10 and 11, the results are highlighted for 2.6 GHz with a bandwidth of 80 MHz using a pulse modulation. Two Mobile-Mark MGRM-WHF omnidirectional antennas were placed on the roof of a Series 8000 continuous train, at the edges of two cars, and spaced 1 meter apart as shown Figure 2.9. The maximal speed of the metro is equal to 50 km/h.

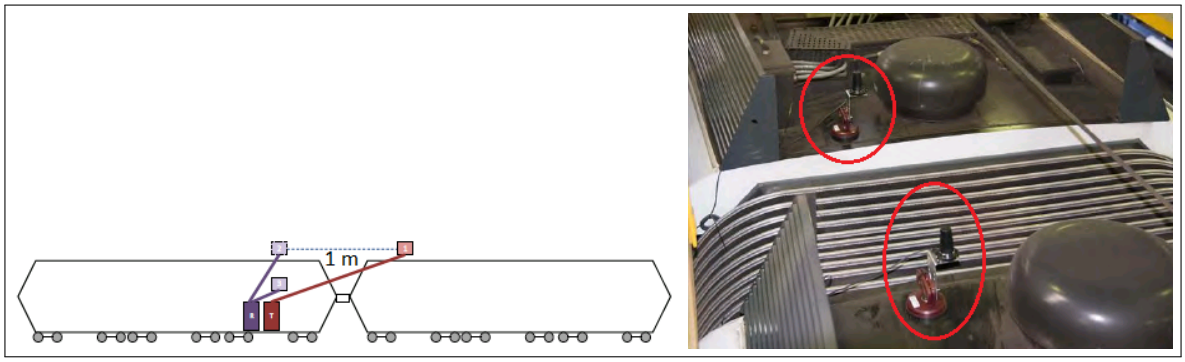

Figure 2.9: Representation of inter-consist link (left) and antennas positions (right) [120]

No tunnel dimensions description are provided in this report, we only know that line 10 and 11 passe through three straight and three curve wide tunnel and three straight and three curve narrow tunnel (table 18 of [120]).

The TDL channel model presented Table 2.14 is the result for the line 10. The RMS delay spread is equal to 62.43 ns and the mean delay is equal to 36.04 ns.

2.4 Conclusion

The characterization of the channel models for railway environments is a large topic due to the diversity of common environments that a train can encounter during a ride. We have considered channel models obtained with measurements and simulations along high speed lines and tunnels. We first described the main geographical environments in railways.

Parameters	Value			
Center frequency	2.6 GHz			
Bandwidth	80 MHz			
Speed	50 km/h			
Antenna configuration	SISO			
Scenario	Delay (ns)	Attenuation (dB)	K-factor (dB)	Standard deviation
Tunnel	0	0	12.33	0.12
	12.5	12.08	12.10	0.11
	25	18.9	10.87	0.16
	37.5	11.3	14.45	0.07
	50	13.1	14.63	0.06
	62.5	14.5	12.97	0.11
	75	12.1	15.62	0.05
	87.5	16.2	15.74	0.05

Table 2.14: TDL channel model for inter-consist link (1 m) over the line 10 of Madrid [120]

In the literature a lot of papers are dealing with a simple description of the channel statistical parameters as for example Path Loss or K-factor. We found only one TDL and two CDL channel model for rural environment, three TDL channel models are reported for viaduct, hilly, and cutting scenario. All the parameters of the TDL and CDL channel models for rural scenario are summarized in Table 2.15, Table 2.16 presented the TDL channel model for viaduct scenario, TDL channel model for hilly terrain are given in Table 2.18 and cutting scenario in Table 2.17. For a same scenario different channel models exist depending on the complexity and accuracy of the parameters. A CDL model is potentially more accurate than a TDL channel model due to the availability of more parameters that can be taken into account. CDL channel model was found only for rural scenario.

The last part of this chapter describes the channel models for tunnel scenario.

As previously mentioned, a lot of papers deal with a simple description of large scale fading parameters. One CDL channel model is fully described in terms of: number of clusters and number of paths per cluster, angle distribution laws.

The literature analysis conducted also shows that there is no available general MIMO channel model to describe the behavior of dynamic subway scenario in tunnel from a radio channel point of view in order to evaluate digital communication system performances. A lot of papers dealing with statistical analysis of measurements in the 2-5 GHz band can provide some results on fadings and delay spread statistics. Several papers also analyze the variation of the spatial correlation degree in the tunnel as a function of antenna polarization or antenna positions. Based on this figures, it is possible also to build simple statistical models such as Kronecker and Weichselberger models. Key holes effect in tunnel has also been briefly presented.

Another possible channel model is a WINNER CDL channel model obtained with dynamic simulations based on an optimized ray-tracing simulator for straight tunnels with rectangular cross section. A TDL channel model for HSL and metro taking into account the presence of trains has also been published in December 2020.

This literature survey has highlighted that there is a very important need for radio channel models that can be used to emulate the radio railway environments in laboratory in order to assess the performances of wireless systems in representative railway environments with zero on site testing.

This analysis has been considered within the H2020 Emulradio4Rail European project in the Shift2rail JU program. This chapter is part of the D1.3 [121] of the project. In addition, we have

proposed a methodology to chose a set of models to be implemented in a Propsim F32 channel emulator for experimental assessment of different radio access technologies, namely: Wi-Fi and LTE in different railway conditions. The different railway models considered and the preliminary results are published in [122].

Reference								**[37]**								**[24]**										**[13]**		
Parameters								Value								Value										Value		
Center frequency								2-6 GHz								450 MHz - 6 GHz										1.85 GHz		
Bandwidth								up to 100 MHz								up to 100 MHz										20 MHz		
Speed								350 km/h								350 km/h										300 km/h		
Antenna configuration								MIMO								MISO										SISO		
Scenario	Cluster	Delay (ns)						Relative power (dB)			AoD (°)	AoA(°)	Delay (ns)					Relative power (dB)			AoD (°)	AoA(°)	Taps	Delay (ns)		Relative power (dB)		
Rural	1	0						0			0	0	0	0	0	0	0	-17.8	-19.5		0	0	1	200		-35.1		
	2	45	50	55	-17.8	-20.1	-21.8				12.7	-80	35	40	45	-16.9	-19.1	-20.9			24	99	2	1200		-49.6		
	3	60				-17.2					-13.6	86	45					-16.8			23	95						
	4	85				-16.15					13.4	84.4	65					-18.3			24	99						
	5	100	105	110	-18.1	-20.4	-22.1				-13.9	87.5	110					-21.2			-25	-106						
	6	115				-15.7					-13	-82.2	110					-17.1			-23	96						
	7	130				-17.7					-13.9	87.5	125					-19.7			-25	-103						
	8	210				-17.3					13.7	86.2	125					-23.8			27	113						
	9												170					-22.9			27	110						
	10												170					-20.9			25	106						
	11												200					-21.9			-26	-108						

Table 2.15: Comparison of TDL and CDL channel models for railway rural scenario

Reference			**[55]**			**[56]**			**[57]**					
Parameters			Value			Value			Value					
Center frequency			2.35 GHz			2.6 MGz			950 MHz			2.15 GHz		
Bandwidth			10 MHz			20 MHz			20 MHz			20 MHz		
Speed			240 km/h			370 km/h			310 km/h			310 km/h		
Antenna configuration			SISO			MIMO 2x2			SISO			SISO		
Scenario	Taps	Scenario	Delay (ns)	Relative power (dB)	Doppler shift	Delay (ns)	Relative power (dB)	Scenario	Delay (ns)	Relative power (dB)	Delay (ns)	Relative power (dB)		
Viaduct	1	RA	0	0	fmax	0	0	Near 1	0	0	0	0		
	2		1300	-13.7	fV	78	-4.304		108.3	-7.3	106.5	-22.95		
	3	TA	0	0	fmax	195	-6.523				428.4	-39.6		
	4		600	-11.2	fV	332	-9.468	Near 2	0	0	0	0		
	5		1300	-14.9	fV				89.5	-9.5	107.3	-21.46		
	6		2000	-15.9	fV									
	7	CA	0	0	fmax									
	8		500	-12.9	fV									
	9		1200	-15.7	fV									
	10		1600	-18.9	fV									
	11		2000	-20.8	fV									
	12		3100	-19.8	fV									
	13		3500	-21.3	fV									
	14		5600	-21	fV									
	15	CEA	0	0	fmax									
	16		400	-15.2	fV									
	17		1200	-19.7	fV									
	18	AA	0	0	fd									

Table 2.16: Comparison of TDL and CDL channel model for railway viaduc scenario

Reference		[57]			[61]				[48]	
Parameters		Value				Value			Value	
Center frequency		950 MHz		2.15 GHz		950 MHz			2.4 GHz	
Bandwidth		20 MHz		20 MHz		20 MHz			5 MHz	
Speed		310 km/h		310 km/h		310 km/h			240 km/h	
Antenna configuration		SISO		SISO		SISO			SISO	
Scenario	Taps	Delay (ns)	Relative power (dB)	Delay (ns)	Relative power (dB)	Scenario	Delay (ns)	Relative power (dB)	Delay (ns)	Relative power (dB)
Cutting	1	0	0	0	0	RA	0	0	0	0
	2	82.9	-36.86	95.7	-32.16		240	-8.6	300	-7.3
	3	138.1	-51.26	180.4	-55.39		360	-12.12	900	-22.9
	4	192.6	-52.93	254.7	-57.35		460	-8.5	2100	-24
	5	241.4	-55.66	305.1	-55.71		1108	-12.12		
	6					CA	0	0		
	7						180	-14.46		

Doppler
fmax
Von(18,147)
0.73*Von(31,24) +0.27*Von(100,131)
Von(81,152)
Von(67,154)
fmax*cos($\theta(t)$)
Von(95,141)

Table 2.17: Comparison of TDL channel model for railway cutting scenario

Reference			**[63]**				**[57]**		**[48]**	
Parameters			Value				Value		Value	
Center frequency			2.4 GHz				2.6 GHz		2.4 GHz	
Bandwidth			40 MHz				20 MHz		5 MHz	
Speed			295 km/h				370 km/h		240 km/h	
Antenna configuration			SISO				SISO		SISO	
Scenario	Taps	Scenario	Delay (µs)	Relative power (dB)	Doppler shift	Scenario	Delay (ns)	Relative power (dB)	Delay (µs)	Relative power (dB)
Hilly terrain	1	AA	0	0	-fmax	Near region	0	0	0	0
	2		280	-8.7	fv		97.65	-6.7742	300	-7.6
	3		640	-17.5	fv		216.7969		600	-22
	4		1350	-25.2	fv	Far region	0	0		
	5	CA	0	0	-fmax		78.12	-3.2298		
	6		200	-11.4	fv		175.77	-7.7951		
	7		450	-27.6	fv		234.36	-11.6046		
	8		520	-12.7	fv		312.48	-16.547		
	9		860	-29	fv					
	10		1160	-28	fv					
	11		1230	-27.6	fv					
	12		1330	-23.8	fv					
	13		1390	-23.1	fv					
	14		1480	-25.9	fv					
	15		1590	-18.7	fv					
	16		1770	-29.1	fv					
	17		2100	-27.7	fv					
	18	DA	0	0	-fmax					
	19		230	-9.2	+fmax					
	20		470	-15.3	+fmax					
	21		1140	-18.7	+fmax					
	22		1790	-22.4	+fmax					
	23	RA	0	0	-fmax					
	24		410	-14.8	+fmax					
	25		2440	-18.3	+fmax					

Table 2.18: Comparison of TDL channel model for railway hilly terrain scenario

Chapter 3

State of the art on Radio channel sounders

3.1 Introduction

As explained in Chapter 1, accurate radio channel models are needed for the design, simulation and performance evaluation of wireless communication systems. The characterization of the radio channel or the channel sounding consists in the measurement of the statistical channel parameters described in the previous chapter such as multipath components behaviour, time dispersion, Doppler spread, angle of arrival and departure of waves, *etc.*

With, increasing complexity of wireless systems, more and more channel parameters are required to model correctly the radio channels. These parameters are extracted from the statistical variations of either the channel time-variant impulse response or its time-variant frequency response in SISO or MIMO configuration. Channel sounders can be differentiated according to the used waveform, the number of antennas, the operational frequency, the bandwidth related to time resolution and their capability to extract various channel properties. Mainly four types of excitation signals are considered in sounding techniques [10]: pulse waveform, pseudo random binary sequences, frequency chirp, OFDM signals.

The sounders can operate respectively in the time domain or in the frequency domain, depending on the transmitted or excitation signal. With the use of millimetric and terahertz bands with the arrival of new 5G NR standard, channel sounders development in these bands rises new challenges.

The rest of the chapter is organized as follows. Section 3.2 and section 3.3 detail the main channel sounding methods in time and frequency. Then, in section 3.4 we will present existing MIMO channel sounders in the literature taking into account recent evolution towards millimetric bands to take into account 5G NR and beyond systems evaluation. The section 3.5 focuses on SDR-based channel sounders in general as they can offer flexibility and modularity. In particular we will introduce SDR-based channel sounders using LTE signals that constitutes the solution we have chosen for the channel sounder developed in this PhD work.

3.2 Sounding methods in the time domain

3.2.1 Pulse sounding

This technique is a direct application of the channel impulse response definition. It consists of transmitting a pulse in the time domain and observing the different echoes of the signal at

the reception [123] by receiving the signal in phase (I) and in quadrature (Q). This is a simple method in theory but it is not so easy to generate pulses as shorter as possible and to extract the received signal in noise context. However, this technique is of particular interest for the measurements of the UWB (Ultra Wide Band) channel [124, 125, 126, 127]. This technique is well adapted to measure spatial or temporal variations of the channel. The main advantages of the pulse sounding technique lies in its low acquisition time and in the possibility to retrieve the impulse responses in real time. The drawbacks concern the difficulty to generate very short pulse with high power, which gives rise to a poor dynamics of the impulse response and restricts the type of configurations that can be characterized at the short distance connection or the Line of Sight configuration.

3.2.2 Pseudo Random Sequence Correlation Sounding

This technique is widely used for channel sounding [128, 129, 130, 131]. The principle of pseudo-random sequence (PR) correlation measurement is to use the auto-correlation properties of PR sequences. It is generated by a shift register consisting of n flip-flop looped by an adder. In this case, the size of the PR sequence is $2^n - 1$ and its auto-correlation is a Dirac of dynamic $20log_{10}(2^n - 1)$. In the frequency domain, the analysed band at -3 dB is equal to the clock frequency of the PR sequence generator. The impulse response $h(t)$ is obtained by a simple auto-correlation between the received signal and the replica of the transmitted signal. The advantage of this method is to be able to configure the sounder dynamic by varying the size of the shift register.

Generally, the correlation is performed in the post-processing phase, in parallel with the calculation of the transmitted power, the positions of the transmitters and receivers or other data related to the impulse response. The duration of an acquisition allowing the calculation of an impulse response is equal to the length of the sequence used (a few µs). The minimal time between two acquisitions is limited by the speed of the digitizer to transfer the digitized samples to a storage memory (PC RAM for example) and to rearm a new acquisition. This time is generally of the order of a millisecond. If the digitization cards are equipped with internal memory, it is even possible to continuously sample the equivalent of several successive sequences and to analyze very fast transient phenomena. The principle of correlation is therefore well suited to all environments and in particular those where the channel varies rapidly (mobile in urban areas). The principle is given on Figure 3.1a.

3.2.3 Sliding correlation Sounding

The sliding correlation method [132, 133, 134] uses also the principle of correlation and the autocorrelation properties of PR codes. The system consists of two identical PR code generators with slightly different clock frequencies, one at the transmitter (clock f_{c_1}) and the other at the receiver (clock f_{c_2}). This difference allows PR sequences to slide in time relative to each other. The sliding correlator consists of multiplying the signal received by the PR sequence from the receiver and performing the sum of the multiplication. At each instant, a point of the correlation between the transmitted signal and the received signal is therefore calculated, corresponding to a point of the impulse response. The digital signal at the output of the correlator is the impulse response dilated in time by a factor $k = \frac{f_{c_1}}{f_{c_2} - f_{c_1}}$. At a given delay τ_m at the output of the correlator, corresponds a real delay $\tau = \tau_m / k$. The k factors are generally high between 1000 and 100000. The calculation of an impulse response lasts kT. The time resolution is of the same order of magnitude than the conventional correlation namely $1/f_{c_1}$. From the frequency point of view, the signal digitized in base band is compressed by a factor k. This compression gives two main advantages:

- A narrow band filter at the output of the correlator eliminates most of the noise and interference included in the analysed band and therefore increases the dynamics of the impulse response.
- The sampling frequency of the digital-to-analog converters required is low (less than MHz). The cost of the converters is reduced even for a time resolution of the order of a nanosecond.

The major drawback of this technique is the duration of the computation of an impulse response, which prohibits the Doppler analysis of a very rapidly varying channel and where the delays can be significant (10 µs). The sliding correlation sounders are very well adapted for the characterization of indoor environments where the channel varies slowly and the delays are not too large (less than 1 ms). This technique is an interesting alternative to frequency sampling. The principle is illustrated in Figure 3.1b.

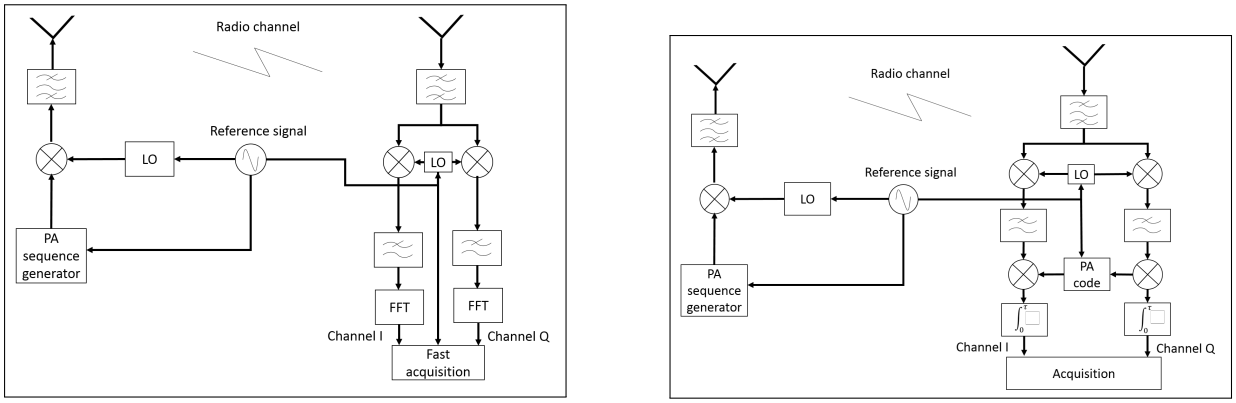

(a) Pseudo random sequence correlation sounding

(b) Sliding correlation sounding principle

Figure 3.1: Channel sounder using correlation [135]

3.3 Sounding methods in the frequency domain

3.3.1 Introduction

The principle of channel sounding in the frequency domain [136], is to scan the frequency band to be analyzed, in a similar way to the operation of spectrum analyzers. For each frequency, the attenuation and phase shift provided by the radio channel are determined. The impulse response is obtained by inverse Fourier transform of the transfer function measured. The two main categories of channel sounders in the frequency domain are the vector network analyser sounder and the frequency sweep (or chirp method) channel sounder.

3.3.2 Vector network analyser based sounders

A very simple implementation of this principle consists in using a vector network analyzer with port 1 connected to the transmitter and port 2 connected to the receiver. The transfer function is determined by parameter $S_{21}(f)$. The main advantage of frequency scanning is the ability to scan a very wide band of the spectrum. The use of very narrow filters in reception leads to very good measurement dynamics but increases the time necessary for the complete determination of a transfer function. On the other hand, the phase can only be determined if the transmitter and the receiver are perfectly synchronized. The local oscillators (LO) of the up and down transpositions must imperatively be controlled on a common reference, which limits the transmitter-receiver distance to a few tens of meters.

This method is adapted to point-to-point applications in indoor environments requiring a large bandwidth. This drawbacks can be avoided using a fiber optic as proposed by [137]. The authors consider a MIMO channel sounder based on a VNA and two virtual arrays. The Rx antenna is directly connected to one port of the VNA using a low-attenuation coaxial cable and a 30 dB low noise amplifier. The signal of the Tx port of the VNA is converted into an optical signal sent through fiber optics, allowing for measurements on large distances. The optical signal is then converted again into radio frequency and amplified. In [138] the MIMO channel sounder that is based on two multiports VNAs. To perform MIMO measurements, one VNA has multiple ports, and a high-speed switch is connected to the other VNA. This channel sounder is restricted to static propagation environments.

3.3.3 Frequency sweep method

The chirp sounder [10] is a frequency method to solve the problem of acquisition duration. The sounding signal is no longer a pure sine wave but a frequency ramp called chirp. There are two methods for calculating the impulse response using a chirp sounder. The first one is to correlate the received signal with a replica of the transmitted signal. Windowing should be applied to reduce the side lobes. This principle is identical to the correlation method, only the sounding signal changes. The advantages, disadvantages and scope of this principle are identical to those of correlation based sounding methods. The second method considers heterodyne reception. This method consists in multiplying the received signal by the transmitted chirp signal and to apply a low-pass filter to the result obtained. By increasing the measurement time, the signal band at the output of the sounder is reduced and the use of fast analog converters, therefore expensive, is avoided. However, as with sliding correlation, Doppler analysis is limited by the time of a measurement. The advantage of chirp sounders lies mainly in the sounding sequence that can be easily generated by a synthesizer with frequency sweep. The band analyzed is no longer limited by the clock frequency of a generator of arbitrary signals or pseudo-random sequences.

The chirp technique [10] offers the same advantages than the sliding correlation technique from a frequency compression point of view. This allows to decrease the analog band B of the receiver and the observation window allowing to acquire the highly delayed paths. This analog band reduction offers a flexibility identical to the sliding correlation technique allowing the implementation of a more efficient acquisition module (quantification on a larger number of bits) and a noise band reduction of a factor $k_{chirp} = \frac{B}{T_{obs}T}$ where T_{obs} is the observation window at receiver, B is the bandwidth and T is the time duration of the chirp.

Theoretically, the temporal resolution, after calibration of the frequency response, is the inverse of the band analyzed but this is degraded by the need to window the measured signal in order to carry out the Fourier transform and not by a material defect in the measurement system. This window will therefore determine the dynamics and the temporal resolution of the measurement system. and example of this technique is illustrated in [139].

3.3.4 Sounding methods based on OFDM signals

3.3.4.1 Introduction

Orthogonal Frequency Division Multiplexing modulation is widely used in recent wireless communications systems due to its capability to avoid inter-symbol interference by inserting a guard interval (GI) [140]. Channel sounders based on OFDM signal implement generally aided channel estimation techniques with known subcarriers, called pilots, inserted in the OFDM symbol. This known information is available at receiver for the estimation of the complex impulse responses.

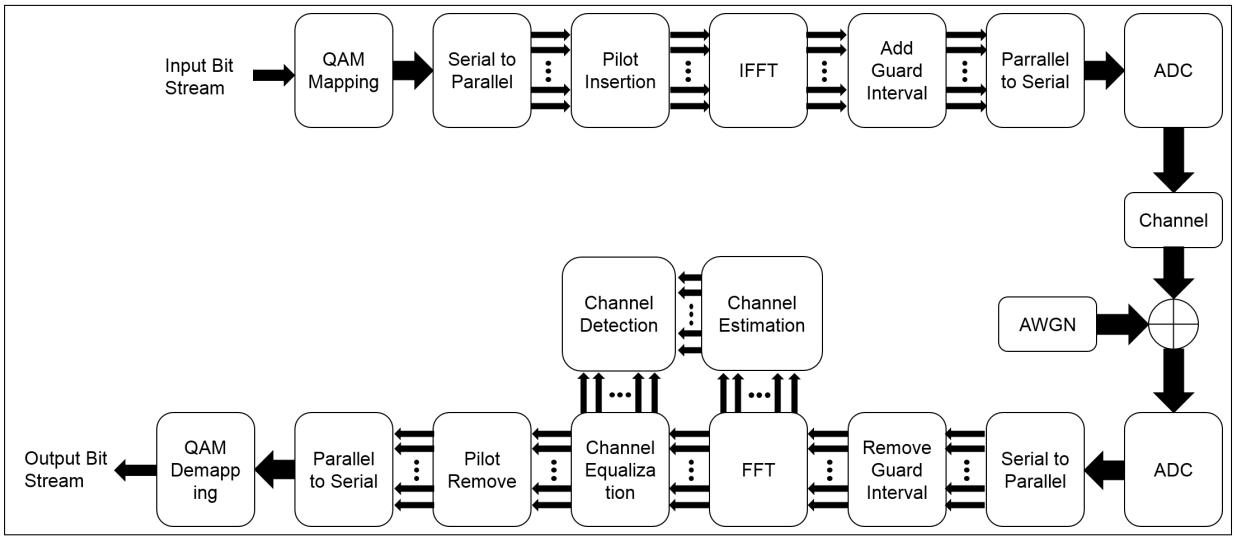

Figure 3.2: Baseband model for OFDM system [141]

The baseband model Figure 3.2 presents the difference stages of an OFDM signal transmission and reception. At the transmitter part, pilots are inserted in the signal after the realization of the pre-constellation modulation and serial to parallel block. At this stage, an IFFT (Inverse Fast Fourier Transform) is applied to the constellation to transform the modulated data into the time domain signal. Then, a guard interval called cyclic prefix (CP) is added in the front of the OFDM symbol to prevent the ISI. Note that the GI corresponds to a part of the end of the OFDM symbol.

Finally the signal pass through a digital to analog converter and is transmitted in the channel. At the receiver side, an analog to digital converter is used to sample the received signal and to convert it into a digital signal. An FFT (Fast Fourier Transform) is applied after removing the guard GI to get the signal in the frequency domain. At this stage, the channel estimation is applied to feed the channel equalizer and remove the channel effect on the data. Finally, after removing the pilots a QAM (Quadratic Amplitude Modulation) demapping is applied to obtain the output bit stream.

At the beginning of 2010, a new standard developed by the 3^{rd} Generation Partnership Project (3GPP) has emerged, based on OFDM. It is called Long Term Evolution (LTE). LTE and his extension LTE-advanced is now the commonly used technology in telecommunication system. This technology increase significantly the number of user by cells and the bandwidth is increased up to 20 MHz, which means to increase also the aggregated data rate by user. The data rate targeted for downlink and uplink is 100 Mbps and 50 Mbps respectively with 20 MHz bandwidth. LTE can be operated in Time Division Duplex (TDD), which mean that uplink and dowlink use the same frequency band and in Frequency Division Duplex (FDD), which splits the uplink and dowlink into two frequency bands with a fix duplex interval [141].

One important block of the system at the receiver side in the OFDM baseband model, is channel estimation, shown in Figure 3.2. Based on multicarrier technology and using a channel estimation method directly implemented in the communication systems, the LTE like signal is commonly used for channel sounding measurement using SDR platforms. We will now describe the principle of the LTE channel sounding method and then we will describe some SDR based channel sounders.

3.3.4.2 LTE signal structure

The transmission resource in LTE is defined in three dimensions [141]: time, frequency and space. The spatial dimension is defined by multiple antenna system in transmission and reception.

The time-frequency resource in the LTE signal is defined by a succession of frames of 10 ms called radio frame. Each radio frame is divided into 10 sub-frames of 1 ms each composed of two time slots of 0.5 ms. Each interval includes 7 OFDM symbols or 6 OFDM symbols for normal and extended cyclic prefix respectively.

The LTE radio resources are organised into radio Resource Block (RB) defined by 12 subcarriers and 7 time symbols (one slot). The smallest unit of resources is called a Resource Element (RE), which is one subcarrier for one OFDM symbol. The RB is composed of 84 RE in normal cyclix prefix and 72 RE in extended cyclic prefix. Figure 3.3 shows the normal cyclix prefix frame structure.

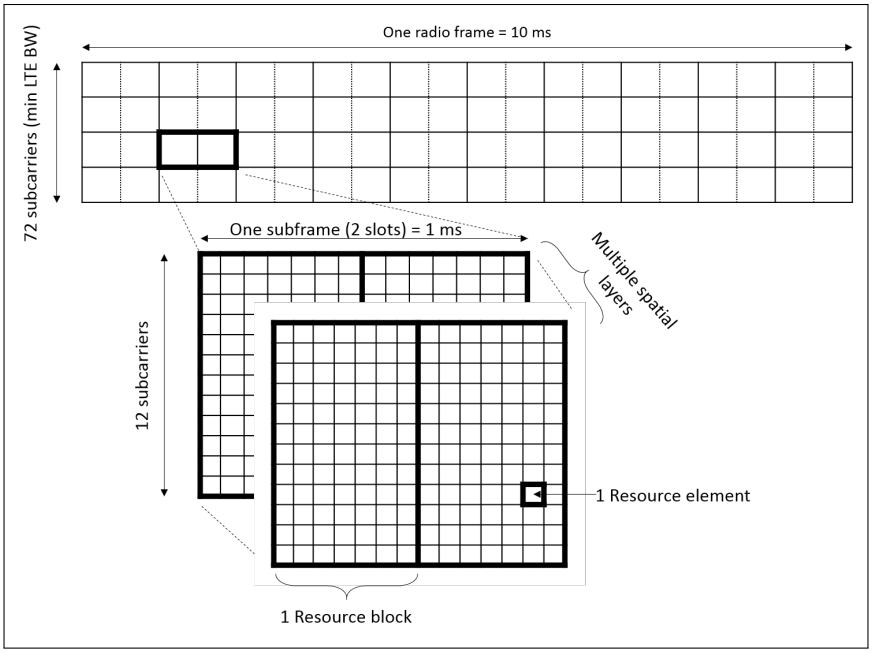

Figure 3.3: Frame structure of LTE for normal cyclix prefix case

The radio resource block can include different type of information as data symbols and pilot symbols known at the transmitter and receiver. Synchronization signal, reference signals, control signalling and critical broadcast system information are RE, which can be used in frame structure to help verification, channel estimation and synchronization.

3.3.4.3 Base station and mobile station synchronization

To synchronize the LTE base station (eNodeB) and the mobile station (UE-User Equipement), two physical signals are used, the Primary Synchronization Signal (PSS) and the Secondary Synchronization Signal (SSS) [141]. These two signals, enable time and frequency synchronization, and provide information about the physical layer identity, cyclic prefix length and duplexing mode (FDD or TDD). PSS and SSS structure is designed to facilitate this acquisition of information. In TDD and FDD, PSS and SSS are periodically transmit every 10 ms (every radio frame). In TDD, the PSS is located in the 3rd and 13th slots at the symbol position three. The SSS is located three symbol earlier as presented Figure 3.4. It means that for a good synchronization, the channel coherence time as to be longer than 4 OFDM symbols.

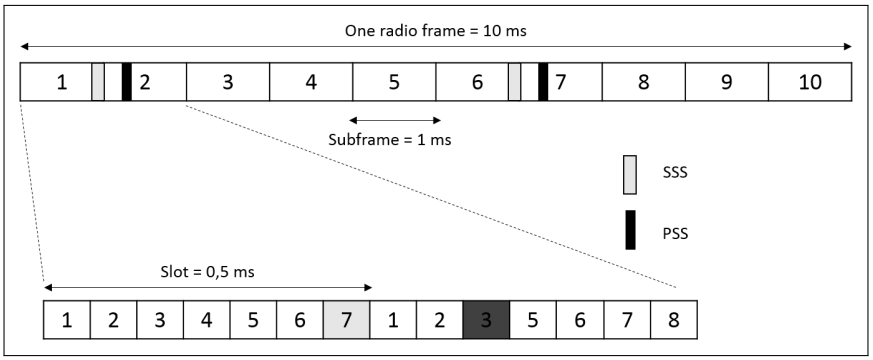

Figure 3.4: PSS and SSS frame and slot structure in time domain for TDD and normal cyclix prefix

At the receiver, the PSS detection is done by an autocorrelation coupled with a maximum likelihood detector to find the maximum correlation following the equation (3.1):

$$m_M^* = argmax_m | \sum_{i=0}^{N-1} Y(i+m) D_M^*(i)|^2 \tag{3.1}$$

where i is the symbol time index, m is the timing offset, N is the PSS time domain signal length, $Y(i)$ is the received signal at time instant i and $S_M(i)$ is the PSS with root M replica signal at time i.

The SSS is based on M-sequences with a sequence of length $2n-1$ with n is the shift register length. Each SSS sequence is built by interleaving in the frequency domain two BPSK-modulated secondary synchronization codes. These two codes are alternated between the first and second SSS in each transmitted radio frame. As the two codes are different, the receiver can determine the 10 ms radio frame timing from a single observation of a SSS. The SSS detection is done after the PSS detection due to the coherent detection method using with the estimated channel coefficient from PSS. This detection is applied with the following equation (3.2):

$$\hat{S_m} = argmin_s(\sum_{n=1}^{N} |y(n) - S(n,n])\hat{h_n}|^2) \tag{3.2}$$

where, the symbols $S(n,n)$ represent the SSS sequences and $\hat{h_n}$ are the estimated channel coefficients.

3.3.4.4 LTE Reference signal

To estimate the channel, a common and simple way is generally to use the Reference Signal (RS) [141]. It is a parametric symbol a priori known by the receiver, which can be inserted to specific RE in time and frequency according to a pattern. Based on standard, a pattern is defined for SISO and MIMO configurations.

According to [141] the minimum mean squared error is maximized for an equidistant RS position in the RB in time and frequency. The position spacing between RS is obtained by taking into account the maximal Doppler spread with a speed of 500 km/h. The Doppler shift can be calculated by $f_d = (f_c \times v/C)$ where f_c is the carrier frequency, v is the receiver speed and C is the speed of light.

For example, with a carrier frequency of 2 GHz, the Doppler shift is approximated 950 Hz. Following Nyquist theorem, to recover the channel the minimal sampling time as to be $T_c = \frac{1}{(2f_d)} = 0.5\ ms$. To apply this result in the radio frame, the RS has to be at least two per slot in time domain in order to estimate the channel correctly. In frequency domain, the RS are positioned every six subcarriers. Figure 3.5 shows the RS pattern for SISO system.

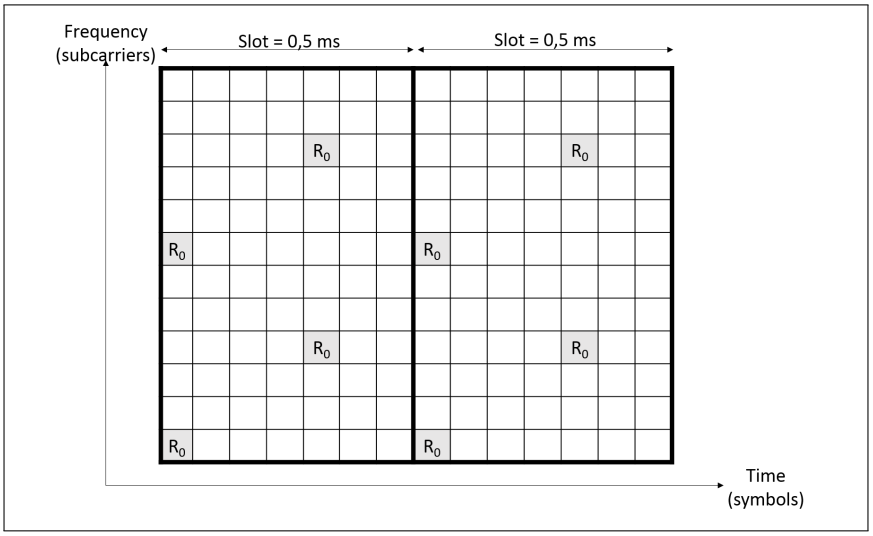

Figure 3.5: Reference Signal pattern for normal cyclic prefix

Due to the development of MIMO system, LTE standard defines new RS patterns for 2 and 4 receiving antennas presented Figure 3.6.

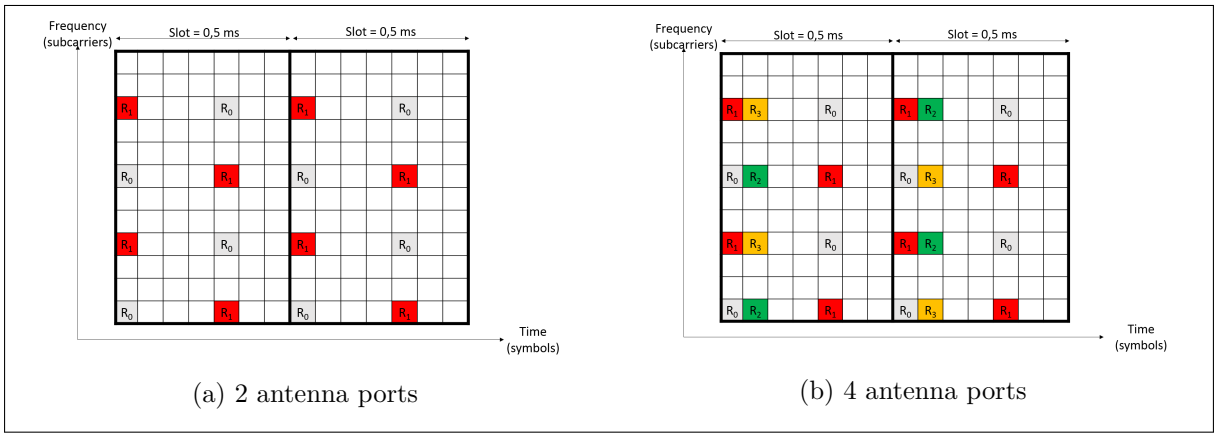

(a) 2 antenna ports

(b) 4 antenna ports

Figure 3.6: Reference Signal pattern for normal cyclic prefix with (a) 2 and (b) 4 antenna ports [141]

3.3.4.5 Pilot patterns

Specific pilot patterns are considered in the literature to optimize channel estimation performances in several type of channels. The different types of existing channel sounders consider different pilot types with specific autocorrelation properties, various pilot positions in the symbol and various channel estimation techniques for OFDM signals.

One can find mainly three basic pilot arrangements techniques [142, 143] depending on the pilot positions in the OFDM symbol, namely the block-type, the comb-type and the lattice-type. For LTE, a fourth solution has been considered to optimize data transmission [141].

Block-type pilot pattern, is built by inserting pilot tones into all subcarriers of OFDM symbols transmitted periodically. This method assumes a slow fading channel to avoid the frequency pilots interference's. A time-domain interpolation is needed to estimate the channel where pilots are unused. In this case the pilots periodicity has to be in accordance with the coherence time of the channel. As the coherence time is inverse form of the Doppler frequency $f_{Doppler}$ of the channel, the periodicity S_t of the pilot symbol can be identify by (3.3). This technique is suitable for frequency selective channels but not for fast-fading channels.

$$S_t \leq \frac{1}{f_D} \tag{3.3}$$

Comb-type pilot organization, consists of inserting pilot tones into all temporal OFDM symbols. However, the pilot tones are partially and periodically disseminated into the frequency subcarriers, which allows a faster fading channel. In this case a frequency interpolation is needed between known subcarriers to estimate the channel where there is no frequency pilot. The periodicity has to be in accordance to the coherence bandwidth. As the coherence bandwidth is calculated by the inverse of the maximal delay spread σ_{max}, the periodicity of the frequency pilot subcarrier S_f can be identify by (3.4). This technique is suitable for fast-fading channels but not for frequency-selective channels.

$$S_f \leq \frac{1}{\sigma_{max}} \tag{3.4}$$

Hybrid combination is a combination of both Block-type and Comb-type pilot pattern. Lattice-type pilot pattern is obtained by inserting pilot tones both in time and frequency domains. In this case, an interpolation in time and frequency is needed. The periodicity of the allocated pilot tones is present in time and frequency and has to follow both previous equations. Figure 3.7 illustrates schematically respectively the block-type, comb-type and lattice-type pilot pattern in time and frequency.

Among, the systems using OFDM modulation, the LTE standard considers the pilot pattern given previously. Some of the recent channel sounders use an LTE like excitation signal with the standard pilot pattern [45, 48]. In the same way, in [13] the channel sounder receiver is able to operate with the LTE standard pilot pattern implemented in public LTE eNodeB.

Recent channel sounders presented in the literature are based on OFDM signal [144, 45, 48, 13, 145, 146, 147, 148, 149, 150]. These sounders are based on SDR platforms. Each of them considers different aided estimation techniques or proposed optimized estimation techniques for OFDM signal. They will be presented in section 3.5.

As mentioned previously the sounder developed during this PhD thesis is one of them. We will detail the sounder and the methodology chosen for the channel estimation in the next chapter. Block-type pilot patter is not optimal for the channel sounder as the purpose is to have the maximal definition of channel estimation in time.

Moreover, as the estimation is applied to each subcarrier, the maximal Doppler shift is minimal. Comb-type pilot pattern is a good option due to the maximal definition in time. The possibility to exploit a certain number of subcarriers is also a good option to increase the maximal Doppler shift. This option is also enabled to disseminate the transmitted antenna in frequency. Lattice-type pilot is a good compromise between time and frequency definition but it is more complex to implement in MIMO configuration due to the sparse of antennas position.

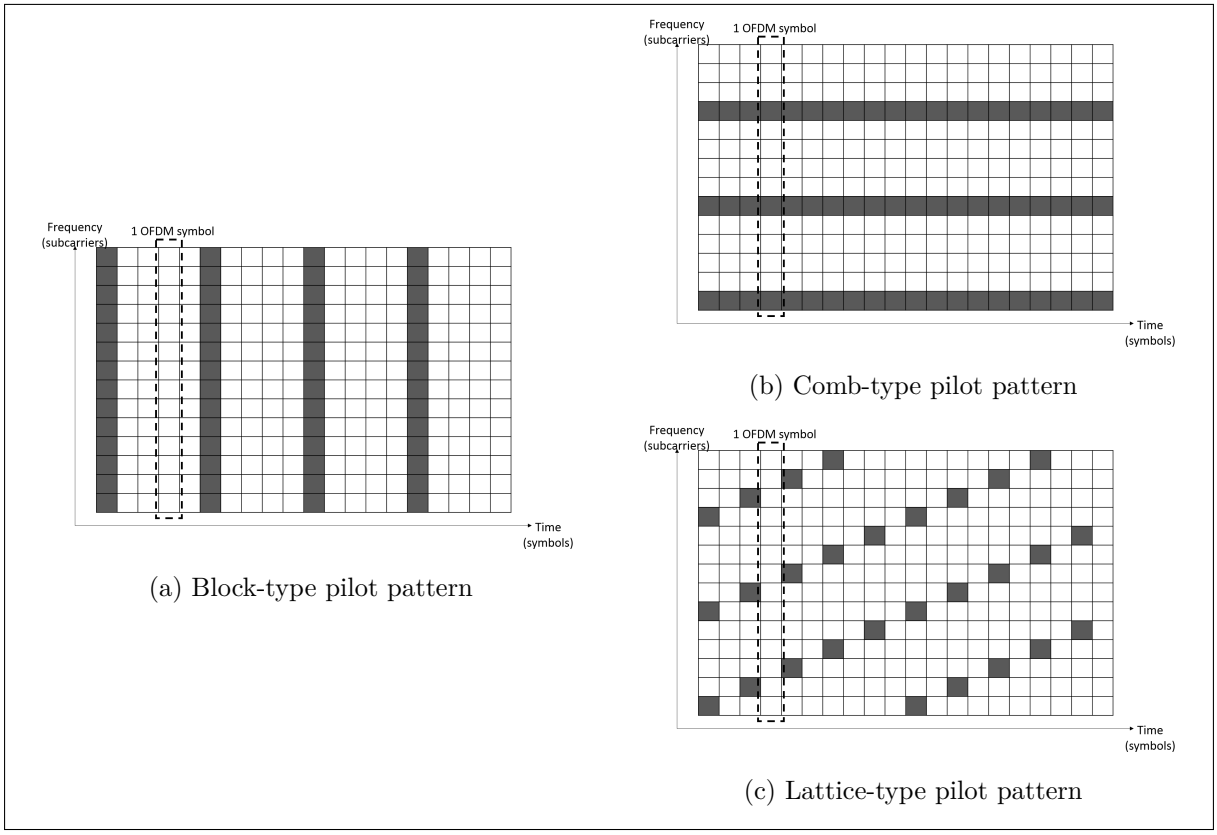

(a) Block-type pilot pattern

(b) Comb-type pilot pattern

(c) Lattice-type pilot pattern

Figure 3.7: Conventional Pilot patterns for channel estimation [142]

3.4 MIMO channel sounders

3.4.1 Introduction

With the development of MIMO wireless systems in the 90s, the need for adequate MIMO channel models has appeared. In Chapter 1 we have recalled the MIMO channel representation and we have presented several of these well known channel models. MIMO channel sounding aims at determining all the individual CIR or transfer functions between each couple of transmitting and receiving antennas. Consequently, the first MIMO channel sounder allows fast antennas switching at transmission and reception and assumed that the channel does not vary between two consecutive measurements (switch between two links). In this case, Time Division Multiplexing (TDM) technique is considered to send the sounding signal on the antennas. Each antenna successively transmits a symbol. A guard period is used between each symbol to avoid inter symbol interference.

Another solution is to consider only the switching at transmitter side and to implement N_{rx} receivers in parallel, each receiver is associated to a receiving antenna. At each measurement record a SIMO (Single Input Multiple Output) channel based on TDM mode. The time for an acquisition is equal to $T_H = 2.(\tau_{max}).N_{tx}$.

The last solution to avoid switching consists in having in parallel Tx RF systems at transmission and Rx RF systems at reception. Frequency Division Multiplexing (FDM) technique is generally used with this architecture. The time of an acquisition is equal to $T_H = 2(\tau_{max})$.

With the arrival of programmable digital components such as FPGA (Field Programmable Gate Arrays) and SDR (Software Defined Radio), the sounding systems has gain more flexibility and

speed and it is possible to transmit and receive simultaneously on all transmitting and receiving antennas. FDM or Code Division Multiplexing (CDM) are considered in order than the receiver can identify the transmitting antenna.

In FDM techniques, each antenna is associated with a sounding signal transmitted over a set of discrete frequencies, distant from Δf, and distinct from one antenna to another. The sounding signals are transmitted simultaneously by all the antennas. On the frequency difference Δf, Mt equally distributed carriers are inserted. The channel is not analyzed at the same frequencies by all the antennas but if one chooses $f < Bc\ 0.9$, the assumption of the flat channel on f must be checked as $\Delta f < B_{c_{0.9}}$, where $B_{c_{0.9}}$ is the coherence band at 90 %.

In CDM techniques, the signals transmitted by the antennas belong to the pseudo random sequences (PR) family. The sounding signals are transmitted simultaneously by all the antennas. The major drawback is that the codes can lose their orthogonality in the presence of multiple paths with delays greater than the duration of a chip of the PR.

3.4.2 Examples of MIMO channel sounders

MIMO channel sounders have been first developed by universities due to all the specifications that are different for each applications and needs. Some commercial channel sounders exist today. The selected sounders will be described hereafter. Post-processing of the recorded data is necessary to extract the channel matrix **H**.

One of the first well known MIMO channel sounder [139] was built by university of Durham (Figure 3.8), for a center frequency of 2.5/3.5/5.2/5.8 GHz with 60 MHz bandwidth.

Figure 3.8: Dhuram University's channel sounder [10]

The excitation signal is a pseudo random binary sequence (PRBS) compressed with a sliding time cross correlator (STCC) used in UMTS band. Each antenna receiver is connected to mixers and splitted from the chirp generator. The maximal length of the CIR is 40 µs for a frequency acquisition of one full matrix at 100 to 250 Hz. The maximal number of antennas available for this channel sounder is 8x8. The synchronization is done by GPS and a 10 MHz rubidium clock. This channel sounder is used for outdoor and indoor measurements without motion. The system recovers the power delay profiles, scattering function and time variant transfer function. This sounder has been enhanced and modified regularly.

The University of Helsinki, IETR of Rennes [151] and Medav RUSK sounders [152] are based on antennas switching. The sounding signal is a pseudo-random sequence based on the spread spectrum techniques. Using a 100 MHz bandwidth, the channel sounder has a temporal resolution of 11.9 ns reduced to 10 ns due to filtering effect. The duration τ_{max} of the impulse response is therefore equal to $\tau_{max} = L.T_s$. The acquisition time of a matrix is equal to: $T_H = 2(\tau_{max}).N_{tx}.N_{rx}$. The factor 2 is related to the guard interval set to τ_{max} necessary after each switching of receiving antenna.

The major advantage of this type of sounder is the flexibility in terms of carrier frequency and bandwidth. However, the acquisition time of a MIMO matrix depends on the number of antennas. [151] presents a CDM based channel sounder, showed in Figure 3.9, working at 3.5 GHz with a variable bandwidth from 12.5 to 100 MHz. The maximal length of a CIR is equal to 1.27 to 81.84 µs with a frequency acquisition of 152 Hz. The synchronization of the system is performed using a 10 MHz rubidium oscillators.

Figure 3.9: Helsinki University's channel sounder [10]

This channel sounder is working with a MIMO matrix of 4x16 antennas. Campaign measurements were done in indoor and outdoor to indoor. The author developed the High resolution algorithm Unitary ESPRIT (Estimation of Signal Parameters via Rotational Invariance Techniques) [153] to recover the spatial diversity of the channel extracting the direction of departure (DOD) and direction of arrival (DOA) of a Uniform Linear Array (ULA) and Uniform rectangular Array (URA) antennas. For a Uniform Circular Array (UCA), the author uses the high resolution algorithm SAGE (Space-Alternating Generalized Expectation Maximization) [154]. The author present a 4x8 MIMO propagation measurement in outdoor environment for LOS and NLOS scenarios at 2.2 GHz. The DOA and DOD are given with their relative power.

DOCOMO has also developed a channel sounder [155] using an OFDM signal. It is able to recover the Angle Of Departure (AOD), Angle of Arrival and Time of Arrival (TOA) of the transmitted waves. This channel sounder is used for outdoor measurement without motion. A switch between antennas allows extraction of the total MIMO matrix. During each OFDM symbol transmission, the Rx antennas are switched one after one. When all Rx antennas has received the OFDM symbol from Tx1, the Tx antenna switch to Tx2. The complex delay profiles are obtained using an IFFT of the transfer function.

The channel sounder is built to work at 2.2255 GHz with 50 MHz bandwidth. The number of transmitting antennas is 8 antennas with vertical polarization by 8 antennas with horizontal

polarization, which is an array of 16 channels. At the receiver side, 96 dual polarized antennas are used, which is an array of 192 channels. The time resolution of this channel sounder is 40 ns and the the number of subcarriers varies from 57 to 1793.

The RUSK sounder is a commercial channel sounder developed by MEDAV GmbH [156]. It was used for different channel measurements in different university [157] [158] [159]. Each channel sounder is developed with their own characteristics relative to the channel measurement objectives.

In [157], the sounder from University of Lund, presented Figure 3.10, operates within 5.150 GHz and 5.750 GHz with a bandwidth of 10 and 240 MHz respectively. The excitation signal is based on an arbitrary waveform generator using a periodic multi-frequency signals. The signal period is $T_s = N_{Tx}.1.6\mu s$ with N_{Tx} the number of transmit antennas. The sampling rate is 320 MHz and 640 MHz for the transmitter and the receiver respectively.

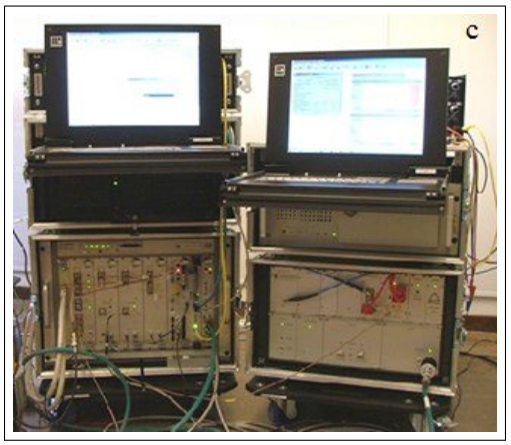

Figure 3.10: Lund University's channel sounder [10]

The antennas structure is composed by 64 dual polarized antenna element at the receiver side using a cylindrical structure. At the transmitter side, 21 dual polarization antennas are linked to a semi-spherical structure. The synchronization is done using a 10 MHz local oscillator. After measures, a post-processing has to be used to extract the channel transfer function. The Least Square estimator is used to estimate the channel transfer function. The author presents a static indoor channel measurement campaign using a 30x30 MIMO system. The author extracts the received powers for all MIMO link and the Direction Of Departure (DOD) and Direction Of Arrival (DoA) for two links.

In [160] , the RUSK channel sounder is used with a 4x4 MIMO system working at 5.6 GHz with a bandwidth of 240 MHz. This channel sounder is used for vehicle to vehicle channel measurement with different speed scenario. The maximum channel measurement speed was done at 110 km/h. The sounding technique used is a multi-carrier principle. The sampling sequence length is 3.2 µs. The channel sounder record channel data during a snapshot time of 307.2 µs which allow 32 500 or 65 000 aquisitions in 10 or 20 s respectively.

Another RUSK channel sounder, presented Figure 3.11, was used by Stanford [159] using a center frequency of 2.45 GHz with a bandwidth of 70 to 240 MHz for indoor, outdoor and outdoor to indoor measurements. This channel sounder is capable to measure a 8x8 MIMO channels. As already explained in previous RUSK channels, the antenna array is connected to a switch to feed antennas. The training sequence length is 3.2 µs and the snapshot duration is 307.2 µs.

Due to a distance trigger wheel, the speed is limited to 1.6 m/s. All RUSK channel sounders used a TDM method with a post-processing with a maximum of 65 536 CIR.

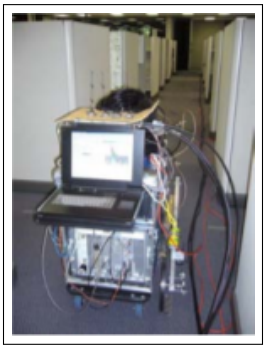

Figure 3.11: Standford University's channel sounder [159]

Orange Lab has developed a channel sounder [161], showed Figure 3.12, with a center frequency from of 2 to 60 GHz with a bandwidth of 62.5 MHz. The excitation signal is a periodical multi-sines sequence with flat spectrum following the frequency time sweep method in [162] applied to complex sequences. This method allows adjusting the amplitude signal to obtain a flat spectrum in frequency domain or a constant envelop in time domain. The sequence defines the maximal duration of the impulse response, which is from 512 ns to 512 µs.

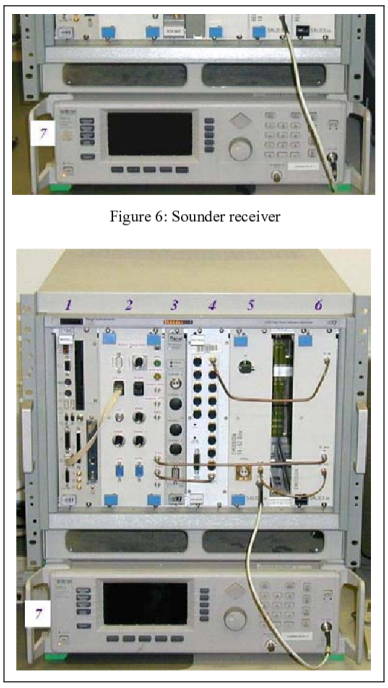

Figure 3.12: Orange Lab's channel sounder [161]

The maximal CIR length is 8.192 µs for a frequency acquisition of 250 Hz. The synchronization between transmitter and receiver is done using a rubidium clock. The minimal time between two measurement points is 0.5 ms using only one antenna and without average sequences. Using an average, the minimal time is 3 ms between two points. Using 10 antennas with a single AGC or multiple AGC, the minimal time between two points is 1.2 ms and 4 ms respectively. The author uses this channel sounder for urban macrocell environment. Relative delay and impulse response dynamic vs received power is given by the author.

3.4.2.1 Summary

The measurement scenarios proposed for the MIMO channel sounders, operating under 6 GHz, presented in this section are summarized in Table 3.1. Table 3.2 summarizes the functional parameters of each MIMO channel sounder reported.

Channel sounder	Scenario	Speed	Synchronization	Parameters
[163]	Indoor	Static	10 MHz rubidium clock	PL, DoD, DoA
[160]	V2V outdoor	110 km/h	-	PDP,DSP,RMS delay spread, RMS Doppler spread
[159]	Indoor, Outdoor, Outdoor to Indoor	1.6 m/s	Cable calibration	MIMO frequency channel matrix
[139]	Indoor-Outdoor	Static	10 MHz rubidium clock	PDP, SF, time variant TF
[155]	Outdoor	Static	-	Delay profile, AoA, AoD
[161]	Outdoor Urban Macrocell	-	Rubidium clock	Relative delay and IR vs received power
[151]	Indoor, Outdoor to Indoor	Static	10 MHz rubidium oscillators	DoD, DoA

Table 3.1: Most common known MIMO channel sounders in the literature : Scenarios

Channel sounder	Frequency (GHz)	Channel sounding method	Bandwidth (MHz)	CIR length (µs)	Sampling rate (Hz)	MIMO matrix length
[163]	5.15	Multi-tones	10-240	1.6-25.6	300-600	30x30
[160]	2.53	Multi-tones	240	3.2	75	4x4
[159]	2.45	Multi-tones	70 - 240	3.2	-	8x8
[139]	2.5-3.5-5.2-5.8	PRBS correlation	60	40	100-250 Hz	8x8
[155]	2.2255	Multi-tones	50	-	-	16x192
[161]	2-60	multi-sines	62.5	8.192	250	1 x 10
[151]	3.5	PRBS correlation	12.5 - 100	1.27 - 81.84	152	4 x 16

Table 3.2: Most common known MIMO channel sounders in the literature : Parameters

3.4.3 Examples of MIMO millimeter waves channel sounders

Spectrum scarcity is an important issue in the telecommunication world. This has recently motivated the exploration of the millimeter-wave (mmW) frequencies for the next generation of mobile communication systems, *i.e.* 5G systems and beyond. 5G mmW frequencies refer to the frequencies between 10 GHz and 100 GHz [164]. The bands foreseen for 5G NR standard are located at 28-30 GHz, 38-40 GHz, the free-licensed band 57–64 GHz, extended to 71 GHz, with 14 GHz of contiguous band [165]. For this reason, several channel sounders have been proposed recently. But, there are only few MIMO mmW channel sounder available in literature due to the difficulties to built. Indeed, the component cost is still very expensive, the calibration is difficult and the sensitivity of the mmW RF circuit required by the system for measurement is hard to obtain [166].

A wideband digital sweep 2x2 MIMO channel sounder at 60 GHz with 6 GHz bandwidth is presented in [167]. It gives an interesting overview of channel measurements and models in the mmW band. The proposed channel sounder is based on frequency sweep sounding as presented in section 3.3.3. The sweep generator is composed with three part. The first one corresponds to the reference clock distribution. The synchronization is done by using a rubidium clock. The second part is a direct digital frequency synthesizer and a first up converter module. Then the third part is composed by a frequency multiplier and a second up converter module. The receiving chain is made of with two ADC devices with a sampling rate of 400 MHz. The receiver part is connected to a rubidium clock to synchronize each start of the frequency sweep for post-processing. The sweep frequency is programmed to be done in 819.2 µs at 4.4 GHz. The authors present two measurement scenarios indoor and outdoor. In both cases, horn antennas are used. The indoor scenario is a 38 m L shape room with glass windows, desk and chairs on one side and a part of glass facade in the other side. The outdoor scenario is an open wider area with building in both sides. Both scenarios are in LOS configuration with static measurement. The author gives the Power Delay Profile (PDP) of both scenarios, path loss to the outdoor environment and an estimated MIMO capacity for indoor environment.

Recently [168] presents dynamic measurements at 60 GHz using an equipment based on a classical channel sounder (RUSK) and mmW front-ends. The front-end up and down converters allow the channel sounder to operates with a center frequency between 55.2 and 70.2 GHz. Frequency synthesizers at 20 GHz and multipliers allow this frequency up. Each transmitter and receiver has a rubidium clock to warranty the synchronization. Each rubidium is independent from each other and a calibration allows synchronization without direct link between them during measurement. The maximal Doppler frequency available is 488 Hz, which means a 8 km/h measurement at 65.2 GHz. Indoor and outdoor measurement campaigns were realized. The indoor environment is a room (Lab) to evaluate the stability and correctness of the CIR. Two different scenarios for outdoor environment are presented. The first one is open field. The distance between the transmitter and the receiver is 120 m. The measurement is done every 20 m. A Leica tachymeter measures the distance. The second outdoor environment is a car parking to test dynamic measurements. A measurement over 28 m is performed using a remote controlled rover. The authors present the path loss of the measurements.

An industrial mmW channel sounder is developed by Keysight Technologies [169]. The excitation signal is a wideband signal correlation with switching antennas. The receiver is a fully parallel acquisition. The synchronization is performed using a 10 MHz rubidium clock. The frequency range of this channel sounder is up to 44 GHz with 1 GHz bandwidth. The number of channel allowing is 8 but it can be extendable up to 104 channels. Parameters as absolute delay, angle of arrival, angle of departure and path loss can be extracted from this sounder.

3.4.4 Conclusion

In this part we presented some classical MIMO channel sounders under 6 GHz, which are generally always in development to increase their capabilities and to be used in millimeter Waves domain due to 5G allocated frequencies. Then we focused on some MIMO millimeter Waves channel sounders with static and low mobility measurements. The mmWaves channel sounders development is a very active field to increase accuracy and capabilities to ensure a good description of the channel in high frequencies for the future 5G and beyond wireless applications.

3.5 SDR based channel sounders

Since several years, SDR based channel sounders are developed as an alternative to existing channel sounders with the aim to be more flexible, adaptable and lighter. This new approach allows the base-band signal processing of the radio frequency signal to be fully set up by software instead of using specialized hardware. It induces the opportunity to reconfigure and fast prototyping a channel sounder. However, the performances are limited due to the internal specification of the SDR system (frequency range, bandwidth, *etc*). Most of them are correlation based channel sounders or OFDM based channel sounder. The software platform used is mainly GNU Radio due to the free open access but some of them are using LabVIEW software.

3.5.1 SDR channel sounders using estimation based on correlation

In [170], the authors present a real time SISO channel sounder for industrial wide band environments at 5.8 GHz for fast time variations. The transmitter part of the channel sounder is a Rohde&Schwarz SMBV100A vector signal generator. The receiver part is based on Ettus USRP X300 piloted by GNU Radio. A PN sequence-based of 1024 samples sounding signal is used as the excitation signal then at the receiver part a cross-correlation method is implemented to extract the characteristics of the channel. Due to the correlation method, the transmitter part and the receiver part are completely independent. This channel sounder operates with a 100 MSps sampling rate and is able to record during 12 s. The time resolution is about 10.24

µs. The channel sounder built is used for indoor measurement with a fast time variable channel, With a 48.8 kHz of Doppler spread, the maximal speed available is 2526 m/s.

In [171] is detailed a SISO channel sounder for rapid measurements using a sliding correlation method in the time domain. The channel sounder is based on USRP piloted with GNU Radio both at transmitter and receiver. This equipment is used in an indoor environment. A Galois linear feedback shift register with a length of 1023 samples is considered as the excitation signal. It is a PN sequence with 60 ns pulse duration. The temporal resolution is 60 ns and the maximal multipath delay is 61 ms. A frequency domain channel sounding method for several transmitters is also presented for outdoor environment. In this case, a sweep frequency signal is transmitted. The frequency resolution is 2 MHz and the number of steps is 10 for a temporal resolution of 27.8 ns. This channel sounder can be exploited in indoor or outdoor scenarios with static measurements.

In [172], the author presents a 2x2 MIMO channel sounder using PN sequences at 2.427 GHz for indoor measurement. The transmitter and receiver are USRP 2922 piloted by LabVIEW software. The excitation signal is obtained with a 802.11.b standard signal. The sampling rate is 33.33 MHz with 2 samples per symbol. The delay resolution is 60 ns for a maximal delay of 15 300 ns. A four stages post-processing is applied to acquire filtered impulse responses with minimal peak error. The first step is to calculate the cross-correlation between I and Q data from measurements and the PN sequence transmitted to acquire the vector impulse response of MIMO channel for each pair of Tx and Rx antennas. Impulse responses are then filtered using the Sousa method [173]. Due to a noise threshold set at 5 %, only the impulse responses higher than 5 % are keep and under 5 % are removed. The second step is to remove the first peak of the impulse responses, which have their peak only once of the four recorded impulse responses. The step three is the same as the step two but it is applied to other peaks. Finally the step four is to average the MIMO CIR. This channel sounder was designed for static outdoor measurement with a time invariant channel.

In [174], a real time channel sounder has been developed to extract the CIR using a WI-FI signal. The channel sounder receiver is based on USRP and Altera Cyclone FPGA piloted with GNU Radio software. This channel sounder can be exploited with any standard 802.11b transmitter. This lead to a limited bandwidth relative to the 802.11b standard. The excitation signal is a PN sequence in 802.11b between 2.4 and 2.8 GHz, which is fixed and not designed for high dynamic range. The receiver part uses a sliding correlation method to calculate the full cross correlation signal in a PN signal period. The CIR are estimated by an average of sample into the symbol periods. The time resolution is 188 ns. This channel sounder can be exploited in indoor or outdoor scenario. The authors make measurement with a vehicle driving at typical speeds on city streets.

In [175], a PN sequence based channel sounder operating from 2.4 to 5.9 GHz is presented. Both transmitter and receiver are based on USRP configured with GNU Radio. The signal is a PN sequence with a BPSK modulation of 4095 chips maximum. The receiver applies a cross correlation on the signal to recover the channel impulse response. The time resolution of the channel sounder is from 31.25 ns to 250 ns with a sampling rate of 64 MSps. The authors present the delay profile and the impulse response for LOS and NLOS measurements. Due to a cable synchronisation between transmitter and receiver, this channel sounder can only be used for indoor static channel measurement.

We can mention also a wide band MIMO channel sounder based on X310 SDR boards developed at IMT-Atlantique [176] for space time channel measurements. This sounder can operate in the 1-6 GHz band for outdoor measurements over 160 MHz. It combines virtual array implementation

with mobile move and real uniform linear array (ULA). Specific antennas arrays and processing technique were developed to take into account Massive MIMO techniques [177].

3.5.2 SRD channel sounder based on OFDM signal

In [178], an indoor channel sounder for device to device and multi hop communications is presented. It is based on USRP configured by GNU Radio software. It is developed using a frequency wide band channel estimation. The excitation signal is a sum of narrow band sinusoids separated by a periodic space. A frame of 1000 samples is sent at each frequency. At the receiver side, when the frame is received at the first frequency f1, a sweep is done to increase the frequency to f2. This sweep process is done synchronously at the transmitter and the receiver. After the record of all frame, the magnitude and phase at all frequencies are aggregated to built the channel frequency response. An IFFT is computed to recover the channel impulse responses. An indoor office campaign as been done at 100 MHz bandwidth with LOS over 27 m. The authors extract the path loss and the shadowing distribution of the channel. This channel sounder was used for indoor office channel measurements without motion.

[145] describes an OFDM based SISO channel sounder using the 802.11.a preamble and complex chirps. The channel sounder is based on USRP piloted with GNU Radio. The excitation signal is composed by three parts. The first one is the 802.11.a preamble, the second part is used to calculate and average the channel transfer function with the 802.11a preamble, then the third part is a QPSK OFDM data symbol to test the validity of the channel transfer function using a threshold decision. The first preamble is used as a cyclic prefix to calculate the channel impulse responses. As the preamble is known by the receiver, the channel impulse responses are calculated by (3.5) :

$$H(f) = \frac{Y(f)}{X(f)} \tag{3.5}$$

where $Y(f)$ is the received signal and $X(f)$ is the transmitted signal. Due to the hardware the channel sounder is able to sound a 2 MHz bandwidth with a 64 MSps sampling frequency rate. This channel sounder was designed for indoor office static channel measurement.

In [146], the author presents a low cost OFDM based channel sounder for outdoor measurements using a drone. The channel sounder is based on two Ettus X310 piloted by GNU Radio. The pilots of the OFDM signal are used as a sounding signal, which allows a sampling of the channel in time and frequency domain. The receiver part receives the signal in frequency domain then it applies a IDFT to recover the channel impulse responses. The development of the channel sounder is done with Embedded SDR working from 70 MHz to 6 GHz and the data rate is up to 40 MSps. The center frequency used is 2.3 GHz with a transmission of 100 OFDM packets with 20 MHz bandwidth. The temporal resolution is 50 ns. Only the CIR is given by the author. This channel sounder can be used for indoor or outdoor measurement with low speed.

In [147], a SISO channel sounder using OFDM signal is detailed. The channel sounder can be used from 4.9 to 5.9 GHz with 200 MHz bandwidth with 10 sub-band of 20 MHz. The excitation signal is sent to each sub-band successively with synchronization to the receiver part. The delay resolution is 5 ns for a CIR length of 1.6 µss centered at the strongest path. At the receiver, the channel transfer function is obtain in each band individually and then combining to acquire the total channel transfer function. The transfer function is calculated by (3.6) :

$$H_k(f) = \frac{Y_k(f)}{X_k(f)} \tag{3.6}$$

where k is the index of the frequency band, $Y_k(f)$ is the received signal and $X_k(f)$ is the transmitted signal.

The IFFT is applied to the whole band to acquire the channel impulse responses. The frame structure is composed by a training part and a data part. The training part is composed as the 802.11.a standard. It begins with ten short training sequences for the frame synchronization and two long training sequences for symbol synchronization. The data part is composed by at least 3 identical OFDM symbols with the second one used to acquire the channel function. The first and third data symbols are considered as the band-guard. In frequency domain, 64 sub-carriers are used instead of 53 in the standard 802.11.a with a 312.5 kHz of periodicity. The channel sounder has a maximal time delay of 3.2 µss. The synchronization is done by a GPS clock. This channel sounder was used for indoor measurements with a maximal speed of 8.6 m/s at 5.8 GHz due to the 166.7 Hz maximal Doppler frequency supported by the channel sounder.

In [148], the author developed a real time 8x8 MIMO channel sounder for vehicle-to-vehicle scenario at 5.9 GHz. The channel sounder is capable to measure a dynamic channel with a maximal Doppler of 806 Hz which is approximately 148 km/h and a measurement rate of 20 Hz. The channel sounder estimates the delay, directional angle and Doppler of the multi-path components using a high resolution parameter estimation algorithm that is developed by the author. A multi-tones waveform is used as the sounding signal similar to the OFDM signal.

3.5.3 SDR channel sounders based on LTE standard pilot pattern

In [45] [179], an LTE based 2x2 MIMO channel sounder for high speed railway is presented. The excitation signal is an LTE FDD standard signal with a frequency range from 20 MHz to 3 GHz and a bandwidth of 20 MHz. The LTE FDD frame structure is designed as a 10 ms frame, which is subdivided into ten sub-frames of 1 ms. Each sub-frame is then split into two slots of 0.5 ms with seven symbols each in case of normal cyclic prefix. In the frequency domain, each sub-carriers are separated with 15 kHz. In the LTE frame structure two different kind of symbols can be used. The data symbol, used to send an unknown information regarding the receiver and the Reference symbol CRS, used to estimate the channel in the LTE downlink. The CRS is the excitation signal for the sounding system. The positions of the CRS are defined by the standard. In this case, and for 4 antennas, the CRS has a maximal periodicity of 0.5 ms in time domain, which correspond to a 2 kHz channel sampling rate and 1 kHz maximal Doppler shift. In frequency domain, the CRS are located every 6 sub-carriers, which mean a 90 kHz spacing. This spacing allows a maximal time delay of 11 µss. In LTE standard, there are 200 CRS that corresponds to a 18 MHz measurable bandwidth and 56 ns of time resolution. The sampling rate is 56 MSps for each channel. The synchronization system is done by GPS and Rubidium clocks. The channel frequency responses are extracted by the correlation of the received signal and the CRS pattern as (3.7) :

$$H(k) = Y(k)X^*(k) \tag{3.7}$$

where $X^*(k)$ is the conjugate of the transmitted signal and $Y(k)$ is the received CRS modulated pattern at subcarrier position k. Then the CIR is computed using the IDFT. This channel sounder was exploited for high speed train scenario along a 16 km network. The scenario was already mentioned in Chapter 2 section 2.3. This channel sounder is capable to operate at speed equals to 285 km/h.

In [48], a channel sounder is used on cellular communications for high speed railway scenarios. The bandwidth equals 100 MHz and the center frequency varies from 2.1 GHz to 2.6 GHz. The maximal sampling rate is 200 MSPs. The author uses a WCDMA (Wide band CDMA) as

the excitation signal in FDD mode with a bandwidth of 5 MHz and a chip rate of 3.84 Mcps. The frame structure is composed by a 10 ms length of 15 slots with a 150 total symbols. The channel estimation is done by the Common Pilot Channel (CPICH) on the down-link. CPICH is defined by a bit sequence which is modulated in QPSK. The CPICH is known at transmitter and receiver sides. The received signal and the conjugate of the CPICH are correlated to acquire the estimation of the CIR.

The authors also use their channel sounder with a LTE standard excitation signal. The LTE standard signal is able to generate a standard frame pattern easily for a MIMO system. The frame structure and the pilot pattern is identical to [45]. The Maximum likelihood approach is used by decorrelating the constant modulus of the CRS in frequency domain to estimate the channel transfer function. Then, an interpolation has to be implement to acquire the overall sub-carriers. The synchronization system is done by GPS with a rubidium clock. Scenarios were already presented in chapter 2, section 2.3. This channel sounder is used for a 240 km/h measurement along a viaduct and road environment.

In [13], the author presents a SISO channel sounder based on LTE public standard signal for high speed scenario. The channel sounder is composed by an USRP-2952 developed with LabVIEW. The excitation signal is an LTE FDD signal. Only the receiver part has been developed by the author. The transmitter part is the public LTE base station. The frame structure of the LTE signal is the same as already presented before. The aim is to use the CRS signal to estimate the channel on the down-link. The positions of the CRS are defined in the standard. Then the IFFT is applied to the CFR to acquire the CIR. The synchronization system is done by a 10 MHz Oven Controlled Crystal Oscillator. The channel sounder was tested at 1.85 GHz with 20 MHz bandwidth. The receiver sampling rate is 30.72 MSps. This channel sounder was used on a 300 km/h high speed line along 30 km. Scenarios were already presented in Chapter 2, section 2.3.

3.5.4 SDR channel sounders based on modified LTE pilot pattern

In [144] a 4x4 MIMO channel sounder based on LTE for high speed train is described. The sounder is based on expressMIMO2 card developed by Eurecom [180]. The excitation signal is based on OFDM using a similar signal as the LTE standard. Channel estimation is based on the pilots. The author have chosen an orthogonal sparse pilot pattern to acquire the individual channel estimations. Each antennas has an unique resource element and no symbol data is transmitted to mitigate the ICI (Inter Carrier Interference). The pilot pattern can be observed in Figure 3.13.

The capabilities of the channel sounder is limited by the hardware. The frequency range is from 300 MHz to 3.8 GHz with a 5, 10 and 20 MHz bandwidth. The sampling rate is proportional to the number of antennas following the relation $N \times 7.68 MSps$ where N is the number of antennas. At receiver side, the channel sounder is composed by two different SDR cards. One is used for 800 MHz of center frequency with three bandwidth of 5 MHz and the second card for 2.6 GHz with two bandwidths of 10 MHz and 20 MHz each. Due to the hard disk speed, the channel sounder can only record continuously with the 5 MHz bandwidth configuration. For the 10 and 20 MHz bandwidth configuration, the channel sounder can save only 1 second out of 2. The estimation of the channel is done at each subcarrier and each symbol time following the expression (3.8) :

$$H_{i,k} = Y_{i,k} X^*_{i,k} \tag{3.8}$$

where i is the OFDM symbol, k is the subcarrier, X is the transmitted symbol vector, Y is the received symbol vector and H is the MIMO transfer function.

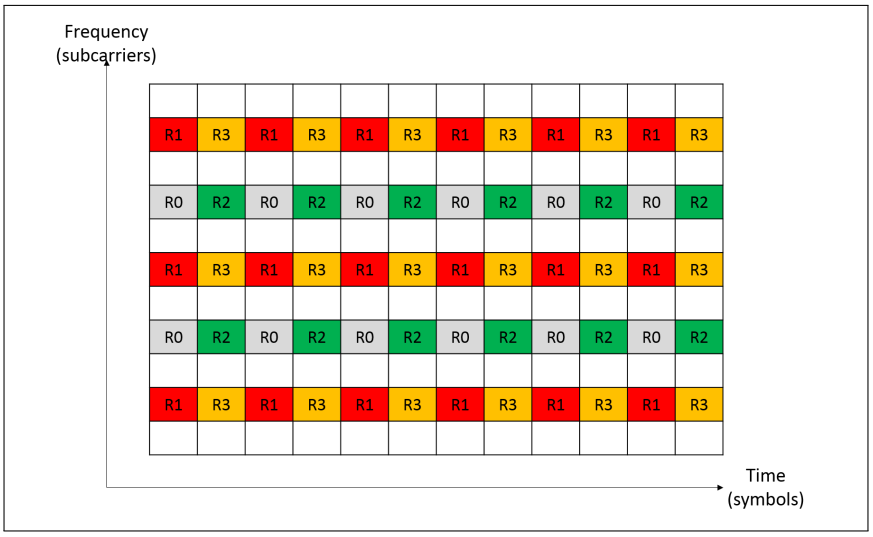

Figure 3.13: Antennas pilot pattern [144]

The CIR is obtain using the FFT of the estimated transfer function. The synchronization of the system is done by using the PSS symbol of the LTE frame. This channel sounder was used during a high speed railway campaign at 300 km/h.

In [149, 181], the author presents a real time 16x16 MIMO channel sounder called MIMOSA developed using 4 FPGA-400 MHz cards for the transmitter and 2 FPGA cards for the receiver. It works at 1.35 GHz with 80 MHz bandwidth. Due to the large amount of antennas, the acquisition time is less than 300 µs for a full parametric MIMO channel transfer matrix. The excitation signal follows the OFDM scheme with 8192 subcarriers that represent a 100 MHz bandwidth. Using a 200 MSps ADC, the author explains that he must reduces the bandwidth at 80 MHz by not feeding subcarriers at lower and higher frequency band of the spectrum. Each antenna has 1024 subcarriers allocated with 97.66 kHz spacing and each antennas subcarriers are delayed one by an other in time domain. Using a 8 x 8 antennas system, the authors switch the polarization to get a 16 x 16 antennas system. This technique allows decreasing the number of RF front end. The frame is composed by two symbols. The first one is used for one polarization and the second one for the orthogonal polarization. Due to the numbers of antennas, the authors exploited the spatial diversity to recover the angle of arrival and departure of the channels. This channel sounder is used for outdoor to indoor scenario with a transmitter-receiver distance of 50 m. The measurement campaigns were conducted statistically. The symbol synchronization is done thanks to a preamble and the system synchronization is done with a 10 MHz rubidium clock.

[150], describes a multi-node 4x4 MIMO channel sounder based on USRP 2953 from National Instruments. The excitation signal is an OFDM signal using pilots built with Zadoff-Chu sequences [182], with a flat frequency response that improves channel estimation and time synchronization. The frame following the TDM scheme with N subframes, where is the number of nodes. Each subframe duration is occupied by only one reference signal node. Each node has a different reference signal. To identify the MIMO link, the frame is composed by two sequences. The first one is associated to the first transmit antenna, then the second sequence is associated to the second transmit antenna. At the receiver, the signal transmitted by the first antenna is identified by cross-correlation. Then the second slot is identified by the TDM structure.

The estimations of the transfer function are calculated using the Least Square estimator over the subcarrier position. The CIR are then calculated with an IDFT. The synchronization system is done at the beginning of the measurement using a Network Time System protocol [183]. This channel sounder was tested with a 2x2 MIMO configuration at 2.3 and 5.7 GHz with 24 MHz bandwidth. The sampling rate is 40 MSps for a reference sequence length of 601. The temporal resolution is 41.66 ns for a maximum time delay of 25.6 ms. This channel sounder were designed for indoor static measurement.

3.6 Conclusion

In this chapter, we presented a state of the art of different methodologies and architecture that can be used for a channel sounder to acquire the channel parameters. Firstly, we presented the time and frequency methodologies, which used different type of excitation signal to recover the CIR or CFR, namely pulse waveform, pseudo random binary sequences, Frequency chirp and OFDM signals. Then, we highlighted different MIMO channel sounders under 6 GHz and in the millimeter Wave domain. We saw that the development of mmW sounders is a very active field of research despite cost and complexity.

Finally, we presented a state of the art of Software Defined Radio channel sounders in the literature. An SDR based channel sounder is a good compromise between performance, cost and mobility.

SDR based channel sounders development has increased rapidly in the last few years due to the low cost of development when using SDR compared to other systems, the reconfigurability and portability of the hardware. One can find mainly two different techniques of estimation using SDR namely techniques based on correlation and techniques based on OFDM signal.

We presented in this part, some SDR based channel sounder using correlation estimation. Then, we detailed few channel sounders using OFDM excitation signal. Finally, we described channel sounders using LTE pilot pattern as a sounding signal.

First, a channel sounder using CRS from standard pilot pattern. As the LTE defines a standard pilot pattern, it is easy to reuse this pattern as a sounding signal. In this way, the receiver can be connected to any LTE public network or to a transmitter using this pattern. LTE standard also defined pilot pattern for multiple antennas, which is a fast way to implement a MIMO channel sounder. The second way to use LTE pilot pattern is to organize the CRS with an arbitrary localization. In this way, it is possible to maximize the channel definition by decreasing interpolation impact in time or frequency. Some papers has been cited using a modified LTE pilot pattern.

Tables 3.3 and 3.4 summarize the channel sounders described with their scenarios and operational parameters respectively.

In Chapter 4 we will present the channel sounder developed during this PhD work. It is a sub 6 GHz channel sounder based on SDR technology and LTE excitation signal. It has been built by modification of a standard SDR-Based LTE communication system. The LTE signal structure allows the estimation based on pilot symbols. Otherwise, in the developed channel sounder, we have replaced the data symbols by additional pilot symbols, allowing an accuracy increase in the symbol estimation. In addition, the choice of SDR platforms offers modularity and possible evolutions. For example, a perspective could be the evolution of the estimation module, by implementing the MMSE estimation instead of the LS estimation.

Channel sounder	Transmitter	Receiver	Scenario	Speed	Synchronization
[170]	Rohde&Schwarz SMBV100A vector signal generator	USRP X300	industrial Indoor	2526 m/s	No synchronization
[171]	USRP E and N series	USRP N series	Indoor - Outdoor	Static	laptop clock timing using network time protocol
[172]	2 USRP	2 USRP	Outdoor	Static	
[174]	Any standard 802.11b	USRP-Altera Cyclone FPGA	Outdoor Residential, commercial and downtown area	typical speeds on city streets	-
[175]	USRP	USRP	Indoor	Static	cable connection
[178]	USRP	USRP	D2D multi-hop Indoor office	Static	Power threshold detection
[145]	USRP-Altera Cyclone FPGA-AD9862BST ADC/DCA	USRP-Altera Cyclone FPGA-AD9862BST ADC/DCA	Indoor office	Static	CFO estimator (MMSE) - Schmidl-Cox algorithm
[146]	USRP X310	USRP X310	Indoor, Outdoor	low speed	OFDM synchronization algorithm
[67]	Sora SDR	Sora SDR	Indoor	8.6 m/s	GPS clock with stability of 1.10^{-11}
[148]	USRP RIO 2953R	USRP RIO 2953R	V2V Outdoor	148 km/h	GPS10eR
[45]	Public base station	RF unit	HST	285 km/h	GPS reference clock
[48]	Public base station	SDR unit	HST	240 km/h	GPS - Rubidium clock
[184]	Public base station	USRP-2952	HST	300 km/h	10 MHz Oven Controlled Crystal Oscillator
[144]	expressMIMO2	expressMIMO2	HST	300 km/h	PSS symbols
[149]	4 FPGA-400 MHz cards	2 FPGA cards	Indoor	Static	10 MHz Rubidium clock
[150]	USRP RIO 2953	USRP RIO 2953	Indoor	Static	Calibration using Network Time System protocol

Table 3.3: SDR channel sounders in the literature : Scenarios

Channel sounder	**Sounding method**	**Frequency (GHz)**	**Bandwidth (MHz)**	**MIMO matrix length**	**Sampling rate (MSps)**	**Extracted parameters**
[170]	PN Correlation	5.8	93	1x1	100	Frequency responses, Doppler spectrum, RMS delay spread
[171]	Sliding correlation	1 - 6	8 - 20	1x1	8	RMS delay spread, PL
[172]	PN Correlation	2.427	-	2x2	33.33	DoD, DoA, PDP
[174]	PN Correlation	2.4 - 2.8	-	1x1	64	Mean excess delay, average and maximum RMS delay spread, PDP
[175]	PN Sliding correlation	2.4 - 2.5 and 4.9 - 5.9	4	1x1	64	Delay profile, IR
[178]	OFDM	-	100	1x3	-	Average PDP, PL, RMS delay spread, coherence bandwidth, shadowing model
[145]	OFDM	2.4	2	1x1	64	Average Magnitude of CTF
[146]	OFDM	0.07 - 6	20	1x1	25 - 100	normalized PDP, CFR
[67]	OFDM	4.9 - 5.9	200	1x1	-	PDP, channel model, noise floor, Excess delay,
[148]	OFDM	5.9	20	8x8	20	Average PDP, angular power spectrum
[45]	LTE FDD	0.02 - 3	20	2x2	56	PDP, DPSD, PL, K-factor , RMS delay spread, Spatial correlation
[48]	WCDMA - LTE FDD	2.1 - 2.6	100	4x4	200	Spatial fading correlation, Doppler spread, K-factor, PDP, RMS delay spread
[184]	LTE FDD	1.85	20	1x1	30.72	PDP, delay and relative power of path
[144]	LTE FDD	0.3 - 3.8	5-10-20	4x4	number of antennas x 7.68	PL, Doppler delay power spectrum, Power ratio
[149]	OFDM	1.35	80	16x16	200	AoA, AoD, ToA, PDP
[150]	OFDM	2.3 - 5.7	24	4x4	40	PL , normalized PDP

Table 3.4: SDR channel sounders in the literature : Parameters

Chapter 4

The SDR based MIMO Channel Sounder developed in the sub 6 GHz band

4.1 Introduction

In the previous chapter, we presented different types of channel sounders. The classification followed is based on the waveform employed as proposed by [10], namely pulse waveform, pseudo random binary sequences, frequency chirp and OFDM signal. We have described several recent channel sounders that consider real LTE signals and particularly, SDR-based channel sounders used in the railway domain.

Based on this state of the art, we present in this chapter the MIMO channel sounder developed during this PhD thesis. This sounder is based on the use of SDR (Software defined Radio) platforms and standardized LTE Time Division Duplex signal in the sub 6 GHz band.

This work represents the main contribution of the PhD thesis, also in terms of effort and technical difficulties encountered. The objective of this chapter is to present the overall sounder architecture as well as the main technical challenges to overcome.

The rest of the chapter is organised as follows. Section 2 is devoted to the Hardware and Software description of the SDR-based channel sounder developed. In section 3, we detail the LTE signal considered and the pilot pattern selected based on the description of the structure of the LTE signal presented in Chapter 2. Then in section 4, we present the estimation techniques implemented in the channel sounder to obtain the Channel Impulse Response. In section 5, we describe how the CIR are recorded in the system in order to allow real time acquisitions. In section 6, the methodology to extract the various channel parameters is detailed. Finally, section 7 is devoted to the description of the different steps for the final validation of the channel sounder.

4.2 Architecture of the SDR-based channel sounder

Thanks to the use of Universal Software Radio Peripheral (USRP) from National Instrument, the channel sounder developed in this PhD work is a fully re-configurable 4×4 MIMO channel sounder. It is based on the architecture of a MIMO LTE TDD communication system, which has been modified in order to operate as a MIMO channel sounder. Modifications are explained

in section 4.2.3. The system is based on 4 USRP Rio-2954 MIMO platforms (2 antennas on each platforms).

The excitation signal is an OFDM waveform derived from a 20 MHz bandwidth LTE TDD signal with a fully re-configurable frame schedule in UL and DL [185]. This specific software integrates all the processing steps of a real LTE standard communication system (modulation, channel estimation, equalization, synchronization...) applied to MIMO system. It is compliant with a given subsets of Release 10 LTE 3GPP. As we will explain later, the full system includes a base station (BS) and a user equipment (UE) also called mobile station (MS). Two USRPs are used for each one as shown by Figure 4.1.

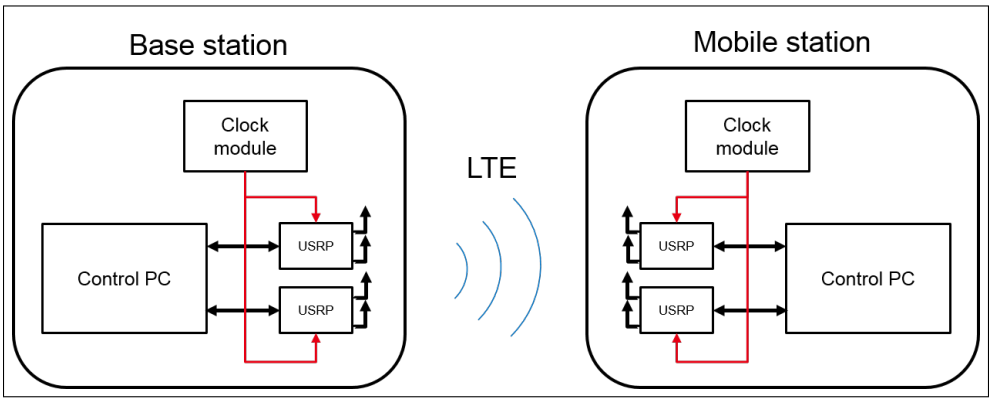

Figure 4.1: Diagram of the channel sounder

The number of antennas can vary from 1 to 4 antennas at the base station and mobile station following the application setup. Even if the USRP platforms offer a bandwidth equals to 160 MHz, the useful signal bandwidth depends on the LTE signal. It cannot be changed and it is fixed to 20 MHz with a cyclic prefix configuration based on normal cyclic prefix.

Table 4.1 summarises the parameters of the channel sounder developed.

Center Frequency	10 MHz - 6 GHz
Bandwidth	20 MHz
Bandwidth used	18 MHz
Sampling rate	30.72 Ms/s
Number of pilots	1200
Subcarrier spacing	15 kHz
Frame structure	TDD
Number of symbol by frame	134
Cyclic prefix length	Normal (7 symbols)
Min delay	55.55 ns
Max delay	66.6 mus
Max output power	-9 dBm
Sensitivity	-65 dBm
Continuous record	1 hour
Antenna supported	1x1 to 4x4

Table 4.1: Parameters of the channel sounder

Figure 4.2 gives a schematic description of the channel sounder developed. The different bricks (mobile station and base station) of the system will be detailed in the next sub sections.

Figure 4.3 is a photography of the channel sounder developed in the laboratory.

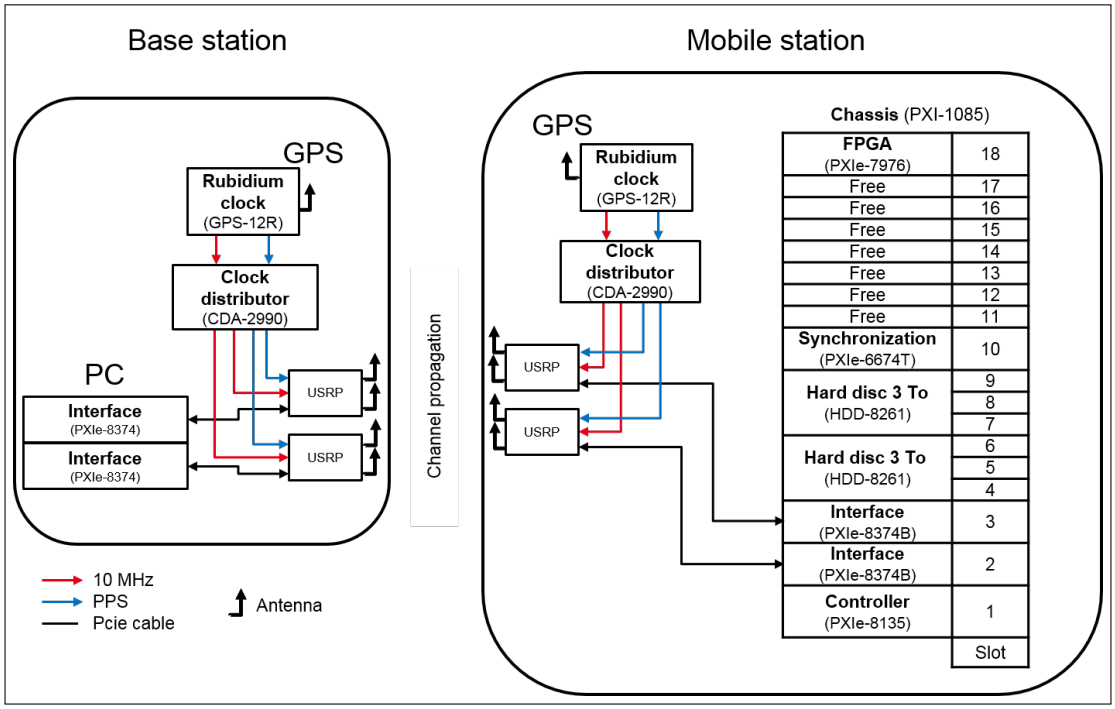

Figure 4.2: Detailed diagram of the channel sounder

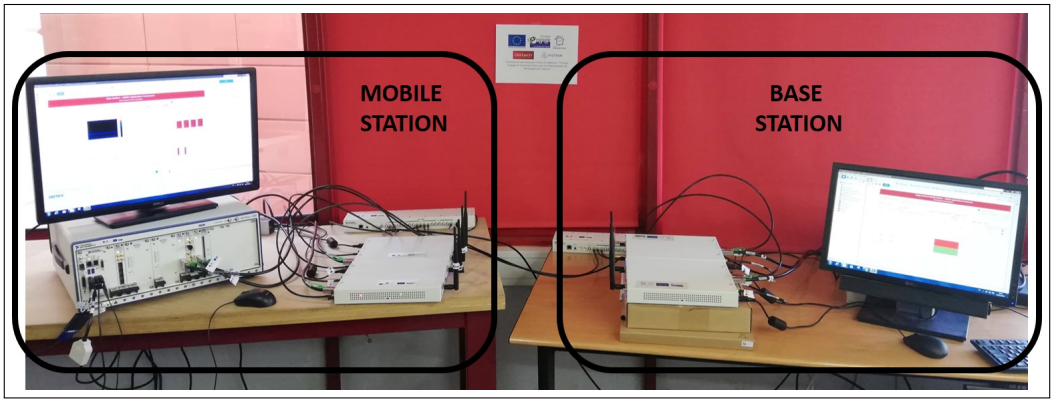

Figure 4.3: Channel sounder in the laboratory

4.2.1 Description of the mobile station

As illustrated on Figure 4.2, the mobile station is composed by two USRP-2954 cards connected to a **chassis PXI-1085** (equivalent to a computer) by a **PXIe-8374** interface. A synchronization signal is sent to the USRPs via the pulse-per-second (PPS) signal and a 10 MHz reference signal from a clock distribution module also called **CDA-2990**. It distributes the PPS and the reference signal on the USRP from an external rubidium clock. A synchronization module **PXIe-6674** is positioned on the center of the chassis to have the same travel time between the modules on each side. A FPGA module **PXie-7976** is required for the MIMO processing and a controller **PXIe-8535** (operating with Windows) composed the chassis. Two **HDD-8261** cards are used to record the channel estimations at each measurement steps. Here after we detail the different bricks of the channel sounder.

- **The USRP-2954** is a re-configurable SDR hardware for rapid prototyping and high performance wireless communication system. It provides a center frequency between 10 MHz and 6 GHz. Composed of two channels, the USRP-2954 can be used for MIMO applications. Each channel can support a maximal output power of 17 dBm to 20 dBm and a maximal input power of -15 dBm. At transmitter and receiver side the gain range varies respectively from 0 to 31.5 dB and from 0 to 37.5 dB. The digital to analog converter has a resolution of 16 bits and 14 bits for the Analog to digital converter. The USRP-2954 is equipped with a 10 MHz GPS-controlled OCXO (oven-controlled crystal oscillator) reference clock. GPS control ensures greater frequency accuracy and better synchronization capabilities.
- **The CDA-2990** is a module to distribute the clock. It is used for the synchronization of the systems that include multiple USRPs. It accepts both external 10 MHz and a PPS input signals and amplifies and distributes the signals to a maximum of eight output ports. The CDA-2990 provides options that can distribute externally supplied signals or GPS-disciplined oscillator (GPSDO), which integrates a GPS-disciplined oven-controlled crystal oscillator (OCXO) that generates the 10 MHz and PPS signals internally. As we are using two USRP-2954, the CDA-2990 will provide the reference and PPS signal from two external rubidium clocks to the USRPs.
- **The PXIe-1085** is a 18-slot chassis with a high-bandwidth of 8 GB/s per PXI Express slot dedicated bandwidth connected with a x8 Gen-3 PCI Express. The hybrid connector type in every peripheral slot enables flexibility in terms of instrumentation module placement. The chassis provides 16 hybrid peripheral slots in position 2-9 and 11-18 used with a center slot in position 10 for the synchronization module. It is important to keep the synchronization module in position 10 to provide the synchronization signal to each slot with the same delay.
- **The PXIe-8135** is an Intel Core i7 embedded controller (equivalent to a PC) for Express systems used with a Windows processor. The controller includes two Ethernet ports, two SuperSpeed USB ports and four Hi-Speed USB ports. Other peripheral I/O allow the connectivity to the display.
- **The PXIe-6674T** generates and routes clocks and triggers between devices in a PXI Express chassis. It can generate two types of clock signals, a highly stable 10 MHz clock based on an on board precision OCXO reference and a second clock from the direct digital synthesis clock generation circuit. The synchronization between modules in the chassis is required to ensure proper operations between them.
- **The PXIe-8374** is an interface module between USRP-2954 and the chassis allowing the communication between USRP and additional FPGA. In the same way, it allows the communication between the USRP and user through the controller (Windows).

- **The PXIe-6592** is an additional Xilinx Kintex-7 XC7K410T FPGA that provides a high speed serial communication up to 10.5 GB/s. This high rate communication allows a high data rate recording on the hard disc to guaranty real time measurements.
- **The PXIe-7976** is an additional K410T FPGA with high performance analog and digital I/O. Programming with LabVIEW FPGA software, it supports peer-to-peer streaming, which directly transfers data to another PXI module without sending data to the host processor. This FPGA with high performance digitizers is used in complement of the FPGA inside the USRP to increase the capabilities of the system. Due to the PXIe-7976 FPGA, the system can support a high complexity program as the MIMO software based on LTE standard.
- **The HDD-8261** in-chassis PXI Express high-speed data storage module features an on board PCI Express SATA controller. The module fits into the chassis, and it occupies three PXI slots. The HDD-8261 has a capacity of 4 TB composed in 4 SATA hard drives of 1 TB. The HDD-8261 allow a fully configurable of each SATA hard drives.
- **The rubidium clock** from Pendulum allows high stability and performance of the system with a 10 MHz reference signal and 1 pps output signal. The GPS-12R is equipped with a standard rubidium oscillator with high stability. The rubidium clock can be used with a GPS connection or an external input signal. The GPS synchronization allows measurements in outdoor situation, while the external synchronization allows the indoor situation. A holdover mode can be used to maintain a certain precision of the oscillator while the GPS signal is lost or the external signal is removed.

4.2.2 Description of the base station

The base station is composed by two USRP-2954 card connected to a computer by a PXIE interface. A synchronization signal is sent to the USRP by a PPS signal and a 10 MHz reference signal from an other CDA-2990. The CDA-2990 distributes the PPS and the reference signal on the USRP from a GPS-12R rubidium clock. The USRPs are controlled using the LabVIEW Communication suite. As the purpose is to build a low cost channel sounder, no other module is added. In this configuration, the base station role is only to send an LTE signal and to maintain the synchronization with the mobile station.

4.2.3 Modification of the initial Communication system into the channel sounder

4.2.3.1 Motivations

One of the objectives of this PhD thesis was to develop a flexible channel sounder for radio channel characterization in railways or roads environments based on SDR and LTE excitation signal.

With the support of National Instrument, it was decided to modify an initial communication systems into a channel sounder thanks to simplifications introduced at the base station side. The *MIMO framework* tool from National Instrument is a software that requires two FPGA, but in our case, only one is used. Consequently, the first modification was to remove all the software parts used by the second FPGA. This means to remove the Data part (all modules that deal with data in the LTE frame) of the *MIMO Framework*, which is not necessary for the channel sounder application because we consider only the pilot symbols of the OFDM frame to calculate the channel frequency response.

We are not considering data. The addition of data can constitutes a source of noise for the pilot-aided channel estimation module. By using only one FPGA, we reduced the global cost of the channel sounder and we improved also the channel estimations. Figure 4.4 and 4.5 show the removed parts of the hardware in the global architecture.

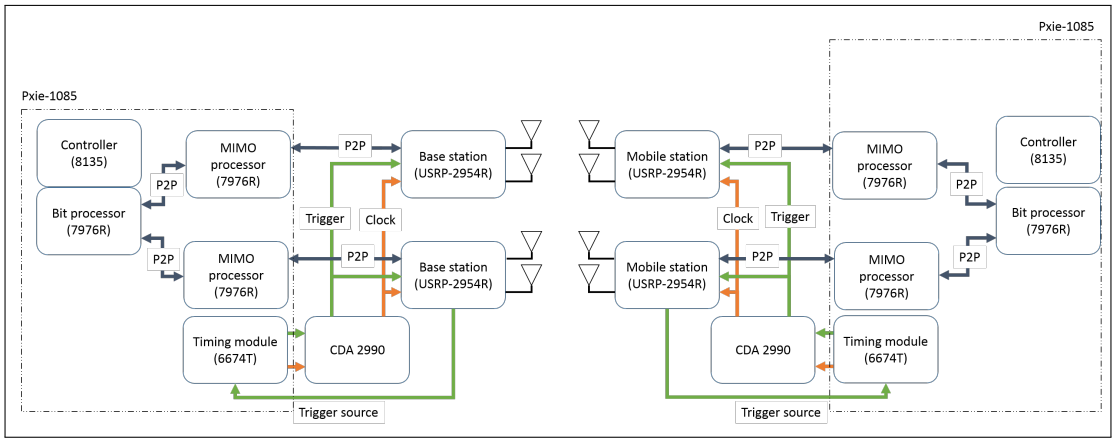

Figure 4.4: Initial equipment for LTE-MIMO system communication

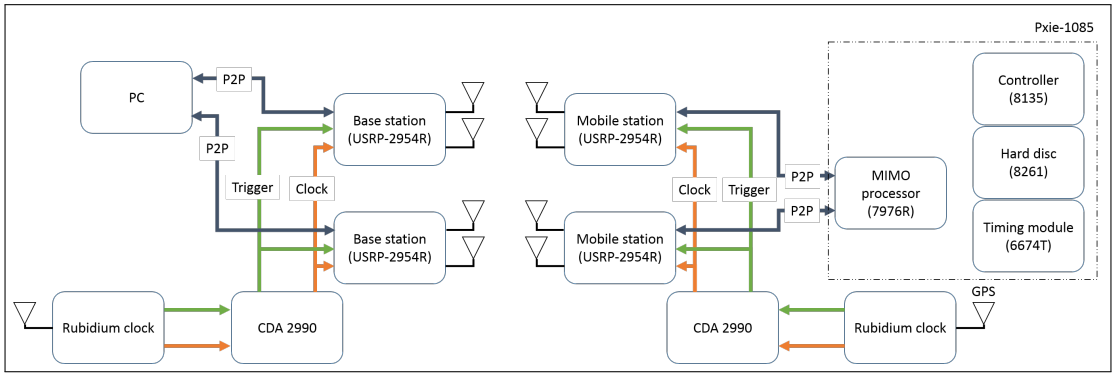

Figure 4.5: Modified equipment for the channel sounder

4.2.3.2 Adaptation

As presented in section 4.2, the base station does not comport external FPGA and chassis, which are necessary to ensure a good operation of the *MIMO Framework* software using at least two different USRP cards. Both USRP 2954R are directly connected to the PC to ensure the connectivity and communication between the Host port (PC) and the FPGA inside the USRP.

In that way, we cannot use the *MIMO Framework* software at the base station. As an alternative, we have considered the *LTE communication* software with less complexity. Two separate sessions of this tool transmit the signal from both USRPs. Initially, each *LTE communication* session deals with one base station USRP with one transmit antenna. The low complexity comes from the fact that there is no real time recorded data and no multi-USRP dependencies. We changed this part to apply a MIMO transmission from each session.

In this way, LTE session 1 pilots the USRP 1 and LTE session 2 pilots the USRP 2. Then, from mobile station point of view we have only one software session that pilots the two USRPs as shown by Figure 4.6.

The LTE signal uses a bidirectional connection to lock the base station and the mobile station. USRP-2954 has an antenna port, which can be an input or an output called "TX1 RX1" as presented Figure 4.7.

The initial configuration of the USRP, in the *MIMO Framework*, is to use the bidirectional port "TX1 RX1" with an internal switch to receive/transmit the LTE symbols of the frame. This kind

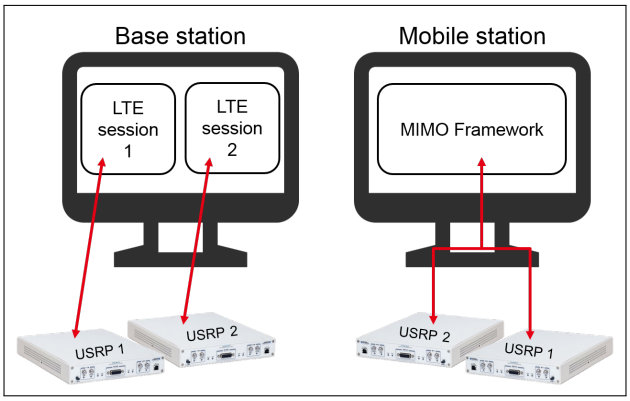

Figure 4.6: Software architecture

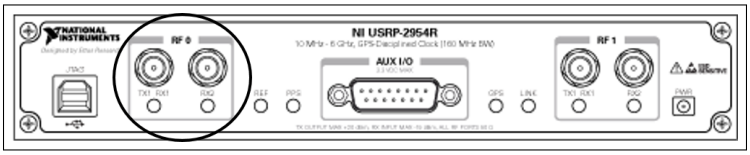

Figure 4.7: Software architecture

of configuration can be a future problem in case of use amplifier stage during the measurement as the amplifier is not necessary bidirectional. The solution applied is to separate the uplink and the downlink antenna port using the port "TX1 RX1" as the transmitted port and port "Rx2" as the received port. We made changes in the *MIMO framework* and the LTE session to allow the possibility to change the decided antenna port of the USRP.

The *MIMO Framework* software uses a complete graphical interface to pilot the signals and to visualize various parameters namely among them, the channel frequency responses and the channel impulse responses for each link of the MIMO channel matrix. This visualisation allows the user to view in real time the channel measurements. The *MIMO Framework* interface is composed of three parts presented in Figure 4.8.

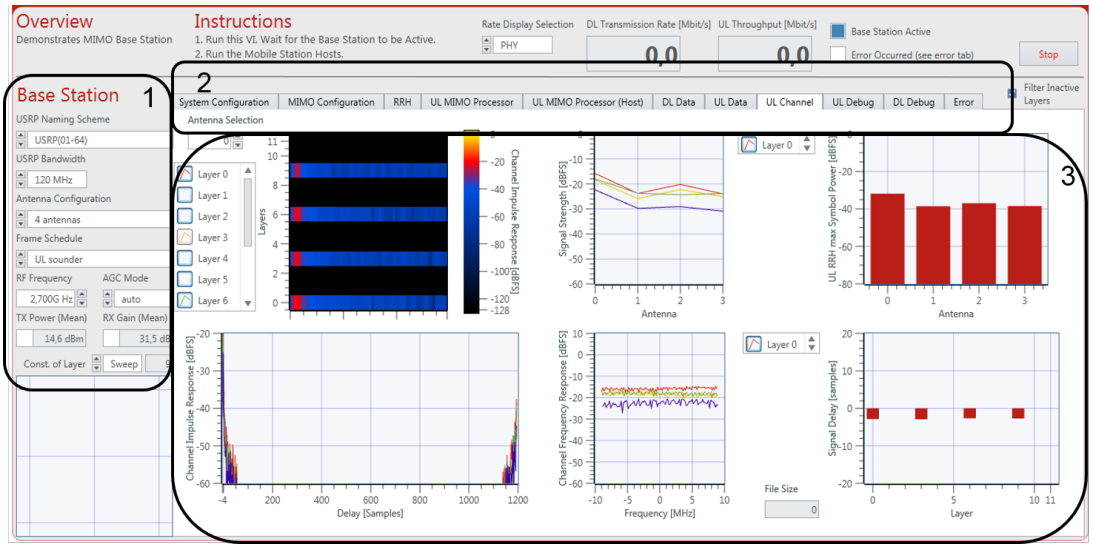

Figure 4.8: *MIMO Framework* graphical user interface

The parameters part, where all the input parameters of the hardware and LTE signal at the same USRPs are presented: the center frequency, the frame used, etc. The second part consists of different diagrams such as system configuration, MIMO configuration, UL channel, etc. In the third part, the user can visualize any type of information about the configuration of the hardware, the output signal, the reception signal and debugging information. One of the tabs is UL channel, on which we can have a real time visualization of the CIR, CFR and received power for each antenna.

These figures are quite useful during a measurement campaign to have a preview on the signal during the measurements even of they are not exactly what we are recorded due to the latency's of the update information. Indeed, all the processing for these figures are done in the Host side and there are updated every second.

The *LTE sessions* are quite similar to the *MIMO Framework* visual but with less information about the received signal. In the LTE session, we found only the information about the hardware configuration, debugging and output/input signal with a view of the spectrum bandwidth and layers detection.

4.3 The sounding module

4.3.1 Waveform of the channel sounding

The frame structure of the LTE-TDD signal is defined by 10 LTE sub-frames of 1 ms each composed of 2 time intervals of 0.5 ms. Each interval includes 7 OFDM symbols [185]. The center frequency of the sounding signal is between 0.05 and 6 GHz with a bandwidth of 20 MHz. The signal sampling frequency depends on the hardware and is equal to 30.72 MHz.

As explained in Chapter 2, the LTE signal is composed of so called *radio resources blocks* defined by 12 sub-carriers of 15 kHz wide and 7 time symbols. They represent the basic radio resource unit allocated to a subscriber. The *radio resources blocks* includes data symbols and symbols known by the transmitter and receiver (pilots, PSS ...), which will help channel estimation and synchronization.

The channel is estimated on each pilot symbol position that constitutes the frame, i.e. over a period of 0.5 ms / 7 (symbols), corresponding to a sampling of the channel equal to 14 kHz. Thus, according to [186], the maximal Doppler frequency that can be measured is 7 kHz (sampling rate/2). Then, for the possible operational frequency of the sounder (1 to 6 GHz), the maximal theoretical speed of the mobile station corresponding to this Doppler frequency is 7.5548e+03 m at 1 GHz and 1.2591e+03 km/h at 6 GHz. The distance between two CIRs at these speeds would be respectively 0.0150 m and 0.0025 m. For a speed equals to 300 km/h (maximal speed for a train), the distance between two measured CIRs is 0.0595 m, corresponding to a possible sampling in distance of $\lambda/5$ and λ respectively for a central frequency of 1 GHz and 6 GHz . The hardware architecture chosen allows this sampling rate to be maintained without loss of data during one hour. The limitation will be caused by the recording process as we will see later.

The excitation signal consists of frames of 20 slots (0 to 19), each consisting of 7 OFDM symbols. The first slot (slot 0) of the frame is used for synchronization between the base station and the mobile station. It consists of three types of symbol (synchronization, pilot on the downlink, pilot on the uplink). The other 19 slots in the frame (slot 1 to 19) are filled with pilot symbols on the uplink.

We consider 4 types of pilot symbols as illustrated by the colors in Figure 4.9. Each transmitting antenna (A0 to A3) at the mobile station uses a unique number of sub-carriers per radio resources block in order to guaranty orthogonality between the pilot symbols. The pilot scheme per radio

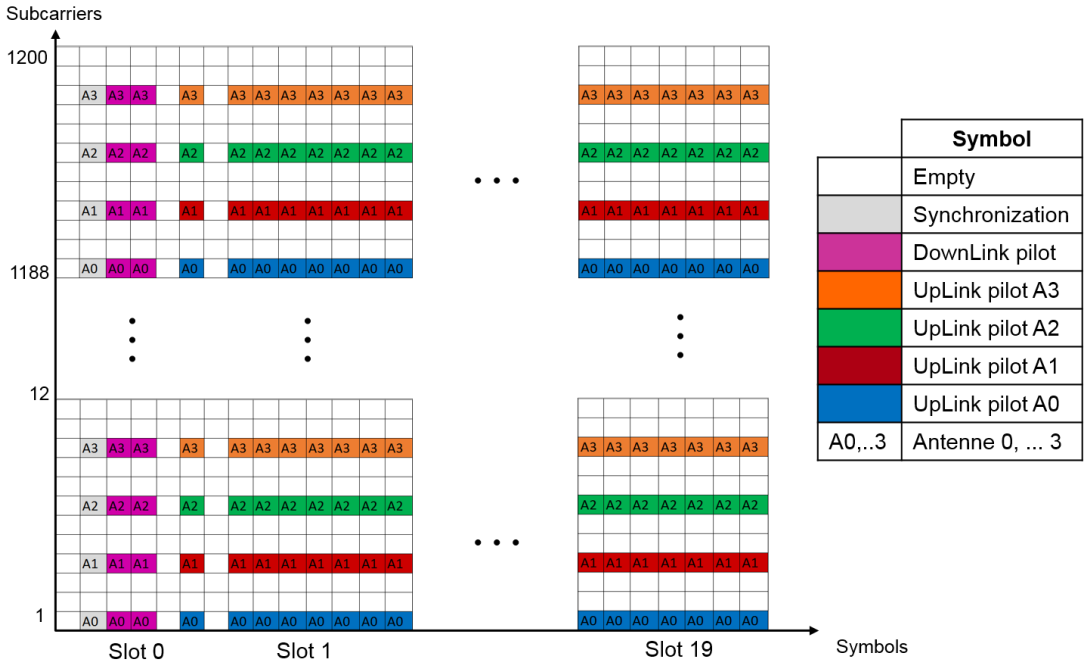

Figure 4.9: Pilot pattern for the channel sounder

resources block is repeated identically up to a maximum of 1200 subcarriers, which thus define the bandwidth of the transmitted signal.

The sounding signal considered is made with 1200 useful subcarriers spaced 15 kHz apart, each defining a useful bandwidth of 18 MHz. The minimal measurable delay is 55.55 ns (1/18 MHz). Each measured transfer function by MIMO link is therefore spaced of 180 kHz (15 kHz x 12 sub-carriers) apart, which results into a maximal measurable delay equal to 5.5 μs. Depending of the environment, the minimal measurable delay could be to large to detect very small paths. As for example in a straight tunnel in [85], paths could be measured with a path delay varying from about 30 ns to few ns. It is a part of the limitation of the developed channel sounder.

There are several studies in the literature dealing with the optimization of pilot schemes to optimize channel estimation for an OFDM modulation [187, 188, 189, 190, 191, 192, 193, 194, 195, 196]. Note that the more the number of pilot symbols increases in a radio resources block, the more the power allocated per pilot decreases. The transmission power is distributed uniformly across all pilots. However, for a channel sounding application if the number of pilot symbols in the frame decreases, the number of channel estimates for a given radio resource block decreases. It is therefore necessary to perform a time and / or frequency interpolation between the channel estimates. Interpolating estimates decreases the accuracy of estimates made outside of the pilot symbols.

Thus, as illustrated in Figure 4.9, in the sounding frame considered for the channel sounder, the data symbols are replaced by pilot symbols in order to increase the number of time estimates, eliminating the need for temporal interpolation and thus increasing the quality of the channel estimation. Interference between symbols, can come from adjacent pilot symbols and can be easily eliminated with conventional interference cancellation techniques.

4.4 Channel estimation implemented in the sounder

4.4.1 Reminder of possible estimation techniques

In this work, we consider one OFDM symbol to perform channel estimation at the mobile station on the received LTE downlink signal. The channel estimation is done using transmitted reference symbols, which are inserted among data subcarriers in the OFDM symbol as described previously and in the pilot aided description in Chapter 2. The pilot assisted channel estimation process is generally divided in two steps.

First, statistical estimation of the channel of OFDM tones consisting of reference symbols is determined using statistical methods, namely Least Squares (LS) and Minimum Mean Squares (MMSE) techniques. Then, the response of the channel at the data subcarriers is subsequently determined by interpolation.

The interpolators used for the purpose of estimation are linear, second order, cubic or time domain interpolators derived from both the statistical and deterministic point of view. [197, 194, 193] can be found that deal with these estimation criteria for pilot assisted channel estimation of OFDM applications from CIR or CFR prospective.

We give here after a brief overview of the two main estimation techniques with a reference to LTE downlink structure. Generally, at the receiver, the ith received OFDM symbol, $Y_{i,k}$ in frequency is given by (4.1). It is the vector coefficient of the received OFDM symbol. $H_{i,k}$ is the coefficient of the CFR vector, $X_{i,k}$ is the vector coefficient of the transmitted OFDM symbol and $N_{i,k}$ is the AWGN. k represents the subcarrier index contained between [0,K-1], where K represents the total number of subcarriers. The expression in (4.1) assumes that inter carrier interference (ICI) is negligible [198].

$$Y_{i,k} = H_{i,k}X_{i,k} + N_{i,k}, 0 \leqslant k \leqslant K-1 \tag{4.1}$$

For Channel Frequency Response (CFR)-based channel estimation, two estimation algorithms can be used, depending on whether statistical knowledge about the CFR is available or not. Without statistical knowledge, CFRs can be treated as deterministic channel. In this case, least-square (LS) estimation can be used as it requires no statistical information about the CFRs. The estimation performance can be greatly improved by exploiting the statistical information as the covariance of the channel matrix. In this case, a linear Minimum Mean-Square Estimation (LMMSE) can be considered.

4.4.1.1 Least Square Estimation

From the receiver side, the pilot positions in each OFDM symbol [199], can be represented as $P(k)$ and transmitted pilot symbols, $X_{i,k}$ with $k \in P(k)$, are known. The LS block estimates the CFR vector coefficients as in (4.2) [198]:

$$H_{i,k}^{LS} = \frac{Y_{i,k}}{X_{i,k}}, k \in P(k) \tag{4.2}$$

Interpolation techniques are used to get the channel coefficients where no pilots are used. The interpolated CFR is $H_{i,k}^{LS}, 0 \leqslant k \leqslant K-1$. Then, substituting $Y_{i,k}$ in $H_{i,k}^{LS}$, the LS estimated CFR can be expressed as in 4.4 where $V_{i,k} = N_{i,k}X_{i,k}$ is the complex Gaussian noise. CIR estimates are obtained using IDFT on CFR as in (4.3) and (4.4):

$$H_{i,k}^{LS} = H_{i,k} + V_{i,k}, k \in [0, K-1] \tag{4.3}$$

$$h_{i,l}^{LS} = h_{i,l} + v_{i,l}, 0 \leqslant l \leqslant L-1 \tag{4.4}$$

In (4.4), the CIR $h_{i,l}$ contains the complex Gaussian noise $v_{i,l}$. Assuming L as channel length, the estimated CIR after $l = L-1$ is forced to zero, called as truncated CIR and given by (4.5). A denoising threshold represented as ξ is applied to remove the complex Gaussian noise. The denoised CIR is given by (4.6):

$$\widehat{h}_{i,l}^{t} = \begin{cases} \widehat{h}_{i,l}, & |\widehat{h}_{i,l}|^2 > \xi \\ 0, & otherwise \end{cases} \tag{4.5}$$

$$\widehat{h}_{i,l} = \begin{cases} h_{i,l}^{LS}, & 0 \leqslant l \leqslant L-1 \\ 0, & L \leqslant l \leqslant K-1 \end{cases} \tag{4.6}$$

4.4.1.2 Minimum Mean Square Estimation

LS channel estimation method is computationally simple, but performances are limited in term of minimization of the mean square error (MSE). Another method to estimate the CIR is LMMSE, which has better MSE performance than LS but it is computationally complex. The derivation of the LMMSE assumes to have the knowledge of the channel. This method intends at the minimization of the mean square error between the exact and estimated CIRs [199].

This estimator is optimal in the sense of mean square error. Although this estimator is optimal, its use is limited by two major drawbacks: its complexity, and the need to know the channel covariance matrix, which is a priori unknown to the receiver.

A lot of other techniques can be used to estimate the channel using pilot-aided channel estimation for OFDM application. Common techniques are described in [200, 201, 202, 203, 204]. We can mention briefly two other methods appearing generally in the literature:

- The Wiener 2D filter, described in [205], is the optimal estimator in the sense of the error average quadratic. It can be seen as a generalization of LMMSE in two dimensions time and frequency. However, its complexity limits its use.
- The maximum likelihood estimate (MLE), described in [206], assume that the CIR is a deterministic and unknown vector given by where no information about the channel statistics or operating SNR is required.

4.4.2 Considered Channel sounder estimation technique in the channel sounder

Despite the optimal performance of some estimation algorithms described in the previous subsection, we have considered the Least Square estimator. This is the less complex algorithm, thus it implies the less consumption of computational resources. This is very important regarding the hardware choice for the channel sounder.

The received signal at the base station can be expressed as the convolution between the transmitted signal $x(t)$ and the channel $h(t, \tau)$.

$$y(t) = x(t) * h(t, \tau) + v(t) \tag{4.7}$$

where $v(t)$ represents the Gaussian additive white noise (AWGN) and * the convolution operator.

Channel estimation is performed in the frequency domain using the LS estimator on each pilot symbol of the signal. The use of this type of estimator requires the knowledge of the transmitted

signal sequence. Let us consider the transmitted pilot symbol x_k, the received signal y_k at the pilot position k given by (4.8):

$$y_p = x_p * h_p + v_p \tag{4.8}$$

where h_p is the channel response and v_p is the additive white Gaussian noise. The LS estimator uses the knowledge of the pilots transmitted to estimate the frequency channel response according to equation (4.9).

$$\hat{H}_k = Y_k . \frac{X_k^*}{|X_k|^2} \tag{4.9}$$

where $\hat{H}_k$ is the estimate of the channel at the position of the pilot k.

At the output of the channel estimation block we obtain all the channel estimates in the frequency domain. The knowledge of the organization of the frame in time and frequency makes it possible to recover the transfer functions of each link between the transmitting and receiving antennas of the system, thus defining the matrix $\mathbf{h}(\mathbf{t}, \tau)$ of the MIMO channel as (4.10).

$$\mathbf{h}(t,\tau) = \begin{bmatrix} h_{11}(t,\tau) & \cdots & h_{1n}(t,\tau) \\ \vdots & \ldots & \vdots \\ h_{m1}(t,\tau) & \cdots & h_{mn}(t,\tau) \end{bmatrix} \tag{4.10}$$

Each transmitting antenna uses a frequency given by a radio resources block every 12 subcarriers as presented previously. There are therefore a total of 100 channel estimates per MIMO link. Linear frequency interpolation is used to estimate the channel at the positions of the subcarriers not used by a pilot symbol. Thus, each transfer function is completely defined. At the end, the estimated channel impulse responses are calculated by the inverse Fourier transform of the transfer functions as in (4.11):

$$\widehat{h_i} = \frac{1}{K} \sum_{k=0}^{K-1} \widehat{H_i} e^{j(\frac{2\pi k}{K})i} \tag{4.11}$$

where $k = 0, 1, ..., K-1$ with i is the symbol index.

In the process used, the pilot symbols are based on normalized QPSK modulation with a power set to 1. At the receiver, the channel estimation is done using this pilot symbol, which is the pilot symbol sent by the transmitter without applying any power. In this way, the channel estimations are done without taking into account the transmitted power set to the USRP. Using a calibration measurement method we will detail in section 4.13, the channel estimation can neglect the effect of the transmitted power. The calibration process considers a cable connection between the mobile station and the base station to avoid any effect of the equipment and cables on the final channel estimation.

4.5 Recording the channel estimations

4.5.1 General principle

One important feature of the channel sounder, is to be able to record the channel estimations in real time during the measurements to increase the possible duration of one measurement campaign. The first idea was to record data directly at the end of the channel estimation block

in the FPGA. In this way, the data recording is done at the same speed than the channel estimations. However, due to the FPGA and hardware architecture, it was not possible to establish a link between FPGA and HDD (Hard Disc) to record data. The record data must pass through the controller named PXIe-8135, also called Host side, before being recorded as presented Figure 4.10.

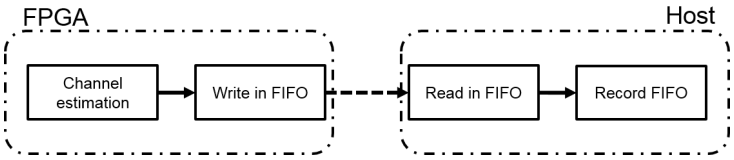

Figure 4.10: FIFO memory path

The chosen solution is to use the host side of the mobile station. We create a FIFO (First In First Out) memory to transmit the channel estimations from the FPGA to the Host part, and then we can record the data from the Host to the HDD. To pass through the host part means to introduce a small delay between the end of the channel estimation block and the recorded part in the Host. As all channel estimations go through the same path, we can neglect the impact of this transition.

However, the frequency of the channel estimation loop in the FPGA is higher than the one in the the host side. This frequency difference leads to a delay between the FPGA FIFO output and the recorded data in a file. After a short time, this delay can cause an overflow in the FPGA, which stop the acquisition. The overflow appears when the RAM system is full. This means that there is more input data in the RAM than the capability of the system to erase old data (recorded data). To solve the error we have to implement a queue in the Host side to locally store the input channel estimations until they are recorded on the disc. This queue cannot be infinite. This creates a limitation on the measurement campaign duration. The maximal length of the queue is reached after approximately one hour of measurements. We estimate that it is enough for railway measurement campaigns.

4.5.2 Organization of the recorded channel estimations in the memory

The computation of the channel estimations are done in the FPGA. As explained before, we consider a FIFO memory to transfer the channel estimation values to the Host part and then to record them in the HDD. We have to follow a specific organization of the recorded data due the estimation method implemented. Figure 4.11 described the path of the channel estimation from the FPGA to the HDD.

In the *MIMO Framework*, four channel pilot estimations are performed in parallel in the FPGA as presented in Figure 4.11.

The channel estimation is computed for each pilot of each receiving antenna. At the start of the process, the first channel estimation is done for the pilots 1 to 4 of the receiving antenna A0. Then, the estimation is done for the first four pilots of the receiving antenna A1 then for the first four pilots of the receiving antennas A_n. Then, the process is applied on the pilots 5 to 8. This principle is applied up to the last four pilots (from the 1200 pilots) of the last receiving antenna A_n.

The four channel estimations in parallel are concatenated for each receiving antenna at the pilot position k to k+3. Figure 4.12, shows how the channel estimations are done and recorded in a vector.

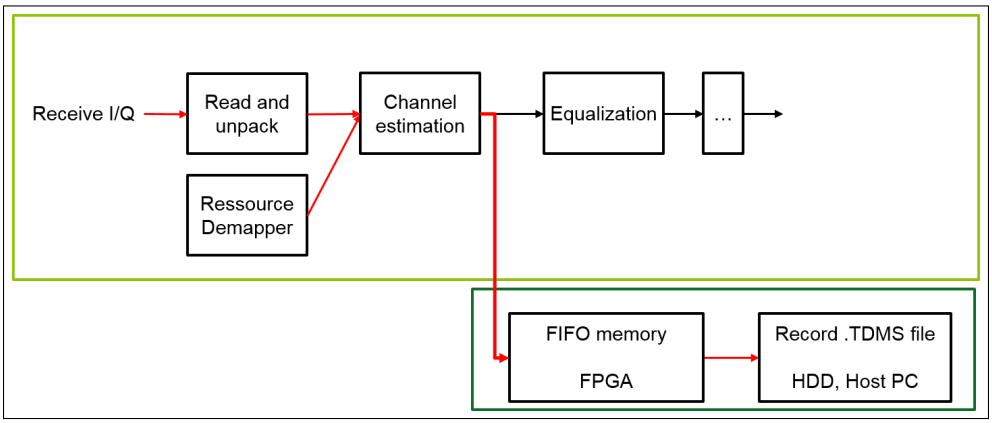

Figure 4.11: Recorded path from FPGA to Host side

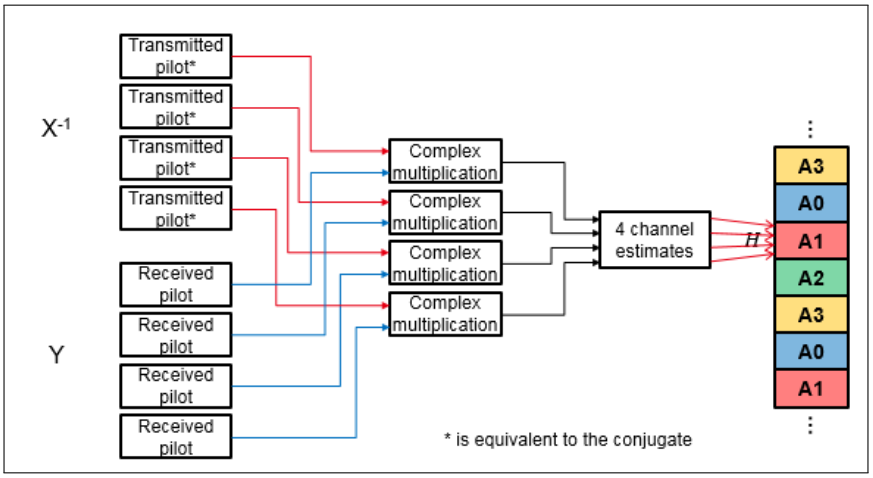

Figure 4.12: Least Square parallel

Each color is relative to a receiving antenna n. X and Y represent a group of 4 pilots sent and received respectively. The LS estimation is done following the equation (4.9) and represented by a complex multiplication.

Then, all channel estimates are concatenated to create the recorded vector H_{record} following equation (4.12). Each OFDM symbol are also concatenated one after one.

$$H_{record} = [H0_{meas(0,3)} H1_{meas(0,3)} ... Hn_{meas(0,3)} H0_{meas(4,7)} ... Hn_{meas(1196,1199)}] \tag{4.12}$$

where H_{record} is the concatenated vector of all estimations, Hn is the estimation applied to the receiving antenna n, and indices $(k, k+3)$ are the estimated pilot position.

As the recorded vector is not a succession of all pilots for each receiving antenna, a post-processing is applied to recover each MIMO link of the MIMO channel. Figure 4.13 presents the organization of the data post-processed. All the 1200 pilots, which composed the recorded vector explained Figure 4.12, are grouped for each receiving antennas. The 1200 pilots define one OFDM symbol received on all antennas. This new matrix is used to have a better understanding of each MIMO link of the channel matrix. Each OFDM symbol is represented by a matrix of size [K , N], where N is the number of received antennas.

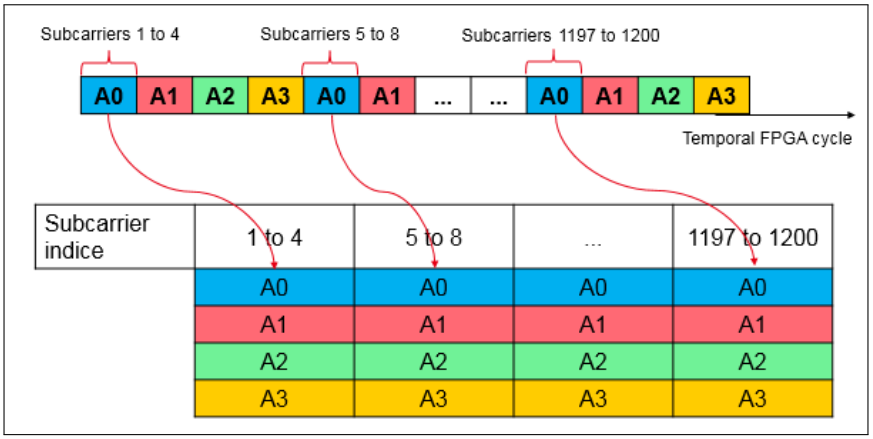

Figure 4.13: Organization of the recorded vector to MIMO link matrix for one OFDM symbol

4.6 Channel sounder validation

4.6.1 Clock synchronization

Synchronizing the transmitter and receiver is a key step in estimating the radio channel. Two synchronizations are done, the first constitute an equipment synchronization thanks to the synchronization of the two rubidium clocks. The second one is applied on the frame, by using a synchronization symbol (PSS) to obtain the frame synchronization as shown section 3.3.4.3.

The synchronization using Rubidium clock is applied by connecting, on each side of the equipment, the rubidium clock to a GPS signal or an external signal at least 72 hours before the measurement campaign. Then, before acquisition, the synchronization between the PPS signal of each rubidium clock, has to be verified using an oscilloscope. If there is a delay between the PPS signals, a shift can be added or removed manually thanks to an option of the rubidium clock. The maximal delay value available for this option is +/- 999 ns.

To do this, we can use a GPS signal at the input of the CDA-2990 modules or rubidium type clocks in tunnel type scenarios where GPS is not received. The two rubidium clocks must be

connected beforehand to avoid time drift of the equipment after decoupling. After decoupling, we obtain a stable synchronization with variations between +0.1 and -0.1 samples (32.5 ns). This variation implies a delay or an advance that will modify the value of the measured delays as well as the amplitudes of the impulse responses.

The objective of the "clock synchronization" validation is to verify if the operation of the channel sounder in a concrete case of tunnel measurements will be possible thanks to the rubidium clocks. In tunnel configuration, it is not possible to obtain the synchronization of the base station and the mobile station with GPS. It is therefore necessary to use the Rubidium clocks to synchronize base station and mobile station independent from each other.

This test aims at replicate the following measurement campaign scenario: no GPS signal access during acquisition and it is possible to reconnect the system (rubidium clocks) outside of acquisition periods. Between each acquisition, one clock is re-synchronized to the other by adding/removing internal delay from one rubidium clock. Then the acquisition takes place for 60 min. We reproduce this operation three times a day and over five days.

The obtained results are presented Figure 4.14. We can see that the PPS delay between both rubidium clock is not up to 150 ns. This means that the system can correctly remove the PPS shift from the rubidium clock and it can make acquisition during five days.

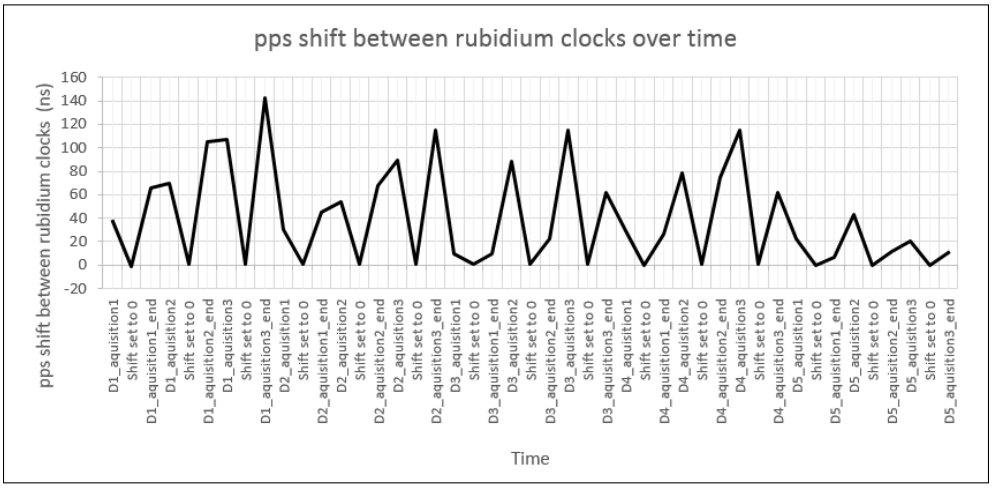

Figure 4.14: PPS shift for campaign measurement in tunnel with GPS

Another verification can be done. In this case, the GPS signal is no longer available after a synchronization phase of the Rubidium clocks for 5 days. Between each acquisition, the synchronization is applied by adding/removing delay from the internal rubidium clock.

Then the acquisition takes place for 60 min. We reproduce this three times a day and over five days. The system (clock oscillator or CDA) is never reconnected to the GPS signal.

In this test, where results are presented Figure 4.15, we can see that the PPS delay between both rubidium clocks is not up to 1000 ns. This means that the system can correctly remove the PPS shift from the rubidium clock and it can make acquisition during five days.

We saw in this validation that the channel sounder is able to make acquisition during five days with and without GPS due to the possibility of the rubidium clock to add or remove a PPS delay up to +/- 999 ns. As we can apply this shift for both rubidium clocks, the channel sounder is able to add or remove a PPS shift up to 1998 ns.

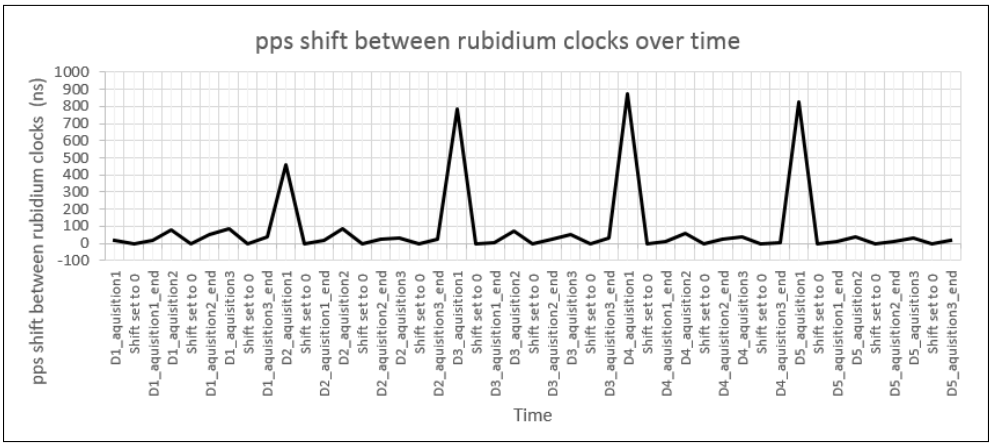

Figure 4.15: PPS shift for campaign measurement in tunnel without GPS

4.6.2 Validation of the measured propagation delay using cables

Several methods are considered to validate the output of the channel sounder in terms of propagation delay. With a channel emulator it could be possible to verify obtained complex impulse responses using a known emulated channel model such as a simple Tapped Delay Line model. To do this test, a MIMO channel emulator is required and this type of equipment was not available.

A second possible test to validate the results is to use several cables of different length to create one or more delayed paths. These delayed paths will appear in the impulse response as delayed and attenuated peaks relative to the main peak (shortest path). The time between the main peak and the secondary peaks must be proportional to the difference in length between the different cables used. The difficulty in this case is to deal with the MIMO case.

We use low loss cables with a velocity rate of 85 percent compared to the speed of light. Two cables are used to obtain a direct path and an echo of this path which will be delayed depending on the size of the cables. We implemented two tests to validate the results. A first using a 30 meter cable and a 60 meter cable and a second test using a 30 meter cable and a 90 meter cable as presented Figure 4.16 and 4.17 respectively.

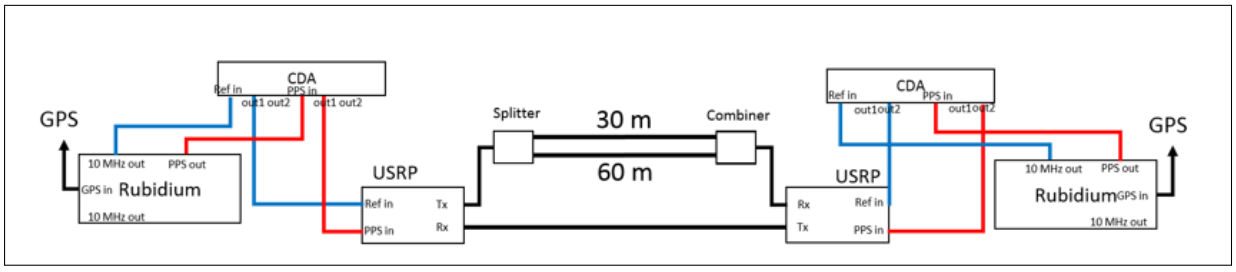

Figure 4.16: Propagation test with cables of 60 meters

The propagation speed in low loss cables is 254 823 589.3 m/s, i.e. a delay of 3.924 ns/m. The only difference in propagation in the cables is the difference in length between the two cables present between the splitter and the combiner.

The time difference between the first signal received from the 30m cable and the second signal received from the 60m cable is 117.7 ns equivalent to the propagation time in 30 meters of cable.

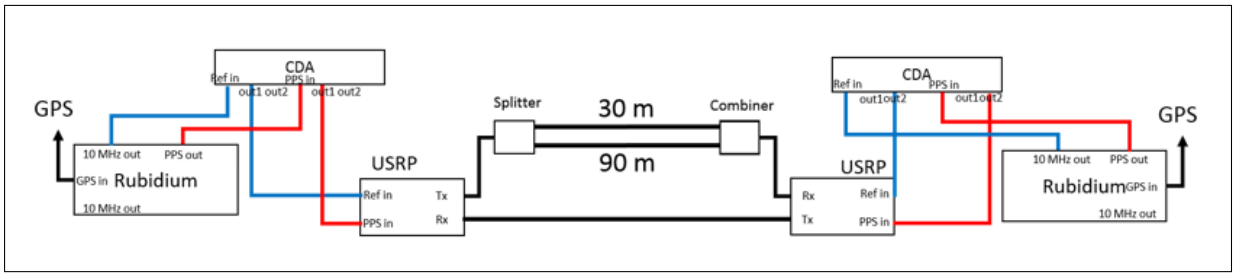

Figure 4.17: Propagation test with cables of 90 meters

From channel sounder, the delayed signal is visible with a delay of 2 samples, as shown Figure 4.18, equivalent to 111.1 ns ($\frac{2}{(30.72*10^6)}$) for a sampling frequency of Fe = 18 MHz (i.e. Te = 55.5 ns). The measured delay of 117.7 ns corresponds to 2.1186 samples at the sampling frequency of the sounder, which is consistent with the channel sounder measurement of 2 samples.

The time difference between the first signal received from the 30 m cable and the second signal received from the 90 m cable is 235.44 ns equivalent to the propagation time in the 60 m of cable. With the channel sounder, the delayed signal is visible with a delay of 4 samples, as shown Figure 4.19, equivalent to 222.2 ns ($\frac{4}{(30.72*10^6)}$). The measured delay of 235.44 ns corresponds to 4.23792 samples at the sampling frequency of the sounder, which is consistent with the channel sounder measurement of 4 samples.

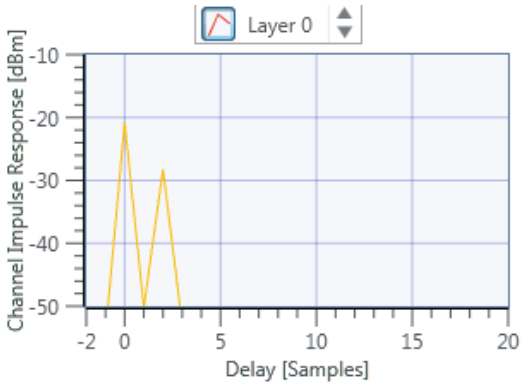

Figure 4.18: Propagation test with cables of 30 and 90 meters

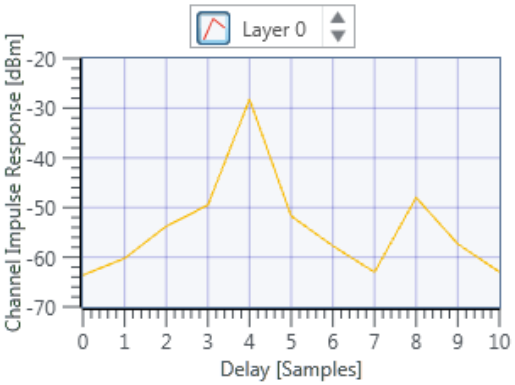

Figure 4.19: Propagation test with cables of 30 and 90 meters

The delays present in the impulse responses are consistent with the theoretical propagation times in the cables. Indeed, the difference between the theoretical value and the value measured with the impulse responses can be explained by the fact that one cannot read the value between two samples. The sampling frequency of the impulse responses corresponding to 18 MHz (55.55 ns/samples).

4.6.3 Validation of the output power

In order to adjust the equipment according to the requirements of the field tests, it is necessary to assess the balance of the radio link between the mobile station and the base station. The transmit power is an import parameter to compensate the attenuation in the channel to reach the receiver with an acceptable level of power. The maximal power output power for the USRP-2954 is 20 dBm in the product specifications. However, after measurements using the USRP-2954, we

found that the output power was different from the specifications using the MIMO Application framework. The output power was 30 dB less than the specifications.

This issue is due to the MIMO Framework design and cannot be upgraded without changing the original VI lock. We are using a spectral analyzer to measure the output power of the USRP-2954. Using the option "Total power" we recover the total power in the bandwidth. For the MIMO AFW the bandwidth is 20 MHz, but the effective bandwidth is 18 MHz. With the interface of MIMO AFW we provide a power to the output USRP-2954. For example, we request an output power of 0 dBm, then with the spectral analyzer we get the total power in band which are -28.5 to -29.7 dBm (depending of the channel output of the USRP-2954).

Figure 4.20 shows the difference between the programmed power and the real power at the output.

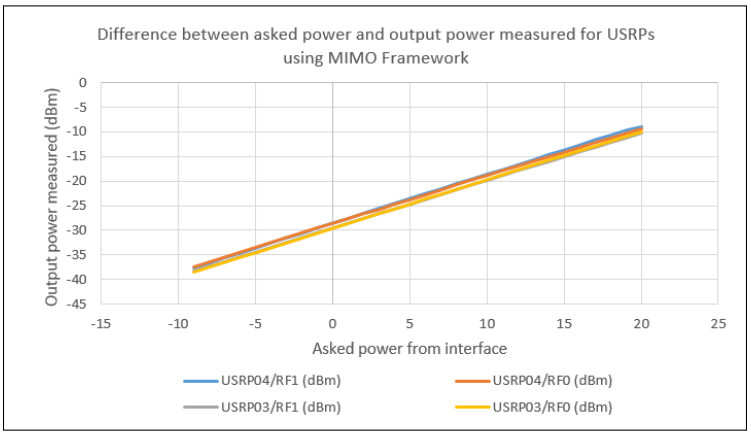

Figure 4.20: Measured power versus asked power

To be sure that the power losses come from the MIMO Framework, we measured the output power of the USRP using a sine wave signal. The output power was 6 dB less than the specifications as presented Figure 4.21.

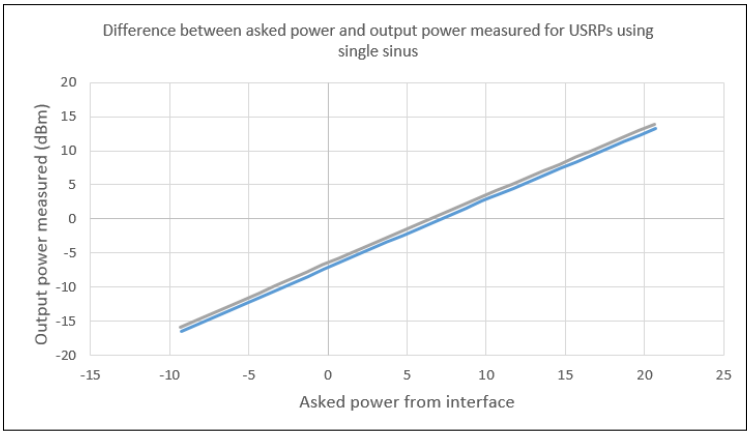

Figure 4.21: Measured power versus asked power for sine wave

These results show a large difference between data sheet specifications and real power measured. The MIMO Framework induces a power loss that cannot be modified. Due to this power loss, the channel sounder must use external amplifier and preamplifier.

The receiver sensitivity is –65 dBm. The maximal transmit power is –9 dBm. To perform continuous channel measurements over several hundred meters, signal amplifiers and Preamplifiers will therefore be required. With an amplification of 44 dB at the transmission side and a pre-amplification of 34 dB in reception, and using a -12 dBm output power and a security gain of 20 dB, the maximal reachable distance for a frequency equals to 3.5 GHz is 2.42 km using Friis formula. Without amplifier, the maximal measured distance is 15.26 m.

4.7 Extraction of the channel characteristics

To extract the channel characteristics, we need first to change the size of the recorded file containing the Channel frequency responses to exploit them with Matlab. Indeed, it is not possible with Matlab to open a large amount of a data vector depending of the RAM size. To do so, the recorded file are split into multiple files of 750 Mo, which correspond approximately to 10 000 frequency responses. All files that represent a measurement campaign are recorded with a .BIN extension, which improves the recording speed during measurement. Figure 4.22 presents an overview of the software organisation.

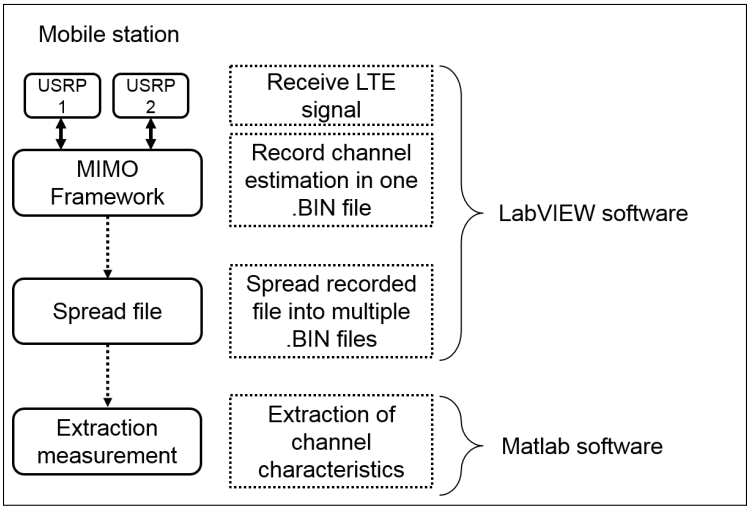

Figure 4.22: Organisation of the software

The channel characteristics are extracted using Matlab code.

First of all, the file extension is changed from .bin to .Mat. Then, we have to organize the data vector. One recorded file is a series of values. The first value of the recorded file represents the real part of the complex number and the second value represents the imaginary part of the channel frequency response. Successively the third one is the real part and the fourth one is the imaginary part and so on. All the complex values are organized in a vector.

Three steps are followed in the post-processing code:

1. the construction of the calibrated **H** matrix,
2. the estimation of the channel frequency responses and the computation of the channel impulse responses,
3. the treatments on the CIRs.

The aim of the calibration step is to suppress the effect of cables, amplification stage, hardware and all other equipment in the system during the measurements. The calibration phase is done using cables to connect the mobile station and the base station with no antenna. Cables used are the same than the ones used for measurement campaign with antennas. We consider low loss cables of 10 m (these cables are also used during the measurements. The characteristics are

given in Chapter 5). We measure the $\mathbf{H}_{calib}$. The estimated channel matrix $\mathbf{H}$ is a division of coefficient element by element between the measured channel matrix $\mathbf{H}_{meas}$ and the calibrated one as presented by equation (4.13):

$$\mathbf{H}_{est}(m,n) = \frac{\mathbf{H}_{meas}(m,n)}{\mathbf{H}_{calib}(m,n)} \tag{4.13}$$

where m and n are respectively the transmitted antenna and received antenna. Based on the estimated complex channel frequency responses, we can calculate the complex channel impulse responses by IFFT and the corresponding Power Delay Profile (PDP).

4.7.1 Extraction of the main channel parameters

Different parameters can be extracted from the CIR to model the channel, namely the path loss, shadowing, power delay profiles to extract Doppler, delay spread, *etc.*.

4.7.1.1 Path Loss and Shadowing

Free space path loss model described in equation (4.14) is the mean power that restricted to a clear and unobstructed LOS between the mobile station and the base station.

$$FSPL(d) = \frac{P_t G_t G_r}{P_r} = \frac{P_t G_t G_r \lambda^2}{(4\pi)^2 d^2 L} \tag{4.14}$$

where, P_r is the received power, P_t is the transmitted power, G_r and G_t are the antenna gain at the receiver and transmitter respectively, d is the distance between the mobile station and the base station in meters, L is the system losses due to the equipment and λ is the wavelength in meters. The shadow fading is the results of the variation of the radio signal power due to the encountering with obstruction over long distance. In [207] authors demonstrates that the mean power of the receiver fluctuates with a log-normal distribution. The Path loss can be modeled with a log-distance representation as expressed in equation 4.15

$$PL(d)[dB] = P_{Tx}[dBm] - P_{Rx}[dBm] = P_0 + 10nlog_{10}(\frac{d}{d_0}) + X_s \tag{4.15}$$

where P_0 is the path loss at the reference distance d_0, and n is the path loss exponent, which describes the path loss trend versus the distance d between the transmitter and the receiver. X_s is a zero-mean Gaussian distributed random variable in dB with a standard deviation σ_x. The path loss exponent and the standard deviation can be calculated from measurement data.

4.7.1.2 Power Delay Profile

The Power Delay Profile estimation is an average of the individual delay profiles defined as the power of the Impulse response at time t_i following equation (4.16) [10]:

$$PDP(\tau) = \frac{1}{N}\sum_{i=1}^{N} |h(\tau, t_i)|^2 \tag{4.16}$$

where N is the number of impulse responses considered. The effect to average a certain number of impulse responses is to reduce the noise peak as explain in [10]. A large number of N impulse responses ensure a noise smoothing. From the PDP, different parameters can be extracted as the first arrival delay, the maximal excess delay, the average delay, the RMS (Root Mean Square) delay spread and the associated coherence bandwidth.

The first arrival delay τ_0 represents the first arrived component, which is typically the LOS path or also the most significant component. From a NLOS point of view, the first arrival delay is relative to the first reflected component.

The maximal excess delay τ_m is the time delay where the last component can be detected by the system. It is calculated applying a threshold on the PDP, which neglect all component bellow. The delay of the last component above the threshold is considering as the maximal excess delay.

The average delay $\hat{\tau}$ is the first moment of the PDP as explained in equation (4.17) [10]:

$$\hat{\tau} = \frac{\sum_{i=1}^{N} \tau_i \cdot PDP(\tau_i)}{\sum_{i=1}^{N} PDP(\tau - i)} - \tau_0 \tag{4.17}$$

The RMS delay spread σ_τ is the square root of the second central moment of the PDP [10]. The RMS is relative to the standard deviation of the mean excess delay and can be calculated by equation (4.18):

$$\sigma_\tau = \sqrt{\hat{\tau^2} - (\hat{\tau})^2}, \hat{\tau^2} = \frac{\sum_{i=1}^{N} \tau_i^2 PDP(\tau_i)}{\sum_{i=1}^{N} PDP(\tau_i)}. \tag{4.18}$$

The RMS delay spread gives an information about the inter-symbol interference by the ratio of RMS delay and symbol time duration.

The Doppler spectrum associated to a certain delay τ_k is the FFT of the O CIR of the subset A as illustrated in Figure 4.23.

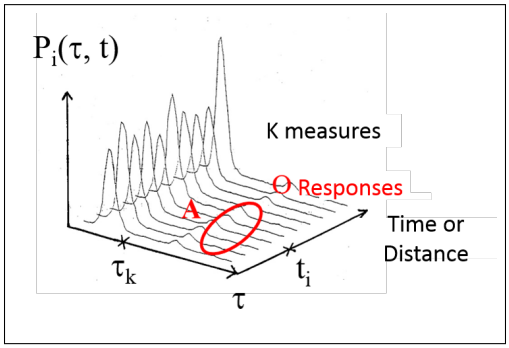

Figure 4.23: Doppler spectrum extraction from the CIRs

4.7.1.3 Angles distribution

Angle of arrival and Angle of departure are an important parameter of the channel characterization for MIMO configuration. It is important to be able to extract the 3D characteristics of the channel (elevation, azimuth, polarization) at transmitter and receiver sides to model the channel with the impact of the antenna array distribution on the wave.

There are different algorithms that allow the extraction of the angular characteristics. MUSIC [208], ESPRIT [153] or SAGE [154] are able to extract the Angle of Arrival, Angle of Departure and polarization. These algorithms are also detailed in [10].

4.7.2 Channel modelling

MUSIC, SAGE and ESPRIT can also model the channel following a TDL or a CDL channel model. But as explained in Chapter 2 they have a certain complexity. Another method, still considered with less complexity, is explained in [132]. This method was used in [209]. In [10],

S. Salous details different modelling processes. Due to all the technical problems experienced to develop the channel sounder, we had not enough time to adapt a method to the data measured.

4.8 Conclusion

In this chapter, we have presented the 4 x 4 MIMO SDR-based channel sounder developed in the sub 6 GHz band based on a LTE-TDD like excitation signal over 20 MHz. The number of pilots is equal to 1200 and the number of symbols per frame is 134. The sampling rate is 30.72 MS/s. The minimal measurable delay is 55.55 ns and the maximal delay is equal to 66.6 μs. The maximal output power is equal to -9 dBm and the sensitivity is equal to -65 dBm. The channel sounder is capable to continuously record the channel frequency responses measured during 1 hour in parallel to the measurements.

We have described the general architecture, the functions and characteristics of the different bricks of the channel sounder made with the combination of hardware and software. In particular we have detailed the modifications performed in order to modify an initial "LTE communication system" based on the *MIMO framework* software and specific hardware into a SDR-Based channel sounder considering a LTE TDD like excitation signal. The Channel estimation implemented is based on the use of specific pilot subcarriers in the LTE frame known at transmission and reception side. All data is replaced by pilots. This choice has permitted also to simplified the LTE communication software by removing the part related to data filling in the software. With such simplification, the channel sounder complexity is reduced as well as the required hardware.

After a brief description of the channel estimation methods using in LTE sounding, namely the Leas Square and Mean least Square, we presented briefly the Least Square estimation implemented. This algorithm is a low complexity algorithm that allows the channel sounder to record in real time the channel estimations. Based on re-configurable software and architecture, the channel sounder can be an increase in term of hardware and software complexity to improve the algorithm used to sound the channel.

The recorded channel estimations are set in a specific position. To extract pilots estimation we apply a reorganization on each recorded pilots. Only after this, the channel frequency responses can be extracted in post-processing. Then, the channel parameters extraction is detailed.

Finally, we have detailed the channel sounder validation with different tests included the propagation time inside different cables length, the output power and synchronization. We saw that there is a power difference between the output power that an USRP can delivered and theoretical output power. Due to that, we will need to had, to the channel sounder setup, an amplification stage to be able to perform the outdoor measurements.

In the next chapter, we will present the results of two measurement campaigns, one indoor and the other outdoor.

Chapter 5

Indoor and outdoor measurements

5.1 Introduction

In the previous chapter, we have described the developed SDR-channel sounder based on LTE signal and we have detailed the different experiments performed to validate the capabilities of the equipment. In this chapter we will present the results obtained for Indoor and Outdoor scenarios with the developed channel sounder. In the first part of this chapter we will present measurements performed in the corridors of the Leost laboratory at 2.7 GHz with a 20 MHz band corresponding to the LTE signal. The scenarios will be described, then we will draw some examples of the CIRs obtained and we will extract the corresponding main channel parameters. A second set of measurements at 3.5 GHz with 20 MHz band is also presented.

In the second part of the chapter we will detail the outdoor measurements performed at 3.5 GHz on the Lille scientific campus. Three scenarios were performed, one Line Of Sight (LOS) configuration at speed equals to 6 and 20 km/h and two Non Line of Sight (NLOS) scenarios with at speed equals to 6 km/h. The CFRs, CIRs, PL and PDP will be extracted from the measurement campaigns and we will provide the main channel parameters for each scenario. We will also highlight all the technical difficulties encountered during the outdoor measurements, which led us to make changes in the layout of the equipment and its use. A second set of measurements at 3.5 GHz is proposed with a modification of amplifier stages.

5.2 Indoor measurements in the laboratory corridors

5.2.1 Indoor Scenarios

The aim of these first tests was to validate the good operation of the system, the correct recording and extraction of the data and also the ability for the sounder to perform the measurements without GPS synchronization (this will be useful for measurements in tunnel).We have chosen two scenarios: LOS and NLOS. The chosen environment for the LOS scenario is a 24 meters long and 1.4 meters wide corridor. The environment for the NLOS scenario is the same 24 meters long and 1.4 meters wide corridor, followed by a second perpendicular corridor with a recess of 5.5 meters. Figure 5.1 and 5.2 give a schematic view of the configurations. Figure 5.3 shows the measurement layout in the chosen corridor at the Leost laboratory.

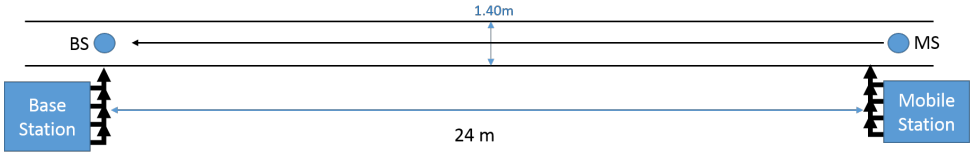

Figure 5.1: Indoor LOS scenario

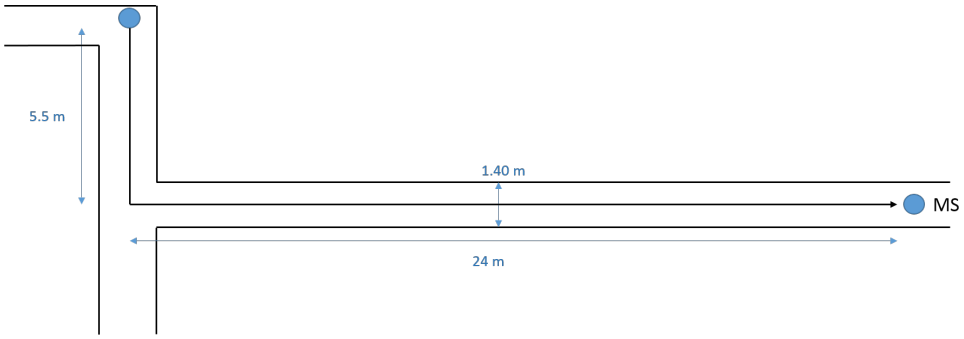

Figure 5.2: Indoor NLOS scenario

Figure 5.3: Corridor for LOS and NLOS measurement

We performed SISO and 2x2 MIMO measurements. To do so, we have considered two types of antennas, one for the Uplink (UL) and the other for the Downlink (DL) of the channel sounding. We remind here that the UL signal is used to synchronize the base station and the mobile station, as for a LTE transmission. For the UL, we choose patch antennas centered at 2.7 GHz available in the laboratory. They are shown in Figure 5.4. The DL signal is used for channel measurements. We considered bi-band (2.4/5.8 GHz) omnidirectional antennas (Siretta Delta 6C) with a +5 dBi gain shown in Figure 5.4. Antennas are positioned using a mast for the BS and fixed to the screen for the MS as presented Figure 5.5 A 1 m SMA cable (0.7 dB loss/m) connects each antenna to the USRPs. The same cables are used at MS and BS for each antenna. The parameters of the channel sounder for these measurements are summarized in Table 5.1. For SISO measurements we operate only one USRP platform for each side (MS and BS).

Parameters	Value
Frequency	2.7 GHz
Transmitted power	-9 dBm
Sensitivity	-65 dBm
DL Antenna gain	+5 dBi
cable losses	1.4 dB
USRP internal gain	30 dB

Table 5.1: Parameters used in indoor campaign

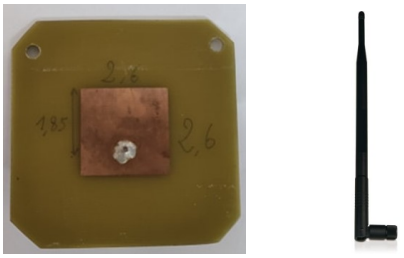

Figure 5.4: Antennas used for the measurements (left for Uplink and right for Downlink)

The Rubidium clocks are synchronized upstream of measurement by GPS synchronization with the GPS antenna on the rooftop of the laboratory at least during 72 hours to make sure that the two rubidium clock has the same reference clock synchronization to the GPS. There is no access to the GPS signal during acquisitions. Between each acquisition, a rubidium clock synchronized with respect to the other by adding or removing the delay on one of the two rubidium clocks. Therefore, before starting the measurements, we manually synchronize the two rubidium clocks as accurately as possible by step of 1 ns.

Figure 5.5: Base station and mobile station setup from left to right respectively

5.2.2 Calibration or back-to-back test

The calibration process or back-to-back test is necessary before post-processing. The antennas are removed from the channel sounder and all ports are connected with cables. The ports used for synchronization are loaded with 50 Ohm. It is important to use the same hardware and cables in the calibration measurement than for the channel measurement. The transmitting parameters have to be the same also than the ones considered for the measurements. We measured each MIMO link of the MIMO matrix individually as shown Figure 5.6 for the MIMO link 11 and 12 respectively. That means, with a 2x2 MIMO configuration, there are 4 links to be calibrated. When all MIMO links are measured individually, the calibration matrix is built in post-processing.

Based on the scenarios presented before, the results are then obtained with post-processing on the CFRs recorded. First we apply the calibration results to the measured results, then we are able to extract the individual CFRs, to deduce the CIRs and to calculate the PDP and to extract the different channel parameters as explained in Chapter 4.

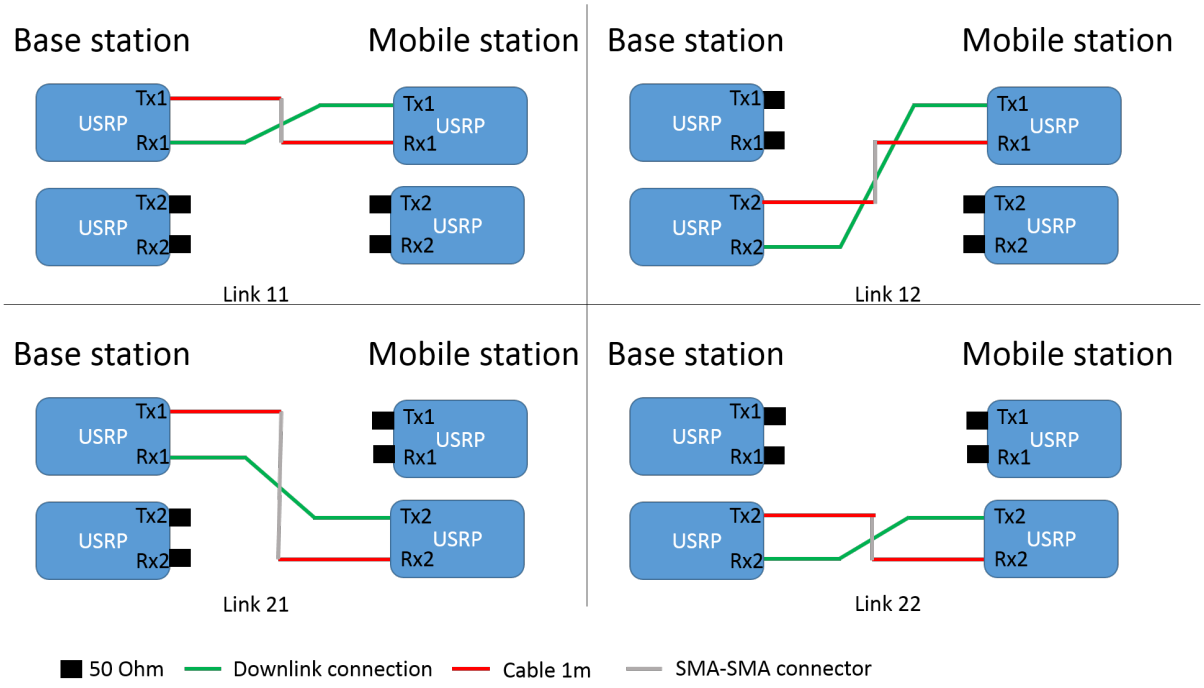

Figure 5.6: Calibration measurement for MIMO links

5.2.3 Results for corridor measurements

5.2.3.1 Results in SISO for LOS scenario with static measurements

For the SISO case, we performed an acquisition every meter starting from 3 m from the BS to the end of the corridor (24 m). For this "static" measurements, we recorded 2000 CFRs at each position but we considered only 1/10 CFR for the results analysis. We show the CFRs for 3, 13 and 24 m in blue, green and red respectively in Figure 5.8. We can observe that the channel is flat over the 20 MHz band. The variation of the CFRs amplitude versus time is given on Figure 5.8 at 2.7GHz for the total 200 recorded CFRs. For the red curves we observed some local lost of power not yet explained.

Figure 5.9 presents the CIRs at the same positions in blue, green and red for 3, 13 and 24 m respectively. We do not observe any backward reflection at the end of the corridor (there is a door in wood). In static measurement, each record is independent from the others. For each distance we have to restart both base station and mobile station. Consequently, the synchronization between recorded files are not kept and we cannot deduce a propagation distance. We can only compare the power of the first received path, which corresponds to the mean value of the CFR presented before.

The path loss is given in Figure 5.10 were the corresponding model is plotted in red and the free path loss in green. The corresponding model is given by equation (5.1). The standard deviation (std) between the measurements and the model is equal to 3.13 dB, corresponding to the slow fading observed.

$$PL(d) = -47 - 10 \times 0.91 log_{10}(d) \tag{5.1}$$

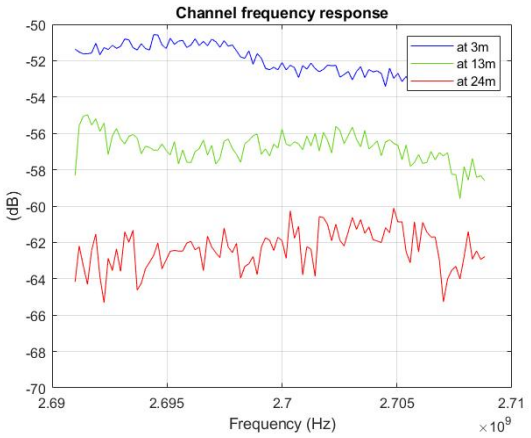

Figure 5.7: CFR for indoor LOS scenario at 3 m, 13 m and 24 m in blue, green and red respectively from the base station

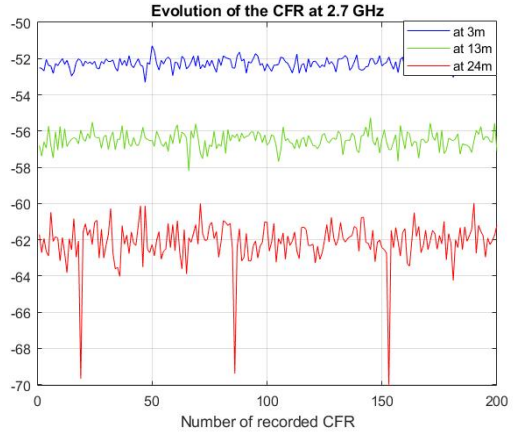

Figure 5.8: Evolution of the CFRs amplitude during one measurement at 2.7 GHz for 3 m, 13 m and 24 m in blue, green and red respectively

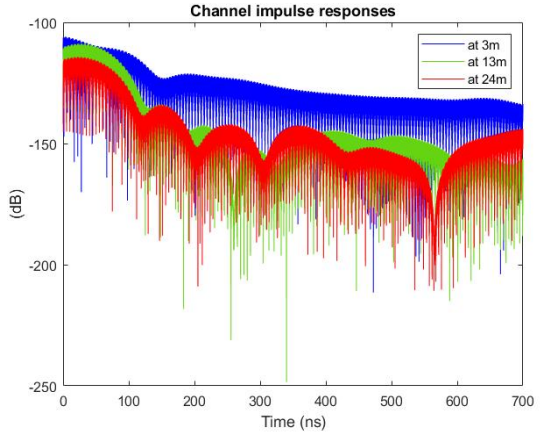

Figure 5.9: CIRs for indoor LOS scenario at 3 m, 13 m and 24 m in blue, green and red respectively from the base station

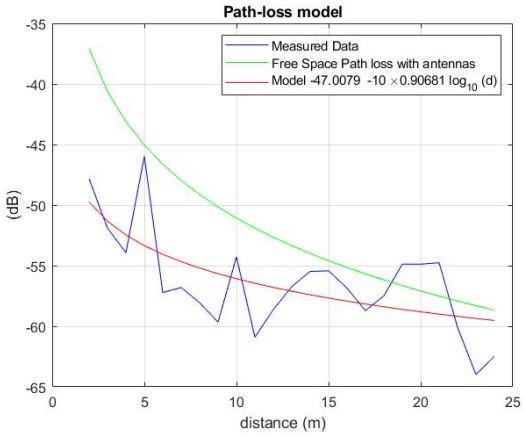

Figure 5.10: Path loss of the measured channel compared to the free space path loss

5.2.3.2 Results for LOS scenario in corridor with very low mobility

In this section we analyze the results for the indoor LOS scenarios with slow mobility. We performed 2x2 MIMO measurements continuously while the MS is approaching the BS moving very slowly pushed by the operator. Figure 5.11 presents the CFRs obtained on the MIMO link 11 at the 3 previous positions (3 m, 13 m and 24 m) respectively in blue, green and red. For a correct recording data, we have to start recording in file before filling the FIFOs in the FPGA. To do this simply, we are using two buttons in the graphical interface: one to start the record and the second to start filling FIFOs. During the measurements, all the automatic gain control of the USRP board were switch off. The corresponding CIRs are given in Figure 5.12 for the four links. Due to the short bandwidth considered (18 MHz effective), it is impossible to observe delays smaller than 55 ns. From the CIR curves, we can observe that the peak corresponding to the maximal amplitude in LOS is shifted by 58.5 ns between the first and last CIR at 3 m and 24 m. That corresponds to the measured distance in the corridor equal to 17.5 m. As explained in static measurement, the difference can be explained by the sampling rate.

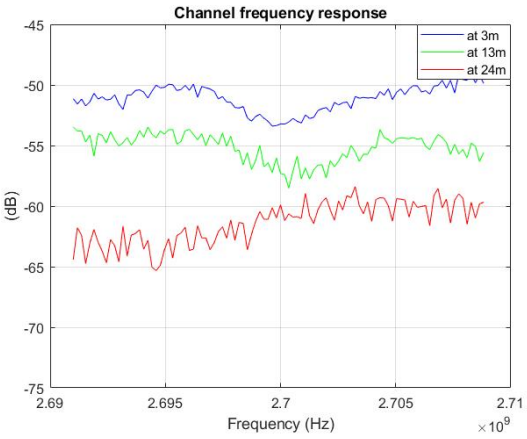

Figure 5.11: CFRs for indoor LOS scenario at 3 m, 13 m and 24 m in blue, green and red respectively from the base station for MIMO link 11

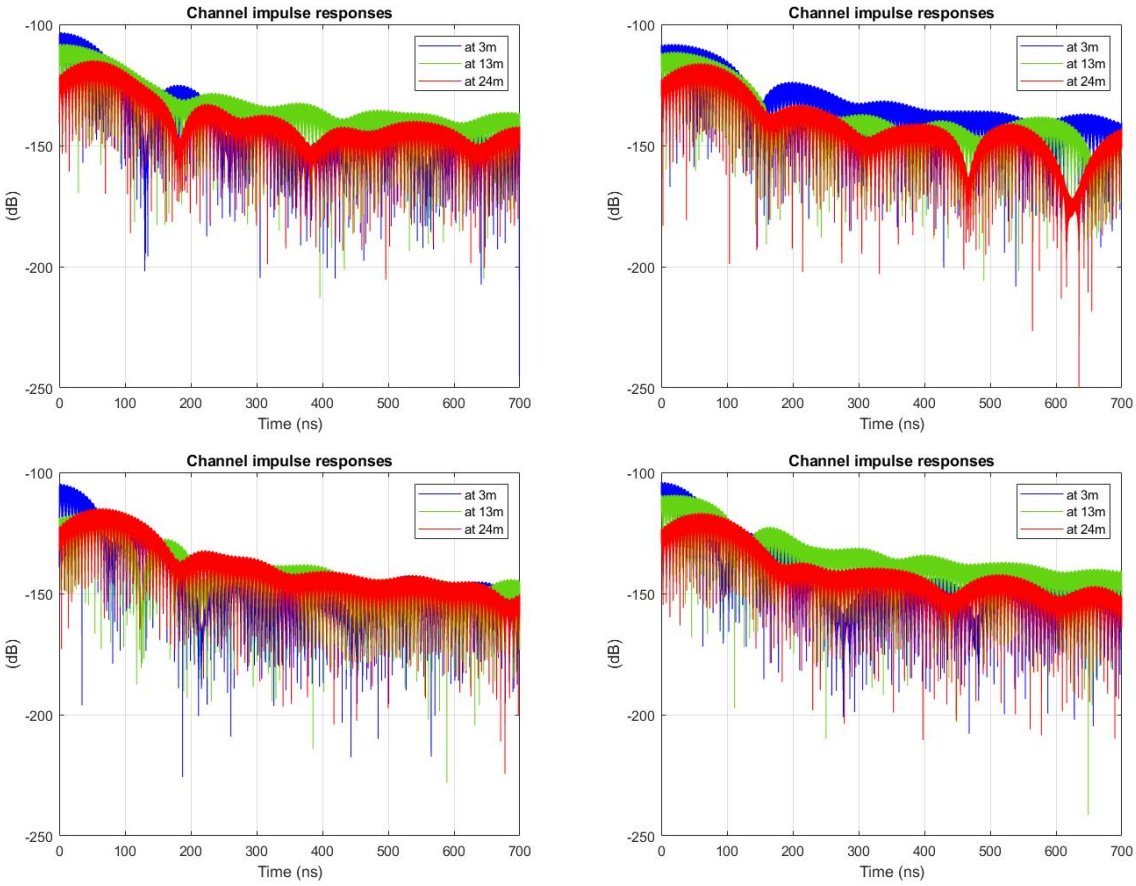

Figure 5.12: Evolution of the CFR amplitude at 3m, 13m and 24m in blue, green and red respectively for MIMO link 11, 12, 21 nd 22 from left to right

The measured path loss for each MIMO link and the corresponding model are presented respectively in blue and red for each MIMO link in Figure 5.13. This representation is not usual but it permits to notice similar behavior on the four links. The average path loss propagation model is computed with the MIMO matrix as the average of each individual path loss on each MIMO link. The PL as a function of distance d between the MS and BS, in red, is approximated with the following equation (5.2) and presented Figure 5.14:

$$PL(d) = -33.47 - 10 \times 2.18 log_{10}(d) \tag{5.2}$$

We can observe an additional attenuation compared to free space. We observe slow fading versus the distance. The standard deviation of the slow fadings is equal to 2.71 dB.

The PDP is obtained following equation (4.16) in Chapter 4. The result is given Figure 5.15. The channel characteristics in terms of delay for several thresholds are summarized in Table 5.2. We fix the threshold values related to the maximal value of the PDP. We consider -20, -30 and -40 dB below the maximal value. The mean delay varies between 1.39 μs to 1.43 μs. The maximal delay varies between 0.16 μs to 2.78 μs. The RMS delay spread σ_τ varies between 0.791 to 0.799 ns. For further analysis related to channel modelling, the chosen threshold will define the number of path presents in the channel. With a threshold fixed at -30 dB, We can deduce that in the corridor, all the multi path components arrive within a window equals to 440 ns.

There are different ways to calculate the Coherence Bandwidth B_c [210, 211]. In first approximation $B_c \propto 1/\sigma_\tau$. For a correlation coefficient c of 0.5 [211], B_c can be expressed as (5.3).

$$B_c = \frac{1}{2.\pi \times \sigma_\tau} \tag{5.3}$$

The coherence bandwidth of the channel is around 200 kHz, which is less than the used bandwidth of the signal (18 MHz). We conclude that the channel can experience frequency selectivity.

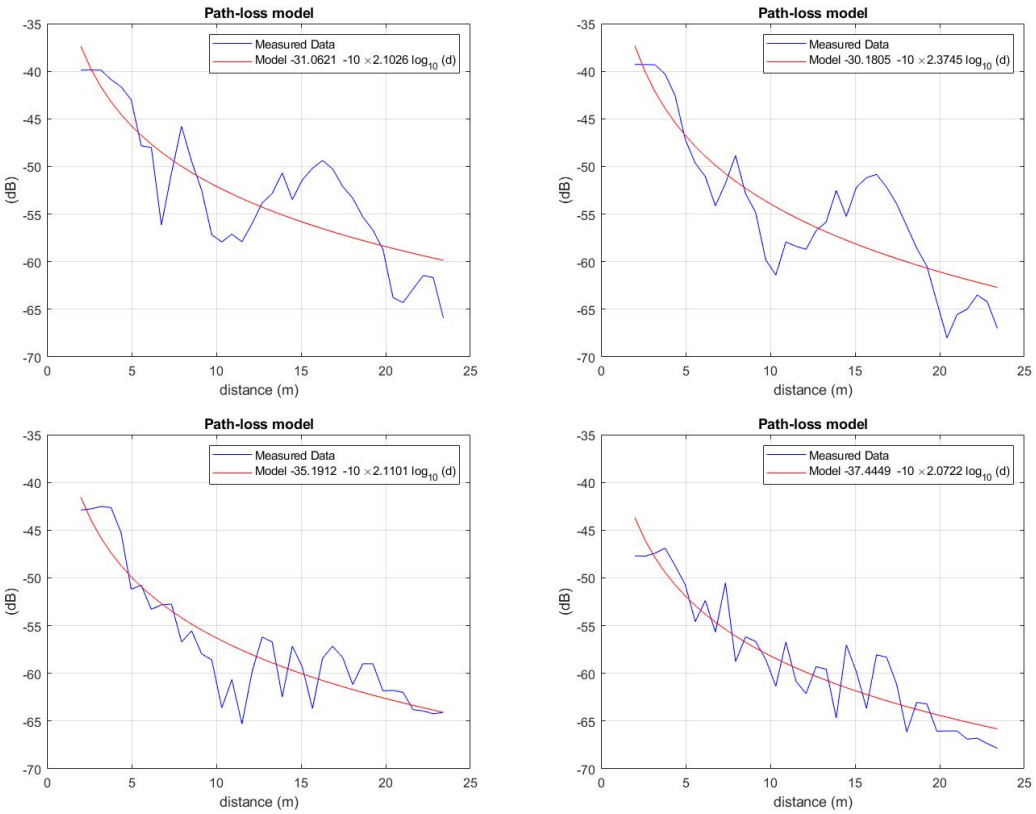

Figure 5.13: Path-Loss in corridor scenario LOS for each MIMO link 11, 12, 21, 22 from left to right

Caracteristics of delay	Threshold (dB)			
	-20	-30	-40	Without
Mean delay (μs)	1.39	1.40	1.41	1.43
Max path Delay (μs)	0.16	0.44	1.71	2.78
RMS Delay (ns)	799	796	792	791
Coherence Bandwidth (MHz)(c=0.5)	0.199	0.200	0.201	0.201

Table 5.2: Characteristics of the channel for corridor LOS scenario

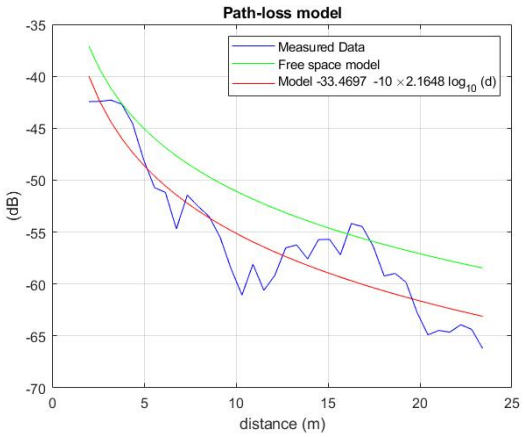

Figure 5.14: Path-Loss in corridor scenario LOS for the MIMO matrix

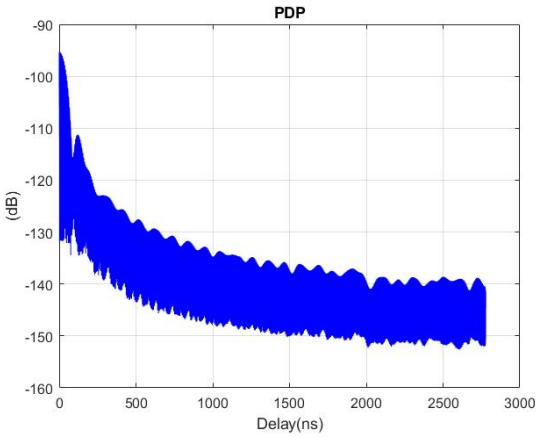

Figure 5.15: PDP in corridor scenario LOS for the MIMO matrix

5.2.3.3 Results for NLOS scenario

As presented in section 5.2.1, the NLOS scenario is composed of two perpendicular corridors. The measurement campaign begins with a 5.5 meters long LOS scenario, then a 10 meters long NLOS scenario. We present only the path loss obtained with the MIMO matrix on Figure 5.16 (measurements in blue, model in red and free space in green). The global model follows equation (5.4):

$$PL(d) = -38.62 - 10 \times 3.05 log_{10}(d) \tag{5.4}$$

The transition between LOS part and NLOS part is visible on the curve between 5 and 6 m. We can observe an additional attenuation between the two slopes (see Figure 5.17) equals approximately to 15 dB. The standard deviation of the slow fadings is equal to 3.99 dB. Due to the NLOS, the std is higher than in LOS scenario (2.71 dB).

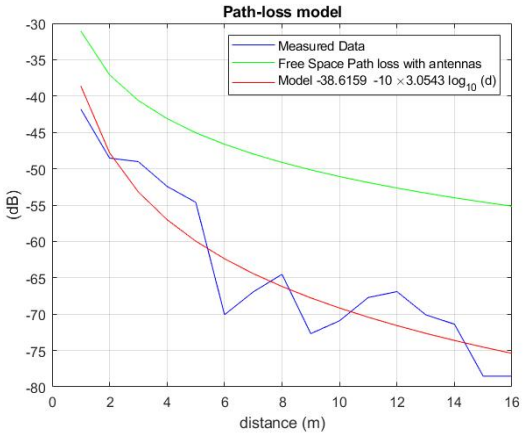

Figure 5.16: Path-Loss in corridor for NLOS scenario

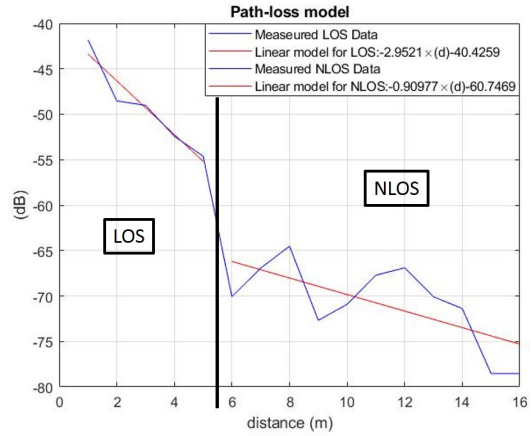

Figure 5.17: Path-Loss in corridor for NLOS scenario

5.2.3.4 Results for new 4x4 MIMO LOS scenario with static acquisition - New measurements

For this scenario, we performed an acquisition every 50 cm, starting at 3 m from the BS to 21 m. We change the output power from -9 dBm previously, to -15 dBm to avoid the saturation of the system at RX level. The received gain is still +30 dB. The acquisition is done for a center frequency equals to 3.5 GHz. The antennas at the base station and the mobile station are typical monopole-like antenna, presented Figure 5.18, operating between 1 GHz and 6 GHz. The antenna pattern is omnidirectional in the azimuth plane XoY. On this plane the maximal gain is about 2.5 dBi at 3.5 GHz as illustrated on Figure 5.19. On the elevation plane the maximal gain is 1 dBi at 3.5 GHz presented in Figure 5.19.

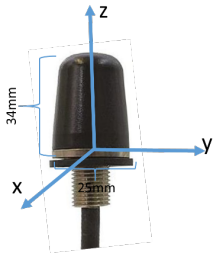

Figure 5.18: Low-profile monopole antenna

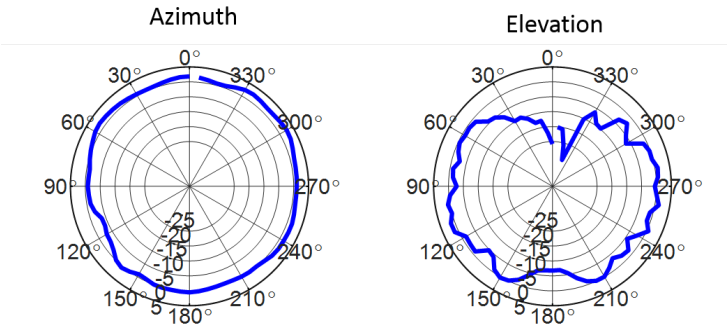

Figure 5.19: Gain pattern in the azimuth and elevation at 3.5 GHz

The BS and MS are presented Figure 5.20 and Figure 5.21 respectively. As explained in previous chapter, we need to use 16 antennas, 4 antennas for UL and 4 for DL at each side of the channel sounder, which make 8 antennas at BS and 8 at MS.

Figure 5.20: Base station in indoor measurement

Figure 5.21: Mobile station in indoor measurement

During these new measurements in indoor we also observed that the first 3 slots of each LTE frame (20 slots) should not be considered because the power is not stable. Figure 5.22 illustrates the effect observed on the first 9 slots. We have not yet found the right explanation. Consequently, for this new static measurements, we delete the first 3 slots of each LTE frame. Consequently, we considered only 950 for the results analysis among the 1000 recorded CFRs.

We present the CFRs obtained for MIMO link 11 at 4, 11 and 17 m in blue, green and red respectively in Figure 5.23. We can observe that the channel is flat over the 18 MHz band for 4 and 11 meters but we observe attenuation of 10 dB around the central frequency. We saw that the attenuation position can change in the measurement due to small variations in the elevation and azimuth plans of the antennas at the same position. The variation of the CFRs amplitude versus time for MIMO link 11 is given on Figure 5.24 at 3.5GHz for one recorded frame (slot4 to slot19). For the red curves (17 m) we observed more amplitude variations as we approach the noise sensitivity of the channel sounder.

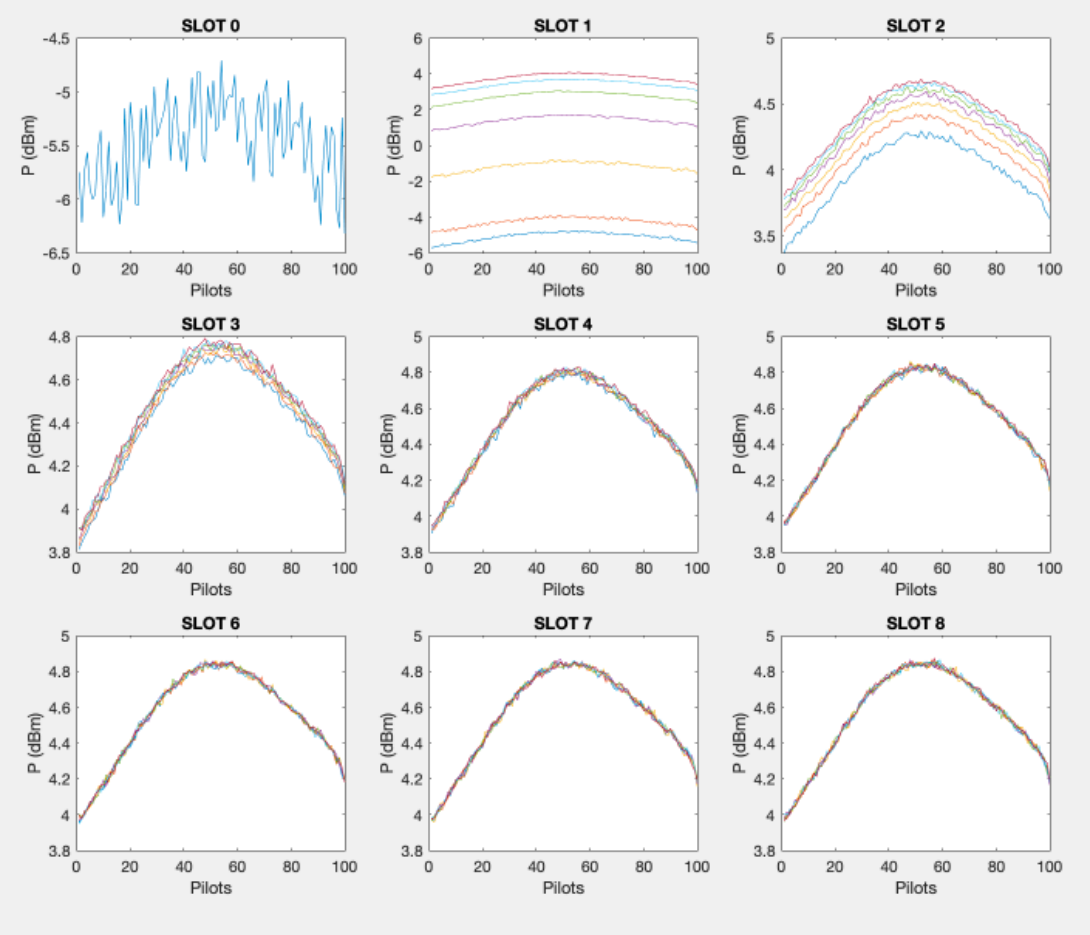

Figure 5.22: CFR of slots

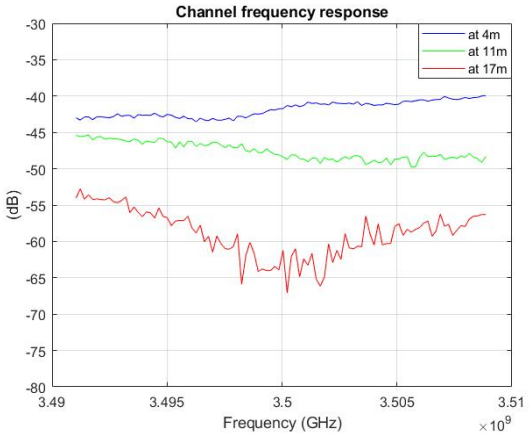

Figure 5.23: CFR for MIMO link 11 for indoor LOS scenario at 4 m, 11 m and 17 m in blue, green and red respectively from the base station

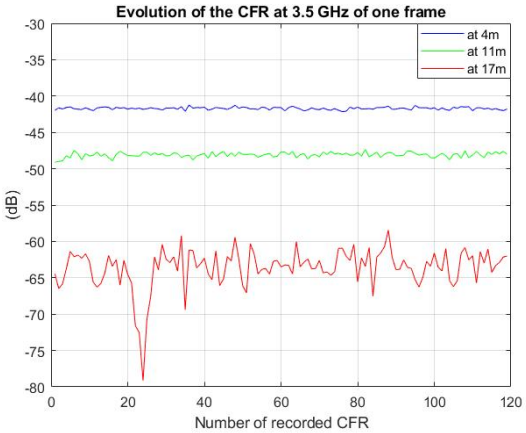

Figure 5.24: Evolution of the CFRs amplitude for MIMO link 11 during one frame at 3.5 GHz for 4 m, 11 m and 17 m in blue, green and red respectively

Figure 5.25 presents the CIRs for MIMO link 11 at the same positions in blue, green and red for 4, 11 and 17 m respectively. In static measurement, we recall that each record is independent from the others.

The path loss is given in Figure 5.26 were the corresponding model is plotted in red and the free path loss in green. The corresponding model is given by equation (5.5). The standard deviation between the measurements and the model is equal to 4.24 dB, corresponding to the slow fading observed.

$$PL(d) = -44.42 - 10 \times 1.89 log_{10}(d) \tag{5.5}$$

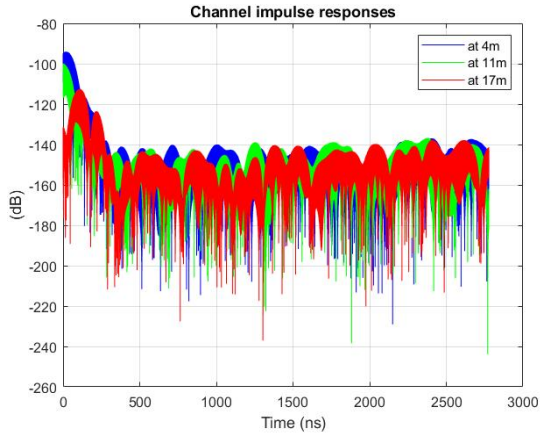

Figure 5.25: CIRs for link 11 for the 4x4 MIMO static measurement indoor LOS scenario at 4 m, 11 m and 17 m in blue, green and red respectively from the BS

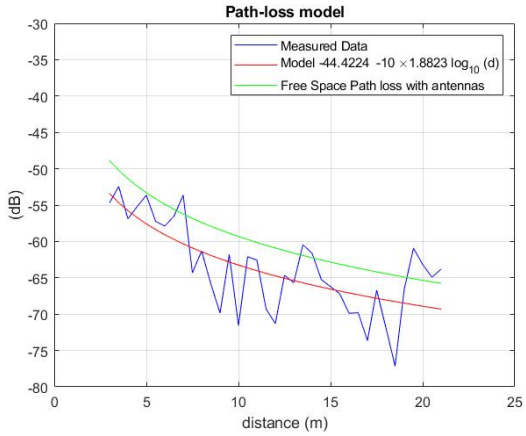

Figure 5.26: Path loss of the 4x4 MIMO static measured channel compared to the free space path loss

5.3 Outdoor measurements

5.3.1 Outdoor scenarios

At the beginning of the PhD, it was planned to have access to railway sites in Spain thanks to Metro de Madrid. The aim of these outdoor measurements was to validate the channel sounder in vehicular scenarios. Two outdoor scenarios in mobility, described below, were chosen near the premises of the University Gustave Eiffel in Villeneuve d'Ascq scientific campus, France. We have used a laboratory van. In agreement with the new 5G bands allocation in sub-6 GHz bands, FR1 of the 5G NR [212], the outdoor channel sounding was performed at 3.5 GHz with a 20 MHz band of the LTE signal. We have considered:

1. a LOS scenario along a 150 m straight road with a succession of trees and buildings on the sides of the road;
2. a 600 m long NLOS scenario starting with the first LOS scenario and continuing the road by passing behind buildings and then going back to the base station;

Two speeds were selected for the first scenario: 6 km/h (the minimal speed of the laboratory truck) and 20 km/h allowing a stable speed quickly and thus reducing the acceleration distance. The second scenario was carried out at 6 km/h allowing to return without stopping the van. Figure 5.27 gives a map view of the runs for the three scenarios: LOS scenario (left), NLOS scenario around buildings (right) and NLOS scenario round trip (below). Figure 5.28 gives a "street view" of the environment chosen. The base station remains static while the mobile station runs at different speed and performs the MIMO 2x2 and MIMO 4x4 measurements at 3.5 GHz on 20 MHz band. An additional measurement was performed in LOS scenario at 3.5 GHz with no amplification at receiver sides (both BS and MS side).

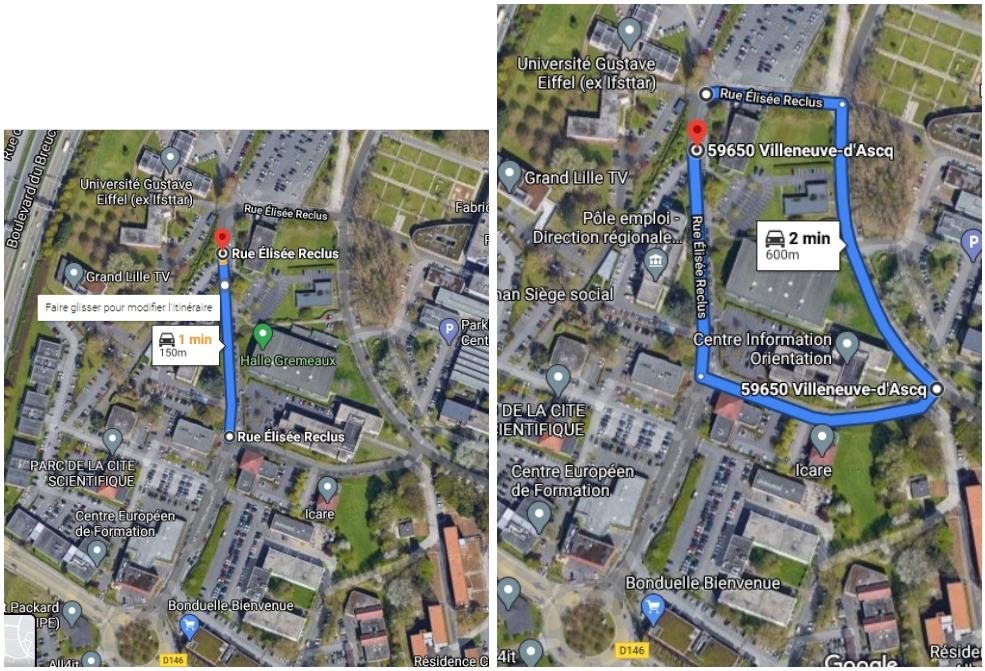

Figure 5.27: Description of LOS scenario (left) and NLOS scenario around buildings (right)

Figure 5.28: LOS scenario environment view

5.3.2 Equipment description for the measurements and parameters

The output power of the channel sounder is equal to -12 dBm and the sensitivity at reception side is equal to -65 dBm. The internal USRP amplification is equal to 25 dB. We are using monopole-like antennas presented in the last indoor measurement (Figure 5.18). Then, for each antenna, we consider a 1 m cable (-0.7 dB/m) followed by a 10 m low-loss cables (-1.8 dB for 10 m) to feed the USRP.

In this configuration and taking into account the attenuation in free space with an additional 15 dB security gain and 5.78 dB ($-0.7 \times 2 - 1.8 \times 2$) of total cable losses, the maximal distance that can be reached is 7.84 m. Consequently, we decided to add pre-amplifiers (+34 dB of gain) at the reception side both for UL and DL, which allows a coverage of 393.14 meters. Then, an amplifier stage offering +44 dB gain is added at both transmission sides (for UL and DL), which allows now a maximal distance in theory of 62 km in free space scenario. The output power of the amplifiers and pre-amplifier is flat over the 20 MHz measurements band considered at 3.5 GHz.

At the beginning of the experiments, we faced to an important electromagnetic perturbation problem generated by the amplifiers and received on the cables that connect the GPS antenna to the rubidium clock. The GPS receiver was not able to detect correctly the satellites, thus the synchronization was no more possible. The solution to overcome the problem was to modify the GPS antenna-to-clock rubidium cable, by a cable with better electromagnetic isolation while bypassing the amplifiers from the outside. In addition, the base station mast, the GPS antenna base station and the GPS antenna of the mobile station must be at a certain distance from each other to avoid interferences observed on the GPS signals. The GPS antennas of the BS and the BS transmitting antennas must be separated at least of 5 meters, while the MS GPS antenna and BS transmit antennas must be separated at least of 13 meters.

The power amplifiers were considered only at the base station. Thus, at the reception level of the mobile station, the power will be sufficient to carry out a channel sounding over several hundred meters. A scheme of the outdoor channel sounder with the amplification stage configuration is presented Figure 5.29 and the sounding parameters are summarized in Table 5.3.

Parameters	Value
Frequency	3.5 GHz
Transmitted power	-12 dBm
Sensitivity	-65 dBm
Antenna gain	2 dBi
Rx Pre-amplifier gain	34 dB
Tx Amplifier gain	44 dB
USRP internal gain	25 dB
Cable losses	5.780 dB

Table 5.3: Parameters for outdoor scenarios

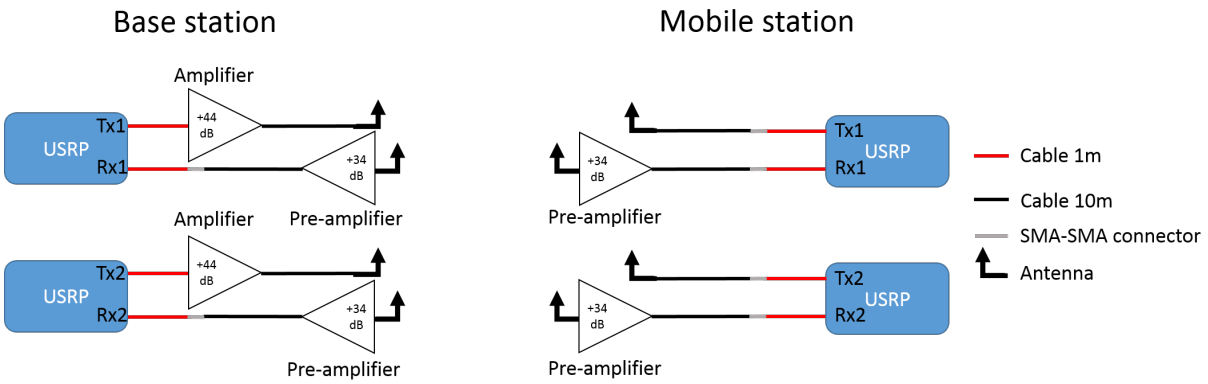

Figure 5.29: Diagram of the amplification stage of the channel sounder for outdoor measurement

At the mobile station, the antennas are placed on the roof of the truck on a specific plexiglass support presented Figure 5.30, allowing a spacing between the transmitting and receiving antennas of 50 cm. The use of a plexiglass plate, and not a ground plane, allows to get closer to the theoretical radiation of the antennas. In addition, the space between each antenna is 20 cm, which is greater than $\lambda/2$ ($\lambda = 8.57$ cm at 3.5 GHz). A schematic view of the antennas arrangement on the plexiglass is given on Figure 5.31. Each square of antennas is receiving antennas only or transmitting antennas only. Pre-amplifiers are placed just below the receiving antennas, which is as near as possible to the antennas. Then, 10 m low-loss cables (-1.8 dB for 10 m) feed the USRPs inside the truck. The GPS antenna is located on the roof of the MS. The mobile station is composed of two USRP cards, the chassis, the rubidium clock and clock distributor as explained Chapter 4.

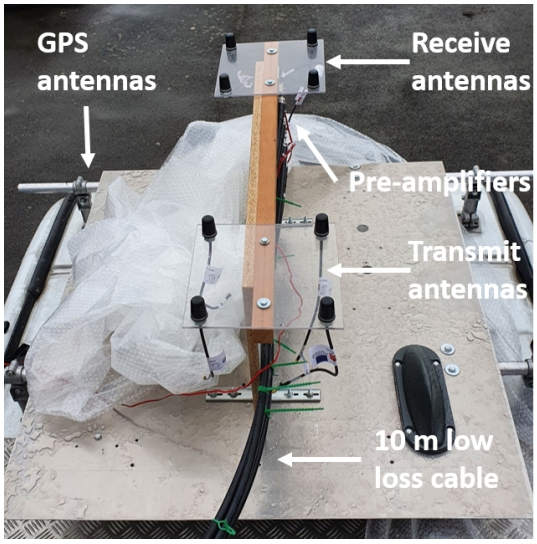

Figure 5.30: Antennas position on the mobile station

Figure 5.31: Antennas position on the support

At the base station, the same antenna support is used and installed on a 4 m high mast to allow sufficient radiation from the antennas to the mobile station as illustrated on Figure 5.32. As for the MS, we placed the pre-amplifiers just below the receiving antennas and 10 m low loss cables feed the USRPs. The BS includes the two USRP cards, the amplifiers, the control PC, the rubidium clock and the clock dispenser as explained Chapter 4.

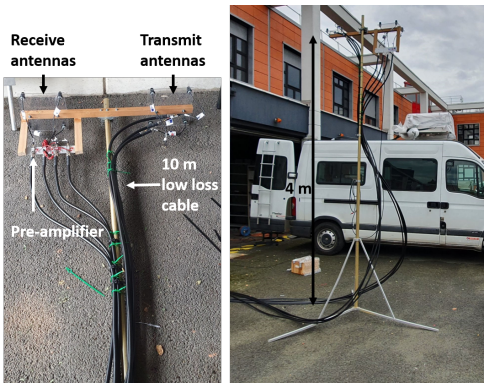

Figure 5.32: Antennas position on the base station

The equipment at BS and MS sides is shown in Figure 5.33.

Figure 5.33: Base station in one laboratory truck and mobile station in the second laboratory truck

To allow the initial synchronization of the base station with the mobile station, the two parts of the sounder should be positioned not far from each other. As explained in Chapter 4, synchronization takes place in two steps. The first step allows a rough synchronization of the PPS signals by rubidium clocks. This step requires to connect an oscilloscope to the base station and the mobile station rubidium clocks. We have to use a cable from both sides of the oscilloscope making sure we have the same length of cable at the BS and the MS to avoid greater or lower delay of the PPS signal that distorts the synchronization of PPS signals.

Figure 5.34 shows the layout of the equipment for the MIMO 2x2 and MIMO 4x4 architecture respectively as described previously for the outdoor measurements.

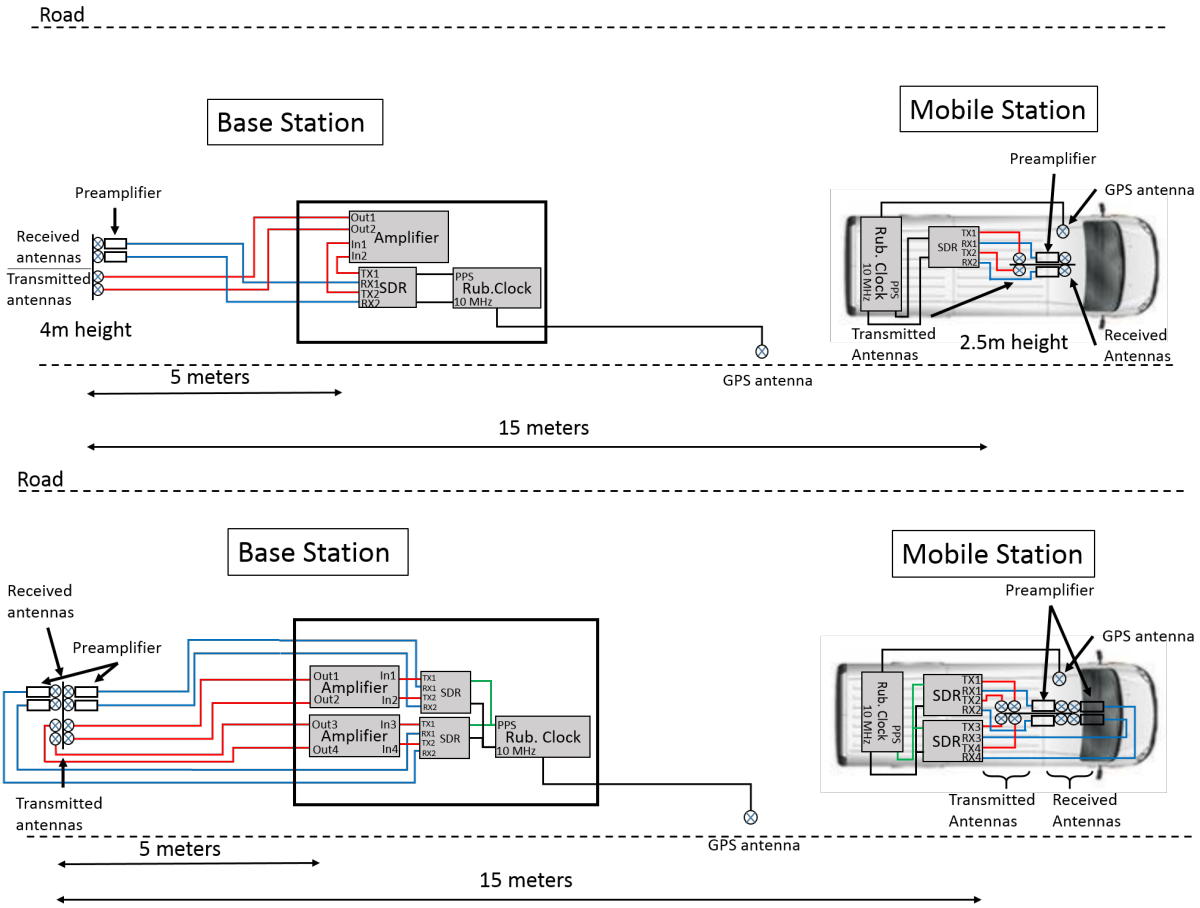

Figure 5.34: Schematic overview of the channel sounder for MIMO 2x2 and MIMO 4x4

5.3.3 Outdoor measurements results

5.3.3.1 Calibration

In this measurement configuration, the calibration should be done with the amplifiers and pre-amplifiers, and all cables used during measurement, which includes the 10 m long cables and 1 m long cables. We measured each link of the MIMO matrix individually as presented Figure 5.35 for the link 11 and 12 respectively. A 90 dB attenuator is placed before each pre-amplifier to protect them. As for indoor calibration for 2x2 and 4x4 MIMO antennas, there are respectively 4 and 16 links to calibrate. When all links of the MIMO matrix are measured individually, the calibrated matrix is built in post-processing. The additional attenuation (-90 dB) should be removed at the end in the processed files.

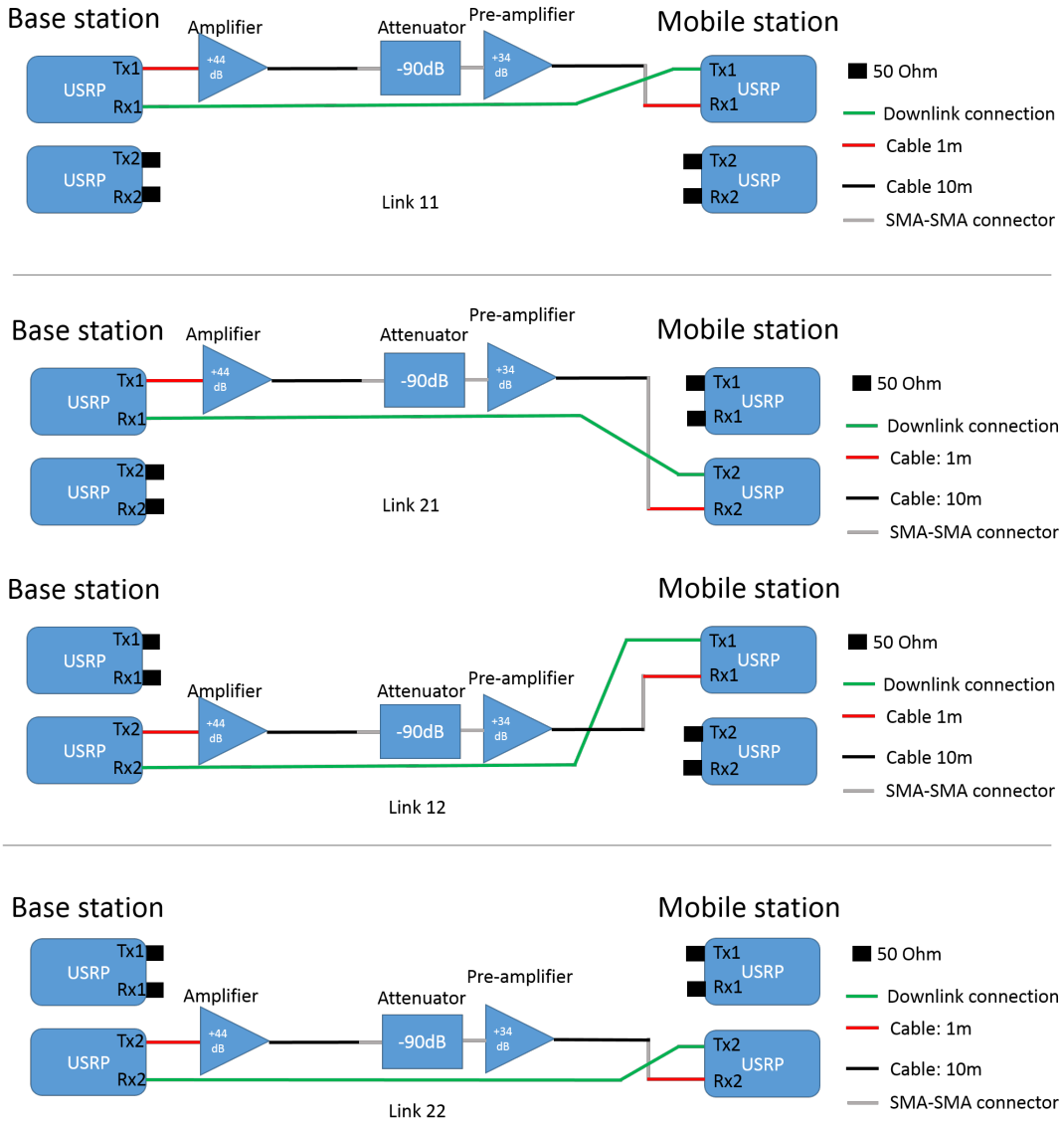

Figure 5.35: Calibration measurement for MIMO links

5.3.3.2 Results analysis and channel parameters

From the measured data we can extract the CFRs, CIRs, PL and PDP. The results for the scenarios at 6 km/h and 20 km/h for MIMO 2x2 configuration are presented for each link of the MIMO channel matrix. Due to the low speed, we record a very large number of CFRs for each measurement, thus, we decided to keep only 1 over 10 CFRs in each recorded file, which gives a sampling distance of 12 cm at 6 km/h and 40 cm at 20 km/h (λ at 3.5 GHz is equal to 8.6 cm).

5.3.3.3 Results for the LOS scenario at 6 km/h

Here we present results based on 6 km/h speed for outdoor scenarios with a MIMO 2x2 configuration. The CFRs and CIRs corresponding to the first (15 m) and last positions (145 m) of the recorded estimated symbol are presented respectively in red and blue. Then, the measured path loss model (red), is compared with the theoretical free space path loss (green). Finally, we present the PDP to extract some channel parameters.

Figure 5.36 present the CFRs at 15 m and 145 m received on each MIMO link. We can observe different behavior on each link. particularly far from the BS. frequency selectivity appears particularly on link 12, 21 and 22. It is very different from the indoor channel measured.

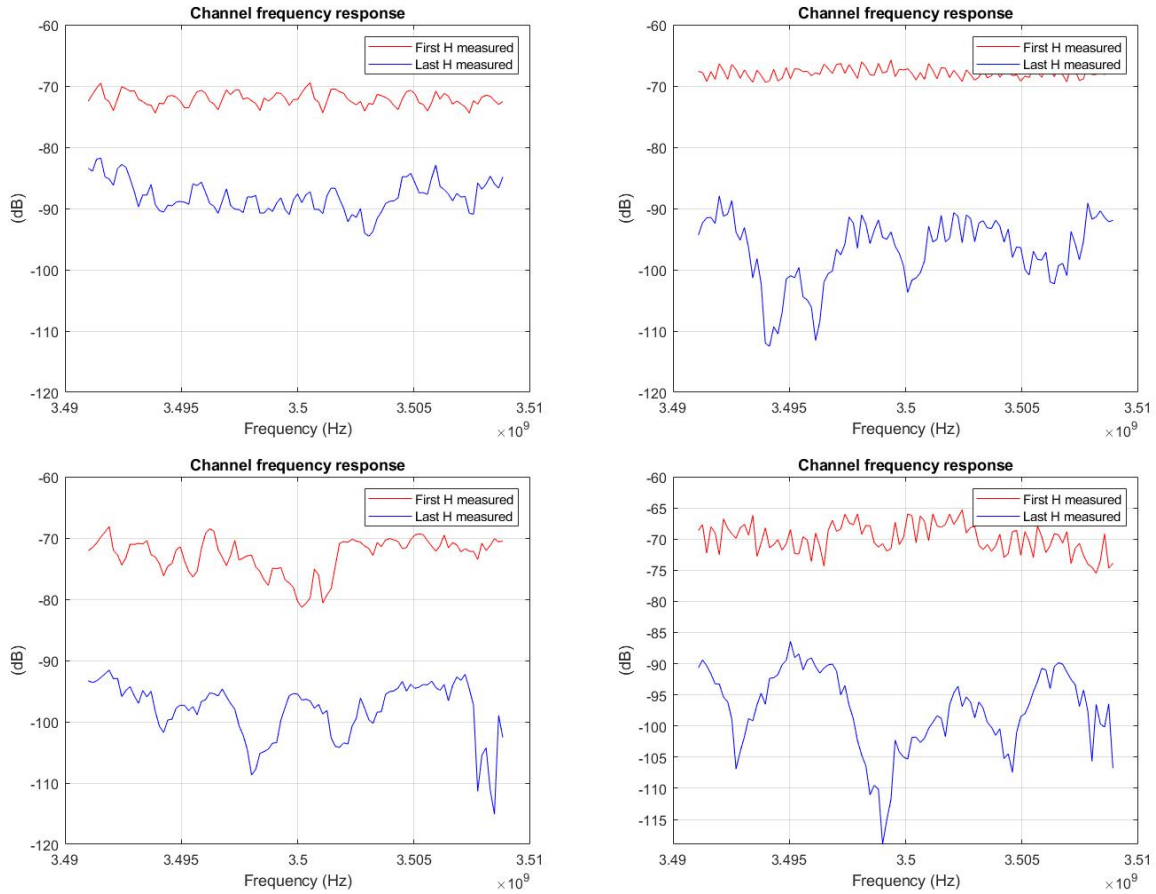

Figure 5.36: Channel frequency responses for each MIMO link from 11 to 22 from left to right

Figure 5.37 present the corresponding CIRs for each MIMO link. We can compute the equivalent distance between the maximal amplitude at the first position (15 m) and the one at last position (145 m). For example, for the MIMO link 11, the delay corresponding to the maximal value of the CIR in red is equal to 47.13 ns and in blue to 501.40 ns. The difference equals to 454.27 ns is equivalent to a propagation distance of 136.19 meters. For the other links we obtain for link 12, 21 and 22 : 133.26 m, 138.92 m and 129.44 m. The error due to the sampling rate is 16.49 meters (+/-55 ns). The values are coherent with the measuring distance.

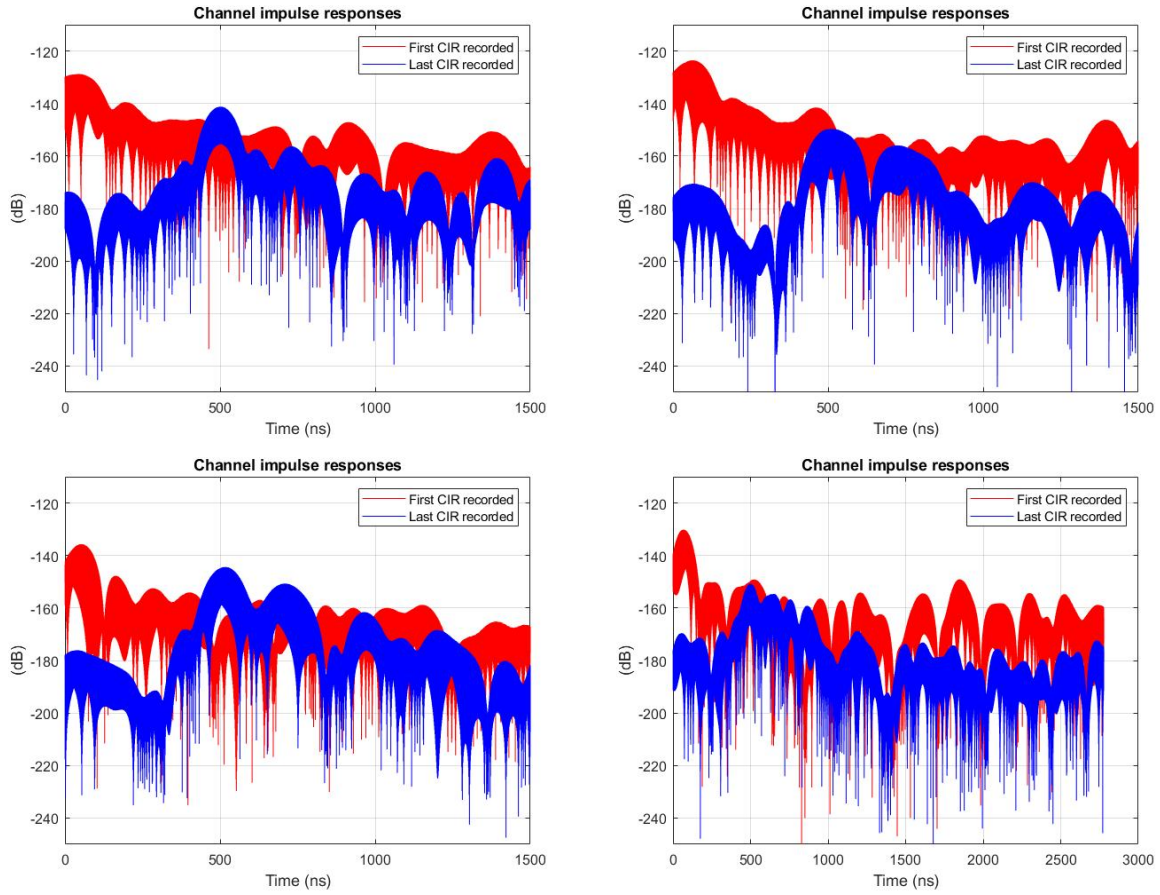

Figure 5.37: Channel impulse responses for each MIMO link from 11 to 22 from left to right

Then we present the path loss for each MIMO link on Figure 5.38 with measurements in blue, the model in red and the free space path loss in green.

The average PL for the MIMO matrix is presented Figure 5.39. The standard deviation of the slow fadings is equal to 3.74 dB.

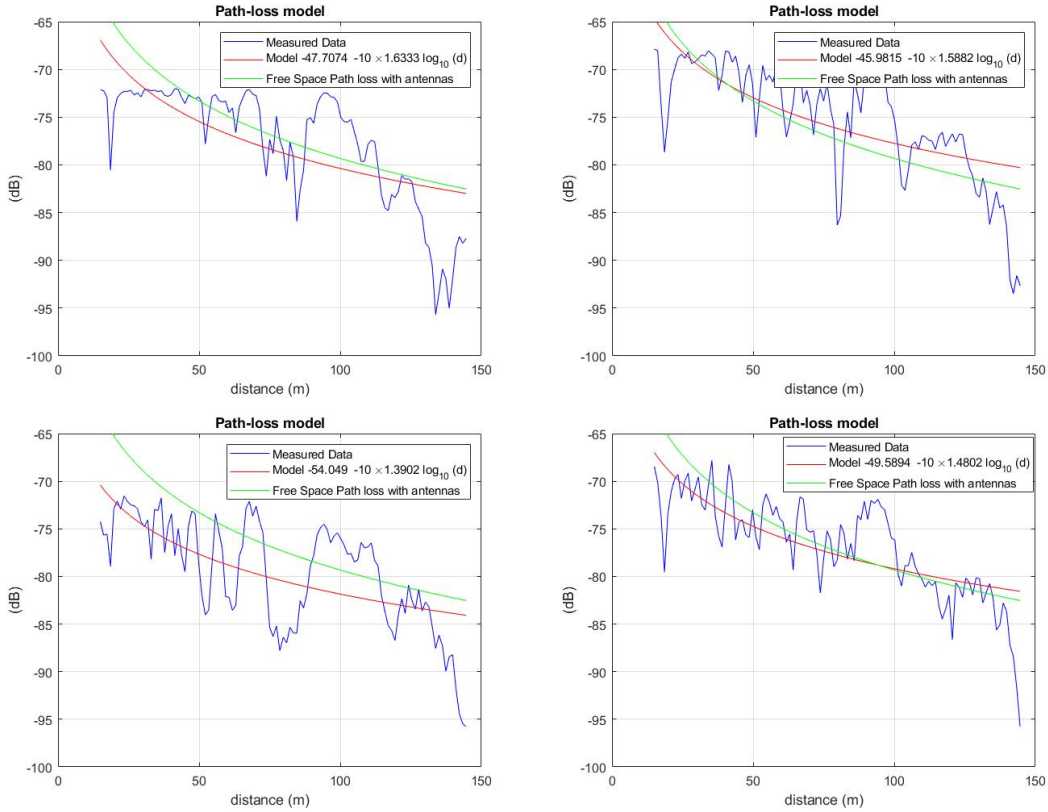

Figure 5.38: Path loss model for LOS scenario at 6 km/h for each MIMO link

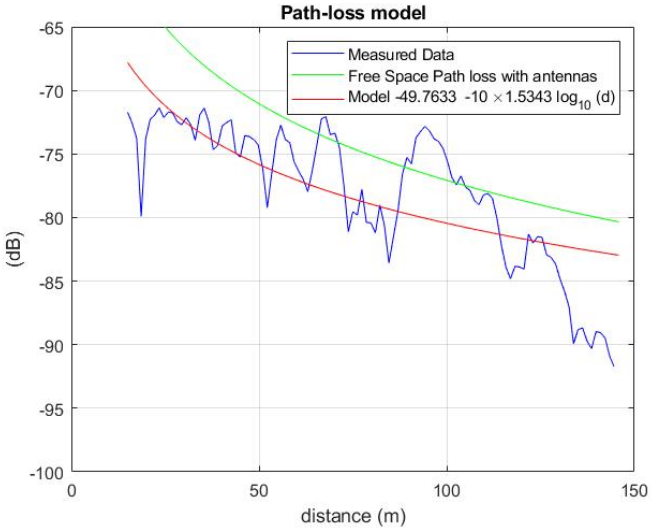

Figure 5.39: Path loss model for LOS scenario at 6 km/h

We can observe on Figure 5.39 an effect of saturation on the measured PL at the beginning of the travel. With the amplification stage, the output power os equal to +44 dB and we add +2 dB for antenna gain. Then, from the calculated received power in free space, the system is in saturation from 0 to 35 meters from the BS as shown Figure 5.40. Unfortunately, this saturation was not visible in real time during the measurement campaign on the GUI. For future evolution

of the system, an appropriate automatic gain control could be added in addition to a real time record of the gain variation on each symbol estimation during measurements.

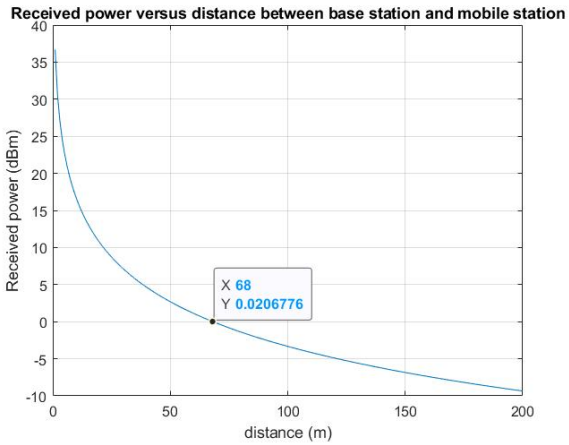

Figure 5.40: Received power at the mobile station

From the CIRs, after alignment in time of all the maximal amplitude value of the CIRs to 0 s, we compute the PDP on the MIMO matrix as the average of the individual PDP. The result is presented Figure 5.41.

We summarise the channel parameters in Table 5.5 for a threshold of -20, -30 and -40 dB relative to the maximal value of the PDP, presented Figure 5.41. The mean delay $\hat{\tau}$ varies from 1.39 μs to 1.42 μs. The maximal delay varies between 0.171 μs to 2.78 μs. The RMS delay spread σ_τ varies from 795 ns to 800 ns. For a threshold equals to -30 dB, the multipath components can arrive in a 2.25 μs window. In addition, the ratio of the RMS delay spread and the symbol time duration (71.43 μs) quantifies the strength of the Inter Symbol Interference (ISI). From our results, the maximal RMS delay spread is greater than 80 times the symbol duration. We can conclude that there is no ISI.

The coherence bandwidth calculated as previously, for a correlation coefficient of 0.5, is equal to 200 kHz, which means that frequency selectivity is present in the channel.

Delays	Threshold (dB)			
	-20	-30	-40	Without
Mean delay (μs)	1.39	1.40	1.41	1.42
Maximal Delay (μs)	0.171	2.25	2.78	2.78
RMS Delay spread (ns)	800	798	795	795
Coherence Bandwidth (MHz)(c=0.5)	0.199	0.199	0.200	0.200

Table 5.4: Characteristics of the channel for 6 km/h LOS scenario

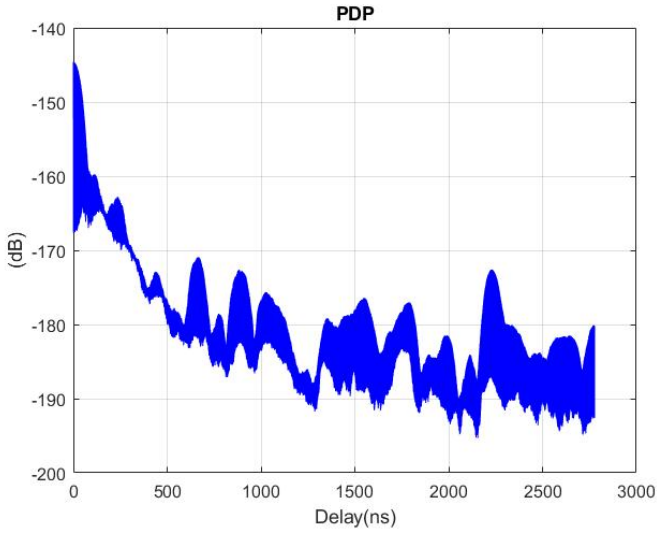

Figure 5.41: PDP model for MIMO matrix at 6 km/h

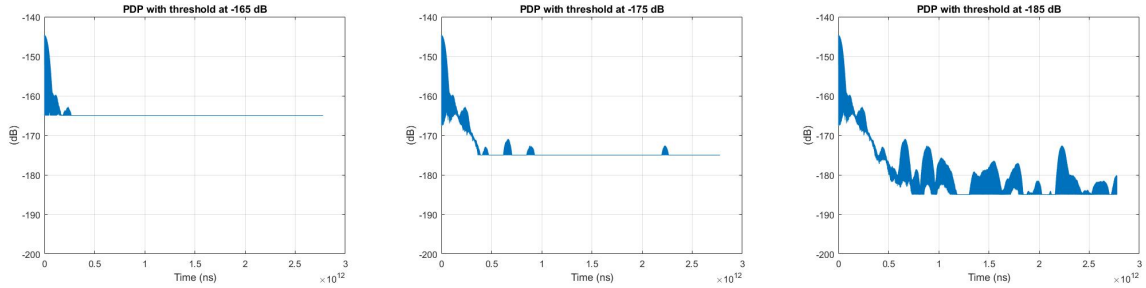

Figure 5.42: PDP with a threshold of -20, -30 and -40 dB of the maximum, from left to right respectively at 6km/h

5.3.3.4 Results for scenario at 20 km/h

Here we present results at 20 km/h for outdoor scenario with a MIMO 2x2 configuration. We present the CFRs and CIRs at 30 m (red) and 145 m (blue) from the BS. Then, the measured path loss model, in red, is presented and compared with the theoretical free space path loss, in green. Finally, we present the PDP and we calculate the channel parameters.

Figure 5.43 presents the CFRs at 30 m (red) and 145 m (blue) from the BS for each MIMO link. We can observe a difference with the curves at 6 km/h. The frequency selectivity seems lower. From MIMO link 11, 12, 21 and 22 we calculate a mean power difference equal to 10.11 dB,

13.34 dB, 9.84 dB and 11.56 dB respectively. We deduce that the power of the CFRs between each MIMO link is around 4 dB illustrating space diversity between the links.

The corresponding CIRs are presented in Figure 5.44 for each MIMO link.

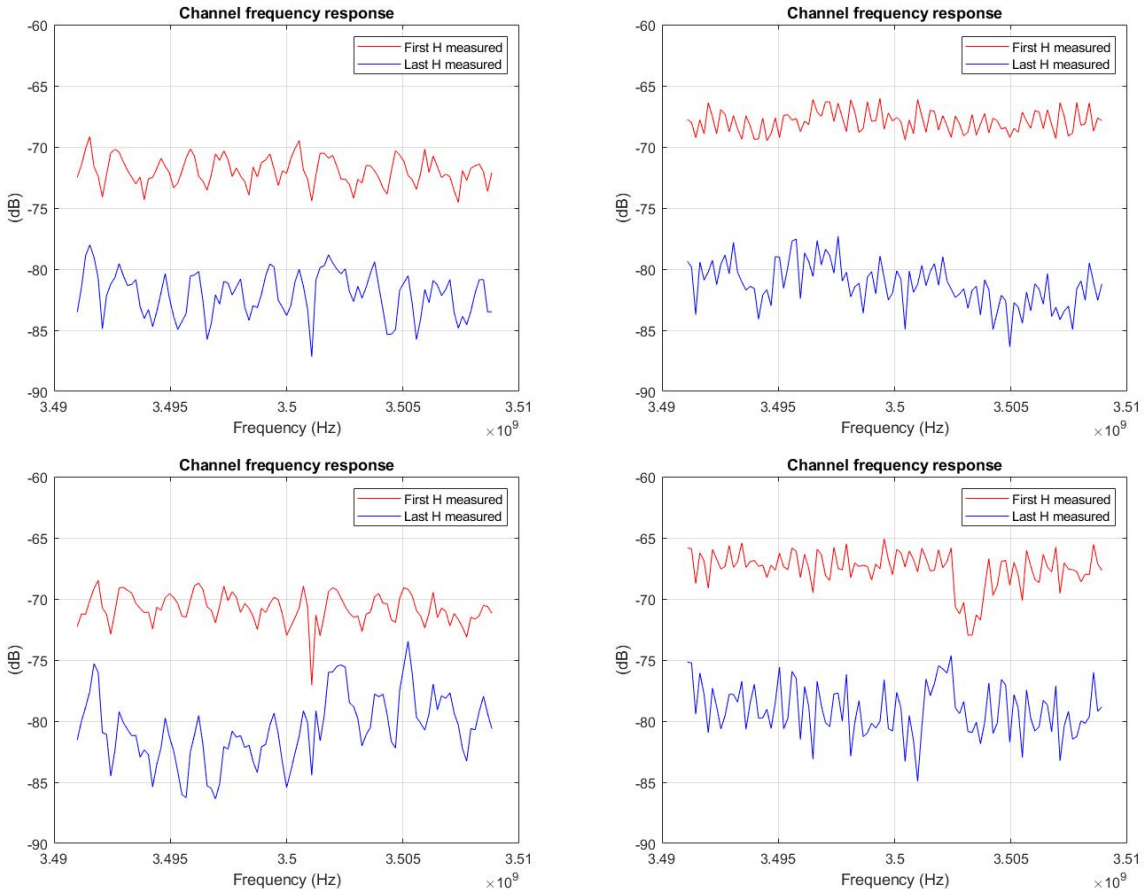

Figure 5.43: Channel frequency responses for each MIMO link from 11 to 22 from left to right

The shift from the first LOS path component observed and the last LOS path component in Figure 5.44, corresponds to the time propagation from the first and last recorded estimated symbol. We deduce the propagation distance for MIMO link 11, 12, 21 and 22 respectively: 115.76 m, 113.13 m, 108.00 m, 114.67 m. The values obtained are closed to 115 m. Due to the time needed to reach 20 km/h, the acquisition distance is 20 meters less than at 6 km/h (135 m). The values obtained on each link are coherent with the effective distance for measurements.

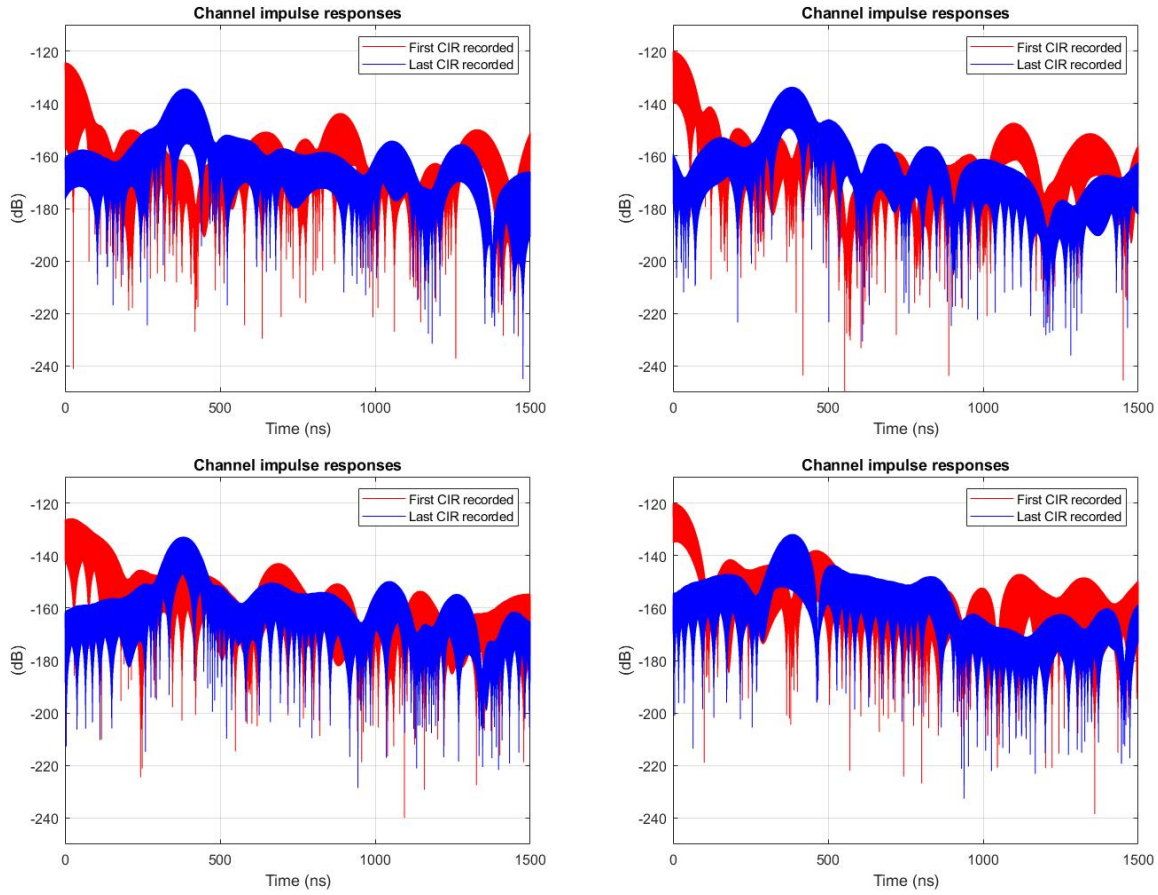

Figure 5.44: Channel impulse responses for each MIMO link from 11 to 22 from left to right

The path loss for each MIMO link are given on Figure 5.45 (measurements in blue and model in red) and compared to free space path loss (green). We notice a good match between measured model and theoretical free space PL curve. We can observed a variation of the path loss exponent on each link between 0.96 to 1.61.

Figure 5.46 shows the average PL for the MIMO matrix. The standard deviation of slow fadings is equal to 2.51 dB.

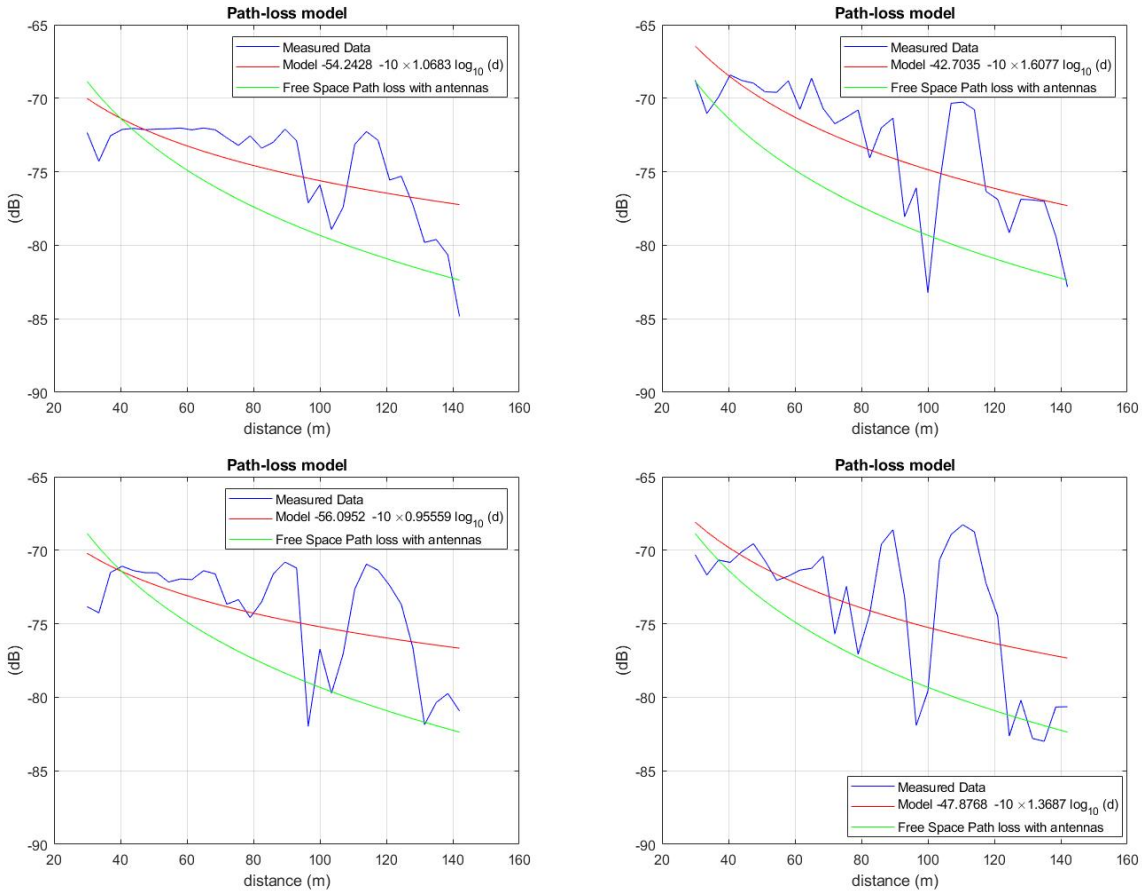

Figure 5.45: Path loss model for each MIMO link from 11 to 22 from left to right at 20 km/h

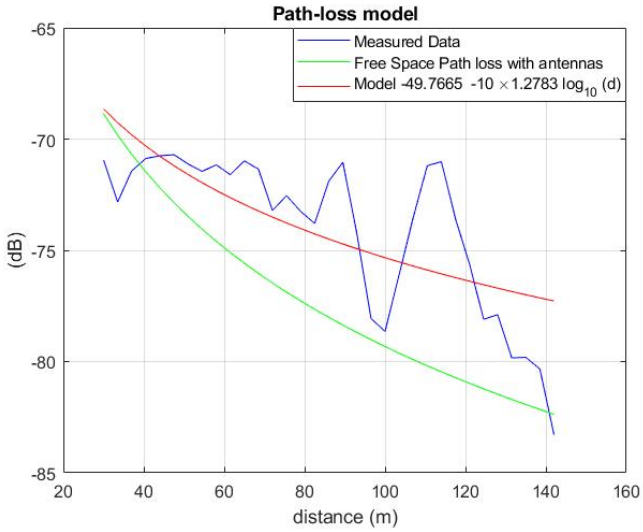

Figure 5.46: Path loss model for the MIMO matrix at 20 km/h

On Figure 5.46 we notice again a saturation effect as for the measurements at 6 km/h. From the CIRs, we calculate the PDP of the MIMO matrix shown in Figure 5.55.

Delays	Threshold (dB)			
	-20	-30	-40	Without
Mean delay (μs)	1.39	1.40	1.41	1.41
Maximal Delay (μs)	0.268	2.26	2.78	2.78
RMS Delay spread (ns)	800	797	794	794
Coherence Bandwidth (MHz)(c=0.5)	0.199	0.199	0.200	0.200

Table 5.5: Characteristics of the channel for 20 km/h LOS scenario

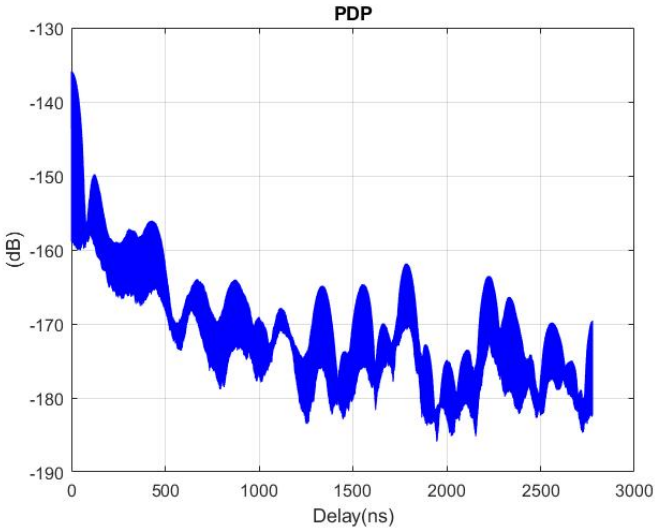

Figure 5.47: PDP for MIMO matrix at 20 km/h

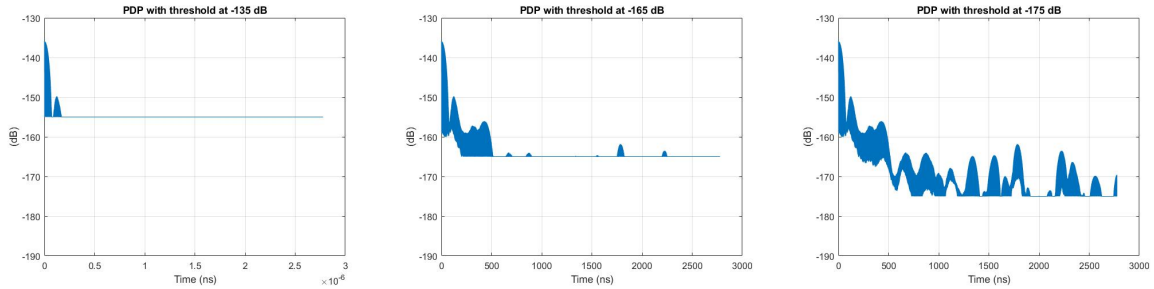

Figure 5.48: PDP with a threshold of -20, -30 and -40 dB of the maximum, from left to right respectively at 20 km/h

From the PDP we can calculate the average delay, $\hat{\tau}$ and RMS delay spread, σ_τ using the formula 4.18 and 4.17 respectively. We summarise the channel parameters in Table 5.5 for a threshold of -20, -30 and -40 dB based on the maximal value of the PDP, and presented Figure 5.56. The mean delay varies from 1.39 to 1.41 μs. The maximal delay varies from 0.268 to 2.78 μs. The RMS delay spread varies from 794 to 800 ns. The values are close to those calculated at 6 km/h. The speed effect is not visible except on the maximal delay spread. The coherence bandwidth of the channel is still equal to 200 kHz, which means frequency selectivity is also present despite it is not really visible on the CFRs.

The ratio between the RMS delay spread and the symbol time duration is equal to 71.43 μs, corresponding to 90 times the duration of the symbol. We can conclude that there are no ISI.

5.3.3.5 Results for scenario around buildings at 6 km/h

Here we present results for the NLOS scenario with a speed equal to 6 km/h in MIMO 2x2 configuration. The scenario starts at 15 m from the BS as in the LOS scenario, then the MS turns around the buildings in the NLOS scenario (the NLOS scenario starts around 150 m) and come back to the BS with LOS during 100 m. Unfortunately, we observe data losses during the measurements that avoid to present all the results. We present Figure 5.49 the CFRs and CIRs with the first, in red, and last, in blue, recorded estimated symbol. The curves in green correspond to the recorded symbol at the end of the LOS scenario (150 m). We present also the PL calculated on MIMO link 11.

First, from the CFR, we verify that the first and last measured CIR have the same mean power (we start at 15 meters from the BS and we stop the acquisition approximately at 15 meters of the BS also). The mean power of the CFRs for MIMO link 11 is equal to -72.12 and -72.04 dBm for the first and last measured CFR respectively. From the CIRs, we observed that the first and last LOS peak have a power of -128.4 dBm and -131.1 dBm. From the PL curve given for MIMO link 11, we visualize easily the power shape corresponding to the scenario. First, the power decreases during the first half of the measurement campaign, and then the power increases when the MS is going towards the BS in the second half of the measurement campaign. The effect of the NLOS due to buildings is well highlighted in the PL curve.

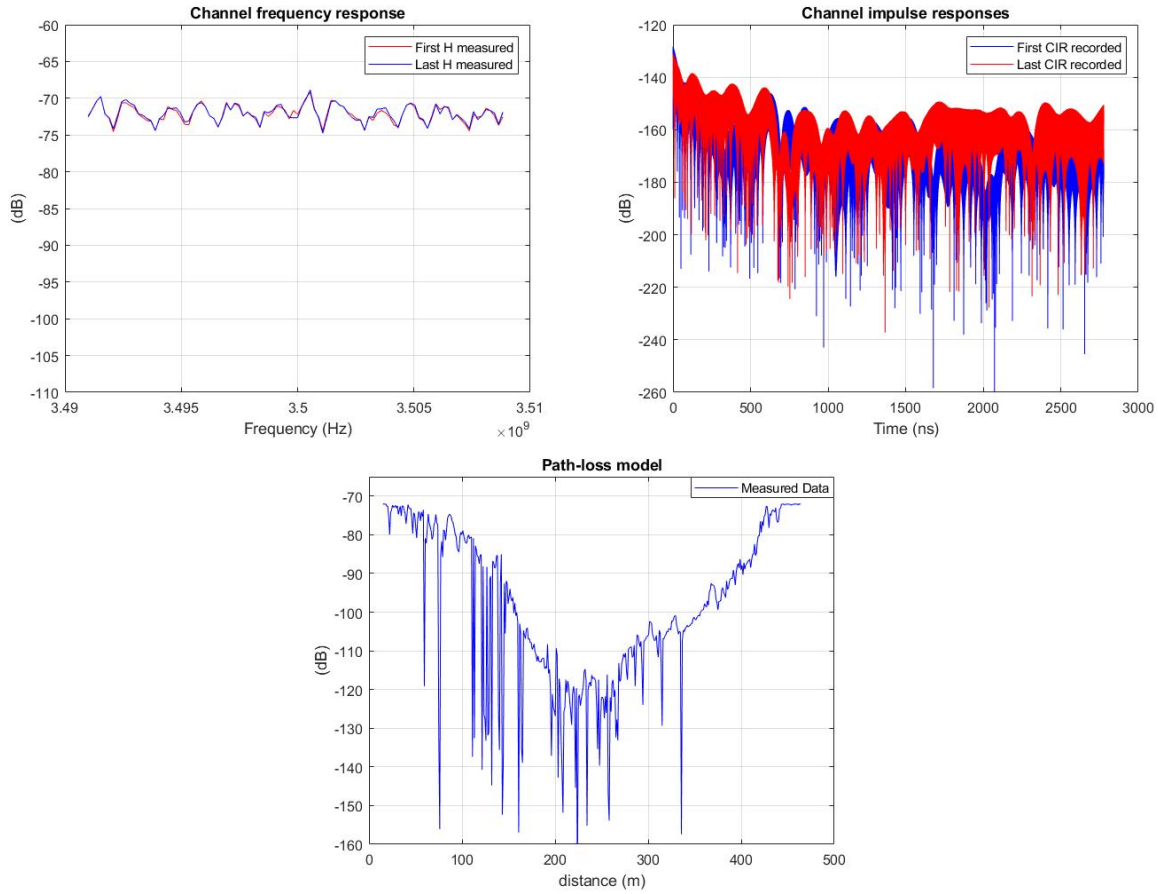

Figure 5.49: CFR and CIR for the MIMO link 11 on left and right respectively

In Figure 5.50 the MIMO link 22 path loss is presented for the second part of the scenario (from 150 m to the end of the measurements close to the BS. We observe the numerous loss of

information and the mask effect of the building. An automatic gain control (AGC) can be used in this situation to prevent the loss data.

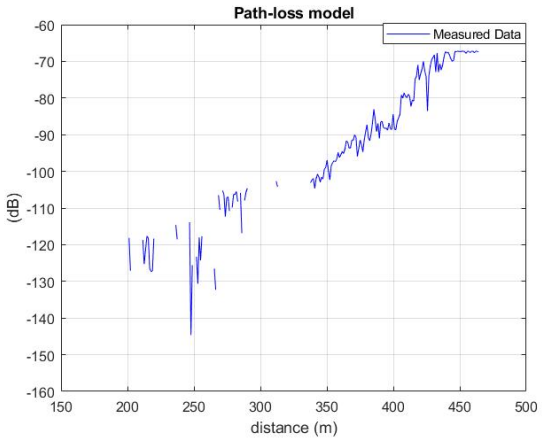

Figure 5.50: PL of the MIMO link 22

5.3.3.6 Results for 2x2 MIMO LOS scenario at 20 km/h without pre-amplifications at receiver

Here we present a new 2x2 MIMO measurements campaign for which we avoided the power saturation. We removed the pre-amplifiers and we kept the 44 dB amplifiers at BS and MS. The output power is +29 dBm. From the MS and BS, the received signal is well detected and stable during the measurements. The calibration was also changed. We present here after the results.

We start by extracting the first and last CFRs and the first and last CIRs of each MIMO link in Figure 5.51 and 5.52 respectively. We can observe that the fadings are more important far from the BS. But we still have space diversity between links due to the difference observed between the CFRs of each link for a same acquisition distance.

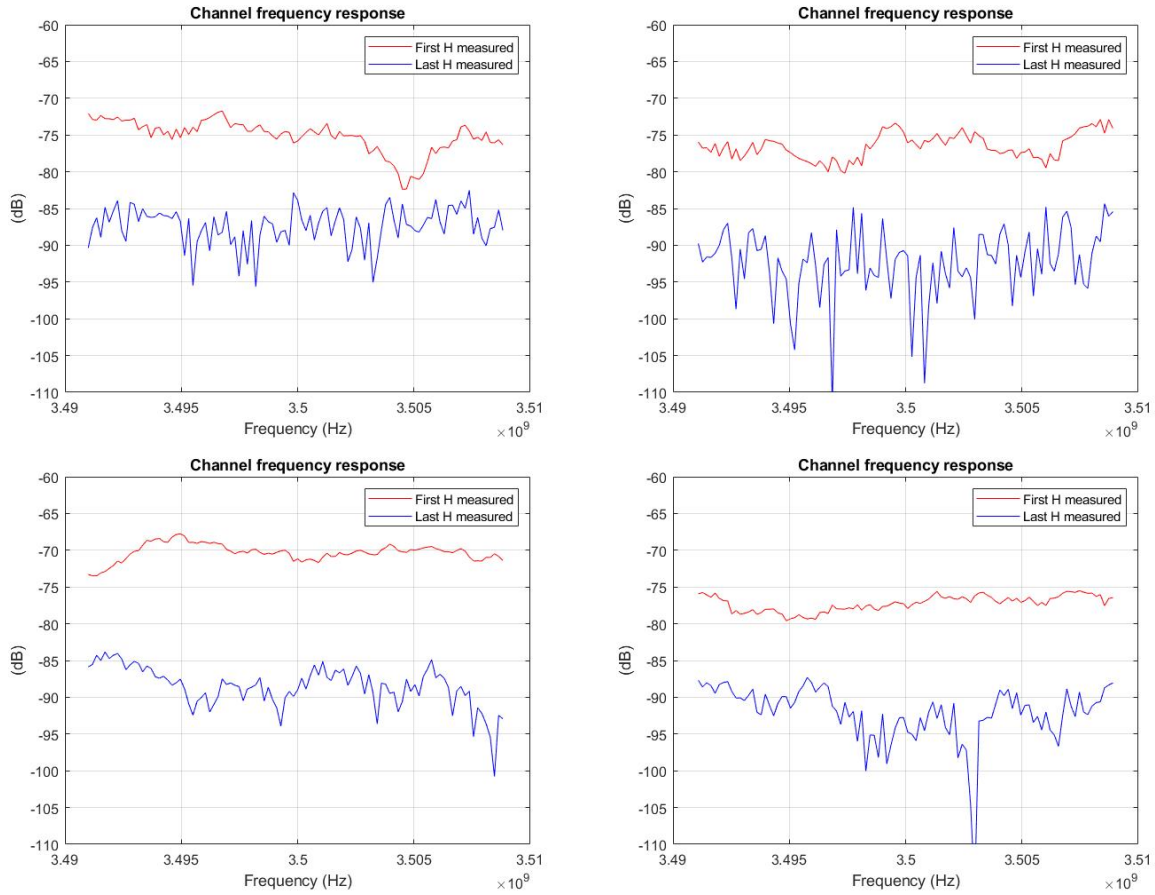

Figure 5.51: Channel frequency responses for each MIMO link from 11 to 22 from left to right

As previously, we can calculate the propagation time between the first LOS path component recorded and the last LOS path recorded, corresponding to the first and last recorded symbol respectively, in Figure 5.52. We deduce the propagation distance for MIMO link 11, 12, 21 and 22 respectively: 108.4 m, 109 m, 105 m, 107 m. The values obtained on each link are coherent with the effective distance for this measurements scenario.

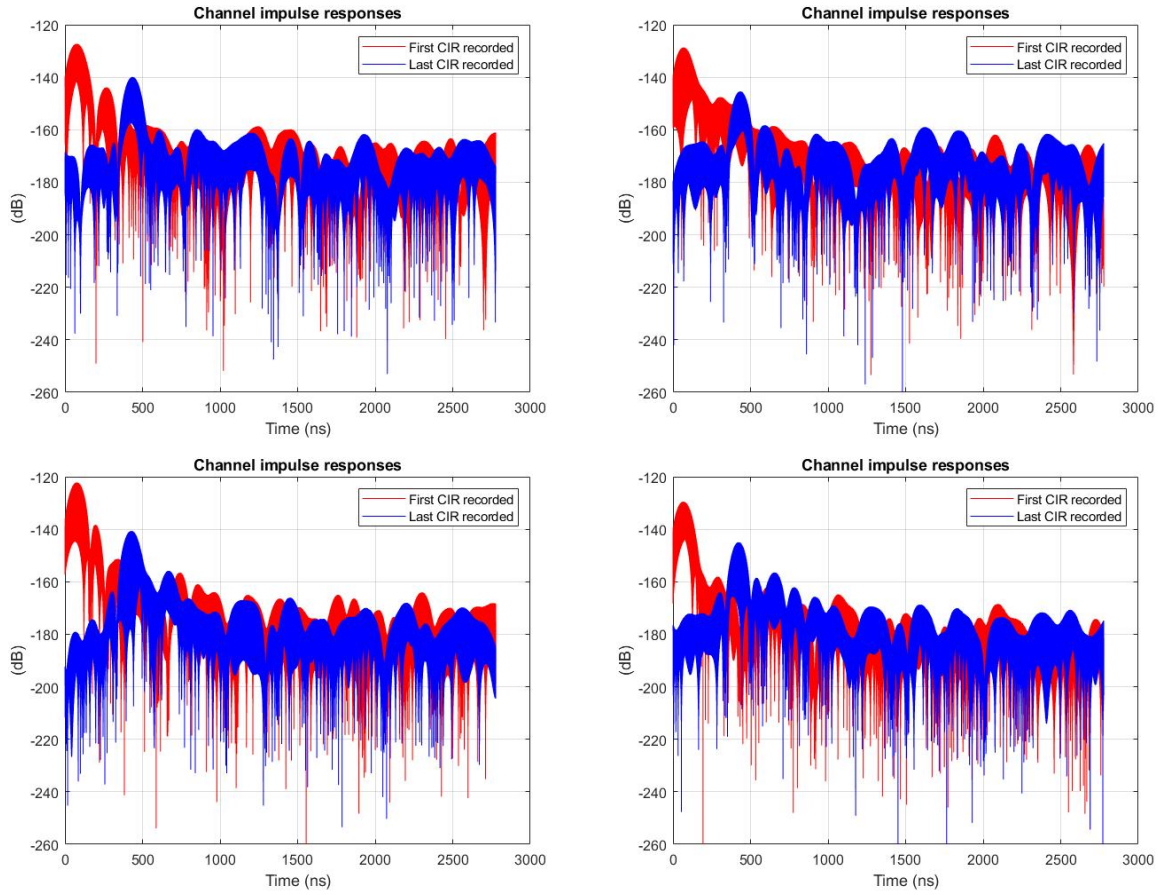

Figure 5.52: Channel impulse responses for each MIMO link from 11 to 22 from left to right

PLs models are presented for each MIMO link and given Figure 5.53. The measurements PL is shown in blue and its corresponding model in red. Results are compared to the free space path loss in green. We notice a good match between measured model and theoretical free space PL curve with a maximal difference lower than 10 dB. Figure 5.54 shows the average PL for the MIMO matrix. The standard deviation of slow fadings is equal to 3.05 dB and the corresponding PL model is presented equation 5.6.

$$PL(d) = -41.62 - 10 \times 2.08 log_{10}(d) \tag{5.6}$$

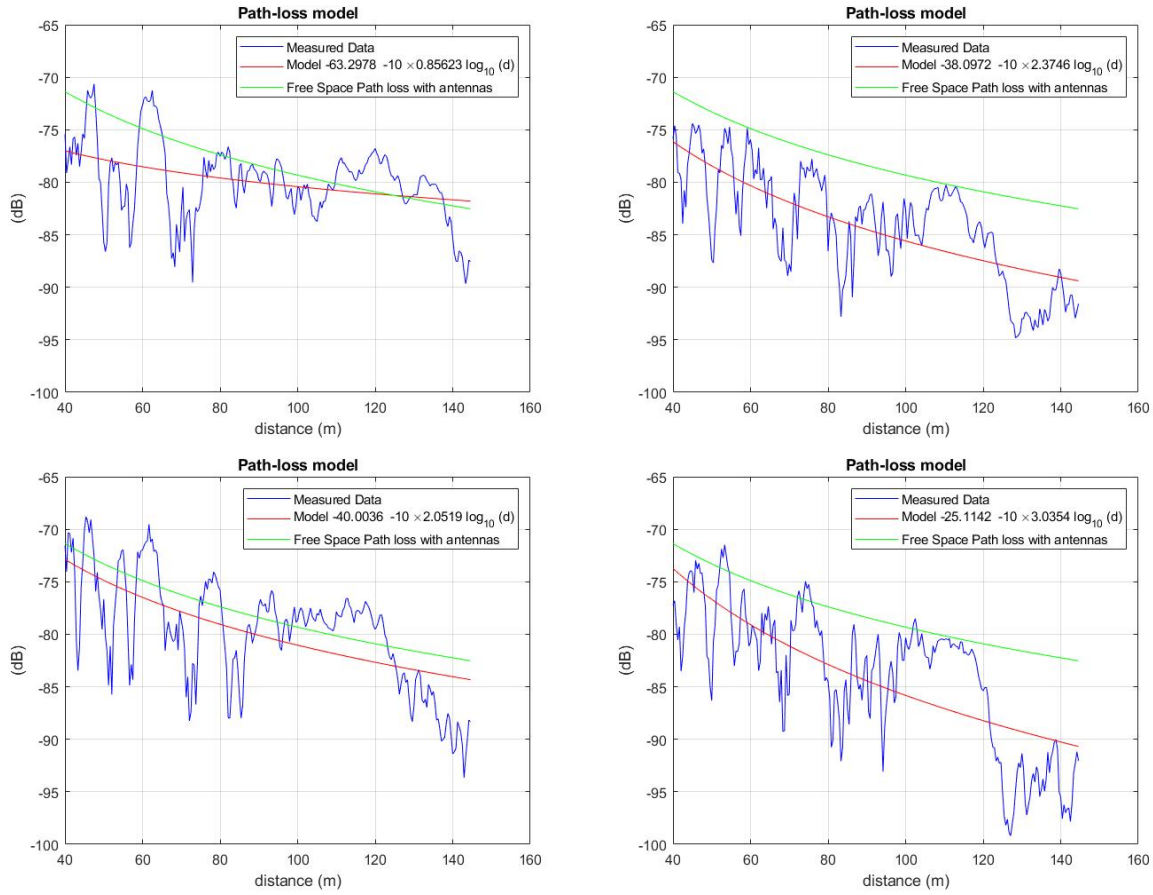

Figure 5.53: Path Loss for each MIMO link from 11 to 22 from left to right

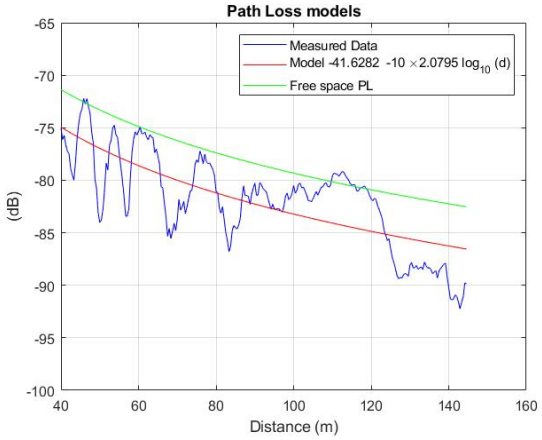

Figure 5.54: Path loss of the channel MIMO matrix compared with the free space path loss

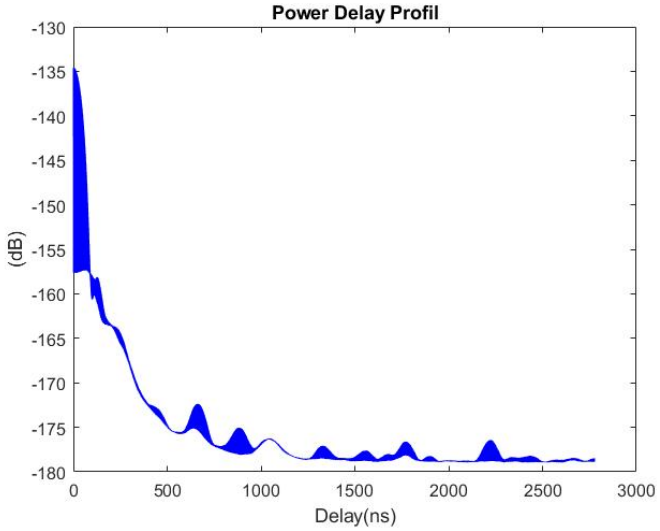

Figure 5.55: PDP for MIMO matrix at 20 km/h

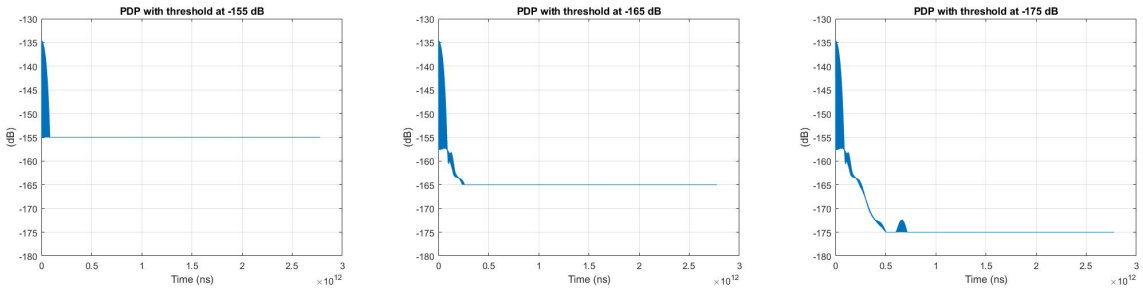

Figure 5.56: PDP with a threshold of -20, -30 and -40 dB of the maximum, from left to right respectively at 20 km/h

From the CFRs, we can calculate the Frequency Doppler spread. First of all, we cut the global recorded file into sub-files. Each sub-file represents a recorded time of 71 ms for a total record of 18 s. We obtain for this scenario at 20 km/h, 252 sub-files filled with 1000 CFRs. To calculate the Frequency Doppler spread, we apply the FFT along time on each sub-file. We have at the end, the representation of the Frequency Doppler spread in time and frequency. We represent here only the positive frequency of the Doppler shift.

The theoretical frequency shift of a moving receiver with a static transmitter is +/-65 Hz at 20 km/h. We can observe, from Figure 5.57, the frequency Doppler spread of each MIMO link and Figure 5.58 the frequency Doppler spread of the MIMO matrix (average of the four MIMO link). We observe a shift at 70 Hz corresponding to the LOS. The Doppler shift measured corresponds to 21.5 km/h speed, which is coherent with the scenario. We remind that the recording begins when the speed of 20 km/h is reached and the stop of the recording is done before the deceleration.

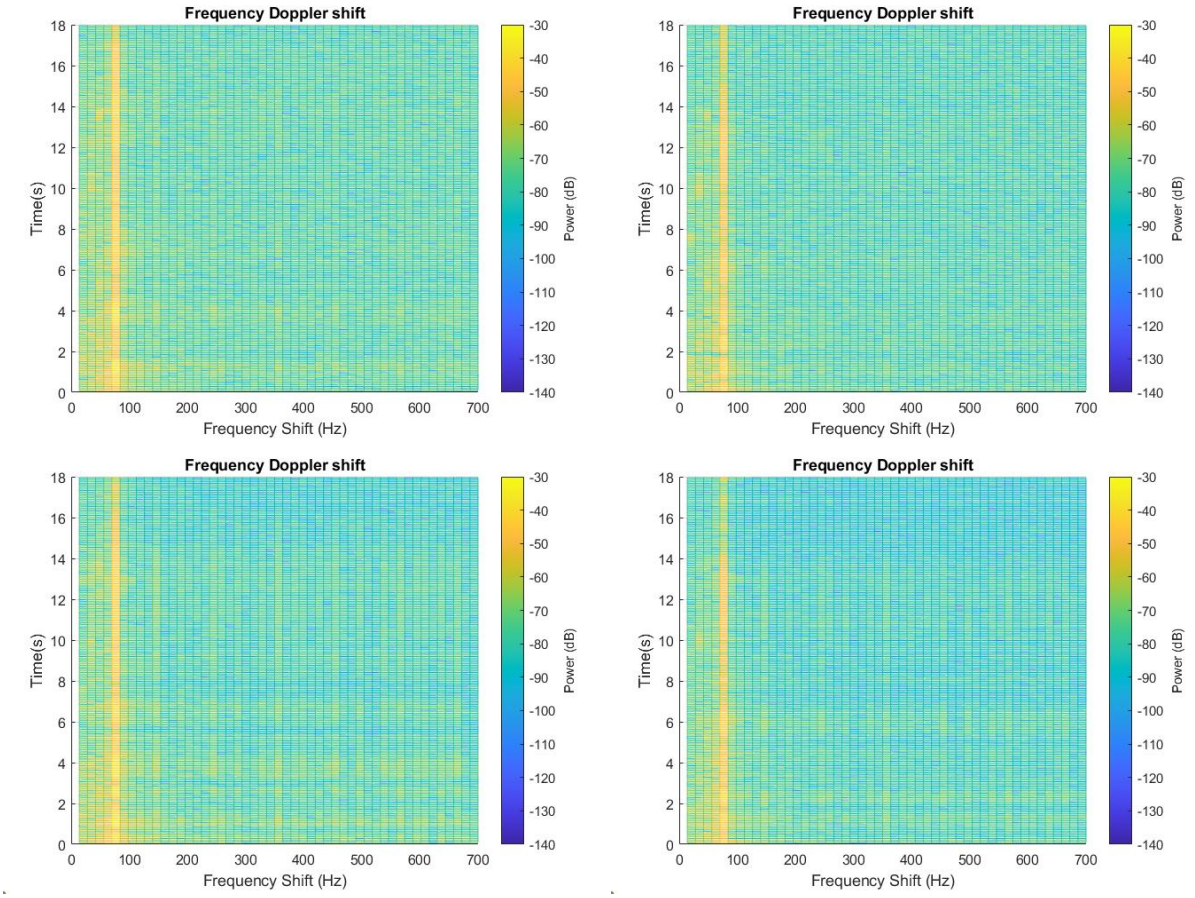

Figure 5.57: Frequency Doppler spread for each MIMO link, from left to right respectively at 20 km/h

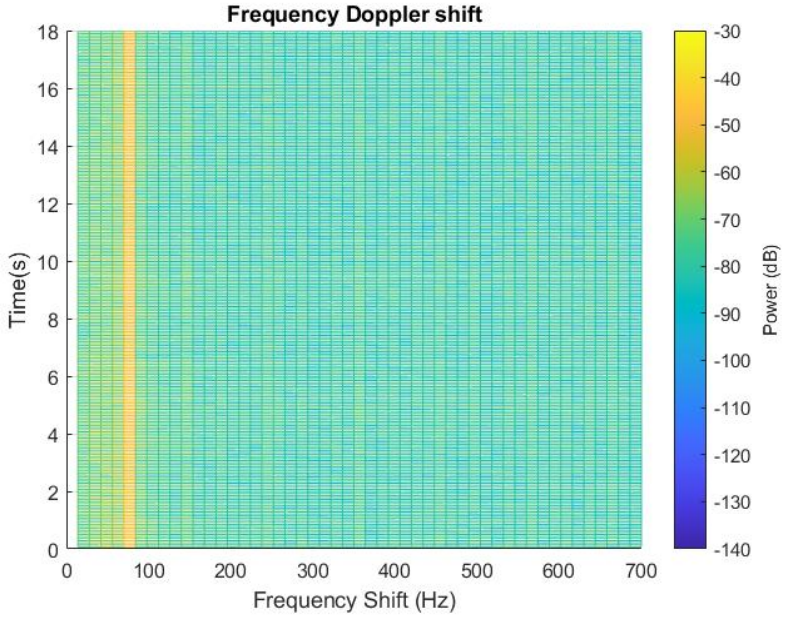

Figure 5.58: Frequency Doppler spread of the MIMO matrix at 20 km/h

5.3.3.7 Outdoor scenarios summary

From LOS scenario, we were able to extract the CFRs recorded during the channel sounding and to calculate the CIRs, PL and PDP. We saw that the path loss measured is close to the free space one. The propagation time between the first estimated symbol and the last estimated symbol corresponds to the measurements distance for the acquisition. Then, we were able to extract the PDP of the MIMO matrix to calculate the average delay and the RMS delay spread depending of the threshold chosen. We summarize all the extracted parameters in Table 5.7. Finally, we highlighted that the developed channel sounder is working correctly. LOS and NLOS scenarios can be considered with a better mentioning of the system and particularly the addition of AGC. We finished this part with a new 2x2 MIMO acquisition at 20 km/h, without using pre-amplifiers to avoid the saturation of the system. We extract all the previous characteristics of the channel and we added the extraction of the frequency Doppler spread, which lead to a new validation of the channel sounder with an estimation of the MS mobility of 21.5 km/h. In its present configuration, the SDR-based channel sounder is limited to the 20 MHz band of the LTE signal. Only 18 MHz is effective in the *MIMO framework* software used. This restricts the minimal observable delay to 55 ns. Nevertheless, the USRP considered allow a 160 MHz band. An evolution of the channel sounder could be to modify the system by increasing the subcarriers spacing in order to be able to operate on a larger bandwidth to allow the observation of minimal delay equals to 6.25 ns. This configuration would allow measurements in metro tunnels.

Scenario	**6 km/h LOS**				**20 km/h LOS**			
Path loss model	$-49.76 - 10 \times 1.53 log_{10}(d)$				$-49.76 - 10 \times 1.28 log_{10}(d)$			
Std (dB)	3.74				2.51			
Delays	Threshold (dB)				Threshold (dB)			
	-20	-30	-40	Without	-20	-30	-40	Without
Mean delay (μs)	1.39	1.40	1.41	1.42	1.39	1.40	1.41	1.41
Maximal Delay (μs)	0.171	2.25	2.78	2.78	0.268	2.26	2.78	2.78
RMS delay spread (ns)	800	798	795	795	800	797	794	794
Coherence Bandwidth (MHz)(c=0.5)	0.199	0.199	0.200	0.200	0.199	0.199	0.200	0.200

Table 5.6: Channel characteristics for LOS scenario at 6 and 20 km/h

Scenario	**2x2 MIMO 20 km/h LOS without amplification at receiver sides**			
Path loss model	$-41.62 - 10 \times 2.08 log_{10}(d)$			
Std (dB)	3.05			
Delays	Threshold (dB)			
	-20	-30	-40	Without
Mean delay (μs)	1.39	1.40	1.40	1.41
Maximal Delay (μs)	0.085	0.26	0.715	2.78
RMS delay spread (ns)	800	798	795	794
Coherence Bandwidth (MHz)(c=0.5)	0.199	0.199	0.200	0.200

Table 5.7: Channel characteristics for the 2x2 MIMO LOS scenario at 20 km/h without amplification at receiver sides

5.4 Conclusion

In this chapter, we have used the developed channel sounder for different scenarios in indoor and outdoor environments. We saw that even with some constraints related to amplification and rubidium clocks, the SDR-Based channel sounder is fully operational and allows good channel characterisation. We are able to extract of the CFRs, CIRs, path loss and PDP to extract

the channel parameters. The channel sounder has been validated at low speed and up to 20 km/h. We solve different problems during the outdoor measurements such as the impact of the amplifiers, which can corrupt the GPS signal and transmitted excitation signal. It is why we decided to remove the amplifiers from the mobile station. The synchronization between base station and mobile station has to be done at 15 meters from each other to allow the base station to detect the mobile station signal.

The different outdoor scenarios showed that we are able to characterize the channel in different situations. The minimal observable delay is equal to 55 ns due to the effective bandwidth of 18 MHz. An evolution to consider the 160 MHz bandwidth available with the USRPs will offer much more scenarios possibilities with a minimal measurable delay equals to 6.25 ns. An other important evolution needed is the addition of an AGC stage in order to prevent the loss of data observed during NLOS situation when the MS is far for the BS.

General Conclusion and Perspectives

Main contributions of the thesis

In the automotive and rail domains, vehicles are entering the era of full automation thanks to wireless sensors and communication systems shifting control functions from the human driver to computers. High data rate, robustness, high reliability and ultra-low latency are required for the wireless communications in the context of autonomous train and safety critical applications. The Future Railway Mobile Communication System is under development at European level within International union of railways and the Joint Undertaking Shift2rail. It will answer all the current and future needs of rail and the shift from the vision of "network as an asset" to a more modern vision of "network as a service". It will be IP based, multi-bearer and resilient to technology evolution and interferences.

Today the test and validation of new wireless communication systems along railway tracks is long and expensive particularly when critical applications are concerned. A new approach called *zero on site testing* and the development of *digital testing methodologies* are key priorities for the Railway sector in order to drastically reduce time and money due to testing and validation procedures along the tracks, and to accelerate time to market.

This PhD work contributes to a larger research framework in which the aim is to develop hardware and software in the loop platforms for early testing and validation in laboratory of any type of wireless communication applications in the railway domains: train-to-ground, train-to-train and intra-train. These new platforms require to emulate, with a high level of representativeness, the radio access networks and the radio channels in the railway context.

The development of radio channel models able to reproduce with a high level of accuracy, the behaviour of railway radio environments, needs to characterize the railway radio channels with adequate radio channel sounder and to be able to model the data measured.

Considering these new demands of the railway domain, in this PhD we have presented the different steps for the development of a 5G sub 6 GHz MIMO channel sounder based on SDR platforms and considering an LTE modified standard signal as the excitation signal. In what follows, we summarize the work discussed in this PhD thesis and we highlight our main contributions and conclusions. Thereafter, we describe the possible perspectives that could be implemented.

In chapter 1, we proposed a literature survey on channel models. First, we described the generalities on mobile radio wave propagation with a brief description of the main mobile radio channel effects and the mathematical representation of the channel for SISO and MIMO configurations. Then, we presented the channel models generally considered to evaluate system performance for cellular applications. We show some largely used standard channel models as SCM, SCME, ITU-A, WINNER, WINNERII/+, and METIS model. We can mention here that the complexity of these channel models is increasing as well as the number of channel parameters

to consider due to the increasing complexity of cellular systems. Starting with a simple TDL model, the new standards used CDL based on SCM including more statistics as the antenna impact with the AoA and AoD and also the radiation function. These standards are developed by the standardization groups as IMT and 3GPP. A comparison between the well known channel models is provided to highlight the different parameters and complexity of each of these models.

In Chapter 2, we focused the literature survey on the channel model available for railway environments. After a brief description of the specificity of each type of railway environment depending on the type of trains, we highlight the fact that mainly models for HSL environments exist. In addition, we saw that the models are mainly short band and that they only provide a description of the PL or K-factor or other parameters related to radio propagation and coverage. Only a few of them are wide band channel models that can be used for performance evaluation. We found only models obtained in HSL environments. Regional, intercity or urban environments are not treated in the literature. For HSL, we can mention one TDL and two CDL channel models for rural environment, three TDL channel models for viaduct, hilly, and cutting scenario. Moreover, for a same type of environment (rural, cutting,...), different channel models exist depending on the measurements scenarios and the complexity and accuracy of the channel parameters considered. In this chapter, we also highlighted the absence of channel models for tunnels scenarios. The channel models are generally described with only the large scale fading parameters. Only one WINNER CDL channel model is fully described in terms of the number of cluster, number of paths per cluster and angle distribution laws. This model was obtained using a ray tracing simulator from University of Poitiers. We can mention very recently a TDL channel model for HSL and metro taking into account the presence of trains, obtained thanks to Ray tracing simulation by Beijing Jiaotong University and published in December 2020. This chapter emphasis that there is a very important need for the development of radio channel models that can be used to emulate the radio railway environments in laboratory in order to assess and validate the performances of wireless systems in representative railway environments.

In chapter 3, we presented the different methodologies in time and frequency to measure the CIR or CFR with the corresponding excitation signal (pulse waveform, pseudo random binary sequences, Frequency chirp and OFDM signals). Then, we detail led the different MIMO channel sounder under 6 GHz and in mmW found in the literature. The development of mmW channel sounder is an active field of research, although the cost and complexity is very high. Finally, we focused on the SDR-based channel sounders category. They allow a good compromise between performance, cost and mobility. Due to the reconfigurable hardware, it is easy to adapt the channel sounder to the purpose of the sounding. Thanks to the SDR platform characteristics, high speed channel measurements can be done exploiting LTE signal. It allows to support a large maximal Doppler frequency thanks to an appropriate pilot pattern.

Chapter 4 presented to the MIMO channel sounder developed during this PhD thesis. Based on SDR platforms and modified standardized LTE signal, it can operate at a center frequency between 10 MHz and 6 GHz with a bandwidth of 20 MHz. We presented all the bricks of the channel sounder: the hardware and software considered for the BS and the MS. Then, the excitation signal based on LTE pilot pattern is specified with the use of the LS estimation algorithm applied in the frequency domain (CFR) to measure the CFR. We have detailed all the validation stages using different approaches. Then we have explained how to extract the different channel parameters thanks to post-processing.

In the last chapter, we described the measurement campaigns performed in indoor and outdoor scenarios. After a description of each scenario in LOS and NLOS, we exploited the channel measurements to extract the CFRs, CIRs and PLs of each of the MIMO links of the MIMO matrix. We detailed some of the technical problems encountered. Nevertheless, we proved that

the channel sounder and post-processing work correctly. We experienced loss of data in NLOS scenario with mobility, which is prevented from the extraction of channel .

Perspectives

In this section, we present the perspectives of this PhD work.

The short term immediate perspective of this work is to continue the validation of the system with additional measurements. First, we will perform a new measurements campaign in a control environment and also at higher speed taking into account all the lessons learnt from the measurements described in the last chapter. The aim is to obtain data to be able to enhance the results exploitation and to be able to model the channel as a TDL or CDL channel model using a methodology from the literature. After this modeling step, we will be able to integrate the channel model in channel emulator.

An additional step is also to use the channel sounder with a channel emulator considering a TDL model and in this way to be able to validate the channel sounder and the post processing.

At the end a measurement campaign would be done in a railway environment and particularly in tunnel like in Metro de Madrid or in train station. Nevertheless, we have to be careful in the choice of the scenario because due to our limited bandwidth, the minimal measurable delay is equal to 55 ns.

Several perspectives can be drawn for what concerns the channel sounder performance enhancement:

- A first perspective will be to modify the estimation stage of the channel sounder. The LS estimation algorithm is used in the channel sounder for a real time recording of CFRs. A perspective is to change the estimation algorithm to increase the precision of the channel estimation. For example the MMSE algorithm can be implemented in the sounder despite an increase of the hardware element as the FPGA and complexity of the integrated software part relative to the algorithm.
  In addition, the used pilot pattern allows the antenna definition only in frequency to have a less complex processing. To increase the estimation accuracy in time and frequency, a sparse pilot pattern can be implemented. This lead to modifications on the software part and post-processing part. Not only on the pilot pattern definition at the BS and MS, but also inside the functional part of the USRPs. Moreover, it will be not possible to use two software instances at the BS for a MIMO 4x4 due to the pilot pattern that have to be synchronized between both USRPs.
- An additional perspective concerns the possibility to increase the bandwidth to be able to measure lower delay. The USRPs allows in theory to exploit a band of 160 MHz. The modifications to be done to the channel sounder will be quite important. The excitation signal should be modified in order to use 160 MHz but also all the receiving stage today based on LTE.
- The channel sounder implementation requires today to use signalling link, and dedicated antennas, which at the end should be avoided. This would require a change mainly at software level
- During the outdoor measurement campaign the signal amplification was a tricky part of the channel characterization. On the one hand we saturated the amplifier at short distances. On the other hand, we loss some data in high loss conditions, typically in NLOS scenarios. Further studies and development of Automatic Gain Control would allow to solve this issue and improve the channel capabilities

- The channel sounder developed is a 4x4 MIMO channel sounder using USRP 2954. Recent SDR platforms allow to consider 4 input ports (USRP 2955). With a similar architecture it could be interesting to analyse the possible evolution towards a 8x8 MIMO channel sounder. Nevertheless this will increase considerably the channel sounder cost. Such an evolution should be combine with the use of larger bandwidth.

Besides the development of the sounder, the main perspective in this area is to perform extensive measurement campaigns to propose railway channel models that are not yet present in the literature. This activity would require an effort, which goes far beyond a PhD thesis and would benefit of collaborative frameworks at national and European level, in which the channel sounder could be exploited.

Bibliography

[1] P. Berlt et al. "Cluster-based radio channel emulation for over-the-air testing of automotive wireless systems". In: *11th European Conference on Antennas and Propagation (EUCAP)*. 2017, pp. 2440–2444.

[2] Jean-Marc Kwadjane. "Apport de la connaissance a priori de la position de l'émetteur sur les algorithmes MIMO adaptatifs en environnement tunnels pour les métros". PhD thesis. Université Lille 1 Sciences et Technologies, 2014.

[3] Gérald Moniak. "Techniques MIMO pour un lien sans fil robuste entre un bus et un poste de contrôle pour une application de surveillance embarquée". PhD thesis. 2007, 1 vol. (161 p.) URL: http://www.theses.fr/2007VALE0008 (visited on 03/17/2021).

[4] John David Parsons. *The mobile radio propagation channel*. Wiley, 2000.

[5] John G Proakis et al. *Communication systems engineering*. Vol. 2. Prentice Hall New Jersey, 1994.

[6] Andrea Goldsmith. *Wireless communications*. Cambridge university press, 2005.

[7] Michel Mfeze and Emmanuel Tonye. "Comparative approach of Doppler spectra for fading channel modelling by the filtered white Gaussian noise method". In: *International Journal of Computer Science and Telecommunications* 6.11 (2015), pp. 1–12. ISSN: 2047-3338.

[8] Hideichi Sasaoka. *Mobile communications*. IOS Press, 2000.

[9] S. Dudoyer et al. "Study of the Susceptibility of the GSM-R Communications Face to the Electromagnetic Interferences of the Rail Environment". In: *IEEE Transactions on Electromagnetic Compatibility* 54.3 (2012), pp. 667–676. DOI: 10.1109/TEMC.2011.2169677.

[10] Sana Salous. *Radio Propagation Measurement and Channel Modelling*. John Wiley & Sons, Mar. 2013. ISBN: 978-1-118-50232-7.

[11] P. Bello. "Characterization of Randomly Time-Variant Linear Channels". In: *IEEE Transactions on Communications Systems* 11.4 (1963), pp. 360–393. DOI: 10.1109/TCOM.1963.1088793.

[12] Philippe Guguen. "Techniques multi-antennes émission-réception; Applications aux réseaux domestiques sans fil". PhD thesis. INSA de Rennes, 2003.

[13] B. Huang et al. "Development of LTE-based channel tester for high-speed scenario". In: *2017 15th International Conference on ITS Telecommunications (ITST)*. 2017, pp. 1–5. DOI: 10.1109/ITST.2017.7972210.

[14] Robert G Gallager. *Information theory and reliable communication*. Vol. 2. Springer, 1968.

[15] Gene H Golub and Charles F Van Loan. *Matrix computations*. Vol. 3. JHU press, 2013.

[16] M. Steinbauer, A. F. Molisch, and E. Bonek. "The double-directional radio channel". In: *IEEE Antennas and Propagation Magazine* 43.4 (2001), pp. 51–63. DOI: 10.1109/74.951559.

[17] A. F. Molisch. "A generic model for MIMO wireless propagation channels in macro- and microcells". In: *IEEE Transactions on Signal Processing* 52.1 (2004), pp. 61–71. DOI: 10.1109/TSP.2003.820144.

[18] Julien Guillet. "Caractérisation et modélisation spatio-temporelles du canal de propagation radioélectrique dans le contexte MIMO". PhD thesis. 2004.

[19] Andreas F Molisch. *Wireless communications*. Vol. 34. John Wiley & Sons, 2012.

[20] J. P. Kermoal et al. "A stochastic MIMO radio channel model with experimental validation". In: *IEEE Journal on Selected Areas in Communications* 20.6 (2002), pp. 1211–1226. DOI: 10.1109/JSAC.2002.801223.

[21] W. Weichselberger et al. "A stochastic MIMO channel model with joint correlation of both link ends". In: *IEEE Transactions on Wireless Communications* 5.1 (2006), pp. 90–100. DOI: 10.1109/TWC.2006.1576533.

[22] J. Kwadjane et al. "Performance of MIMO precoders in tunnels for train-to-wayside communications". In: (2014), pp. 1–4. DOI: 10.1109/URSIGASS.2014.6929355.

[23] ITU-R Recommendation. "Guidelines for evaluation of radio transmission technologies for IMT-2000". In: *Rec. ITU-R M. 1225* (1997).

[24] M Series. *Guidelines for evaluation of radio interface technologies for IMT-Advanced*. Tech. rep. 2009, pp. 1–72.

[25] A. A. M. Saleh and R. Valenzuela. "A Statistical Model for Indoor Multipath Propagation". In: *IEEE Journal on Selected Areas in Communications* 5.2 (1987), pp. 128–137. DOI: 10.1109/JSAC.1987.1146527.

[26] A. Abdi and M. Kaveh. "A space-time correlation model for multielement antenna systems in mobile fading channels". In: *IEEE Journal on Selected Areas in Communications* 20.3 (2002), pp. 550–560. DOI: 10.1109/49.995514.

[27] Q. H. Spencer et al. "Modeling the statistical time and angle of arrival characteristics of an indoor multipath channel". In: *IEEE Journal on Selected Areas in Communications* 18.3 (2000), pp. 347–360. DOI: 10.1109/49.840194.

[28] P. Petrus, J. H. Reed, and T. S. Rappaport. "Geometrical-based statistical macrocell channel model for mobile environments". In: *IEEE Transactions on Communications* 50.3 (2002), pp. 495–502. DOI: 10.1109/26.990911.

[29] D. Shiu et al. "Fading correlation and its effect on the capacity of multielement antenna systems". In: *IEEE Transactions on Communications* 48.3 (2000), pp. 502–513. DOI: 10.1109/26.837052.

[30] Da-shan Shiu. *Wireless communication using dual antenna arrays*. Vol. 529. Springer Science & Business Media, 2000.

[31] D. Gesbert et al. "MIMO wireless channels: capacity and performance prediction". In: *Globecom '00 - IEEE. Global Telecommunications Conference. Conference Record (Cat. No.00CH37137)*. Vol. 2. 2000, 1083–1088 vol.2. DOI: 10.1109/GLOCOM.2000.891304.

[32] *3GPP TR 25.996 V14.0.0 (2017-03) 3rd Generation Partnership Project Technical Specification Group Radio Access Network Spatial channel model for Multiple Input Multiple Output (MIMO) simulations*. Tech. rep. 2017.

[33] Peter Almers et al. "Survey of channel and radio propagation models for wireless MIMO systems". In: *EURASIP Journal on Wireless Communications and Networking* 2007 (2007), pp. 1–19. DOI: 10.1155/2007/19070.

[34] R. H. Clarke. "A statistical theory of mobile-radio reception". In: *The Bell System Technical Journal* 47.6 (1968), pp. 957–1000. DOI: 10.1002/j.1538-7305.1968.tb00069.x.

[35] D. S. Baum et al. "An interim channel model for beyond-3G systems: extending the 3GPP spatial channel model (SCM)". In: *2005 IEEE 61st Vehicular Technology Conference*. Vol. 5. 2005, 3132–3136 Vol. 5. DOI: 10.1109/VETECS.2005.1543924.

[36] "Path-Based Spatial Channel Modeling - Spirent". In: URL: https://www.spirent.com/Assets/WP/WP_Path-Based-Spatial-Channel-Modeling (visited on 05/28/2018).

[37] Pekka Kyösti et al. *IST-4-027756 WINNER II D1.1.2 V1.2 WINNER II Channel Models*. Tech. rep. EBITG, TUI, UOULU, CU/CRC, NOKIA, 2008.

[38] Juha Meinilä et al. *Document Title: D5. 3: WINNER+ Final Channel Models*. Tech. rep. 2010.

[39] Pekka Kyösti et al. *IST-4-027756 WINNER II D1.1.2 V1.0 WINNER II Channel Models*. Tech. rep. EBITG, TUI, UOULU, CU/CRC, NOKIA, 2007.

[40] S. Hairoud et al. "WINNER model for subway tunnel at 5.8 GHz". In: *12th International Conference on ITS Telecommunications*. 2012, pp. 743–747. DOI: 10.1109/ITST.2012.6425280.

[41] Vuokko Nurmela et al. "Deliverable D1. 4 METIS channel models". In: *Proc. Mobile Wireless Commun. Enablers Inf. Soc.(METIS)*. 2015, p. 1.

[42] K. Guan, Z. Zhong, and B. Ai. "Assessment of LTE-R Using High Speed Railway Channel Model, Qingdao, China". In: *2011 Third International Conference on Communications and Mobile Computing*. Apr. 2011, pp. 461–464. DOI: 10.1109/CMC.2011.34.

[43] L. Tian et al. "Channel modeling based on random propagation graphs for high speed railway scenarios". In: *2012 IEEE 23rd International Symposium on Personal, Indoor and Mobile Radio Communications - (PIMRC)*. 2012, pp. 1746–1750. DOI: 10.1109/PIMRC.2012.6362632.

[44] T. Zhou et al. "Channel sounding for high-speed railway communication systems". In: *IEEE Communications Magazine* 53.10 (2015), pp. 70–77. DOI: 10.1109/MCOM.2015.7295466.

[45] T. Zhou et al. "Implementation of an LTE-Based Channel Measurement Method for High-Speed Railway Scenarios". In: *IEEE Transactions on Instrumentation and Measurement* 65.1 (2016), pp. 25–36. DOI: 10.1109/TIM.2015.2477166.

[46] Tomás Domınguez-Bolaño et al. "Experimental characterization of LTE wireless links in high-speed trains". In: *Wireless Communications and Mobile Computing* 2017 (2017). DOI: 10.1155/2017/5079130.

[47] Jingya Yang et al. "A simplified multipath component modeling approach for high-speed train channel based on ray tracing". In: *Wireless Communications and Mobile Computing* 2017 (2017). DOI: 10.1155/2017/8517204.

[48] Liu Liu et al. "A highly efficient channel sounding method based on cellular communications for high-speed railway scenarios". In: *EURASIP Journal on Wireless Communications and Networking* 2012.1 (2012), pp. 1–16. DOI: 10.1186/1687-1499-2012-307.

[49] A. Ghazal et al. "A Non-Stationary IMT-Advanced MIMO Channel Model for High-Mobility Wireless Communication Systems". In: *IEEE Transactions on Wireless Communications* 16.4 (2017), pp. 2057–2068. DOI: 10.1109/TWC.2016.2628795.

[50] J. Bian et al. "A WINNER+ Based 3-D Non-Stationary Wideband MIMO Channel Model". In: *IEEE Transactions on Wireless Communications* 17.3 (2018), pp. 1755–1767. DOI: 10.1109/TWC.2017.2785249.

[51] R. He et al. "Measurements and Analysis of Propagation Channels in High-Speed Railway Viaducts". In: *IEEE Transactions on Wireless Communications* 12.2 (2013), pp. 794–805. DOI: 10.1109/TWC.2012.120412.120268.

[52] K. Guan et al. "Deterministic Propagation Modeling for the Realistic High-Speed Railway Environment". In: *2013 IEEE 77th Vehicular Technology Conference (VTC Spring)*. 2013, pp. 1–5. DOI: 10.1109/VTCSpring.2013.6692506.

[53] Rongchen Sun et al. "Nonisotropic scattering characteristic in an alternant tree-blocked viaduct scenario on high-speed railway at 2.35 GHz". In: *International Journal of Antennas and Propagation* 2014 (2014). DOI: 10.1155/2014/642894.

[54] D. He et al. "Ray-tracing simulation and analysis of propagation for 3GPP high speed scenarios". In: *2017 11th European Conference on Antennas and Propagation (EUCAP)*. 2017, pp. 2890–2894. DOI: 10.23919/EuCAP.2017.7928437.

[55] L. Liu et al. "Position-Based Modeling for Wireless Channel on High-Speed Railway under a Viaduct at 2.35 GHz". In: *IEEE Journal on Selected Areas in Communications* 30.4 (2012), pp. 834–845. DOI: 10.1109/JSAC.2012.120516.

[56] W. Qian et al. "Results and analysis for a novel 2x2 channel measurement applied in LTE-R at 2.6 GHz". In: *2014 IEEE Wireless Communications and Networking Conference (WCNC)*. 2014, pp. 177–181. DOI: 10.1109/WCNC.2014.6951943.

[57] Jianwen Ding et al. "Broadband wireless channel in composite high-speed railway scenario: Measurements, simulation, and analysis". In: *Wireless Communications and Mobile Computing* 2017 (2017). DOI: 10.1155/2017/2897636.

[58] T. Zhou et al. "Measurements and Analysis of Angular Characteristics and Spatial Correlation for High-Speed Railway Channels". In: *IEEE Transactions on Intelligent Transportation Systems* 19.2 (2018), pp. 357–367. DOI: 10.1109/TITS.2017.2681112.

[59] R. He et al. "Short-Term Fading Behavior in High-Speed Railway Cutting Scenario: Measurements, Analysis, and Statistical Models". In: *IEEE Transactions on Antennas and Propagation* 61.4 (2013), pp. 2209–2222. DOI: 10.1109/TAP.2012.2235399.

[60] L. Tian, J. Zhang, and C. Pan. "Small Scale Fading Characteristics of Wideband Radio Channel in the U-Shape Cutting of High-Speed Railway". In: *2013 IEEE 78th Vehicular Technology Conference (VTC Fall)*. 2013, pp. 1–6. DOI: 10.1109/VTCFall.2013.6692415.

[61] R. Sun et al. "Channel Measurement and Characterization for HSR U-Shape Groove Scenarios at 2.35 GHz". In: *2013 IEEE 78th Vehicular Technology Conference (VTC Fall)*. 2013, pp. 1–5. DOI: 10.1109/VTCFall.2013.6692131.

[62] W. Qian et al. "Propagation characteristics of high speed railway radio channel based on broadband measurements at 2.6 GHz". In: *2014 IEEE Wireless Communications and Networking Conference (WCNC)*. 2014, pp. 166–170. DOI: 10.1109/WCNC.2014.6951941.

[63] Yan Zhang et al. "Measurement-based delay and Doppler characterizations for high-speed railway hilly scenario". In: *International Journal of Antennas and Propagation* 2014 (2014). DOI: 10.1155/2014/875345.

[64] K. Guan et al. "Propagation Measurements and Analysis for Train Stations of High-Speed Railway at 930 MHz". In: *IEEE Transactions on Vehicular Technology* 63.8 (2014), pp. 3499–3516. DOI: 10.1109/TVT.2014.2307917.

[65] Y. Zhang et al. "Impact of Different Parameters on Channel Characteristics in a High-Speed Train Ray Tracing Tunnel Channel Model". In: *2017 IEEE 85th Vehicular Technology Conference (VTC Spring)*. 2017, pp. 1–5. DOI: 10.1109/VTCSpring.2017.8108210.

[66] K. Guan et al. "Measurements and Analysis of Large-Scale Fading Characteristics in Curved Subway Tunnels at 920 MHz, 2400 MHz, and 5705 MHz". In: *IEEE Transactions on Intelligent Transportation Systems* 16.5 (2015), pp. 2393–2405. DOI: 10.1109/TITS.2015.2404851.

[67] J. Li et al. "Radio channel measurements and analysis at 2.4/5GHz in subway tunnels". In: *China Communications* 12.1 (2015), pp. 36–45. DOI: 10.1109/CC.2015.7084382.

[68] C. Gentile, F. Valoit, and N. Moayeri. "A raytracing model for wireless propagation in tunnels with varying cross section". In: *2012 IEEE Global Communications Conference (GLOBECOM)*. 2012, pp. 5027–5032. DOI: 10.1109/GLOCOM.2012.6503917.

[69] K. Guan et al. "Complete Propagation Model in Tunnels". In: *IEEE Antennas and Wireless Propagation Letters* 12 (2013), pp. 741–744. DOI: 10.1109/LAWP.2013.2270937.

[70] L. Zhang et al. "Delay Spread and Electromagnetic Reverberation in Subway Tunnels and Stations". In: *IEEE Antennas and Wireless Propagation Letters* 15 (2016), pp. 585–588. DOI: 10.1109/LAWP.2015.2462022.

[71] Concepcion Garcia-Pardo et al. "Double directional channel measurements in an arched tunnel and interpretation using ray tracing in a rectangular tunnel". In: *Progress In Electromagnetics Research* 22 (2012), pp. 91–107. DOI: 10.2528/PIERM11070110.

[72] K. Guan et al. "Measurement of Distributed Antenna Systems at 2.4 GHz in a Realistic Subway Tunnel Environment". In: *IEEE Transactions on Vehicular Technology* 61.2 (2012), pp. 834–837. DOI: 10.1109/TVT.2011.2178623.

[73] K. Guan et al. "Propagation mechanism modelling in the near region of circular tunnels". In: *IET Microwaves, Antennas & Propagation* 6 (3 Feb. 2012), 355–360(5). ISSN: 1751-8725. DOI: 10.1049/iet-map.2011.0381.

[74] K. Guan et al. "Scenario modules and ray-tracing simulations of millimeter wave and terahertz channels for smart rail mobility". In: *2017 11th European Conference on Antennas and Propagation (EUCAP)*. 2017, pp. 113–117. DOI: 10.23919/EuCAP.2017.7928471.

[75] X. Ye et al. "Tunnel and Non-Tunnel Channel Characterization for High-Speed-Train Scenarios in LTE-A Networks". In: *2016 IEEE 83rd Vehicular Technology Conference (VTC Spring)*. 2016, pp. 1–5. DOI: 10.1109/VTCSpring.2016.7504514.

[76] H. Zheng and X. Nie. "GBSB Model for MIMO Channel and Its Space-Time Correlataion Analysis in Tunnel". In: *2009 International Conference on Networks Security, Wireless Communications and Trusted Computing*. Vol. 1. 2009, pp. 8–11. DOI: 10.1109/NSWCTC.2009.192.

[77] Y. Jia et al. "Measurement and statistical analysis of 1.89GHz radio propagation in a realistic mountain tunnel". In: *2015 International Conference on Wireless Communications Signal Processing (WCSP)*. 2015, pp. 1–5. DOI: 10.1109/WCSP.2015.7341050.

[78] D. J. Cichon, T. C. Becker, and W. Wiesbeck. "Determination of time-variant radio links in high-speed train tunnels by ray optical modeling". In: *IEEE Antennas and Propagation Society International Symposium. 1995 Digest*. Vol. 1. 1995, 508–511 vol.1. DOI: 10.1109/APS.1995.530069.

[79] X. Cai et al. "An Empirical Random-Cluster Model for Subway Channels Based on Passive Measurements in UMTS". In: *IEEE Transactions on Communications* 64.8 (2016), pp. 3563–3575. DOI: 10.1109/TCOMM.2016.2578923.

[80] X. Chen et al. "Research on Doppler spread of multipath channel in subway tunnel". In: *2014 IEEE International Conference on Communiction Problem-solving*. 2014, pp. 56–59. DOI: 10.1109/ICCPS.2014.7062216.

[81] C. Briso-Rodriguez, J. M. Cruz, and J. I. Alonso. "Measurements and Modeling of Distributed Antenna Systems in Railway Tunnels". In: *IEEE Transactions on Vehicular Technology* 56.5 (2007), pp. 2870–2879. DOI: 10.1109/TVT.2007.900500.

[82] E. Masson et al. "4×4 MIMO channel sounding in tunnels for train-to-wayside communications". In: *2012 International Conference on Wireless Communications in Underground and Confined Areas, Clermont-Ferrand*. 2012, pp. 1–5. DOI: 10.1109/ICWCUCA.2012.6402480.

[83] L. Zhang et al. "Broadband radio communications in subway stations and tunnels". In: *2015 9th European Conference on Antennas and Propagation (EuCAP)*. 2015, pp. 1–5.

[84] D. He et al. "Stochastic channel modeling for railway tunnel scenarios at 25 GHz". In: *ETRI Journal* 40.1 (2018), pp. 39–50. DOI: 10.4218/etrij.2017-0190.

[85] R.He et al. In: *IET Microwaves, Antennas & Propagation* 7 (11 Aug. 2013), 934–941(7). ISSN: 1751-8725. DOI: 10.1049/iet-map.2013.0159.

[86] Yann Cocheril et al. "On the importance of the MIMO channel correlation in underground railway tunnels". In: *Journal of Communication* 4.4 (2009), pp. 224–231.

[87] H. Qiu et al. "Emulation of Radio Technologies for Railways: A Tapped-Delay-Line Channel Model for Tunnels". In: *IEEE Access* 9 (2021), pp. 1512–1523. DOI: 10.1109/ACCESS.2020.3046852.

[88] C. Wang et al. "Channel Measurements and Models for High-Speed Train Communication Systems: A Survey". In: *IEEE Communications Surveys Tutorials* 18.2 (2016), pp. 974–987. DOI: 10.1109/COMST.2015.2508442.

[89] Sencity Rail Antenna. *1399.17. 0039 HUBER+ SUHNER data sheet*. Tech. rep. 2010.

[90] Yu Liu et al. "Channel measurements and models for high-speed train wireless communication systems in tunnel scenarios: A survey". In: *Science China Information Sciences* 60.10 (2017), p. 101301. DOI: 10.1007/s11432-016-9014-3.

[91] Y. Zhang et al. "A General Coupling-Based Model Framework for Wideband MIMO Channels". In: *IEEE Transactions on Antennas and Propagation* 60.2 (2012), pp. 574–586. DOI: 10.1109/TAP.2011.2173436.

[92] A. Emslie, R. Lagace, and P. Strong. "Theory of the propagation of UHF radio waves in coal mine tunnels". In: *IEEE Transactions on Antennas and Propagation* 23.2 (1975), pp. 192–205. DOI: 10.1109/TAP.1975.1141041.

[93] Jorge Avella Castiblanco. *Electromagnetic modeling for antenna design and specifications in tunnels of arbitrary cross-section and answering to the electromagnetic constraints of the environment of the railway domain.* Thèse de doctorat dirigée par Berbineau, Marion Ney, Michel Seetharamdoo, Divitha et Gallée, François Micro et nanotechnologies, acoustique et télécommunications Lille 1 2013. 2013. URL: http://www.theses.fr/2013LIL10189 (visited on 05/28/2018).

[94] Sergiy Y Reutskiy. "The methods of external excitation for analysis of arbitrarily-shaped hollow conducting waveguides". In: *Progress In Electromagnetics Research* 82 (2008), pp. 203–226. DOI: 10.2528/PIER08022701.

[95] A. V. Popov and Ning Yan Zhu. "Modeling radio wave propagation in tunnels with a vectorial parabolic equation". In: *IEEE Transactions on Antennas and Propagation* 48.9 (2000), pp. 1403–1412. DOI: 10.1109/8.898773.

[96] S. Mahmoud. "Characteristics of Electromagnetic Guided Waves for Communication in Coal Mine Tunnels". In: *IEEE Transactions on Communications* 22.10 (1974), pp. 1547–1554. DOI: 10.1109/TCOM.1974.1092093.

[97] M Agunaou et al. "Propagation d'ondes électromagnétiques hyperfréquences à l'intérieur d'un métro-Modélisation numérique de l'influence des changements de section". In: *Recherche Transports Sécurité* 64 (1998), pp. 55–68.

[98] K. Guan et al. "Stochastic Modeling for Extra Propagation Loss of Tunnel Curve". In: *2016 IEEE 83rd Vehicular Technology Conference (VTC Spring)*. 2016, pp. 1–5. DOI: 10.1109/VTCSpring.2016.7504491.

[99] Emilie Masson. "Etude de la propagation des ondes électromagnétiques dans les tunnels courbes de section non droite pour des applications métro et ferroviaire". Theses. Université de Poitiers, Dec. 2010. URL: https://tel.archives-ouvertes.fr/tel-00615291 (visited on 05/28/2018).

[100] Katherine D. Laakmann and William H. Steier. "Waveguides: characteristic modes of hollow rectangular dielectric waveguides". In: *Appl. Opt.* 15.5 (May 1976), pp. 1334–1340. DOI: 10.1364/AO.15.001334. URL: http://ao.osa.org/abstract.cfm?URI=ao-15-5-1334 (visited on 05/28/2018).

[101] D. G. Dudley and S. F. Mahmoud. "Linear source in a circular tunnel". In: *IEEE Transactions on Antennas and Propagation* 54.7 (2006), pp. 2034–2047. DOI: 10.1109/TAP.2006.877195.

[102] D. G. Dudley et al. "On wireless communication in tunnels". In: *2007 IEEE Antennas and Propagation Society International Symposium*. 2007, pp. 3305–3308. DOI: 10.1109/APS.2007.4396243.

[103] Jorge Avella Castiblanco. "Electromagnetic modeling for antenna design and specifications in tunnels of arbitrary cross-section and answering to the electromagnetic constraints of the environment of the railway domain". PhD thesis. 2013. URL: http://www.theses.fr/2013LIL10189 (visited on 03/17/2021).

[104] M. Lienard et al. "Investigation on MIMO channels in subway tunnels". In: *IEEE Journal on Selected Areas in Communications* 21.3 (2003), pp. 332–339. DOI: 10.1109/JSAC.2003.809627.

[105] J. -. Molina-Garcia-Pardo et al. "Wideband analysis of large scale and small scale fading in tunnels". In: *2008 8th International Conference on ITS Telecommunications*. 2008, pp. 270–273. DOI: 10.1109/ITST.2008.4740269.

[106] E. Masson et al. "MIMO channel characterization in subway tunnel for train-to-wayside applications". In: (2012), pp. 732–736. DOI: 10.1109/ITST.2012.6425278.

[107] M. Lienard et al. "Investigation on MIMO channels in subway tunnels". In: *IEEE Journal on Selected Areas in Communications* 21.3 (2003), pp. 332–339. DOI: 10.1109/JSAC.2003.809627.

[108] J. Molina-Garcia-Pardo et al. "MIMO Channel Capacity With Polarization Diversity in Arched Tunnels". In: *IEEE Antennas and Wireless Propagation Letters* 8 (2009), pp. 1186–1189. DOI: 10.1109/LAWP.2009.2035299.

[109] A. E. Forooshani, R. D. White, and D. G. Michelson. "Effect of antenna array properties on multiple-input–multiple-output system performance in an underground mine". In: *IET Microwaves, Antennas & Propagation* 7 (13 Oct. 2013), 1035–1044(9). ISSN: 1751-8725.

[110] A. E. Forooshani, A. A. Lotfi-Neyestanak, and D. G. Michelson. "Optimization of Antenna Placement in Distributed MIMO Systems for Underground Mines". In: *IEEE Transactions on Wireless Communications* 13.9 (2014), pp. 4685–4692. DOI: 10.1109/TWC.2014.2341587.

[111] A. E. Forooshani, C. Y. T. Lee, and D. G. Michelson. "Effect of Antenna Configuration on MIMO-Based Access Points in a Short Tunnel With Infrastructure". In: *IEEE Transactions on Communications* 64.5 (2016), pp. 1942–1951. DOI: 10.1109/TCOMM.2016.2538769.

[112] D. Gesbert et al. "MIMO wireless channels: capacity and performance prediction". In: *Globecom '00 - IEEE. Global Telecommunications Conference. Conference Record (Cat. No.00CH37137)*. Vol. 2. 2000, 1083–1088 vol.2. DOI: 10.1109/GLOCOM.2000.891304.

[113] David Gesbert and Jabran Akhtar. "Breaking the barriers of Shannon's capacity: An overview of MIMO wireless systems". In: *Signal Processing* 1.B2 (2002), B3.

[114] J. Moreno et al. "Keyhole Estimation of an MIMO-OFDM Train-to-Wayside Communication System on Subway Tunnels". In: *IEEE Antennas and Wireless Propagation Letters* 14 (2015), pp. 88–91. DOI: 10.1109/LAWP.2014.2356076.

[115] D. Chizhik et al. "Keyholes, correlations, and capacities of multielement transmit and receive antennas". In: *IEEE Transactions on Wireless Communications* 1.2 (2002), pp. 361–368. DOI: 10.1109/7693.994830.

[116] P. Almers, F. Tufvesson, and A. F. Molisch. "Keyhole Effect in MIMO Wireless Channels: Measurements and Theory". In: *IEEE Transactions on Wireless Communications* 5.12 (2006), pp. 3596–3604. DOI: 10.1109/TWC.2006.256982.

[117] D. G. Dudley et al. "Wireless propagation in tunnels". In: *IEEE Antennas and Propagation Magazine* 49.2 (2007), pp. 11–26. DOI: 10.1109/MAP.2007.376637.

[118] J. A. Valdesueiro, B. Izquierdo, and J. Romeu. "On 2×2 MIMO Observable Capacity in Subway Tunnels at C-Band: An Experimental Approach". In: *IEEE Antennas and Wireless Propagation Letters* 9 (2010), pp. 1099–1102. DOI: 10.1109/LAWP.2010.2095816.

[119] C. Sanchis-Borras et al. "Performance Evaluation of MIMO-OFDM in Tunnels". In: *IEEE Antennas and Wireless Propagation Letters* 11 (2012), pp. 301–304. DOI: 10.1109/LAWP.2012.2191130.

[120] Ronald Raulefs et al. *Projet ROLL2RAIL: New dependable rolling stock for a more sustainable, intelligent and comfortable rail transport in Europe. Deliverable D2.2 - Characterisation of the Railway Environment for Radio Transmission.* Research Report. IFSTTAR - Institut Français des Sciences et Technologies des Transports, de l'Aménagement et des Réseaux, Jan. 2016, 186p. URL: https://hal.archives-ouvertes.fr/hal-01664165 (visited on 03/17/2021).

[121] Juan Moreno et al. *Deliverable D 1.3 - Characterization of the railway environment: channel models & general characteristics.* Tech. rep. Emulradio4Rail project - Grant 826152, Dec. 2020.

[122] M. Berbineau et al. "Channel Models for Performance Evaluation of Wireless Systems in Railway Environments". In: *Accepted for publication in IEEE Access* (2021).

[123] W. R. Young and L. Y. Lacy. "Echoes in Transmission at 450 Megacycles from Land-to-Car Radio Units". In: *Proceedings of the IRE* 38.3 (1950), pp. 255–258. DOI: 10.1109/JRPROC.1950.230736.

[124] Guttorm Ringstad Opshaug and Per Enge. "GPS and UWB for Indoor Navigation". In: (2001), pp. 1427–1433.

[125] S. M. Yano. "Investigating the ultra-wideband indoor wireless channel". In: *Vehicular Technology Conference. IEEE 55th Vehicular Technology Conference. VTC Spring 2002 (Cat. No.02CH37367).* Vol. 3. 2002, 1200–1204 vol.3. DOI: 10.1109/VTC.2002.1002804.

[126] M. Terre et al. "Major characteristics of UWB indoor transmission for simulation". In: *The 57th IEEE Semiannual Vehicular Technology Conference, 2003. VTC 2003-Spring.* Vol. 1. 2003, 19–23 vol.1. DOI: 10.1109/VETECS.2003.1207493.

[127] Q. Li and W. S. Wong. "Measurement and analysis of the indoor UWB channel". In: *2003 IEEE 58th Vehicular Technology Conference. VTC 2003-Fall (IEEE Cat. No.03CH37484).* Vol. 1. 2003, 1–5 Vol.1. DOI: 10.1109/VETECF.2003.1284966.

[128] C. Moy, G. El Zein, and J. Citerne. "Performance of hybrid spread spectrum DS/FH RAKE receivers for troposcatter links at 5 GHz". In: *1998 IEEE 5th International Symposium on Spread Spectrum Techniques and Applications - Proceedings. Spread Technology to Africa (Cat. No.98TH8333).* Vol. 2. 1998, 571–575 vol.2. DOI: 10.1109/ISSSTA.1998.723849.

[129] K. Kalliola et al. "3-D double-directional radio channel characterization for urban macrocellular applications". In: *IEEE Transactions on Antennas and Propagation* 51.11 (2003), pp. 3122–3133. DOI: 10.1109/TAP.2003.816393.

[130] Ronan COSQUER. "Conception d'un sondeur de canal MIMO - Caractérisation du canal de propagation d'un point de vue directionnel et doublement directionnel". Theses. INSA de Rennes, Oct. 2004.

[131] T. Zwick, C. Fischer, and W. Wiesbeck. "A stochastic multipath channel model including path directions for indoor environments". In: *IEEE Journal on Selected Areas in Communications* 20.6 (2002), pp. 1178–1192. DOI: 10.1109/JSAC.2002.801218.

[132] D. Cox. "Delay Doppler characteristics of multipath propagation at 910 MHz in a suburban mobile radio environment". In: *IEEE Transactions on Antennas and Propagation* 20.5 (1972), pp. 625–635. DOI: 10.1109/TAP.1972.1140277.

[133] Neal Patwari. "Measured and modeled time and angle dispersion characteristics of the 1.8 GHz peer-to-peer radio channel". PhD thesis. Virginia Tech, 1999.

[134] William George Newhall. "Wideband propagation measurement results, simulation models, and processing techniques for a sliding correlator measurement system". PhD thesis. Virginia Tech, 1997.

[135] Albin Dunand. "Contribution à la caractérisation du canal de propagation en environnement macrocellulaire urbain à 2. 2 GHz". PhD thesis. 2008, 1 vol. (X–211 p.) URL: http://www.theses.fr/2008POIT2349 (visited on 03/17/2021).

[136] S Guerin, C Pradal, and P Khalfa. "Indoor propagation narrow band and wide band measurements around 60 GHz using a network analyzer". In: *EURO COST* (1995).

[137] J. Molina-Garcia-Pardo et al. "MIMO Channel Capacity With Polarization Diversity in Arched Tunnels". In: *IEEE Antennas and Wireless Propagation Letters* 8 (2009), pp. 1186–1189. DOI: 10.1109/LAWP.2009.2035299.

[138] J. Molina-Garcia-Pardo, J. Rodriguez, and L. Juan-Llacer. "MIMO Channel Sounder Based on Two Network Analyzers". In: *IEEE Transactions on Instrumentation and Measurement* 57.9 (2008), pp. 2052–2058. DOI: 10.1109/TIM.2008.922091.

[139] S. Salous et al. In: 152 (6 Dec. 2005), 912–918(6). ISSN: 1350-2425. DOI: 10.1049/ip-com:20045346.

[140] T. Hwang et al. "OFDM and Its Wireless Applications: A Survey". In: *IEEE Transactions on Vehicular Technology* 58.4 (2009), pp. 1673–1694. DOI: 10.1109/TVT.2008.2004555.

[141] Stefania Sesia, Issam Toufik, and Matthew Baker. *LTE-the UMTS long term evolution: from theory to practice*. John Wiley & Sons, 2011.

[142] Yong Soo Cho et al. *MIMO-OFDM wireless communications with MATLAB*. John Wiley & Sons, 2010.

[143] Raghad K Mohammed. "Comparing various channel estimation techniques for OFDM systems using MATLAB". In: *International Journal of Wireless & Mobile Networks (IJWMN) Vol* 11 (2019). DOI: dx.doi.org/10.2139/ssrn.3420582.

[144] F. Kaltenberger et al. "Broadband wireless channel measurements for high speed trains". In: *2015 IEEE International Conference on Communications (ICC)*. 2015, pp. 2620–2625. DOI: 10.1109/ICC.2015.7248720.

[145] Harry WH Jones, Pawel A Dmochowski, and Paul D Teal. "Channel sounding with software defined radio". In: *Honors project, Victoria University of Wellington* (2009).

[146] H. Boeglen et al. "An SDR based channel sounding technique for embedded systems". In: *2017 11th European Conference on Antennas and Propagation (EUCAP)*. 2017, pp. 3286–3290. DOI: 10.23919/EuCAP.2017.7928583.

[147] J. li et al. "System Design and Calibration for Wideband Channel Sounding With Multiple Frequency Bands". In: *IEEE Access* 5 (2017), pp. 781–793. DOI: 10.1109/ACCESS.2017.2649679.

[148] R. Wang et al. "A real-time MIMO channel sounder for vehicle-to-vehicle propagation channel at 5.9 GHz". In: *2017 IEEE International Conference on Communications (ICC)*. 2017, pp. 1–6. DOI: 10.1109/ICC.2017.7996407.

[149] P. Laly et al. "Flexible real-time MIMO channel sounder for multidimensional polarimetric parameter estimation". In: *2015 IEEE Conference on Antenna Measurements Applications (CAMA)*. 2015, pp. 1–3. DOI: 10.1109/CAMA.2015.7428142.

[150] D. A. Wassie et al. "An Agile Multi-Node Multi-Antenna Wireless Channel Sounding System". In: *IEEE Access* 7 (2019), pp. 17503–17516. DOI: 10.1109/ACCESS.2019.2895412.

[151] H. Farhat et al. "A Dual Band MIMO Channel Sounder at 2.2 and 3.5 GHz". In: *2008 IEEE Instrumentation and Measurement Technology Conference*. 2008, pp. 1980–1985. DOI: 10.1109/IMTC.2008.4547373.

[152] L. Bernadó et al. "Time- and Frequency-Varying K-Factor of Non-Stationary Vehicular Channels for Safety-Relevant Scenarios". In: *IEEE Transactions on Intelligent Transportation Systems* 16.2 (2015), pp. 1007–1017. DOI: 10.1109/TITS.2014.2349364.

[153] M. Haardt et al. "2D unitary ESPRIT for efficient 2D parameter estimation". In: *1995 International Conference on Acoustics, Speech, and Signal Processing*. Vol. 3. 1995, 2096–2099 vol.3. DOI: 10.1109/ICASSP.1995.478488.

[154] B. H. Fleury et al. "Channel parameter estimation in mobile radio environments using the SAGE algorithm". In: *IEEE Journal on Selected Areas in Communications* 17.3 (1999), pp. 434–450. DOI: 10.1109/49.753729.

[155] K. Kitao et al. "Basic study on spatio-temporal dynamic channel properties based on channel sounder measurements". In: *2009 Asia Pacific Microwave Conference*. 2009, pp. 1064–1067. DOI: 10.1109/APMC.2009.5384371.

[156] R. S. Thoma et al. "Identification of time-variant directional mobile radio channels". In: *IEEE Transactions on Instrumentation and Measurement* 49.2 (2000), pp. 357–364. DOI: 10.1109/19.843078.

[157] V. Kolmonen et al. "A Dynamic Dual-Link Wideband MIMO Channel Sounder for 5.3 GHz". In: *IEEE Transactions on Instrumentation and Measurement* 59.4 (2010), pp. 873–883. DOI: 10.1109/TIM.2009.2026608.

[158] Reiner S. Thoma et al. *EURASIP Book Series on Signal Processing and Communications*. Vol. 3. 2006, pp. 240–270.

[159] Nicolai Czink, Bernd Bandemer, and A Paulraj. "Stanford july 2008 radio channel measurement campaign". In: vol. 620. Citeseer, 2008.

[160] L. Bernadó et al. "Delay and Doppler Spreads of Nonstationary Vehicular Channels for Safety-Relevant Scenarios". In: *IEEE Transactions on Vehicular Technology* 63.1 (2014), pp. 82–93. DOI: 10.1109/TVT.2013.2271956.

[161] J. Conrat, P. Pajusco, and J. Thiriet. "A Multibands Wideband Propagation Channel Sounder from 2 to 60 GHz". In: *2006 IEEE Instrumentation and Measurement Technology Conference Proceedings*. 2006, pp. 590–595. DOI: 10.1109/IMTC.2006.328629.

[162] E. Van der Ouderaa, J. Schoukens, and J. Renneboog. "Peak factor minimization of input and output signals of linear systems". In: *IEEE Transactions on Instrumentation and Measurement* 37.2 (1988), pp. 207–212. DOI: 10.1109/19.6053.

[163] Y. Konishi et al. "Channel sounding technique using MIMO software radio architecture". In: *Proceedings of the 5th European Conference on Antennas and Propagation (EUCAP)*. 2011, pp. 2546–2550.

[164] Theodore S Rappaport et al. *Millimeter wave wireless communications*. Pearson Education, 2015.

[165] Naser Al-Falahy and Omar Y.K. Alani. "Millimetre wave frequency band as a candidate spectrum for 5G network architecture: A survey". In: *Physical Communication* 32 (2019), pp. 120–144. ISSN: 1874-4907. DOI: https://doi.org/10.1016/j.phycom.2018.11.003. URL: https://www.sciencedirect.com/science/article/pii/S1874490717305827 (visited on 05/28/2018).

[166] G. R. MacCartney and T. S. Rappaport. "A Flexible Millimeter-Wave Channel Sounder With Absolute Timing". In: *IEEE Journal on Selected Areas in Communications* 35.6 (2017), pp. 1402–1418. DOI: 10.1109/JSAC.2017.2687838.

[167] S. Salous et al. "Wideband MIMO Channel Sounder for Radio Measurements in the 60 GHz Band". In: *IEEE Transactions on Wireless Communications* 15.4 (2016), pp. 2825–2832. DOI: 10.1109/TWC.2015.2511006.

[168] M. Soliman et al. "Design and Evaluation of a Millimeter Wave Channel Sounder for Dynamic Propagation Measurements". In: *2018 IEEE 88th Vehicular Technology Conference (VTC-Fall)*. 2018, pp. 1–5. DOI: 10.1109/VTCFall.2018.8690620.

[169] Keysight. *5G Channel sounding, Reference Solution*. URL: https://www.keysight.com/en/pd-2574038/5g-channel-sounding-reference-solution?cc=US&lc=eng (visited on 05/28/2018).

[170] N. H. Fliedner, D. Block, and U. Meier. "A Software-Defined Channel Sounder for Industrial Environments with Fast Time Variance". In: *2018 15th International Symposium on Wireless Communication Systems (ISWCS)*. 2018, pp. 1–6. DOI: 10.1109/ISWCS.2018.8491207.

[171] M. N. Islam et al. "A wireless channel sounding system for rapid propagation measurements". In: *2013 IEEE International Conference on Communications (ICC)*. 2013, pp. 5720–5725. DOI: 10.1109/ICC.2013.6655507.

[172] M. E. Anggraeni, P. Handayani, and G. Hendrantoro. "Double-directional outdoor MIMO channel measurement at 2.4 GHz using SDR". In: *2016 International Seminar on Intelligent Technology and Its Applications (ISITIA)*. 2016, pp. 255–260. DOI: 10.1109/ISITIA.2016.7828667.

[173] E. S. Sousa, V. M. Jovanovic, and C. Daigneault. "Delay spread measurements for the digital cellular channel in Toronto". In: *IEEE Transactions on Vehicular Technology* 43.4 (1994), pp. 837–847. DOI: 10.1109/25.330145.

[174] D. Maas et al. "Channel Sounding for the Masses: Low Complexity GNU 802.11b Channel Impulse Response Estimation". In: *IEEE Transactions on Wireless Communications* 11.1 (2012), pp. 1–8. DOI: 10.1109/TWC.2011.111611.091774.

[175] Mutsawashe Gahadza, Minseok Kim, and J. Takada. "Implementation of a channel sounder using GNU radio opensource SDR platform". In: 2009.

[176] P. Pajusco et al. "Space Time Channel Sounding Method using SAR Approach". In: *2019 13th European Conference on Antennas and Propagation (EuCAP)*. 2019, pp. 1–4.

[177] P. Pajusco et al. "Massive antenna array for space-time channel sounding". In: *2017 11th European Conference on Antennas and Propagation (EUCAP)*. 2017, pp. 865–868. DOI: 10.23919/EuCAP.2017.7928631.

[178] A. Merwaday et al. "USRP-based indoor channel sounding for D2D and multi-hop communications". In: *WAMICON 2014*. 2014, pp. 1–6. DOI: 10.1109/WAMICON.2014.6857800.

[179] T. Zhou et al. "A Study on a LTE-Based Channel Sounding Scheme for High-Speed Railway Scenarios". In: *2013 IEEE 78th Vehicular Technology Conference (VTC Fall)*. 2013, pp. 1–5. DOI: 10.1109/VTCFall.2013.6692065.

[180] Bassem Zayen, Florian Kaltenberger, and Raymond Knopp. *FOR SPECTRALLY AGILE COMMUNICATION*. John Wiley & Sons, 2015, p. 99.

[181] Pierre Laly. "Sondeur de canal MIMO temps réel et applications". Thèse de doctorat dirigée par Liénard, Martine Micro et nanotechnologies, acoustique et télécommunications Lille 1 2016. PhD thesis. 2016. URL: http://www.theses.fr/2016LIL10168 (visited on 03/17/2021).

[182] Y. Wen, W. Huang, and Z. Zhang. "CAZAC sequence and its application in LTE random access". In: *2006 IEEE Information Theory Workshop - ITW '06 Chengdu*. 2006, pp. 544–547. DOI: 10.1109/ITW2.2006.323692.

[183] Softros Systems. Network Time System. 2018. URL: https://nts.softros.com/ (visited on 03/17/2021).

[184] B. Huang et al. "Development of LTE-based channel tester for high-speed scenario". In: *2017 15th International Conference on ITS Telecommunications (ITST)*. 2017, pp. 1–5. DOI: 10.1109/ITST.2017.7972210.

[185] National Instrument. *LabVIEW Communication MIMO Application Framework, v1.1*. Tech. rep. 2017.

[186] T. Zhou et al. "Implementation of an LTE-Based Channel Measurement Method for High-Speed Railway Scenarios". In: *IEEE Transactions on Instrumentation and Measurement* 65.1 (2016), pp. 25–36. DOI: 10.1109/TIM.2015.2477166.

[187] X. Ma et al. "Sparse Channel Estimation for MIMO-OFDM Systems in High-Mobility Situations". In: *IEEE Transactions on Vehicular Technology* 67.7 (2018), pp. 6113–6124. DOI: 10.1109/TVT.2018.2811368.

[188] B. Gong et al. "Block Distributed Compressive Sensing-Based Doubly Selective Channel Estimation and Pilot Design for Large-Scale MIMO Systems". In: *IEEE Transactions on Vehicular Technology* 66.10 (2017), pp. 9149–9161. DOI: 10.1109/TVT.2017.2715345.

[189] Z. Sheng et al. "Pilot Optimization for Estimation of High-Mobility OFDM Channels". In: *IEEE Transactions on Vehicular Technology* 66.10 (2017), pp. 8795–8806. DOI: 10.1109/TVT.2017.2694821.

[190] X. Ren, M. Tao, and W. Chen. "Compressed Channel Estimation With Position-Based ICI Elimination for High-Mobility SIMO-OFDM Systems". In: *IEEE Transactions on Vehicular Technology* 65.8 (2016), pp. 6204–6216. DOI: 10.1109/TVT.2015.2471085.

[191] Pingzhi Fan Ning Sun Jingxian Wu. In: *IET Communications* 9 (13 Sept. 2015), 1677–1682(5). DOI: 10.1049/iet-com.2014.0952.

[192] X. Ren, W. Chen, and M. Tao. "Position-Based Compressed Channel Estimation and Pilot Design for High-Mobility OFDM Systems". In: *IEEE Transactions on Vehicular Technology* 64.5 (2015), pp. 1918–1929. DOI: 10.1109/TVT.2014.2341712.

[193] C. Qi et al. "Pilot Design Schemes for Sparse Channel Estimation in OFDM Systems". In: *IEEE Transactions on Vehicular Technology* 64.4 (2015), pp. 1493–1505. DOI: 10.1109/TVT.2014.2331085.

[194] N. Sun and J. Wu. "Maximizing Spectral Efficiency for High Mobility Systems with Imperfect Channel State Information". In: *IEEE Transactions on Wireless Communications* 13.3 (2014), pp. 1462–1470. DOI: 10.1109/TWC.2014.012314.130772.

[195] D. Hu et al. "Optimal pilot sequence design for channel estimation in MIMO OFDM systems". In: *IEEE Communications Letters* 10.1 (2006), pp. 1–3. DOI: 10.1109/LCOMM.2006.1576550.

[196] M. Dong and L. Tong. "Optimal design and placement of pilot symbols for channel estimation". In: *IEEE Transactions on Signal Processing* 50.12 (2002), pp. 3055–3069. DOI: 10.1109/TSP.2002.805504.

[197] S. G. Kang, Y. M. Ha, and E. K. Joo. "A comparative investigation on channel estimation algorithms for OFDM in mobile communications". In: *IEEE Transactions on Broadcasting* 49.2 (2003), pp. 142–149. DOI: 10.1109/TBC.2003.810263.

[198] Pallaviram Sure and Chandra Mohan Bhuma. "A survey on OFDM channel estimation techniques based on denoising strategies". In: *Engineering Science and Technology, an International Journal* 20.2 (2017), pp. 629–636. DOI: 10.1016/j.jestch.2016.09.011.

[199] J. -. van de Beek et al. "On channel estimation in OFDM systems". In: *1995 IEEE 45th Vehicular Technology Conference. Countdown to the Wireless Twenty-First Century.* Vol. 2. 1995, 815–819 vol.2. DOI: 10.1109/VETEC.1995.504981.

[200] J. Rinne and M. Renfors. "Pilot spacing in orthogonal frequency division multiplexing systems on practical channels". In: *IEEE Transactions on Consumer Electronics* 42.4 (1996), pp. 959–962. DOI: 10.1109/30.555792.

[201] O. Edfors et al. "OFDM channel estimation by singular value decomposition". In: *IEEE Transactions on Communications* 46.7 (1998), pp. 931–939. DOI: 10.1109/26.701321.

[202] Y. Li, L. J. Cimini, and N. R. Sollenberger. "Robust channel estimation for OFDM systems with rapid dispersive fading channels". In: *IEEE Transactions on Communications* 46.7 (1998), pp. 902–915. DOI: 10.1109/26.701317.

[203] Y. Li. "Pilot-symbol-aided channel estimation for OFDM in wireless systems". In: *IEEE Transactions on Vehicular Technology* 49.4 (2000), pp. 1207–1215. DOI: 10.1109/25.875230.

[204] R. Negi and J. Cioffi. "Pilot tone selection for channel estimation in a mobile OFDM system". In: *IEEE Transactions on Consumer Electronics* 44.3 (1998), pp. 1122–1128. DOI: 10.1109/30.713244.

[205] P. Hoeher, S. Kaiser, and P. Robertson. "Two-dimensional pilot-symbol-aided channel estimation by Wiener filtering". In: *1997 IEEE International Conference on Acoustics, Speech, and Signal Processing.* Vol. 3. 1997, 1845–1848 vol.3. DOI: 10.1109/ICASSP.1997.598897.

[206] M. Morelli and U. Mengali. "A comparison of pilot-aided channel estimation methods for OFDM systems". In: *IEEE Transactions on Signal Processing* 49.12 (2001), pp. 3065–3073. DOI: 10.1109/78.969514.

[207] J. J. Egli. "Radio Propagation above 40 MC over Irregular Terrain". In: *Proceedings of the IRE* 45.10 (1957), pp. 1383–1391. DOI: 10.1109/JRPROC.1957.278224.

[208] R. Schmidt. "Multiple emitter location and signal parameter estimation". In: *IEEE Transactions on Antennas and Propagation* 34.3 (1986), pp. 276–280. DOI: 10.1109/TAP.1986.1143830.

[209] Jean-François Pardonche. "Systèmes de transmission sans fil multi-émetteurs, multi-récepteurs pour des applications transports : étude des modèles de canal de propagation". PhD thesis. 2004, 1 vol. (162 p.) URL: http://www.theses.fr/2004LIL10002.

[210] Simon R. Saunders. *Antennas and Propagation for Wireless Communication Systems.* Wiley, US, 1999, p. 409. ISBN: 0-471-98609-7.

[211] Samuel Betrencourt. "Caractérisation du canal de propagation en tunnel routier et ferroviaire : applications". PhD thesis. Université de Lille, 2000. URL: http://www.theses.fr/2000LIL10037.

[212] *3GPP Specification # 38.101-1 v17.0.0 - NR; User Equipment (UE) radio transmission and reception; Part 1: Range 1 Standalone*. Tech. rep. URL: https://portal.3gpp.org/desktopmodules/Specifications/SpecificationDetails.aspx?specificationId=3283 (visited on 03/17/2021).